ST. PETERSBURG STATE POLYTECHNICAL UNIVERSITY

JOURNAL

Physics and Mathematics

VOLUME 18, No.3, 2025

НАУЧНО-ТЕХНИЧЕСКИЕ ВЕДОМОСТИ

САНКТ-ПЕТЕРБУРГСКОГО ГОСУДАРСТВЕННОГО ПОЛИТЕХНИЧЕСКОГО УНИВЕРСИТЕТА

Физико-математические науки

ТОМ 18, №3
2025

НАУЧНО-ТЕХНИЧЕСКИЕ ВЕДОМОСТИ САНКТ-ПЕТЕРБУРГСКОГО ГОСУДАРСТВЕННОГО ПОЛИТЕХНИЧЕСКОГО УНИВЕРСИТЕТА. ФИЗИКО-МАТЕМАТИЧЕСКИЕ НАУКИ

Contents

Содерж ние

CONDENSED MATTER PHYSICS

CRITICAL SCATTERING OF SYNCHROTRON RADIATION IN THE LEAD ZIRCONATE-TITANATE (PZT2.4) USING THE LAST MODEL FOR THE SOFT MODE

S. B. Vakhrushev[1,2,3], S. A. Reimers[2,3]✉, Iu. A. Bronwald[1]

[1] Ioffe Institute, St. Petersburg, Russia;

[2] Peter the Great St. Petersburg Polytechnic University, St. Petersburg, Russia;

[3] Pacific National University, Khabarovsk, Russia

✉ serafim.reimers@yandex.ru

Abstract. In this work, an experimental and theoretical studies of critical scattering for the $PbZr_{0.976}Ti_{0.024}O_3$ (PZT2.4) compound in the vicinity of the Brillouin zone center have been carried out taking into account the mode coupling. The scattering measurements were carried out at the European Synchrotron Radiation Facility (ESRF). One-dimensional profiles of the scattering intensity dependence on the wave vector were obtained using specially developed programs. The Last model was used for the optical soft mode in the Brillouin zone center. The frequencies and polarization vectors of the renormalized modes were determined by quantitative analysis of the scattering profile for the soft direction [1 0 1]. Good agreement between the calculated results of the model and the experimental data was achieved. The polarization vector's change of the lowest transverse acoustic mode was traced as a function of the reduced wave vector.

Keywords: ferroelectric, antiferroelectric, phase transition, lattice dynamics, critical scattering

Citation: Vakhrushev S. B., Reimers S. A., Bronwald Iu. A., Critical scattering of synchrotron radiation in the lead zirconate-titanate (PZT2.4) using the Last model for the soft mode, St. Petersburg State Polytechnical University Journal. Physics and Mathematics. 18 (3) (2025) 9−19. DOI: https://doi.org/10.18721/JPM.18301

КРИТИЧЕСКОЕ РАССЕЯНИЕ СИНХРОТРОННОГО ИЗЛУЧЕНИЯ В ЦИРКОНАТЕ-ТИТАНАТЕ СВИНЦА (PZT2.4) С ИСПОЛЬЗОВАНИЕМ МОДЕЛИ ЛАСТА ДЛЯ МЯГКОЙ МОДЫ

С. Б. Вахрушев[1,2,3], С. А. Реймерс[2,3✉], Ю. А. Бронвальд[1]

[1] Физико-технический институт им. А. Ф. Иоффе РАН, Санкт-Петербург, Россия;

[2] Санкт-Петербургский политехнический университет Петра Великого, Санкт-Петербург, Россия;

[3] Тихоокеанский государственный университет, г. Хабаровск, Россия

✉ serafim.reimers@yandex.ru

Аннотация. В работе проведено экспериментальное и теоретическое исследование критического рассеяния для соединения $PbZr_{0,976}Ti_{0,024}O_3$ (PZT2.4), в окрестности центра зоны Бриллюэна с учетом межмодового взаимодействия. Измерение рассеяния проводилось на Европейском источнике синхротронного излучения (ESRF). Одномерные профили зависимости интенсивности рассеяния от волнового вектора были получены с использованием специально разработанных программ. Для оптической мягкой моды в центре зоны Бриллюэна была использована модель Ласта. Путем количественного анализа профиля рассеяния для мягкого направления [1 0 1] определены частоты и векторы поляризации перенормированных мод. Достигнуто хорошее согласие модельного расчета с экспериментальными данными. Прослежено изменение вектора поляризации низшей поперечной акустической моды как функции приведенного волнового вектора.

Ключевые слова: сегнетоэлектрик, антисегнетоэлектрик, фазовый переход, динамика решетки, критическое рассеяние

Ссылка для цитирования: Вахрушев С. Б., Реймерс С. А., Бронвальд Ю. А. Критическое рассеяние синхротронного излучения в цирконате-титанате свинца (PZT2.4) с использованием модели Ласта для мягкой моды // Научно-технические ведомости СПбГПУ. Физико-математические науки. 2025. Т. 18. № 3. С. 9–19. DOI: https://doi.org/10.18721/JPM.18301

Introduction

Comprehensive analysis of X-ray or neutron diffraction patterns of any crystal, even the most perfect ones, shows a diffuse component consisting of some streaks, spots or halos around the main reflections in addition to the sharp Bragg peaks. This background component is commonly known as diffuse scattering. It provides valuable data about the inherently present static or dynamic disorder. Lonsdale and Smith [1] described the very first observations of diffuse scattering in the early 20th century.

There are many excellent books and reviews on the general aspects of diffuse scattering and its application to analysis of diverse physical problems. The most common type of such scattering is thermal diffuse scattering (TDS) by crystal lattice vibrations [2, 3]. The TDS intensity I can be described by the following expression:

$$I_{TDS}(\mathbf{Q}) = I_0 \sum_\lambda \frac{1}{\omega_\lambda^2(\mathbf{q})} \left| F_\lambda(\mathbf{Q}, \mathbf{q}) \right|^2 \delta(\mathbf{Q} - \mathbf{q} - \boldsymbol{\tau}), \tag{1}$$

where $\mathbf{Q}$ is the scattering vector; $\mathbf{q} = \mathbf{Q} - \boldsymbol{\tau}$ is the reduced wave vector; $\boldsymbol{\tau}$ is the reciprocal lattice vector; ω_λ is the frequency of mode λ; $F_\lambda(\mathbf{Q,q})$ is the inelastic structure factor.

The factor $F_\lambda(\mathbf{Q,q})$ is determined by the crystal structure (the position r_μ of the atoms in the unit cell) and the polarization vectors of the phonon modes $\mathbf{e}_\mu^\lambda(\mathbf{q})$:

$$F_\lambda(\mathbf{Q,q}) = \sum_\mu \frac{f_\mu(\mathbf{Q})}{\sqrt{2M_\mu}} e^{-W_\mu(\mathbf{Q})} e^{i\mathbf{Q}\cdot\mathbf{r}_i} (\mathbf{Q}\cdot\mathbf{e}_\mu^\lambda(\mathbf{q})), \qquad (2)$$

where M_μ is the atomic mass; $e^{-W_\mu(\mathbf{Q})}$ is the Debye−Waller factor; $\mathbf{r}_\mu$ is the position of atom μ in the unit cell; $\mathbf{e}_\mu^\lambda(\mathbf{q})$ is the phonon eigenvector for wave vector $\mathbf{q}$ and mode λ, corresponding to atom μ; $f_\mu(\mathbf{Q})$ is the atomic form factor.

It follows from Eq. (1) that TDS by acoustic phonons should be observed in the vicinity of Bragg peaks in all crystals. The frequency of acoustic phonons with small reduced wave vectors is proportional to the magnitude of q. Thus, TDS intensity is inversely proportional to q^2 and the anisotropy is determined by the anisotropy of the sound velocity.

Another important type of TDS is critical scattering by fluctuations in the order parameter in crystals undergoing a phase transition. Critical scattering can be localized around different points of the Brillouin zone, and this localization depends on the symmetry of the order parameter.

Critical scattering in ferroelectrics is of particular interest to us and we intend to focus on it closely in the paper. Apparently, this type of scattering in ferroelectrics was described for the first time in [4]. Similar to the case of diffuse scattering by acoustic phonons, critical scattering in ferroelectrics is concentrated in the vicinity of the Brillouin zone center.

One of the characteristics of critical scattering in intrinsic ferroelectrics is significant suppression of the longitudinal scattering component. This phenomenon was first discovered in [5]. In the case of a cubic isotropic ferroelectric, the expression for the intensity of critical scattering in the paraelectric phase takes the form

$$I(\mathbf{Q} = \boldsymbol{\tau} + \mathbf{q}) = \frac{I_0 \kappa^2 \sin^2\left(\widehat{\mathbf{Q,q}}\right)}{q^2 + \kappa^2}, \qquad (3)$$

where I_0 is the peak scattering intensity at $\mathbf{q} = 0$, proportional to static susceptibility χ_0; κ^2 is the square of the inverse correlation length of short-range ferroelectric order.

Cross-sections of surfaces with constant diffuse scattering intensity by planes containing the vector $\boldsymbol{\tau}$ yield constant-intensity contours in the form of two tangent circles (lemniscates) with a zero intensity line coinciding with $\boldsymbol{\tau}$. Taking into account cubic anisotropy somewhat complicates the expressions, however, the intensity remains equal to zero in the case of $\mathbf{q} \parallel \boldsymbol{\tau}$.

Thus, diffuse scattering in the paraelectric phase in the vicinity of the Brillouin zone center includes two components: thermal diffuse scattering by acoustic phonons and critical scattering from the soft mode. Analysis of the data for the vicinities of several nodes of the reciprocal lattice allows to separate these components.

However, the problem becomes significantly more complicated in the presence of mode coupling between transverse optical and acoustic modes. The problem of mode coupling in ferroelectric perovskites was theoretically analyzed in detail in [6−8]. It was found that this coupling leads to significant renormalization of phonon frequencies at $\mathbf{q} \neq 0$ and mixing of polarization vectors of these modes. The Vaks model was applied in [9] to analyze the phonon spectra of potassium tantalate ($KTaO_3$) and in [10−12] to analyze the critical dynamics in lead zirconate ($PbZrO_3$). Renormalization of phonon mode frequencies was correctly described in all cases. As for the mixing of polarization vectors in these papers, only general expressions were given for the polarization vectors $\mathbf{v}_{\lambda\mu\alpha}$ (α is the Cartesian coordinate, λ and μ are defined above) of renormalized modes in terms of phonon eigenvectors at $q = 0$, where there is no coupling. However, their specific type was not determined due to the uncertainty of the eigenvector for soft mode. The diffuse scattering patterns given in [10−12] can only be regarded as qualitative, since they take into account only the directions of ion displacements.

Our paper analyzes diffuse scattering in a solid solution of lead zirconate titanate $PbZr_{0.976}Ti_{0.024}O_3$ (PZT2.4) using the Last model to describe the eigenvector of the soft mode.

Experimental

The measurements were carried out for a sample measuring approximately $1.00 \times 0.05 \times 0.05$ mm, cut from a single crystal of PZT2.4 solid solution grown at the Southern Federal University using the technology described in [13]. The sample was ground and etched in boiling hydrochloric acid to remove the damaged surface layer.

The experiment was conducted using the equipment of the European Synchrotron Radiation Facility (ESRF). The needle-like sample was mounted into a special holder. The holder had the angular range of 150°, allowing to cover a large volume of the reciprocal space. The sample was placed in a nitrogen flux to control its temperature. The wavelength of incident radiation was 0.95 E. A low-noise Pilatus 2M detector was used; the distance from the sample to the detector was 135 mm. The measurements were carried out both under cooling and under heating with a temperature step of 1 °C over a range from 30 to 300 °C.

Software tools developed in MatLab and Java were used to construct one-dimensional profiles of the dependence of scattering intensity on the wave vector. Such diffuse scattering profiles were obtained from a three-dimensional intensity distribution by voxelization. Instead of traditional cubic voxels, we used a voxel that was a straight circular cylinder whose axis coincides with the direction of the profile. Varying the parameters of the cylindrical voxel, we selected its optimal size providing the necessary statistics: a sufficient number of primary detector pixels inside the voxel and the resolution of the wave vector $\mathbf{q}$. The voxel radius was 0.2 r.l.u. (reciprocal lattice unit equal to $2\pi/a$), the step was 0.1 r.l.u.

Vaks model with calculation of eigenvectors

We adopted the hypothesis that diffuse scattering is associated with the lowest phonon modes. As shown in [6, 7, 9], calculation and analysis of the corresponding lattice dynamics are simplified in the long-wavelength limit if high-energy optical modes are neglected; in this case, the latter do not give a significant contribution to diffuse scattering. The resulting simplified Hamiltonian takes into account only five modes: three acoustic (2TA (transverse) + LA (longitudinal)) and two low-energy transverse optical (2TO).

The simplified Hamiltonian has the following form:

$$H^{(5)} = \frac{1}{2}\sum_q \left[\dot{\mathbf{u}}_{-q}\dot{\mathbf{u}}_q + \mathbf{u}_{-q}\hat{A}(\mathbf{q})\mathbf{u}_q + \dot{\mathbf{x}}_{-q}\dot{\mathbf{x}}_q + \lambda\mathbf{x}_{-q}\mathbf{x}_q + \mathbf{x}_{-q}\hat{S}(\mathbf{q})\mathbf{x}_q + 2\mathbf{u}_{-q}\hat{V}(\mathbf{q})\mathbf{x}_q \right], \tag{4}$$

where u_1, u_2, u_3 and x_1, x_2 (components of vectors $\mathbf{u}$ and $\mathbf{x}$) are the normal coordinates for modes 2TA + LA and 2TO in the reference frame $(X'Y'Z')$, with the Z'-axis parallel to the reduced wave vector $\mathbf{q}$, respectively; B, $\hat{S}$, $\hat{V}$ are tensors.

These tensors describe the contribution of short-range interactions and can be written as

$$\hat{A}(\mathbf{q}) = q^2\left(A_a g^a + A_l g^l + A_t g^t \right), \tag{5}$$

$$\hat{S}(\mathbf{q}) = q^2\left(S_a g^a + S_t g^t \right), \tag{6}$$

$$\hat{V}(\mathbf{q}) = q^2\left(V_a g^a + V_t g^t \right), \tag{7}$$

where $g^t_{\alpha\beta} = \delta_{\alpha\beta} - n_\alpha n_\beta$; $g^l_{\alpha\beta} = n_\alpha n_\beta$; $g^a_{\alpha\beta} = \gamma_{\alpha\beta\gamma\delta}n_\gamma n_\delta$.

In this equation, $\mathbf{n} = \mathbf{q}/q$ is a unit vector in the direction of $\mathbf{q}$; $\gamma_{\alpha\beta\gamma\delta}$ is a tensor invariant with respect to the symmetry operations of a cubic point group such that

$$\gamma_{\alpha\beta\gamma\delta} = 1 \text{ for } \alpha = \beta = \gamma = \delta \text{ and } \gamma_{\alpha\beta\gamma\delta} = 0 \text{ in all other cases.}$$

The tensor $B(\mathbf{q})$ defines the speed of sound and can be determined from the elastic modulus C, the tensor $\hat{S}(\mathbf{q})$ defines the curvature of the transverse optical mode and the tensor $\hat{V}(\mathbf{q})$ defines the constant of interaction between acoustic and optical branches.

The five-mode Hamiltonian was represented as the sum of isotropic and anisotropic components:

$$H^{(5)}(\mathbf{q}) = H_{is}\left(|q|, \lambda, S_t, A_t, V_t, A_l\right) + H_{anis}\left(\mathbf{q}, S_a, A_a, V_a\right), \tag{8}$$

12

$$H_{is} = \begin{pmatrix} \lambda + S_t q^2 & 0 & V_t q^2 & 0 & 0 \\ 0 & \lambda + S_t q^2 & 0 & V_t q^2 & 0 \\ V_t q^2 & 0 & A_t q^2 & 0 & 0 \\ 0 & V_t q^2 & 0 & A_t q^2 & 0 \\ 0 & 0 & 0 & 0 & A_l q^2 \end{pmatrix}, \tag{9}$$

$$H_{anis} = q^2 \begin{pmatrix} S_a h_{11} & S_a h_{12} & V_a h_{11} & V_a h_{12} & V_a h_{13} \\ S_a h_{12} & S_a h_{22} & V_a h_{12} & V_a h_{22} & V_a h_{23} \\ V_a h_{11} & V_a h_{12} & A_a h_{11} & A_a h_{12} & A_a h_{13} \\ V_a h_{12} & V_a h_{22} & A_a h_{12} & A_a h_{22} & A_a h_{23} \\ V_a h_{13} & V_a h_{23} & A_a h_{13} & A_a h_{23} & A_a h_{33} \end{pmatrix}, \tag{10}$$

where

$$h_{11} = \frac{2 n_2^2 n_3^2}{n_\perp^2}, \quad h_{12} = \frac{(n_1 n_2 n_3)}{n_\perp^2}(n_3^2 - n_2^2),$$

$$h_{22} = 2 n_1^2 \left(n_\perp^2 - \frac{n_2^2 n_3^2}{n_\perp^2} \right), \quad h_{13} = \frac{n_2 n_3}{n_\perp}\left(n_2^2 - n_3^2 \right),$$

$$h_{33} = n_1^4 + n_2^4 + n_3^4, \quad h_{23} = \frac{n_1}{n_\perp}\left(n_1^2 n_\perp^2 - n_2^4 - n_3^4 \right),$$

$$n_\perp^2 = n_2^2 + n_3^2,$$

Diagonalization of the Hamiltonian $H^{(5)}(\mathbf{q})$ allows to obtain a set of frequencies $\omega_\lambda(\mathbf{q})$ of renormalized modes and a matrix of polarization vectors $D_\lambda(\mathbf{q})$ expressed in terms of the eigenvectors of uncoupled modes in the $X'Y'Z'$ coordinate system considered above. As a first approximation of the eigenvectors, we can select the polarization vectors of phonon modes in the center of the Brillouin zone $V_{\mu a}^{\lambda_0}$ (λ_0 is the number of non-renormalized phonon branch, μ is the number of the atom in the unit cell, α is the Cartesian coordinate).

We use the following numbering of atoms in the cell:

1 for Pb, $\mathbf{r}_1$ = (0 0 0); 2 for Zr (Ti), $\mathbf{r}_2$ = (½ ½ ½); 3 for O$_I$, $\mathbf{r}_3$ = (½ 0 ½);

4 for O$_{II}$, $\mathbf{r}_4$ = (0 ½ ½); 5 for O$_{III}$, $\mathbf{r}_5$ = (½ ½ 0). $\mathbf{r}_i$ is the coordinate of the ith atom in the cell in fractions of the lattice parameter a= 4.6 Å.

The matrix $D_{\lambda j}$ can be transformed into a three-dimensional array of eigenvectors $p_{\nu \lambda l \alpha}$ in the Cartesian coordinate system if the metric matrix $M(\mathbf{n})$ is used [9]:

$$M(\mathbf{n}) = \begin{pmatrix} 0 & n_\perp & n_1 \\ -\dfrac{n_3}{n_\perp} & -\dfrac{n_1 n_2}{n_\perp} & n_2 \\ \dfrac{n_2}{n_\perp} & -\dfrac{n_1 n_3}{n_\perp} & n_3 \end{pmatrix}, \tag{11}$$

$$pv_{\lambda 1 a} = M \times D_{\lambda, j}, \quad j = 3, 4, 5,$$

$$pv_{\lambda 2 a} = M \times (D_{\lambda, j}, 0), \quad j = 1, 2, \tag{12}$$

The case $l = 1$ corresponds to the contribution of non-renormalized acoustic phonons and $l = 2$ corresponds to the contribution of non-renormalized optical phonons.

Let us introduce the eigenvector matrices $e^{(1)}_{\alpha\mu}$ and $e^{(2)}_{\alpha\mu}$ which are the partial contributions of the atom μ to the displacements corresponding to the acoustic and optical modes, respectively. The index $\alpha = 1, 2, 3$ determines the direction of the displacements.

The values of the elements $e^{(1)}_{\alpha\mu}$ can be determined from the condition that the displacements of all atoms in the cell be equal [14]:

$$u_{\alpha\mu} = \frac{e^{(1)}_{\alpha\mu}}{\sqrt{m_\mu}} = \text{const.} \tag{13}$$

Such a priori definition of $e^{(2)}_{\alpha\mu}$ is impossible for a soft optical mode. The irreducible representation Γ_{15} enters the mechanical representation for the perovskite structure four times, so accordingly, three optical modes of this symmetry should be observed. The Ewald mode, the Last mode, and the Axe mode are often chosen as such modes with mutually orthogonal polarization vectors [15]. It is typically assumed that the soft mode for lead-containing ferroelectrics with a rhombohedral structure is the Last mode. It is also assumed that the Pb^{2+} cation is displaced relative to the group of ions formed by the oxygen octahedron and the central cation.

To simplify the problem, we use the diatomic approximation, assuming that the optical mode can be described if the above group is regarded as a virtual A2 cation.

For the acoustic mode, we can write the following representation without loss of generality:

$$e^{(1)}_{\alpha\mu} = \begin{pmatrix} \sqrt{m_{Pb}} & \sqrt{m_{A2}} & \sqrt{m_{A2}} & \sqrt{m_{A2}} & \sqrt{m_{A2}} \\ \sqrt{m_{Pb}} & \sqrt{m_{A2}} & \sqrt{m_{A2}} & \sqrt{m_{A2}} & \sqrt{m_{A2}} \\ \sqrt{m_{Pb}} & \sqrt{m_{A2}} & \sqrt{m_{A2}} & \sqrt{m_{A2}} & \sqrt{m_{A2}} \end{pmatrix} CC_1. \tag{14}$$

with the normalizing coefficient

$$CC_1 = \sqrt{m_{Pb} + 4m_{A2}},$$

where m_{Pb} is the mass of the Pb^{2+} cation, m_{A2} is the sum of the masses of all ions included in the virtual A2 ion.

Evidently,

$$u_{\alpha\mu} = \frac{e^{(1)}_{\alpha\mu}}{\sqrt{m_\mu}} = \text{const.}$$

For the optical mode, taking into account the constancy of the center of mass, we obtain:

$$e^{(2)}_{\alpha\mu} = \begin{pmatrix} -\sqrt{m_{A2}/m_{Pb}} & 1/4 & 1/4 & 1/4 & 1/4 \\ -\sqrt{m_{A2}/m_{Pb}} & 1/4 & 1/4 & 1/4 & 1/4 \\ -\sqrt{m_{A2}/m_{Pb}} & 1/4 & 1/4 & 1/4 & 1/4 \end{pmatrix} CC_2 \tag{15}$$

with the normalizing coefficient $CC_2 = \sqrt{m_{A2}/m_{Pb} + 1/4}.$

Indeed, the displacement of the center of mass turns out to equal zero:

$$\frac{\left(\sqrt{m_{A2}/m_{Pb}}\right)m_{Pb}}{\sqrt{m_{Pb}}}-4\frac{1}{4}\frac{m_{A2}}{\sqrt{m_{A2}}}=\sqrt{m_{A2}}-\sqrt{m_{A2}}=0. \tag{16}$$

We build an array of $5 \times 5 \times 3$ eigenvectors (number of modes $\times$ number of atoms $\times$ 3 coordinates) $v_{\lambda\mu\alpha}$:

$$v_{\lambda\mu\alpha}=pv_{\lambda1\alpha}\times e_{\alpha\mu}^{(1)}+pv_{\lambda2\alpha}\times e_{\alpha\mu}^{(2)}. \tag{17}$$

Then we can write the following expression for the structure factor of the mode λ:

$$F_\lambda\left(\mathbf{Q},\mathbf{q}\right)=\frac{f_{Pb}}{\sqrt{m_{Pb}}}e^{i\mathbf{Qr_1}}\left(\sum_{\alpha=1..3}\left(Q_\alpha v_{\lambda1\alpha}\right)\right)+$$

$$+\frac{1}{\sqrt{m_{A2}}}\left\{f_{Zr}e^{i\mathbf{Qr_2}}\left(\sum_{\alpha=1..3}\left(Q_\alpha v_{\lambda2\alpha}\right)\right)+f_O\left[e^{i\mathbf{Qr_3}}\left(\sum_{\alpha=1..3}\left(Q_\alpha v_{\lambda3\alpha}\right)\right)+\right. \tag{18}$$

$$\left.\left.+e^{i\mathbf{Qr_4}}\left(\sum_{\alpha=1..3}\left(Q_\alpha v_{\lambda4\alpha}\right)\right)+e^{i\mathbf{Qr_5}}\left(\sum_{\alpha=1..3}\left(Q_\alpha v_{\lambda5\alpha}\right)\right)\right]\right\}.$$

The values of the atomic scattering factors are calculated by the formulas given in [16].

Analysis of experimental data

We analyzed one-dimensional scans along the [1 0 1] direction through the reciprocal lattice nodes (1 0 −1) and (0 0 3). The diffuse scattering intensity at point $\mathbf{Q}$ was calculated as follows:

$$I\left(\mathbf{Q}\right)=I_0\sum_{\lambda=1}^{5}F_\lambda^2\left(\mathbf{Q},\mathbf{q}\right)\frac{1}{\omega_\lambda^2\left(\mathbf{q}\right)}+\mathrm{Bck}, \tag{19}$$

where $\omega_\lambda^2(\mathbf{q})$ is the square of the frequency of the renormalized mode λ, equal to λth eigenvalue of the Hamiltonian $H^{(5)}(\mathbf{q})$; the expression $F_\lambda^2(\mathbf{Q},\mathbf{q})$ is calculated by Eq. (18); I_0 is the scale factor; the term Bck is the background.

Parameters A_l, A_t, A_a, S_t, S_a (in $(\mathrm{meV})^2/(\mathrm{r.l.u.})^2$) were assumed to be equal to the values for pure lead zirconate, given in [12]:

$$A_l = 2508, A_t = 879, A_a = -111, S_t = 1800, S_a = -610.$$

The results were processed in two stages. At the first stage, the parameters V_t, ω_0^2, the scale multiplier and background were fitted for the node (1 0 −1). Since the experimental data for different nodes were normalized differently, only the scale factor and background were fitted for node (0 0 3) and the remaining parameters were taken from the fit for node (1 0 −1).

Experimental data in Fig. 1 are shown by dots and their statistical errors are shown by vertical bars. The central region $-0.05 \le q \le 0.05$ to which Bragg scattering makes a contribution was excluded from the fit. It can be seen that the calculated curves completely coincide with the experimental ones within the limits of statistical errors.

As a result of the fitting, we obtained the following parameter values:

$$V_t = 1073\ (\mathrm{meV})^2/(\mathrm{r.l.u.})^2, \omega_0^2 = 4.58\ (\mathrm{meV})^2.$$

For comparison, we calculated the diffuse scattering intensity without taking into account the polarization vectors (red dashed lines in Fig. 1). In this case, the dependence $\omega_\lambda^2(\mathbf{q})$ and directions of atomic displacements $pv_{\lambda l\alpha}$ (12) were used.

For acoustic phonons, taking into account expression (18), we can write an expression for structure factors at $q = 0$ ($\mathbf{Q} = \tau$):
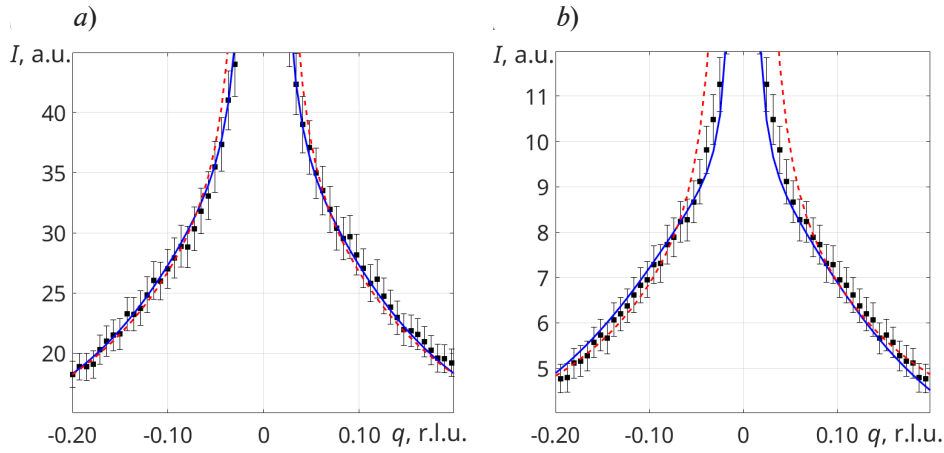
Fig. 1. Experimental (points) and calculated (lines) dependences of diffuse scattering intensity I on reduced wave vector $\mathbf{q}$ for two scattering vectors: $\mathbf{Q} = (1 + q, 0, -1 + q)$ (*a*) and $(q, q, 3)$ (*b*) Calculated data were obtained using polarization vectors (blue solid lines) and taking into account only the type of dispersion curves and the direction of displacements (red dashed lines). The statistical errors of the experiment are shown by vertical bars

$$F \sim f_{Pb} + f_{Zr}\cos(\pi(h+k+l)) +$$
$$+ f_o(\cos(\pi(h+k)) + \cos(\pi(h+k))\cos(\pi(h+k))). \tag{20}$$

Therefore,

$$F_{(1\,0\,-1)} \sim f_{Pb} + f_{Zr} - f_O,$$
$$F_{(0\,0\,3)} \sim f_{Pb} - f_{Zr} - f_O. \tag{21}$$

In the case of node (1 0 −1) with the larger structure factor, renormalization of the polarization vectors for acoustic phonons makes a relatively small contribution to intensity, that is, such a simplified calculation gives only qualitative agreement with the experiment (see Fig. 1,*a*).

On the other hand, renormalization of the polarization vectors plays an important role in the case of node (0 0 3) with a small elastic structure factor. It should be noted here that data analysis in the vicinity of several nodes of the reciprocal lattice is required to reliably determine the parameters of the Hamiltonian $H^{(5)}(\mathbf{q})$. The fundamental principles for determining dispersion curves were addressed in [2]. While exact determination of phonon dispersion curves is impossible in the general case, the polarization vectors can be found.

We established the dependency $\nu_{\lambda\mu\alpha}(q)$. Fig. 2 shows the reduced displacements

$$u_{\lambda\mu\alpha}^N = \frac{\nu_{\lambda\mu\alpha}}{\sqrt{m_\mu}}$$

along the *x*-axis ($\alpha = 1$) for lead ($\mu = 1$) and zirconium ($\mu = 2$) atoms for the lowest phonon mode (which is transverse acoustic polarized in the (x 0 z) plane). At $q = 0$, the given displacements are equal, as they should be for acoustic vibrations. As q increases, the contribution of lead displacements increases dramatically. The obtained result is in good agreement with the assumption made in [10] that it is the softening
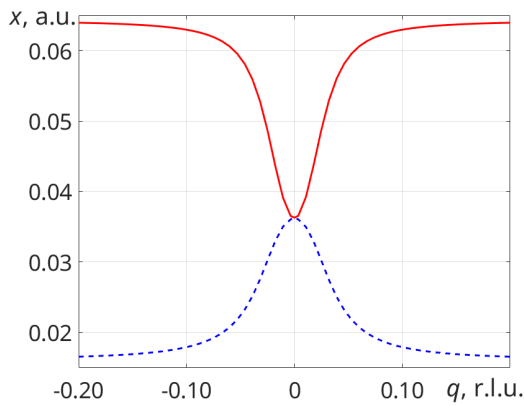
Fig. 2. Dependences of reduced displacements along the *x*-axis for lead (red solid line) and zirconium (blue dashed line) for the lowest phonon mode

of the renormalized transverse acoustic phonon branch that causes the transition to the antiferroelectric phase and that this transition is associated with antiparallel displacements of lead ions.

Conclusion

The study develops an approach to quantifying diffuse scattering in the vicinity of the Brillouin zone center in perovskite-like crystals in the presence of mode coupling. Phonon dispersion curves were calculated using the Vaks model. The polarization vectors of renormalized phonon modes were described as a linear combination of eigenvectors of transverse acoustic and optical phonons in the center of the Brillouin zone, where mode coupling is absent. The Last model was used to describe the soft mode associated with the ferroelectric phase transition. This model assumes that the lead cation oscillates relative to a rigid-body group of atoms including an oxygen octahedron and a central cation. The mixing coefficients depending on the reduced wave vector were determined from diagonalization of the five-mode Hamiltonian. The developed approach was used to analyze diffuse scattering in solid solution of the PZT2.4 ferroelectric.

A comparison between the experimental data and the calculations was carried out for the vicinity of the reciprocal lattice nodes (1 0 −1) and (0 0 3). It was confirmed that the proposed formalism provides a good description of the experimental data in both nodes simultaneously.

The approach we proposed and developed allows to efficiently analyze data simultaneously in several Brillouin zones and reliably determine the parameters of the dynamic Hamiltonian. We established the dependence of reduced atomic displacements on the reduced magnitude of the wave vector, confirming the predominant role of renormalization of the acoustic phonon branch for the antiferroelectric transition associated with antiparallel displacements of the lead ion.

REFERENCES

1. **Lonsdale K.Y., Smith H.,** An experimental study of diffuse X-ray reflexion by single crystals, Proc. R. Soc. Lond. A. 179 (976) (1941) 8−50.

2. **Xu R., Chiang T. C.,** Determination of phonon dispersion relations by X-ray thermal diffuse scattering, Z. Kristallogr. Cryst. Mater. 220 (12) (2005) 1009−1016.

3. **Welberry T. R., Weber T.,** One hundred years of diffuse scattering, Crystallogr. Rev. 22 (1) (2016) 2−78.

4. **Comes R., Lambert M., Guinier A.,** Dйsordre linйaire dans les cristaux (cas du silicium, du quartz, et des pйrovskites ferroйlectriques), Acta Cryst. A26 (2) (1970) 244−254.

5. **Cochran W.,** Dynamical, scattering and dielectric properties of ferroelectric crystals, Adv. Phys. 18 (72) (1969) 157−192.

6. **Vaks V. G.,** Vvedenie v mikroskopicheskuyu teoriyu segneto-elektrikov. [Introduction to the microscopic theory of ferroelectrics], Nauka Publishing, Moscow, 1973 (in Russian).

7. **Vaks V. G.,** Phase transitions of the displacement type in ferroelectrics, J. Exp. Theor. Phys. 27 (3) (1968) 486−494.

8. **Axe J. D., Harada J., Shirane G.,** Anomalous acoustic dispersion in centrosymmetric crystals with soft optic phonons, Phys. Rev. B. 1 (3) (1970) 1227−1234.

9. **Farhi E., Tagantsev A. K., Currat R., et al.,** Low energy phonon spectrum and its parameterization in pure $KTaO_3$ below 80 K, Eur. Phys. J. B. 15 (4) (2000) 615−623.

10. **Tagantsev A. K., Vaideeswaran K., Vakhrushev S. B., et al.,** The origin of antiferroelectricity in $PbZrO_3$, Nat. Commun. 4 (1) (2013) 2229−2236.

11. **Burkovsky R. G., Tagantsev A. K., Vaideeswaran K., et al.,** Lattice dynamics and antiferroelectricity in $PbZrO_3$ tested by X-ray and Brillouin light scattering, Phys. Rev. B. 90 (14) (2014) 144301.

12. **Andronikova D. A., Burkovsky R. G., Filimonov A. V., et al.,** Phonon dispersion calculations using the Vaks model in antiferroelectric lead zirconate, J. Adv. Dielectr. 5 (02) (2015) 1550016.

13. **Leontiev N. G., Smotrakov V. G., Fesenko E. G.,** Phase diagram of $PbZr_{1−x}Ti_xO_3$ with $x < 0.1$, Inorg. Mater. 18 (3) (1982) 374.

14. **Sylyom J.,** Fundamentals of the physics of solids, Vol. 1., Springer-Verlag, Inc, Berlin, Heidelberg, 2007.

15. **Harada J., Axe J. D., Shirane G.,** Determination of the normal vibrational displacements in several perovskites by inelastic neutron scattering, Acta Cryst. A26 (6) (1970) 608−612.

16. Graz center of physics. Atomic form factors. http://lampx.tugraz.at/~hadley/ss1/crystaldiffraction/atomicformfactors/formfactors.php. Accessed May 16, 2025.

СПИСОК ЛИТЕРАТУРЫ

1. **Lonsdale K.Y., Smith H.** An experimental study of diffuse X-ray reflexion by single crystals // Proceedings of the Royal Society of London. Series A. 1941. Vol. 179. No. 976. Pp. 8−50.

2. **Xu R., Chiang T. C.** Determination of phonon dispersion relations by X-ray thermal diffuse scattering // Zeitschrift fьr Kristallographie-Crystalline Materials. 2005. Vol. 220. No. 12. Pp. 1009−1016.

3. **Welberry T. R., Weber T.** One hundred 2025s of diffuse scattering // Crystallography Reviews. 2016. Vol. 22. No. 1. Pp. 2−78.

4. **Comes R., Lambert M., Guinier A.** Dйsordre linйaire dans les cristaux (cas du silicium, du quartz, et des pйrovskites ferroйlectriques) // Acta Crystallographica. Section A: Foundations and Advances. 1970. Vol. A26. Part 2. Pp. 244−254.

5. **Cochran W.** Dynamical, scattering and dielectric properties of ferroelectric crystals // Advances in Physics. 1969. Vol. 18. No. 72. Pp. 157−192.

6. **Вакс В. Г.** Введение в микроскопическую теорию сегнетоэлектриков. М.: Наука, 1973. 327 с.

7. **Вакс В. Г.** О фазовых переходах типа смещения в сегнетоэлектриках // Журнал экспериментальной и теоретической физики. 1968. Т. 54. № 3. С. 910−926.

8. **Axe J. D., Harada J., Shirane G.** Anomalous acoustic dispersion in centrosymmetric crystals with soft optic phonons // Physical Review B. 1970. Vol. 1. No. 3. Pp. 1227−1234.

9. **Farhi E., Tagantsev A. K., Currat R., Hehlen B., Courtens E., Boatner L. A.** Low energy phonon spectrum and its parameterization in pure $KTaO_3$ below 80 K // The European Physical Journal B. 2000. Vol. 15. No. 4. Pp. 615−623.

10. **Tagantsev A. K., Vaideeswaran K., Vakhrushev S. B., et al.** The origin of antiferroelectricity in $PbZrO_3$ // Nature Communications. 2013. Vol. 4. No. 1. Pp. 2229−2236.

11. **Burkovsky R. G., Tagantsev A. K., Vaideeswaran K., et al.** Lattice dynamics and antiferroelectricity in $PbZrO_3$ tested by X-ray and Brillouin light scattering // Physical Review B. 2014. Vol. 90. No. 14. P. 144301.

12. **Andronikova D. A., Burkovsky R. G., Filimonov A. V., Tagantsev A. K., Vakhrushev S. B.** Phonon dispersion calculations using the Vaks model in antiferroelectric lead zirconate // Journal of Advanced Dielectrics. 2015. Vol. 5. No. 02. P. 1550016.

13. **Леонтьев Н. Г., Смотраков В. Г., Фесенко Е. Г.** Фазовая диаграмма $PbZr_{1-x}Ti_xO_3$ при $x <$ 0,1 // Известия Академии наук СССР. Неорганические материалы. 1982. Т. 18. № 3. С. 449−453.

14. **Sylyom J.** Fundamentals of the physics of solids. Vol. 1. Berlin, Heidelberg: Springer-Verlag, Inc, 2007. 697 p.

15. **Harada J., Axe J. D., Shirane G.** Determination of the normal vibrational displacements in several perovskites by inelastic neutron scattering // Acta Crystallographica. Section A: Foundations and Advances. 1970. Vol. A26. Part 6. Pp. 608−612.

16. Graz center of physics. Atomic form factors. Режим доступа: http://lampx.tugraz.at/~hadley/ss1/crystaldiffraction/atomicformfactors/formfactors.php (Дата обращения: 16.05.2025).

THE AUTHORS

VAKHRUSHEV Sergey B.
Ioffe Institute of RAS, St. Petersburg, Russia;
Peter the Great St. Petersburg Polytechnic University, St. Petersburg, Russia;
Pacific National University, Khabarovsk, Russia
26 Polytekhnicheskaya St., St. Petersburg, 194021, Russia
s.vakhrushev@mail.ioffe.ru
ORCID: 0000-0003-4867-1404

REIMERS Serafim A.
Peter the Great St. Petersburg Polytechnic University, St. Petersburg, Russia;
Pacific National University, Khabarovsk, Russia
29 Politekhnicheskaya St., St. Petersburg, 195251, Russia
serafim.reimers@yandex.ru
ORCID: 0009-0009-9951-758X

BRONWALD Iurii A.
Ioffe Institute of RAS
26 Polytekhnicheskaya St., St. Petersburg, 194021, Russia
yuramel@gmail.com
ORCID: 0000-0003-0225-0487

СВЕДЕНИЯ ОБ АВТОРАХ

ВАХРУШЕВ Сергей Борисович − *доктор физико-математических наук, главный научный сотрудник, заведующий лабораторией нейтронных исследований Физико-технического института имени А. Ф. Иоффе РАН, профессор Высшей инженерно-физической школы Санкт-Петербургского политехнического университета Петра Великого; ведущий научный сотрудник Тихоокеанского государственного университета.*
194021, Россия, г. Санкт-Петербург, Политехническая ул., 26
s.vakhrushev@mail.ioffe.ru
ORCID: 0000-0003-4867-1404

РЕЙМЕРС Серафим Андреевич − *аспирант Высшей инженерно-физической школы Санкт-Петербургского политехнического университета Петра Великого; младший научный сотрудник Тихоокеанского государственного университета.*
195251, Россия, г. Санкт-Петербург, Политехническая ул., 29
serafim.reimers@yandex.ru
ORCID: 0009-0009-9951-758X

БРОНВАЛЬД Юрий Алексеевич − *научный сотрудник Физико-технического института имени А. Ф. Иоффе РАН.*
194021, Россия, г. Санкт-Петербург, Политехническая ул., 26
yuramel@gmail.com
ORCID: 0000-0003-0225-0487

SIMULATION OF PHYSICAL PROCESSES

THE INFLUENCE OF NONLINEAR PARAMETRIC EXCITATION ON THE INTERACTION OF FORCED, PARAMETRIC AND SELF-OSCILLATIONS

A. A. Alifov✉

Mechanical Engineering Research Institute of the RAS, Moscow, Russia

✉ alishir@mail.ru

Abstract. In order to reveal the effect of nonlinear (cubic) parametric excitation (NPE) on the interaction of forced, parametric, and self-oscillation with a limited-power energy source, a widely used computed model of a self-oscillating system receiving energy from such a source was used. Solutions of nonlinear differential equations of the model were constructed using the direct linearization method (DLM), which is distinguished from the known ones by its simplicity its simplicity and low time costs. The friction force characteristic causing self-oscillations was linearized by DLM. Equations for the amplitude, oscillation phase and the velocity of the energy source in nonstationary and stationary motion cases were derived. Using the Routh − Hurwitz criteria, the stability of stationary movements was considered. The influence of NPE on the interaction of forced, parametric and self-oscillations was investigated by calculations. The latter showed NPE to change the shape of the amplitude curves inherent in linear action and to have a significant impact on the motion stability.

Keywords: interaction, forced oscillations, parametric oscillations, self-oscillations, nonlinearity, direct linearization method

ВЛИЯНИЕ НЕЛИНЕЙНОГО ПАРАМЕТРИЧЕСКОГО ВОЗБУЖДЕНИЯ НА ВЗАИМОДЕЙСТВИЕ ВЫНУЖДЕННЫХ, ПАРАМЕТРИЧЕСКИХ И АВТОКОЛЕБАНИЙ

А. А. Алифов✉

Институт машиноведения им. А. А. Благонравова РАН, Москва, Россия

✉ alishir@mail.ru

Аннотация. С целью выявления действия нелинейного (кубического) параметрического возбуждения (НПВ) на взаимодействие вынужденных, параметрических и автоколебаний при источнике энергии ограниченной мощности использована широко применяемая расчетная модель автоколебательной системы, получающая энергию от такого источника. Решения нелинейных дифференциальных уравнений модели построены методом прямой линеаризации (ПЛ), которому свойственны простота и малые затраты времени. Характеристика силы трения, вызывающая автоколебания, линеаризована методом ПЛ. Выведены уравнения для амплитуды, фазы колебаний и скорости источника энергии в нестационарном и стационарном случаях движения. С использованием критериев

Рауса − Гурвица рассмотрена устойчивость стационарных движений. Влияние НПВ на взаимодействие вынужденных, параметрических и автоколебаний исследовано и расчетным путем; расчеты показали, что НПВ изменяет форму амплитудных кривых, присущих линейному воздействию, оказывает существенное влияние на устойчивость движения.

Ключевые слова: взаимодействие, вынужденные колебания, параметрические колебания, автоколебания, нелинейность, метод прямой линеаризации

Introduction

The interaction of forced, parametric and self-oscillations is the most complex of the four classes of mixed oscillations according to the classification introduced in monograph [1]; they consist of a combination of oscillation types [2−4]. Of these four classes of mixed oscillations, the interaction of forced and parametric oscillations under cubic nonlinear parametric excitation (NPE) is considered in [5] without taking into account the properties of the energy source.

Taking the specified properties into account gained significance in connection with environmental problems, climate change and the reduction of energy resources. The need to take into account the properties of the energy source, which in the theory of oscillations is associated with the well-known Sommerfeld effect, is consistently stressed in fundamental monograph [6]. Many works have been published in this field all over the world, including books and articles [1, 7−17]. The connection between the level of energy consumed during the operation of parts, the accuracy of their processing and the oscillations is shown [18].

In this paper, we consider mixed forced, parametric and self-oscillations with NPE and limited power of the energy source. The direct linearization method (DLM) was used to solve nonlinear differential equations describing these oscillations [19].

Calculation model

Under the influence of frictional force, self-oscillations arise in many technical objects [20−24]. The model we consider is widely used to describe them (Fig. 1). A body with mass m is connected to the housing by means of a spring and a damper. It lies on a belt driven by a motor of limited-power with the torque $M(\dot{\varphi})$ and the total moment of inertia I of the rotating parts. A friction force $T(U)$ arises between the body and the belt, depending on the relative velocity U:

$$U = V - \dot{x}, \; V = r_0\dot{\varphi},$$

where r_0 is the radius of the pulley rotating the belt, r_0 = const; $\dot{\varphi}$ is the angular velocity of the motor rotor.

Taking into account the external driving force $\lambda\sin(v_1 t)$ and NPE $bx^3\cos(vt)$ acting on the body, the equations of motion of the system have the following form:
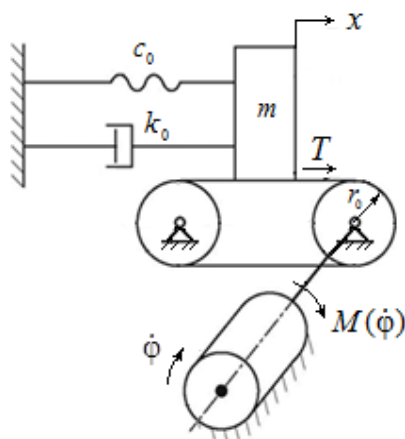
Fig. 1. Model of system considered:
body mass m; angular velocity of motor rotor $\dot{\varphi}$; torque $M(\dot{\varphi})$; friction force T; radius r_0 of the pulley rotating the belt; spring constant c_0 and damping ratio k_0

$$m\ddot{x} + k_0\dot{x} + c_0 x = T(U) + \lambda \sin \nu_1 t - bx^3 \cos \nu t \tag{1}$$

$$I\ddot{\varphi} = M(\dot{\varphi}) - r_0 T(U)$$

where k_0, c_0, λ, b, ν_1, ν are constants.

We take the friction force as a functional dependence, which is widespread in real (including cosmic) conditions [25]:

$$T(U) = T_0(\mathrm{sgn}\, U - \alpha_1 U + \alpha_3 U^3), \tag{2}$$

where T_0 is the normal reaction force, $T_0 = \mathrm{const}$; α_1, α_3 are constants; $\mathrm{sgn}\, U = 1$ at $U > 0$ and $\mathrm{sgn}\, U = -1$ at $U < 0$. In the case of $U = 0$, i.e., at relative rest, the inequalities $-T_0 \leq T(0) \leq T_0$ hold true.

Using the DLM [19], we replace the nonlinear components of the friction force $T(U)$ with a linear component:

$$T(U) = T_0(\mathrm{sgn}\, U + B_T + k_T \dot{x}), \tag{3}$$

where $B_T = -\alpha_1 u + \alpha_3 u^3 + 3N_2\alpha_3 u a^2 p^2$, $k_T = -\alpha_3 \overline{N}_3(a^2 p^2 - h)$, $h = 3(u_0^2 - u^2)/\overline{N}_3$, $u_0^2 = \alpha_1/3\alpha_3$,

$N_2 = (2r + 1)/(2r + 3)$, $\overline{N}_3 = (2r + 3)/(2r + 5)$.

The quantity r, included in the expressions for numerical coefficients N_2 and $\overline{N}_3$, represents a linearization accuracy parameter whose value is not limited, but it is sufficient to select it in the interval $(0, 2)$. The coefficients $\overline{N}_n$ and N_n are compared in [26] with the coefficients obtained by averaging [27−30] for different values of the degree of nonlinearity n, establishing the acceptable agreement for the results obtained by both methods.

In view of substitution (3), Eqs. (1) take the form

$$m\ddot{x} + k\dot{x} + c_0 x = T_0(\mathrm{sgn}\, U + B_T) + \lambda \sin \nu_1 t - bx^3 \cos \nu t, \tag{4}$$

$$I\ddot{\varphi} = M(\dot{\varphi}) - r_0 T_0(\mathrm{sgn}\, U + B_T + k_T \dot{x}),$$

where $k = k_0 - T_0 k_T$.

Solution of the equations

As shown in monograph [1], the solutions of equations with function (2) at $U > 0$ and $U < 0$ are fundamentally different, so they should be considered separately.

We represent these cases with expressions

$$u \geq ap,\; u < ap,$$

where $u = r_0\Omega$ (Ω is the averaged velocity $\dot{\varphi}$).

Let us consider solutions (4) for the main resonances with frequencies $\omega \approx \nu_1$ and $\omega \approx \nu/2$, since they are of primary practical interest.

Using the change of variables with averaging [19], we obtain the expressions

$$x = a \cos \psi,\; \dot{x} = -ap \sin \psi,\; \psi = pt + \xi,\; p = \nu/2,\; \dot{\varphi} = \Omega. \tag{5}$$

Next, we consider two cases.

i) $u \geq ap$, then

$$\frac{da}{dt} = -\frac{1}{4pm}\left(2aA + 2\lambda \cos \xi - 0.5ba^3 \sin 2\xi\right),$$

$$\frac{d\xi}{dt} = \frac{1}{4pma}\left[2am(\omega_0^2 - p^2) + 2\lambda \sin \xi + ba^3 \cos 2\xi\right], \tag{6a}$$

$$\frac{du}{dt} = \frac{r_0}{I}\left[M(\frac{u}{r_0}) - r_0 T_0(1 + B_T)\right];$$

ii) $u < ap$, then

$$\frac{da}{dt} = -\frac{1}{4pm}\left[2aA + 2\lambda\cos\xi - 0.5ba^3\sin 2\xi - \frac{8T_0}{\pi ap}\sqrt{a^2 p^2 - u^2}\right],$$

$$\frac{d\xi}{dt} = \frac{1}{4pma}\left[2am(\omega_0^2 - p^2) + 2\lambda\sin\xi + ba^3\cos 2\xi\right], \tag{6b}$$

$$\frac{du}{dt} = \frac{r_0}{I}\left[M(\frac{u}{r_0}) - r_0 T_0(1 + B_T) - \frac{r_0 T_0}{\pi}(3\pi - 2\psi_*)\right],$$

where $\omega_0^2 = c_0/m$.

The conditions $\dot{a} = 0$, $\dot{\xi} = 0$ in the case $u \geq ap$ provide the following relations for determining the stationary values of a and ξ:

$$(\lambda^2 b^2 a^6 + b^2 a^6 L - \lambda^4 + 2\lambda^2 L - L^2 - 4b^2 a^8 A^2)^2 - 4\lambda^2 b^4 a^{12} L = 0,$$

$$\tag{7}$$

$$\mathrm{tg}\xi = D(Dba^3 - 4\lambda)/8aA,$$

where $L = \lambda^2 + ba^4[ba^2 + 2m(\omega_0^2 - p^2)]$, $A = p(k_0 - T_0 k_T)$, $D = 2(\lambda \pm \sqrt{L})/ba^3$.

To determine the stationary values of the velocity u from the third equation in (6a), we have, provided that $\dot{u} = 0$, an expression of the form

$$M(u/r_0) - S(u) = 0, \tag{8}$$

where $S(u)$ is the load on the energy source from the oscillatory system.

In the case $u < ap$, to determine the amplitude of stationary oscillations, we have an approximate dependence $ap \approx u$ and the stationary values of the velocity u are determined by Eq. (8) taking into account the expression for the load

$$S(u) = r_0 T_0[(1 + B_T) + \pi^{-1}(3\pi - 2\psi_*)],$$

following from the third equation in (6b) for $\dot{u} = 0$.

Stability of stationary oscillations

To determine the stability of stationary oscillations of the system, we compose the variational equations for Eqs. (6), for which we use the Routh−Hurwitz criteria. As a result, we obtain the following conditions:

$$D_1 > 0,\ D_3 > 0,\ D_1 D_2 - D_3 > 0,$$

where $D_1 = -(b_{11} + b_{22} + b_{33})$,

$$D_2 = b_{11}b_{33} + b_{11}b_{22} + b_{22}b_{33} - b_{23}b_{32} - b_{12}b_{21} - b_{13}b_{31},$$

$$D_3 = b_{11}b_{23}b_{32} + b_{12}b_{21}b_{33} + b_{22}b_{13}b_{31} - b_{11}b_{22}b_{33} - b_{12}b_{23}b_{31} - b_{13}b_{21}b_{32}.$$

In the case of velocities $u \geq ap$, we have expressions of the form

$$b_{11} = \frac{r_0}{I}\left(Q - r_0 T_0\frac{\partial B_T}{\partial u}\right),\ b_{12} = -\frac{r_0^2 T_0}{I}\frac{\partial B_T}{\partial a},\ b_{13} = 0,$$

$$b_{21} = a\frac{T_0}{2m}\frac{\partial k_T}{\partial u},\ b_{22} = -\frac{1}{8pm}\left\{4p\left[k_0 + T_0\bar{N}_3\alpha_3(3a^2 p^2 - h)\right] - 3ba^2\sin 2\xi\right\},$$

$$b_{23} = \frac{1}{4pm}\left[2\lambda\sin\xi + ba^3\cos 2\xi\right],\ b_{31} = 0,$$

$$b_{32} = -\frac{1}{2pma^2}(\lambda\sin\xi - ba^3\cos 2\xi), \; b_{33} = \frac{1}{2pma}\left[\lambda\cos\xi - ba^3\sin 2\xi\right].$$

In the case $u < ap$, only the coefficients change and the expressions take the form

$$b_{11} = \frac{r_0}{I}\left[Q - r_0 T_0\frac{\partial B_T}{\partial u} - \frac{2r_0 T_0}{\pi\sqrt{a^2 p^2 - u^2}}\right], \; b_{12} = -\frac{r_0^2 T_0}{I}\left[\frac{\partial B_T}{\partial a} + \frac{2u}{\pi a\sqrt{a^2 p^2 - u^2}}\right],$$

$$b_{21} = \frac{a}{2m}\left[T_0\frac{\partial k_T}{\partial u} + \frac{4u T_0}{\pi a^2 p^2\sqrt{a^2 p^2 - u^2}}\right],$$

$$b_{22} = -\frac{1}{8pm}\left\{4p\left[k_0 + T_0\bar{N}_3\alpha_3(3a^2 p^2 - h)\right] - 3ba^2\sin 2\xi\right\} - \frac{2T_0 u^2}{\pi ma^2 p^2\sqrt{a^2 p^2 - u^2}},$$

where $\dfrac{\partial B_T}{\partial u} = -(\alpha_1 - 3\alpha_3 u^2 - 3\alpha_3 N_2 a^2 p^2), \; \dfrac{\partial B_T}{\partial a} = 6N_2\alpha_3 uap^2, \; \dfrac{\partial k_T}{\partial u} = -6\alpha_3 u, \; Q = dM(u/r_0)/du.$

Calculations

To obtain information on the effect of cubic NPE on the dynamics of mixed forced, parametric and self-oscillations, calculations were performed using the following parameter values:

$$\omega_0 = 1\text{ s}^{-1}, \; b = 0.686\text{ N·cm}^{-1}, \; \lambda = 0.196\text{ N}, \; k_0 = 0.196\text{ N·s·cm}^{-1}, \; T_0 = 4.9\text{ N},$$

$$\alpha_1 = 0.84\text{ s·cm}^{-1}, \; \alpha_3 = 0.18\text{ s}^3\text{·cm}^{-3}, \; r_0 = 1\text{ cm}, \; I = 9.8\text{ N·S·cm}^2.$$

When calculating the amplitude for the linearization coefficient k_T, the number $\bar{N}_3 = 3/4$ was used, which is obtained with the linearization accuracy parameter value $r = 1.50$. For the linearization coefficient B_T, the number $N_2 = 3/5$ ($r = 0.65$) was used. The quantities in the figures and in the text below are normalized.

Fig. 2 shows the frequency response curves $a(\nu)$ obtained by calculations based on Eq. (7). The horizontal lines labeled a_a correspond to the amplitudes of self-oscillations arising at velocities $u = 1.14$ and 1.20.
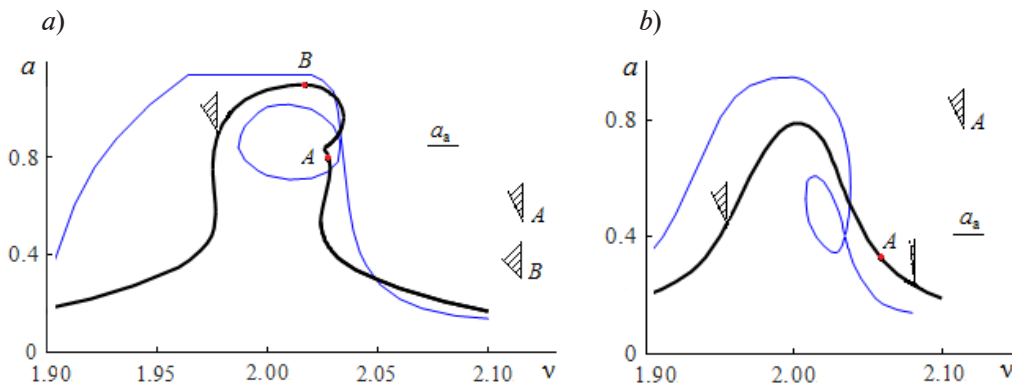
Fig. 2. Frequency response curves at velocities $u = 1.14$ (*a*) and 1.20 (*b*).
The blue curves are shown for comparison and represent a linear parametric excitation
of the form $x\cos(\nu t)$. The horizontal lines labeled a_a show the level of self-oscillation amplitudes.
The shaded sectors reflect the slope Q of the energy source characteristic ($Q = dM(u/r_0)/du$)
and correspond to stable amplitudes (at point *A* and in other positions)

The horizontal section on the blue curve (see Fig. 2,*a*) corresponds to the approximate dependence $ap \approx u = 1.14$. The oscillations are stable for the energy source characteristics whose slope Q lies within the shaded sector ($Q = dM(u/r_0)/du$).

The blue curves represent the linear parametric excitation $x\cos(vt)$ and are shown for comparison with NPE $x^3\cos(vt)$. This comparison shows the difference in the effect of linear and nonlinear parametric excitations on the dynamics of the system. The amplitude levels, shapes of the excitation curves and widths of the resonance regions differ for these excitations. A difference may also be observed in the number of amplitudes at the same frequency. For example, it can be seen from Fig. 2,*a* that the frequencies near point *A* have three amplitudes under linear excitation, and four under nonlinear excitation. On the other hand, Fig. 2,*b* shows that frequencies with more than one amplitude are absent under NPE but present under linear excitation.

The solution to differential equations (1) was also obtained numerically. The characteristic of the energy source for the solution was taken in the form

$$M(\dot{\varphi}) = M_0 - Q\dot{\varphi}.$$

The slope varied within the range $0 < Q \le 20$, where the value of $Q = 20$ corresponds to an angle of approximately 87°. As an example, Fig. 3 shows a graph for one of the solutions obtained for different values of the parameters M_0, Q, p. The numbers in the frames (in blue) were obtained computationally. In the case of the solution shown in Fig. 3, the values of the parameters $M_0 = 5.9889$, $Q = 5$ were taken, allowing to reach the mode with the average angular velocity of the motor rotor $\dot{\varphi} = 1.1401$ (Y in the frame in the figure); this mode corresponds sufficiently well to the velocity $u = 1.14$. The value $a \approx 0.991$ was obtained for the amplitude (Y in the frames), close to the value of 1.07 obtained by solving Eq. (7).

Fig. 3. Dependences x(*t*) and $\dot{\varphi}(t)$ for the values of the motor parameters $M_0 = 5.9889$, $Q = 5$. The data were obtained at $p = 1$

We also analyzed the influence of the parameters M_0, Q, characterizing the energy source, on dynamic processes. As noted above, the solutions of the equations for the cases $u \ge ap$, $u < ap$ are fundamentally different, and there exists some boundary value of the velocity u_b separating these cases. A transition from one state to another can happen in the system at the boundary value of the velocity u_b. It depends on the slope of the energy source characteristic and its location relative to the curve of the load on the source. The transition takes place at flat characteristics $M(\dot{\varphi})$ and is associated with the load $S(u)$ on the energy source from the oscillatory system, depending on function (2), expressed by Eq. (8).

As an example, Fig. 4 shows a graph of the above-mentioned transition at certain values of motor parameters and energy source characteristic. Given the same slope $Q = 0.4986$ (the angle of inclination is about 26°), a very small ($1\cdot10^{-10}$) difference in the values of M_0, equal to 0.

As noted above, the amplitude of stationary oscillations at $u < ap$ is determined by the approximate dependence $ap \approx u$. Since the load on the energy source depends on the amplitude of the oscillations, its graphs differ under conditions u

Fig. 4. Time evolution of the *x*-coordinate and angular velocity of the rotor φ(*t*) for the characteristic $M_0 = 0.8780994695$ (data were obtained at $p = 1$)
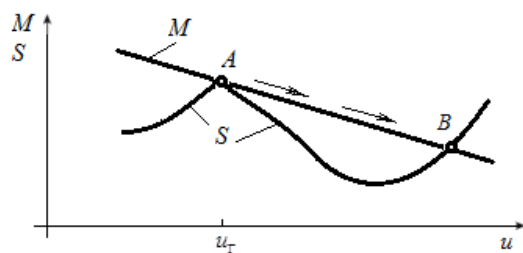
Fig. 5. Dependences of load S and torque M on velocity u in its narrow variation range; u_b is the boundary value of the velocity

$\geq ap$ and $u < ap$. Fig. 5 schematically shows only fragments of the curves for the dependences of the load S and the torque M on the velocity u, over a narrow variation range of u, where the transition from point A to point B takes place (corresponding to the data in Fig. 4) at a fixed position of the energy source characteristic at the boundary velocity u_b corresponding to point A. Different transitions with a description of the full load curves for different classes of oscillations are described in detail in monograph [1], so they are not given here.

In addition to the results presented in this paper, differential equations (6) were also solved numerically. The results are not shown here due to limitations of space. We only note that the results of these solutions are in good agreement with those for Eqs. (7).

Conclusion

As follows from our findings, nonlinear parametric excitation has specific characteristics compared with linear parametric oscillation, namely:

it significantly changes the shape of the amplitude curves;

it has a considerable effect on the stability of oscillations.

Comparing the results for these excitations, we find for the interaction of an oscillatory system with nonlinear parametric excitation (in the case of an energy source with limited power) that a number of effects of the same nature occur as with linear parametric excitation. It seems inappropriate to describe the nature of these effects here, since they have been thoroughly explored in monograph [1].

REFERENCES

1. **Alifov A. A., Frolov K. V.,** Interaction of nonlinear oscillatory systems with energy sources. Hemisphere Publishing Corporation, New York, Washington, Philadelphia, London, 1990.

2. **Andronov A. A., Vitt A. A., Khaikin S. E.,** Theory of vibration, Nauka Publishing, Moscow, 1981 (in Russian).

3. **Migulin V. V., Medvedev V. I., Mustel E. R., Parygin V. N.,** Osnovy teorii kolebaniy [Foundations of vibration theory], 2-nd edition, Nauka Publishing, Moscow, 1988 (in Russian).

4. **Biderman V. L.,** Teoriya mekhanicheskikh kolebaniy [Theory of mechanical vibrations], Vysshaya Shkola [The Higher School Publishing], Moscow, 1980 (in Russian).

5. **Alifov A. A.,** Vliyaniye nelineynogo parametricheskogo vozbuzhdeniya na vzaimodeystviye parametricheskikh i vynuzhdennykh kolebaniy [Effect of nonlinear parametric excitation on the interaction between parametric and forced oscillations], Proc. 15-th All-Russian Sci. & Techn. conf. "Dinamika nelineynykh diskretnykh elektrotekhnicheskikh i elektronnykh system" [Dynamics of nonlinear discrete electrotechnical and electronic systems], June 02, 2023, Cheboksary: Chuvash State University Named after I. N. Ulyanov (2023) 7−8.

6. **Kononenko V. O.,** Vibrating systems with limited power-supply, Iliffe, London, 1969.

7. **Frolov K. V.,** Izbrannyye Trudy v 2 t [Selected works in 2 Vols.], Nauka Publishing, Moscow, 2007 (in Russian).

8. **Rubanik V. P., Starik L. K.,** Ob ustoychivosti avtokolebaniy reztsa v sluchaye neidealnogo istochnika energii [On stability of cutter's self-oscillations in the case of a nonideal energy source], Nauchnyye trudy vuzov Lit. SSR. Vibrotekhnika [Scientific Transactions of Higher Schools of Lithuanian SSR, Ser. Vibrotechnics] (2(11)) (1971) 205−212 (in Russian).

9. **Abdiyev F. K.,** Avtokolebaniya sistemy s zapazdyvaniyem i s neidealnym istochnikom energii [Self-oscillations of a delayed system with a nonideal energy source], Izv. AN AzSSR. Seriya Fiziko-Tekhnicheskie i Matematicheskie Nauki [News of the Academy of Sciences of the Azerbaijan SSR: Ser. Physical, Technical and Mathematical Sciences]. (4) (1983) 134−139 (in Russian).

10. **Bharti S. K., Bisoi A., Sinha A., et al.,** Sommerfeld effect at forward and backward critical speeds in a rigid rotor shaft system with anisotropic supports, J. Sound Vib. 442 (3 March) (2019) 330−349.

11. **Sinha A., Samantaray A. K., Bhattacharyya R.,** Self-synchronization of two unbalanced DC motor-driven rotors on a common movable platform, In book: Badodkar D., Dwarakanath T. (Eds.) Machines, mechanism and robotics, Proc. iNaCoMM 2017. Book ser. "Lecture Notes in Mechanical Engineering", Springer, Singapore (2018) 207−217.

12. **Jha A. K., Dasgupta S. S.,** Attenuation of Sommerfeld effect in an internally damped eccentric shaft-disk system via active magnetic bearings, Meccanica. 54 (1−2) (2019) 311−320.

13. **Varanis M., Balthazar J.M., Silva A., et al.,** Remarks on the Sommerfeld effect characterization in the wavelet domain, J. Vib. Control. 25 (1) (2019) 98−108.

14. **Rocha R. T., Balthazar J. M., Tusset A. M., et al.,** On a non-ideal magnetic levitation system: nonlinear dynamical behavior and energy harvesting analyses, Nonlinear Dyn. 95 (4) (2019) 3423−3438.

15. **Sinha A., Bharti S. K., Samantaray A. K., Bhattacharyya R.,** Sommerfeld effect in a single-DoF system with base excitation from motor driven mechanism, Mech. Mach. Theory. 148 (June) (2020) 103808.

16. **Chernysheva J., Gorskiy A., Sereda A.,** The effect of Sommerfeld and wagon dynamics, Electronics & Electrical Equipment of Transport. (1) (2019) 8−10 (in Russian).

17. **Eshchin E. K.,** On the Sommerfeld effect and hidden oscillations in the minning machines asynchronous, Russian Electromechanics. 66 (1) (2023) 80−85 (in Russian).

18. **Alifov A. A.,** About calculation of self-oscillatory system delayed and limited excitation, Proc. Int. Sci. Tech. Conf. "Measurement and Quality: Problems, Prospects", Nov. 21−23, 2018, AzTU, Baku, Azerbaijan (2018) 289−293.

19. **Alifov A. A.,** Metody pryamoy linearizatsii dlya rascheta nelineynykh system [Methods of direct linearization for calculation of nonlinear systems], Research Center "Regular and Chaotic Dynamics", Moscow − Izhevsk, 2015 (in Russian).

20. **Klimov D. M.,** On one type of self-excited vibrations in a system with dry friction, Mech. Solids. 38 (3) (2003) 1−7.

21. **Panovko Ya. G.,** Osnovy prikladnoy teorii kolebaniy i udara [Fundamentals of applied theory of oscillations and impact], Mashinostroyeniye Publishing, Leningrad, 1976 (in Russian).

22. **Murashkin L. S., Murashkin S. L.,** Prikladnaya nelineynaya mekhanika stankov [Applied nonlinear mechanics of machine tools], Mashinostroyeniye Publishing, Leningrad, 1977 (in Russian).

23. **Ponomarev A. S., Sokolov V. I., Kozhukhar' A. A.,** Poperechnyye avtokolebaniya silovykh stolov, vyzvannyye silami treniya [Transverse self-oscillations of force tables caused by friction forces], Bulletin of the Kharkiv Polytechnic Institute. Ser. Machine Engineering. 8 (130) (1977) 67−69.

24. **Korityssky Ya. I.,** Krutilnyye avtokolebaniya vytyazhnykh priborov pryadilnykh mashin pri granichnom trenii v oporakh skolzheniya [Torsional self-oscillations of spinning machine drafting devices with boundary friction in sliding bearings], In book: Collected works "Nonlinear vibrations and transition processes in machines", Nauka Publishing, Moscow, 1972.

25. **Bronovets M. A., Zhuravlev V. F.,** On self-excited vibrations in friction source measurement systems, Mech. Solids. 47 (3) (2012) 261−268.

26. **Alifov A. A. O.,** Mixed forced parametric, and self-oscillations with a nonideal energy source and lagging forces, Izvestiya VUZ. Nonlinear Dynamics. 29 (5) (2021) 739−750 (in Russian).

27. **Bogoliubov N. N., Mitropolsky Y. A.,** Asymptotic methods in the theory of non-linear oscillations, CRC Press, Florida, USA, 1961.

28. **Moiseev N. N.,** Asimptoticheskiye metody nelineynoy mekhaniki [Asymptotic methods of nonlinear mechanics], Nauka Publishing, Moscow, 1981 (in Russian).

29. **Butenin N. V., Neymark Yu. I., Fufayev N. A.,** Vvedeniye v teoriyu nelineynykh kolebaniy [Introduction to the theory of nonlinear oscillations], Nauka Publishing, Moscow, 1976 (in Russian).

30. **Chelomey V. N.** (Chairman), Vibratsii v technike: spravochnik [Vibrations in machinery: Handbook], in 6 Vols., Vol. 2. Vibrations of nonlinear mechanical systems, Edited by Blekhman I. I., Publishing House of Mechanical Engineering, Moscow, 1979 (in Russian).

СПИСОК ЛИТЕРАТУРЫ

1. **Alifov A. A., Frolov K. V.** Interaction of nonlinear oscillatory systems with energy sources. New York, Washington, Philadelphia, London: Hemisphere Publishing Corporation, 1990. 327 p.

2. **Андронов А. А., Витт А. А., Хайкин С. Э.** Теория колебаний. М.: Наука. Гл. ред. физ.-мат. лит. 1981. 568 с.

3. **Мигулин В. В., Медведев В. И., Мустель Е. Р., Парыгин В. Н.** Основы теории колебаний. Под ред. В. В. Мигулина. 2-е изд., перераб. М.: Наука. Гл. ред. физ.-мат. лит. 1988. 392 с.

4. **Бидерман В. Л.** Теория механических колебаний. М.: Высшая школа, 1980. 408 с.

5. **Алифов А. А.** Влияние нелинейного параметрического возбуждения на взаимодействие параметрических и вынужденных колебаний // Материалы XV Всероссийской научно-технической конференции «Динамика нелинейных дискретных электротехнических и электронных систем». Чебоксары, 02 июня 2023 года. Чебоксары: Чувашский государственный университет имени И. Н. Ульянова, 2023. С. 7−8.

6. **Кононенко В. О.** Колебательные системы с ограниченным возбуждением. М.: Наука, 1964. 236 с.

7. **Фролов К. В.** Избранные труды. В 2 тт. Т. 1. Вибрация и техника. М.: Наука, 2007. 349 с.

8. **Рубаник В. П., Старик Л. К.** Об устойчивости автоколебаний резца в случае неидеального источника энергии // Научные труды высших учебных заведений Литовской ССР. Серия «Вибротехника». 1971. № 2 (11). С. 205−212.

9. **Абдиев Ф. К.** Автоколебания системы с запаздыванием и с неидеальным источником энергии // Известия АН АзССР. Серия физико-технических и математических наук. 1983. № 4. С. 134−139.

10. **Bharti S. K., Bisoi A., Sinha A., Samantaray A. K., Bhattacharyya R.** Sommerfeld effect at forward and backward critical speeds in a rigid rotor shaft system with anisotropic supports // Journal of Sound and Vibration. 2019. Vol. 442. 3 March. Pp. 330−349.

11. **Sinha A., Samantaray A. K., Bhattacharyya R.** Self-synchronization of two unbalanced DC motor-driven rotors on a common movable platform // Badodkar D., Dwarakanath T. (Eds.). Machines, mechanism and robotics. Proceedings of iNaCoMM 2017. Book Ser. "Lecture Notes in Mechanical Engineering", Springer, Singapore, 2018. Pp. 207−217.

12. **Jha A. K., Dasgupta S. S.** Attenuation of Sommerfeld effect in an internally damped eccentric shaft-disk system via active magnetic bearings // Meccanica. 2019. Vol. 54. No. 1−2. Pp. 311−320.

13. **Varanis M., Balthazar J. M., Silva A., Mereles A. G., Pederiva R.** Remarks on the Sommerfeld effect characterization in the wavelet domain // Journal of Vibration and Control. 2019. Vol. 25. No. 1. Pp. 98−108.

14. **Rocha R. T., Balthazar J. M., Tusset A. M., Souza S. L. T., Janzen F. C., Arbex H. C.** On a non-ideal magnetic levitation system: nonlinear dynamical behavior and energy harvesting analyses // Nonlinear Dynamics. 2019. Vol. 95. No. 4. Pp. 3423−3438.

15. **Sinha A., Bharti S. K., Samantaray A. K., Bhattacharyya R.** Sommerfeld effect in a single-DoF system with base excitation from motor driven mechanism // Mechanism and Machine Theory. 2020. Vol. 148. June. P. 103808.

16. **Чернышева Ю. В., Горский А. Н., Середа А. Г.** Эффект Зоммерфельда и динамика вагонов // Электроника и электрооборудование транспорта. 2019. № 1. С. 8−10.

17. **Ещин Е. К.** Об эффекте Зоммерфельда и скрытых колебаниях в асинхронном электроприводе горных машин // Известия высших учебных заведений. Электромеханика. 2023. Т. 66. № 1. С. 80−85.

18. **Alifov A. A.** About calculation of self-oscillatory system delayed and limited excitation // Proceedings of the International Scientific and Technical Conference "Measurement and Quality: Problems, Prospects"; November 21−23, 2018, AzTU, Baku, Azerbaijan. Pp. 289−293.

19. **Алифов А. А.** Методы прямой линеаризации для расчета нелинейных систем. Москва−Ижевск: НИЦ «Регулярная и хаотическая динамика». 2015. 74 с.

20. **Климов Д. М.** Об одном виде автоколебаний в системе с сухим трением // Известия Российской академии наук. Механика твердого тела. 2003. № 3. С. 6−12.

21. **Пановко Я. Г.** Основы прикладной теории колебаний и удара. Ленинград: Машиностроение, 1976. 320 с.

22. **Мурашкин Л. С., Мурашкин С. Л.** Прикладная нелинейная механика станков. Ленинград: Машиностроение, 1977. 192 с.

23. **Пономарев А. С., Соколов В. И., Кожухарь А. А.** Поперечные автоколебания силовых столов, вызванные силами трения // Вестник Харьковского политехнического института. Машиностроение. 1977. Т. 8. № 130. С. 67−69.

24. **Коритысский Я. И.** Крутильные автоколебания вытяжных приборов прядильных машин при граничном трении в опорах скольжения // «Нелинейные колебания и переходные процессы в машинах». Сб. статей АН СССР под ред. К. В. Фролова. М.: Наука, 1972. 303 с.

25. **Броновец М. А., Журавлёв В. Ф.** Об автоколебаниях в системах измерения сил трения // Известия Российской академии наук. Механика твердого тела. 2012. № 3. С. 3−11.

26. **Алифов А. А.** Смешанные вынужденные, параметрические и автоколебания при неидеальном источнике энергии и запаздывающих силах // Известия высших учебных заведений. Прикладная нелинейная динамика. 2021. Т. 29. № 5. С. 739−750.

27. **Боголюбов Н. Н., Митропольский Ю.А.** Асимптотические методы в теории нелинейных колебаний. М.: Наука, 1974. 504 с.

28. **Моисеев Н. Н.** Асимптотические методы нелинейной механики. М.: Наука, 1981. 400 с.

29. **Бутенин Н. В., Неймарк Ю. И., Фуфаев Н. А.** Введение в теорию нелинейных колебаний. М.: Наука, 1976. 256 с.

30. Вибрации в технике. Справочник. В 6 тт. Ред. совет: В. Н. Челомей (пред., гл. ред.). Т. 2. Колебания нелинейных механических систем. Под ред. И. И. Блехмана. 1979. 351 с.

THE AUTHOR

ALIFOV Alishir Ali
Mechanical Engineering Research Institute of the RAS
4 Malij Haritonjevskij lane, Moscow, 101000, Russia
alishir@mail.ru
ORCID: 0000-0003-2327-068

СВЕДЕНИЯ ОБ АВТОРЕ

АЛИФОВ Алишир Али оглы − *доктор технических наук, главный научный сотрудник лаборатории динамических процессов Института машиноведения имени А. А. Благонравова Российской академии наук.*
101000, Россия, г. Москва, Малый Харитоньевский пер., 4
alishir@mail.ru
ORCID: 0000-0003-2327-068X

MATHEMATICAL PHYSICS

AN OPTIMIZED LANCZOS TAU-METHOD

A. L. Bulyanitsa[1,2]✉, A. S. Berdnikov[1], A. A. Evstrapov[1]

[1] Institute for Analytical Instrumentation of RAS, St. Petersburg, Russia;

[2] Peter the Great St. Petersburg Polytechnic University, St. Petersburg, Russia

✉ antbulyan@yandex.ru

Abstract. The paper puts forward an effective algorithm for producing approximate polynomial solutions for linear ordinary differential equations (LODEs) and sets of LODEs with polynomial coefficients and polynomial right-hand side functions. The algorithm is an upgraded version of the Lanczos Tau-method and provides the optimal deviation of the approximate solution from the exact one according to the minimax norm for a given interval. With minor modification, the algorithm allows one to find approximate expressions for the derivatives of the exact solutions with sufficiently greater accuracy than the derivatives of the approximate solutions are capable of providing that.

Keywords: minimax norm, Chebyshev polynomial, optimal approximation, linear ordinary differential equation, Tau-method

ОПТИМИЗИРОВАННЫЙ ТАУ-МЕТОД ЛАНЦОША

А. Л. Буляница[1,2]✉, А. С. Бердников[1], А. А. Евстрапов[1]

[1] Институт аналитического приборостроения РАН, Санкт-Петербург, Россия;

[2] Санкт-Петербургский политехнический университет Петра Великого, Санкт-Петербург, Россия

✉ antbulyan@yandex.ru

Аннотация. В статье обсуждается эффективный алгоритм получения приближенных полиномиальных решений для линейных обыкновенных дифференциальных уравнений и систем линейных обыкновенных дифференциальных уравнений с полиномиальными коэффициентами и полиномиальными правыми функциями. Алгоритм является усовершенствованной версией тау-метода К. Ланцоша и дает возможность получать оптимальное отклонение приближенного решения от точного в соответствии с минимаксной нормой для заданного отрезка. При незначительной модификации алгоритм позволяет находить приближенные выражения для производных точных решений с существенно большей точностью, чем способны обеспечивать производные приближенных решений.

Ключевые слова: минимаксная норма, полином Чебышева, оптимальная аппроксимация, линейное обыкновенное дифференциальное уравнение, тау-метод

Introduction

The Lanczos Tau-method[1] allows to obtain approximate polynomial solutions for linear ordinary differential equations (LODEs) with polynomial coefficients and polynomial right-hand functions [1, 2]. These solutions should have maximum accuracy in a finite interval under consideration in accordance with the minimax norm, which is the opposite of approximation by ordinary least squares and/or approximation by series of orthogonal polynomials of various types [3—5].

This article discusses the reasons why polynomial solutions obtained using the original Lanczos algorithm may turn out to be suboptimal and suggests effective ways to improve the algorithm. General theoretical considerations are supported by numerical examples.

Initially, the Tau-method was proposed in [1] and subsequently described in detail in monograph [2] with a large number of illustrative examples. The basic mathematical definitions allowing to rigorously describe the method are given in [6]. A case considered in [7] concerns an interval divided into small segments, subsequently applying the Tau-method to each small segment to obtain a smooth and accurate approximate piecewise polynomial solution.

Another approach to improving the accuracy of this method is described in [8]. Recurrent schemes of the Tau-method, when the degree of the approximating polynomial is increased in steps, without recalculating it from zero, are considered in [9, 10]. The errors of approximate solutions are analyzed in [11, 12]. Extensions of the Tau-method to linear differential equations with coefficients differing from polynomial to nonlinear differential equations, partial differential equations, etc., are discussed in [13—15].

Revived interest in techniques for constructing approximate solutions of ODEs, systems of integral equations and other objects can be traced in recent publications. The Lanczos Tau-method is also used, but with the construction of a shifted Legendre basis for solving time-delay systems [16]; the approximation of differential operators is applied (the same as in our paper) with shifted Chebyshev polynomials [17], expansions of functions with respect to Hermite and Laguerre polynomials are presented [18].

In addition, the special Tau Toolbox was developed[2], in particular for solving ODEs (including nonlinear ones) and their systems, as well as integral equations [19—21]. Applications of this toolbox to expansion of solutions with respect to Sobolev polynomials and solutions of singular integral equations can be found in [22, 23]. The coefficients of approximating formulas are sought in [24] when the Chebyshev alternation is reached. This approach is used in the approximation of Fermi—Dirac functions based on an iterative procedure.

More recent studies consider Chebyshev approximations of functions [25, 26]; several textbooks deal with a wider range of issues related to the search for approximate solutions and substantiation of their properties [27—29].

Thus, interest in this major research problem does not weaken.

---

[1] The name Tau-method was proposed and introduced by Cornelius Lanczos (a Hungarian physicist and mathematician) in [1]: the additional free terms for the Chebyshev polynomials on the right-hand side of differential equations were denoted with the subscripts τ.

[2] The package can be downloaded from the website https://bitbucket.org/tautoolbox/tautoolbox/src/main/.

The Tau-method was originally formulated as a way to approximate special functions of mathematical physics that could be expressed using ODEs. This method has become a powerful and accurate tool for numerical solution of complex differential and functional equations. The approach proposed by Lanczos is to approximate the solution of a given problem by calculating the exact solution of some approximate problem close to the original one. The solution of the differential equation along this path is approximated by a polynomial which is an exact solution to the differential equation obtained by adding the polynomial terms of the perturbation to its right-hand side. The perturbation terms are chosen so as to guarantee the existence of an analytical polynomial solution to the perturbed equation.

If the coefficients of the equation and/or the initial conditions and/or the boundaries of the interval depend on any parameters, then the output is an algebraic expression depending on these parameters. This is an undoubted advantage of the Tau-method, compared with classical numerical methods that produce individual solutions for fixed numerical values of parameters. The method can greatly simplify analysis, allowing to optimize solutions to parameter-dependent differential equations.

The following section contains various definitions and theorems to be used further for this study.

The section 'Example solution of equation by Tau-method' illustrates the steps of the Lanczos Tau-method; here a linear differential equation with polynomial coefficients and a known analytical non-polynomial solution is solved.

The section 'Difference between errors and residuals' analyzed the fundamental difference between the error (the discrepancy between the exact and approximate solutions) and the differential residual (the parasitic value on the right-hand side of the differential equation after substituting the approximate solution). Minimization of the differential residual is not equivalent to minimization of the error, and therefore Chebyshev polynomials or some other orthogonal polynomials used to minimize the differential residual do not provide an optimal approximate solution.

The following section describes an optimized Tau-method for solving reduced LODEs with polynomial coefficients. The integral form of a LODE and Picard's theorem make it possible to prove the statement that the residual of integral form is proportional to the error of the approximate solution. Therefore, if the perturbation of integral form is the sum of Chebyshev polynomials, the approximate solution obtained by the Tau-method is close to optimal. The optimized Tau-method introduces perturbations both to the right-hand side of the differential equation and to the initial conditions of the approximate solution (the latter differs significantly from the original Tau-method).

The section 'Discussion' compares the approaches to the problem and analyzes the advantages of the proposed modification of the method.

The main results are summarized in Conclusion.

Necessary definitions and general theorems

This section contains definitions and general theorems used later in this study. Details and proofs of the corresponding statements can be found in books [3−5].

Definition 1. A polynomial of the form

$$P(x) = a_0 + a_1 x + \ldots + a_n x^n$$

of degree n is the minimax approximation of the given function $f(x)$ with the given weight $w(x) \neq 0$ on the given interval $x \in [x_a, x_b]$, if $P(x)$ is the solution to the variational problem

$$\max_{x \in [x_a, x_b]} \left| w(x)\big(f(x) - P(x)\big) \right| \to \min \tag{1}$$

where minimization is performed over all possible sets of coefficients $a_0, a_1, \ldots, a_{n-1}, a_n$.

Definition 2. A reduced polynomial of the form

$$P(x) = a_0 + a_1 x + \ldots + a_{n-1} x^{n-1} + x^n$$

of degree n is called the polynomial of least deviation from zero on the given interval $x \in [x_a, x_b]$ with the given weight $w(x) \neq 0$ if $P(x)$ is the solution to the variational problem

$$\max_{x \in [x_a, x_b]} \left| w(x) P(x) \right| \to \min, \tag{2}$$

where minimization is performed over all possible sets of coefficients $a_0, a_1, \ldots, a_{n-1}$.

The lower part $a_0 + a_1 x + ... + a_{n-1} x^{n-1}$ of a polynomial of degree n of least deviation from zero is a polynomial of degree $n - 1$ providing a minimax approximation (solution to variational problem (1)) for the function $f(x) = -x^n$ with the weight $w(x)$.

Definition 3. A set of m points

$$x_1 < x_2 < ... < x_m$$

is called a Chebyshev alternation of size m for a function $h(x)$ on the interval $[x_a, x_b]$ if the points $x_k \in [x_a, x_b]$ are alternating local minima and maxima of $h(x)$ with equal absolute values, so that

$$h(x_k) = (-1)^k \varepsilon \text{ and } |\varepsilon| = \max|h(x)| \text{ for } x \in [x_a, x_b].$$

Theorem 1 (de la Vallée Poussin theorem). *Suppose there is a polynomial $Q(x)$ of degree n, a function $f(x)$, an interval $[x_a, x_b]$ and a weight function $w(x) \neq 0$. Let us also assume that there are $n + 2$ points (de la Vallée Poussin alternation)*

$$x_a \leq x_1 < x_2 < ... < x_{n+2} \leq x_b,$$

in which the expression $w(x)[f(x) - Q(x)]$ has nonzero values with alternating signs:

$$+\lambda_1, -\lambda_2, ..., + (-1)^{n+2} \lambda_{n+2}$$

(it is assumed that $\lambda_k > 0$ for $\forall k$)).
If λ is the minimax deviation from zero for

$$w(x) [f(x) - P(x)],$$

where the optimal polynomial $P(x)$ is the solution of the variational problem (1), then

$$\lambda \geq \min\{\lambda_1, \lambda_2, ..., \lambda_{n+2}\}.$$

If the given points x_k are also local minima and maxima for $w(x)[f(x) - Q(x)]$, then

$$\lambda \leq \max\{\lambda_1, \lambda_2, ..., \lambda_{n+2}\}.$$

Theorem 2 (Chebyshev's alternation theorem). *If there exists a Chebyshev alternation of size $n + 2$ on the interval $[x_a, x_b]$ for the function $w(x) [f(x) - P(x)]$, where $w(x) \neq 0$ and $f(x)$ are the given functions, and $P(x)$ is a polynomial of degree n, then this polynomial $P(x)$ is the only solution to variational problem (1). If the functions $w(x) \neq 0$ and $f(x)$ are continuous on the interval $[x_a, x_b]$, then variational problem (1) has a unique solution $P(x)$, and this solution satisfies the condition of Chebyshev's theorem, i.e., there is a Chebyshev alternation of dimension $n + 2$ on the interval $[x_a, x_b]$ for the function $w(x)[f(x) - P(x)]$.*

Theorem 3 (Chebyshev criterion). *If a Chebyshev alternation of size $n + 1$ exists for a function $w(x) P(x)$ on the interval $[x_a, x_b]$, where $w(x) \neq 0$ is the given function, and $P(x)$ is a polynomial of degree n with the leading coefficient equal to unity, then the polynomial $P(x)$ is a unique solution to the variational problem (2), i.e., the polynomial of least deviation from zero. If the function $w(x) \neq 0$ is continuous on the interval $[x_a, x_b]$, then variational problem (2) has a unique solution, and this solution satisfies the Chebyshev criterion, i.e., a Chebyshev alternation of size $n + 1$ exists for function $w(x) P(x)$ on the interval $[x_a, x_b]$.*

Algorithms allowing to calculate polynomials for minimax approximations and polynomials of least deviation from zero for the given weight $w(x) \neq 0$ on the given interval $[x_a, x_b]$ are considered in [30−32].

Definition 4. Polynomials $T_n(x)$ of degree n, defined as

$$T_n(x) = \cos(n \arccos x)$$

for $-1 \leq x \leq +1$ are called first-kind Chebyshev polynomials.

According to Definition 2 and Theorem 3, the polynomials $T_n(x)/2^{n-1}$ are polynomials of degree n that deviate least from zero on the interval $x \in [-1, +1]$ with weight $w(x) = 1$. The deviation is equal to $1/2^{n-1}$.

Definition 5. Let there be an ordinary differential equation of the form

$$L[x(t)] = 0,$$

where $L[x(t)]$ is a certain differential operator.

If the following equality holds true for the trial function $x(t)$:

$$L[x(t)] = Q(t),$$

then $Q(t)$ is called the differential residual of $x(t)$.

Definition 6. Let there be an integral equation

$$x(t) = K[x(t)],$$

equivalent to the differential equation

$$L[x(t)] = 0,$$

where $K[x(t)]$ a certain integral operator.

If the following equality holds true for the trial function $x(t)$:

$$x(t) - K[x(t)] = R(t),$$

then $R(t)$ is called the integral residual of $x(t)$.

Definition 7. Let there be an ordinary differential equation

$$L[x(t)] = 0,$$

such that $x^*(t)$ is the exact solution of the equation. If $x(t)$ is an approximate solution of the equation, then the difference

$$\Delta x(t) = x(t) - x^*(t)$$

is called the error of the approximate solution $x(t)$.

Remark 1. Differential residuals, integral residuals and errors for systems of ODEs are introduced similarly.

Example solution of equation by Tau-method

The Lanczos method gives approximate polynomial solutions on a certain fixed interval for LODEs with polynomial coefficients and polynomial right-hand sides of the form

$$L[x(t)] = x^{(n)}(t) + a_1(t)x^{(n-1)}(t) + \ldots + a_{n-1}(t)x'(t) + a_n(t)x(t) - f(t) = 0,$$

where $a_k(t)$, $f(t)$ are polynomials; $x(t)$ is an unknown function.

For illustration, consider a simple example:

$$L[x(t)] = x''(t) + tx'(t) + 2x(t) = 0,$$

$$x(0) = 0,\ x'(0) = 1. \tag{3}$$

The exact solution of Eq. (3) is $x^*(t) = t\exp(-t^2/2)$. Suppose that the exact solution is unknown and it is necessary to find an approximate solution to problem (3) at $0 \leq t \leq 4$. The Weierstrass approximation theorem (see, for example, monograph [33]) guarantees that any continuous function can be approximated on a fixed interval of finite size with arbitrarily high accuracy by a polynomial of the appropriate degree. This statement serves as the basis for finding an approximate solution in the form of a polynomial for the given problem.

We search for an approximate solution to problem (3) as a 7th-degree polynomial with indefinite coefficients b_k:

$$x(t) = b_0 + b_1 t + b_2 t^2 + \ldots + b_7 t^7. \tag{4}$$

After substituting expression (4) into Eq. (3), the right-hand side (differential residual) turns out to be a polynomial:

$$Q(t) = (2b_0 + 2b_2) + (3b_1 + 6b_3)t + (4b_2 + 12b_4)t^2 + (5b_3 + 20b_5)t^3 +$$
$$+ (6b_4 + 30b_6)t^4 + (7b_5 + 42b_7)t^5 + 8b_6 t^6 + 9b_7 t^7. \tag{5}$$

We need to bring differential residual (5) as close to zero as possible; for example, by satisfying the condition $Q(t) \equiv 0$. However, this is possible only when the exact solution of the equation is a polynomial of the required (or lower) degree. The statement 'bring the residual as close to zero as possible' is not clearly defined and cannot be regarded as unambiguous in a mathematical sense. For example, we set as many coefficients of the lower-degree terms in residual (5) as possible equal to zero, provided that some coefficients are used to satisfy the initial conditions. This is sufficient for residual (5) to exclude terms with multipliers 1, t, t^2, t^3, t^4, t^5 and even t^6. Then the solution is as follows:

$$b_0 = b_2 = b_4 = b_6 = 0, \; b_1 = 1, \; b_3 = -1/2, \; b_5 = 1/8, \; b_7 = -1/48,$$

$$Q(t) = -3/16t^7. \tag{6}$$

As expected, this result is a truncated Taylor series for the function $t\exp(-t^2/2)$. Fig. 1 shows a comparison of the exact solution with the approximate polynomial solution (4) with coefficients (6) for $t \in [0,4]$. Obviously, this solution is unsatisfactory, despite the high degree of the polynomial.
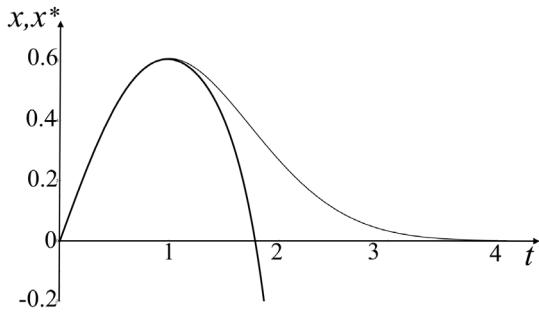
Fig. 1. Exact $(x^*(t))$ and approximate $(x(t))$ solutions of differential equation (3) (thin and bold lines, respectively); the coefficients of the polynomial $x(t)$ are determined by Eqs. (6)

One of the possible reasons for this failure is that although the differential residual $Q(t) = -3t^7/16$ is small near the point $t = 0$, this residual is unreasonably large in the vicinity of the point $t = 4$. Apparently, if we require that the residual be approximately the same over the entire interval, then we can expect a significantly better result.

The first step proposed by Lanczos *is* to remove the ill-defined empirical conditions. In the new formulation of the problem, it is necessary to find the coefficients b_0, $b_1 - b_7$, τ_6, τ_7 for which function (5) satisfies the conditions

$$x(0) = 0, \; x'(0) = 1, \; L[x(t)] \equiv \tau_6 t^6 + \tau_7 t^7.$$

The problem has not actually changed, but now the system of equations is well-defined from an algebraic standpoint. The corresponding SLAE has a unique solution. Naturally, this solution coincides with solution (6).

The next important step proposed by Lanczos consists in replacing the differential residual $\tau_6 t^6 + \tau_7 t^7$ (i.e., a function that is small at one end of the interval but large at the other end) with a differential residual

$$\tau_6 \overline{T}_6(t) + \tau_7 \overline{T}_7(t),$$

where $\overline{T}_6(t)$ and $\overline{T}_7(t)$ are transformed Chebyshev polynomials $T_6(t)$ and $T_7(t)$ of the corresponding degree [2, 34, 35].

These polynomials are rescaled from $t \in [-1, +1]$ to $t \in [0, 4]$ and deviate least from zero on the interval $t \in [0.4]$:

$$\tau_6 \overline{T}_6(t) + \tau_7 \overline{T}_7(t),$$

$$\overline{T}_6(t) = T_6\left(\frac{t}{2} - 1\right), \; \overline{T}_7(t) = T_7\left(\frac{t}{2} - 1\right),$$

$$T_6(\tau) = 32\tau^6 - 48\tau^4 + 18\tau^2 - 1,$$

$$T_7(\tau) = 64\tau^7 - 112\tau^5 + 56\tau^3 - 7\tau.$$

35

Now the differential residual $Q(t)$ on the right-hand side of the equation is approximately the same at all points of the interval under consideration. Then it is logical to assume that the error of the approximate solution is also approximately the same over the entire interval. This hypothesis is supported by the fact that the error of the approximate solution is zero at all points of the interval provided that the residual $Q(t)$ is zero at all of its points. However, minimization of the residual does not necessarily mean minimization of the error (see the example below).

Solution (4), obtained for Eq. (3) using the Lanczos Tau-method, contains the following coefficients:

$$b_0 = 0, \; b_1 = 1.000000000, \; b_2 \approx 0.052400600, \; b_3 \approx -0.880052000,$$

$$b_4 \approx 0.442647000, \; b_5 \approx -0.091658100, \tag{7}$$

$$b_6 \approx 0.006894820, \; b_7 \approx -0.000023572.$$

Fig. 2 illustrates the discrepancy between the exact and approximate polynomial solutions (4) with coefficients (7) obtained using the Lanczos Tau-method. The approximate solution $x(t)$ lies in the range of $0-0.6$ with the maximum error on the interval $t \in [0.4]$ equal to 0.012. The graphs of the exact and approximate solutions are virtually indistinguishable. Fig. 2 shows the graphs for error and differential residual. It can be seen that the accuracy of the approximate solution obtained using the Lanczos Tau-method is satisfactory.
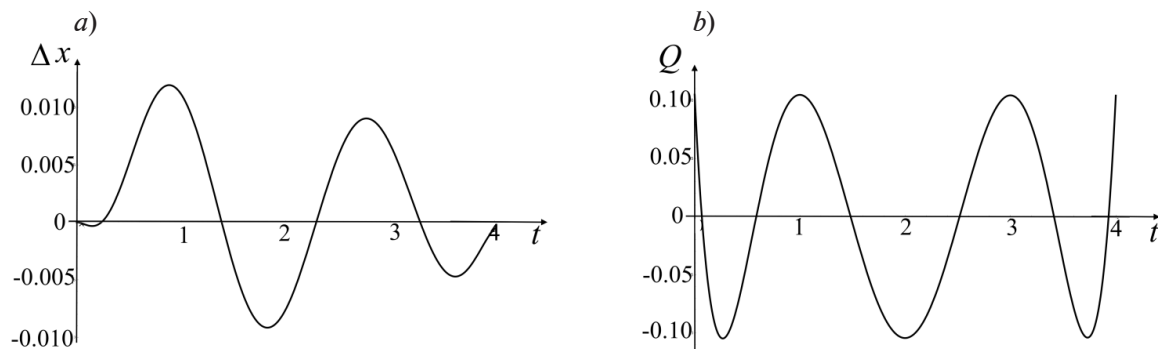
Fig. 2. Error of approximate solution obtained by Lanczos Tau-method (*a*)
and its differential residual (*b*)

Monograph [34] shows that expanding the approximate solution into a truncated Chebyshev series often yields higher accuracy than the Lanczos method. However, approximate solutions obtained using the truncated Chebyshev series also do not guarantee the highest possible accuracy. The goal of this study is to create a modification of the Lanczos Tau-method providing the highest possible accuracy of the approximate solution.

Indeed, a small (with respect to the minimax norm) differential residual in the differential equation does not mean a small minimax error of the solution. As an example, consider the equation $y''(t) + y(t) = 0$ with an exact solution

$$y^*(t) = c_1 \cos t + c_2 \sin t$$

and the equation $z''(t) + z(t) = \varepsilon \sin t$ with the exact solution

$$z^*(t) = c_1 \cos t + c_2 \sin t - \varepsilon(t \cos t - \sin t)/2.$$

No matter how small the differential residual $Q(t) = \varepsilon \sin t$ is in the second equation, the difference between these two solutions with the same initial conditions becomes arbitrarily large as the interval $t \in [0, T]$ increases.

Difference between errors and residuals

The error $\Delta x(t)$ is the difference between the exact solution $x^*(t)$ and the approximate solution $x(t)$. The differential residual $Q(t)$ is the deviation of the right-hand side of the differential

equation after an approximate solution is substituted. The theorem on the unique solution for ODEs states:

"*If the differential residual is zero everywhere, then the error is zero everywhere, and vice versa.*"

The Lanczos Tau-method is an attempt to make the differential residual as close to zero as possible, assuming that this keeps the error as close to zero as possible. As proved above, this statement is incorrect.

To find the relationship between the error and the differential residual, it is necessary to use the integral form of the equation. Suppose that there is an equation

$$y^{(n)}(t) + c_1(t)y^{(n-1)}(t) + \ldots + c_n(t)y + c(t) = 0, \tag{8}$$

where $c_1(t)$, $c_2(t)$, ..., $c_n(t)$ and $c(t)$ are continuous on the interval $t \in [t_0, T]$. Eq. (8) is equivalent to the equation

$$y(t) = y_0 + y_0'(t - t_0) + \ldots + y_0^{(n-1)} \frac{(t - t_0)^{n-1}}{(n-1)!} -$$
$$- \int\limits_{t_0}^{t} \ldots \int\limits_{t_0}^{t} \left[c_1(t)y^{(n-1)}(t) + \ldots + c_n(t)y(t) + c(t) \right] dt \ldots dt, \tag{9}$$

where $y(t_0) = y_0$, $y'(t_0) = y'_0$, ..., $y^{(n-1)}(t_0) = y^{(n-1)}_0$ are the initial conditions for Eq. (8).

Picard's theorem [36] on the existence and uniqueness of a solution to a LODE uses, in particular, a recurrent sequence of functions $y_k(t)$ defined by the equalities

$$y_{k+1}(t) = N[y_k(t)], \tag{10}$$

where $N[y(t)]$ is the integral operator on the right-hand side of expression (9).

Regardless of the initial function $y_0(t)$ and the size of the considered finite interval $t \in [t_0, T]$, iterations quickly converge to the solution of integral equation (9), i.e., to the solution $y(t)$ of differential equation (8). The given solution is unique and definite for any $t \in [t_0, T]$.

Analyzing the proof of Picard's theorem, we find that

$$\max_{t \in [t_0, T]} |y(t) - y_k(t)| \leq C \max_{t \in [t_0, T]} |y_{k+1}(t) - y_k(t)|, \tag{11}$$

where the constant C is determined only by the coefficients of Eq. (8) and the interval $[t_0, T]$. A more accurate estimate leads to the equality $C = C_0/k!$

Importantly, the constant C in Eq. (11) does not depend on the choice of initial function $y_0(t)$, chain of functions $y_k(t)$ or solution $y(t)$.

This result can be formulated as follows.

Theorem 4 (about the integral residual). *Assume that $y(t) = N[y(t)]$ is the integral equation (9) obtained from differential equation (8); $y(t)$, $z(t)$ are the exact and approximate solutions of Eqs. (8) and (9), respectively; $R(t)$ is the integral residual for $z(t)$, given by the relation*

$$z(t) = N[z(t)] + R(t). \tag{12}$$

Then the error $y(t) - z(t)$ satisfies the relation

$$\max_{t \in [t_0, T]} |y(t) - z(t)| \leq C \max_{t \in [t_0, T]} |R(t)|, \tag{13}$$

where the constant C is determined only by the coefficients of Eq. (8) and the interval $[t_0, T]$.

P r o o f . Integration by parts gives the relations

$$\int_{t_0}^{t} c_{n-1}(t) y'(t) dt = c_{n-1}(t) y(t) - c_{n-1}(t_0) y(t_0) - \int_{t_0}^{t} c'_{n-1}(t) y(t) dt,$$

$$\int_{t_0}^{t} dt \left(\int_{t_0}^{t} c_{n-2}(t) y''(t) dt \right) = \int_{t_0}^{t} dt \left(c_{n-2}(t) y'(t) - c_{n-2}(t_0) y'(t_0) - \int_{t_0}^{t} c'_{n-2}(t) y'(t) dt \right) =$$

$$= c_{n-2}(t) y(t) - c_{n-2}(t_0) y(t_0) - \int_{t_0}^{t} c'_{n-2}(t) y(t) dt - c_{n-2}(t_0) y'(t_0) \frac{(t-t_0)}{1!} -$$

$$- \int_{t_0}^{t} dt \left(c'_{n-2}(t) y(t) - c'_{n-2}(t_0) y(t_0) - \int_{t_0}^{t} c''_{n-2}(t) y(t) dt \right) = \tag{13}$$

$$= c_{n-2}(t) y(t) - \int_{t_0}^{t} 2 c'_{n-2}(t) y(t) dt + \int_{t_0}^{t} dt \left(\int_{t_0}^{t} c''_{n-2}(t) y(t) dt \right) -$$

$$- c_{n-2}(t_0) y(t_0) - c_{n-2}(t_0) y'(t_0) \frac{(t-t_0)}{1!} + c'_{n-2}(t_0) y(t_0) \frac{(t-t_0)}{1!},$$

$$\int_{t_0}^{t} dt \left(\int_{t_0}^{t} dt \left(\int_{t_0}^{t} c_{n-3}(t) y'''(t) dt \right) \right) = \dots$$

Integral equation (9) is transformed into an equivalent integral equation of the form

$$y(t) = H(t) + \int_{t_0}^{t} dt \left(h_1(t) y(t) + \int_{t_0}^{t} dt \left(h_2(t) y(t) + \dots + \int_{t_0}^{t} dt \left(h_n(t) y(t) + c(t) \right) \right) \right),$$

where $h_k(t)$ are some continuous functions (e.g., polynomials) defined by coefficients $c_k(t)$ after integration by parts; $H(t)$ is a polynomial of degree $n-1$ with the coefficients given by complex expressions involving the values of the known functions (coefficients of the equation and their derivatives) at $t = t_0$ and the known initial conditions for $y(t)$.

Importantly, $H(t)$ does not depend on the unknown solution $y(t)$.

Iterations

$$y_{k+1}(t) = H(t) + \int_{t_0}^{t} dt \left(h_1(t) y_k(t) + \int_{t_0}^{t} dt \left(h_2(t) y_k(t) + \dots + \int_{t_0}^{t} dt \left(h_n(t) y_k(t) + c(t) \right) \right) \right)$$

converge quickly under any initial condition $y_0(t)$. To prove this, we introduce the notations

$$\Delta y_k(t) = y_{k+1}(t) - y_k(t), \ M = \max_{t \in [t_0, T]} \left| \Delta y_0(t) \right|, \ H_k = \max_{t \in [t_0, T]} \left| h_k(t) \right|.$$

The iterations for $\Delta y_k(t)$ take the form

$$\Delta y_{k+1}(t) = \int_{t_0}^{t} dt \left(h_1(t) \Delta y_k(t) + \int_{t_0}^{t} dt \left(h_2(t) \Delta y_k(t) + \dots + \int_{t_0}^{t} h_n(t) \Delta y_k(t) dt \right) \right),$$

whence we obtain the following estimates for the interval $t \in [t_0, T]$:

$$|\Delta y_0(t)| \le M,$$

$$|\Delta y_1(t)| \le M(\Delta T H_1 \Delta t + \Delta T^2 H_2 \Delta t^2/2! + \ldots + \Delta T^n H_n \Delta t^n/n!) \le MG\Delta t,$$

$$|\Delta y_2(t)| \le MG(\Delta T H_1 \Delta t^2/2! + \Delta T^2 H_2 \Delta t^3/3! + \ldots) \le MG^2 \Delta t^2/2!$$

$$\ldots\ldots\ldots\ldots\ldots\ldots\ldots\ldots\ldots\ldots\ldots\ldots\ldots\ldots$$

$$|\Delta y_k(t)| \le MG^k \Delta t^k/k!,$$

where $\Delta t = (t - t_0)/\Delta T$, $\Delta T = T - t_0$; $0 \le \Delta t \le 1$, G is a constant:

$$G = \Delta T H_1 + \Delta T^2 H_2 + \ldots + \Delta T^n H_n.$$

A sequence of iterative values

$$y_{k+1}(t) = y_0(t) + \Delta y_0(t) + \Delta y_1(t) + \ldots + \Delta y_k(t)$$

converges uniformly on the interval $t \in [t_0, T]$, since the sum of the increments $\Delta y_k(t)$ is majorized by uniformly absolutely-convergent series:

$$|\Delta y_0(t) + \Delta y_1(t) + \ldots + \Delta y_k(t)| \le |\Delta y_0(t)| + |\Delta y_1(t)| + \ldots +$$

$$+ |\Delta y_k(t)| + \ldots \le M \exp(G\Delta t).$$

Therefore, there is a limit $y_{k+1}(t) \to y(t)$; it gives the solution $y(t)$ of integral equation (9) and differential equation (8), as well as an error estimate:

$$|y(t) - y_0(t)| \le |\Delta y_0(t)| + |\Delta y_1(t)| + \ldots + |\Delta y_k(t)| + \ldots \le$$

$$\le M \exp(G\Delta t) \le MC, \tag{14}$$

although this may turn out to be a very rough estimate of the constant C used in inequality (12).

Let $y_0(t) = z(t)$, where $z(t)$ satisfies Eq. (12). Then the following equalities hold true:

$$y_1(t) = N[z(t)] = z(t) - R(t), \quad \Delta y_0(t) = y_1(t) - y_0(t) = -R(t),$$

$$M = \max|\Delta y_0(t)| = \max|R(t)|.$$

Combining this relation with Eq. (14), we obtain relation (12).

Theorem 4 is proved.

This proof bears significant similarities to the proof of Picard's theorem for systems of LODEs [30], but with minor modifications. Inequality (13) means that in order to minimize the difference between the approximate solution $z(t)$ and the exact solution $y(t)$, we should minimize the modulus of the function $R(t)$ in Eq. (12). Returning from Eq. (9) to Eq. (8), equality (12) is transformed into equality

$$z^{(n)}(t) + c_1(t)z^{(n-1)}(t) + \ldots + c_n(t)z + c(t) = Q(t) = d^n R(t)/dt^n. \tag{15}$$

Eq. (15) shows that the differential residual for the Tau-method is the nth derivative of the error with an accuracy up to a constant factor (see inequality (13)). In particular, if the sum of Chebyshev polynomials is used as a perturbation for the right-hand side of differential equations, as is done in the original Lanczos method, then the error of the approximate solution is an n-fold integral of the sum composed of Chebyshev polynomials. Therefore, the error of the approximate solution for high-order differential equations may be far from the function deviating least from zero.

Similar statements are true for systems of LODEs with continuous coefficients.

Optimized Tau-method for solving differential equations

Suppose that there is a LODE (8) where the leading coefficient is equal to, and the remaining coefficients and the free term are polynomials of the independent variable. As discussed in the previous section, an optimal approximate solution is obtained by selecting the right-hand side in the form

$$R(t) = \sum_k \tau_k \overline{T}_{k+n}(t), \tag{16}$$

where $\overline{T}_{k+n}(t)$ are first-kind Chebyshev polynomials of least deviation from zero, with an argument scaled from the interval $[-1, +1]$ to the interval $[t_0, T]$; τ_k are constants to be determined later.

The number of terms in sum (16) and the degrees of the polynomials correspond to the differential residual in the right-hand side of differential equation (8) after substituting an approximate polynomial solution with indefinite coefficients.

If the integral form

$$z(t) = y_0 + y_0'(t-t_0) + \ldots + y_0^{(n-1)}\frac{(t-t_0)^{n-1}}{(n-1)!} + \sum_k \tau_k \overline{T}_{k+n}(t) -$$

$$- \int_{t_0}^t \ldots \int_{t_0}^t \left[c_1(t) z^{(n-1)}(t) + \ldots + c_n(t) z(t) + c(t) \right] dt \ldots dt. \tag{17}$$

is converted to a differential equation, the output signal is equal to

$$z^{(n)}(t) + c_1(t) z^{(n-1)}(t) + \ldots + c_n(t) z + c(t) = \sum_k \tau_k \overline{S}_k(t), \tag{18}$$

where the polynomials $\overline{S}_k(t)$ are defined as

$$\overline{S}_k(t) = d^n \overline{T}_{k+n}(t) / dt^n.$$

Similarly to the original Lanczos method, Eq. (18) allows to determine both the coefficients of the approximate solution $z(t)$ and the coefficients τ_k. In addition, analysis of Eq. (17) shows that the initial conditions of the approximate solution $z(t)$ should be calculated as

$$z_0^{(j)} = \left. \frac{d^j z(t)}{dt^j} \right|_{t=t_0} = y_0^{(j)} + \sum_k \tau_k \left. \frac{d^j \overline{T}_{k+n}(t)}{dt^j} \right|_{t=t_0}, \; j = 0, 1, \ldots, n-1. \tag{19}$$

Combining Eqs. (19) and linear equations derived from Eq. (18), we can unambiguously find all the indefinite coefficients. This result can be formulated as follows.

Theorem 5. *Let the optimized Tau-method be obtained by combining relations (18) for the differential residual of the approximate solution $\underline{z}(t)$ and relations (19) for the initial conditions of the approximate solution $z(t)$, where $\overline{S}_k(t) = d^n \overline{T}_{k+n}(t) / dt^n$ and $\overline{T}_{k+n}(t)$ are Chebyshev polynomials of degree $k + n$, recalculated from the interval $[-1, +1]$ to the interval $[t_0, T]$. Then the error of the approximate solution $z(t)$, calculated as an exact analytical solution of the perturbed problem (18), (19), satisfies the relation*

$$\max_{t \in [t_0, T]} |y(t) - z(t)| \leq C \max_{t \in [t_0, T]} \left| \sum_k \tau_k \overline{T}_{k+n}(t) \right| \leq C \sum_k |\tau_k|, \tag{20}$$

where the constant C in Eq. (20) is determined only by the coefficients of Eq. (8) and the interval $[t_0, T]$, and the approximate solution $z(t)$ obtained by this technique is close to the optimal minimax approximation of the exact solution y(t).

P r o o f. The statement of the theorem follows directly from Theorem 4 if the weighted sum of scaled first-kind Chebyshev polynomials is used as the integral residual. The final inequality in Eq. (20) follows from the fact that the minimax norm of each of the scaled Chebyshev polynomials on the interval under consideration equals unity.

Theorem 5 is proved

Remark 2. Strictly speaking, the sum of several scaled Chebyshev polynomials is not the polynomial that deviates least from zero on the interval under consideration, and therefore the approximate solution obtained differs from the optimal minimax approximation of the exact solution of the differential equation. The deviation of the error of the approximate solution from the error of the true minimax approximation to the exact solution $y(t)$ is determined by the de la Vallée Poussin theorem (see Theorem 1) after analysis of the local minima and maxima of the value of the right-hand side in inequality (20).

Remark 3. In the case when exact initial conditions are required, the polynomials $\overline{T}_{k+n}(t)$ are represented as

$$\overline{T}_{k+n}(t) = (t - t_0)^n T_n^* \left((t - t_0)/(T - t_0) \right),$$

where $T_n^*(t)$ are the polynomials deviating least from zero, with the weight t^n on the normalized interval $t \in [0,1]$.

This procedure gives a large error but allows to set accurate initial conditions. Algorithms for numerical calculation of polynomials are discussed in [25−27].

Example. Consider an approximate solution of problem (3) in the form of a polynomial

$$x(t) = c_0 + c_1 t + c_2 t^2 + c_3 t^3 + c_4 t^4 + c_5 t^5 + c_6 t^6 + c_7 t^7. \tag{21}$$

Substituting this solution into Eq. (3), we conclude (see Eq. (5)) that two auxiliary polynomials $\overline{S}_6(t)$ and $\overline{S}_7(t)$ with the leading terms t^6 and t^7 are required:

$$\overline{S}_6(t) = \frac{d^2 \overline{T}_8(t)}{dt^2}, \ \overline{S}_7(t) = \frac{d^2 \overline{T}_9(t)}{dt^2},$$

$$\overline{T}_8(t) = T_8\left(\frac{t}{2} - 1\right), \ \overline{T}_9(t) = T_9\left(\frac{t}{2} - 1\right),$$

$$T_8(\tau) = 128\tau^8 - 256\tau^6 + 160\tau^4 + 32\tau^2 - 1,$$

$$T_9(\tau) = 256\tau^9 - 576\tau^7 + 432\tau^5 - 120\tau^3 + 9\tau.$$

In view of Eqs. (19) for the initial conditions, we obtain the following relations:

$$x''(t) + t x'(t) + 2x(t) \equiv \tau_6 \overline{S}_6(t) + \tau_7 \overline{S}_7(t),$$

$$x(0) - \tau_6 \overline{T}_8(0) - \tau_7 \overline{T}_9(0) = 0,$$

$$x'(0) - \tau_6 \overline{T}_8'(0) - \tau_7 \overline{T}_9'(0) = 1.$$

We obtain the following solution of the corresponding SLAE with respect to unknown coefficients:

$$c_0 \approx 0.00234716, \ c_1 \approx 0.92262700,$$

$$c_2 \approx 0.41914500, \ c_3 \approx -1.45266000,$$

$$c_4 \approx 0.78428300, \ c_5 \approx -0.20136600, \tag{22}$$

$$c_6 \approx 0.02406430, \ c_7 \approx -0.00106550.$$

Figs. 3 and 4 illustrate the accuracy of the approximate solution and its first and second-order derivatives. Since there are no visual differences between the graphs of approximate and exact solutions, such graphs are not shown in Fig. 3. The maximum error on the interval $t \in [0.4]$ is 0.0023 for the approximate solution; the error for the first-order derivative is 0.0770; the absolute error for the second-order derivative reaches 0.8400.
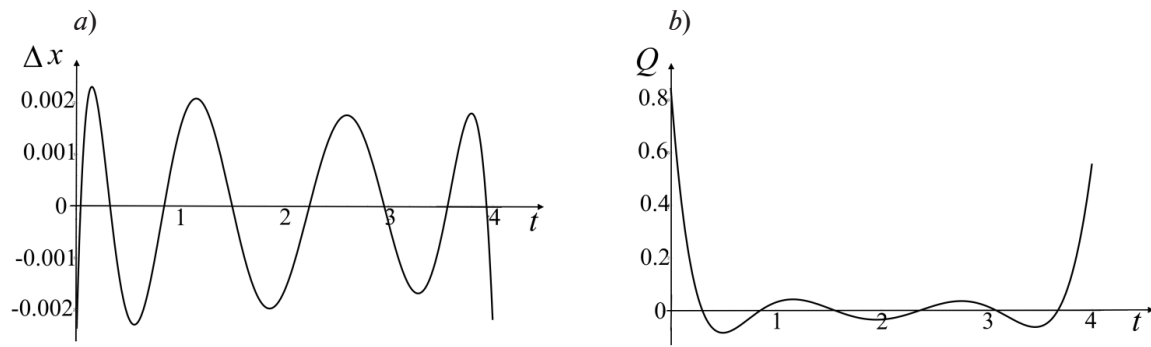
Fig. 3. Characteristics of approximate solution of Eq. (3) obtained by the optimized Tau-method: *a* is the error of this solution, *b* is its differential residual
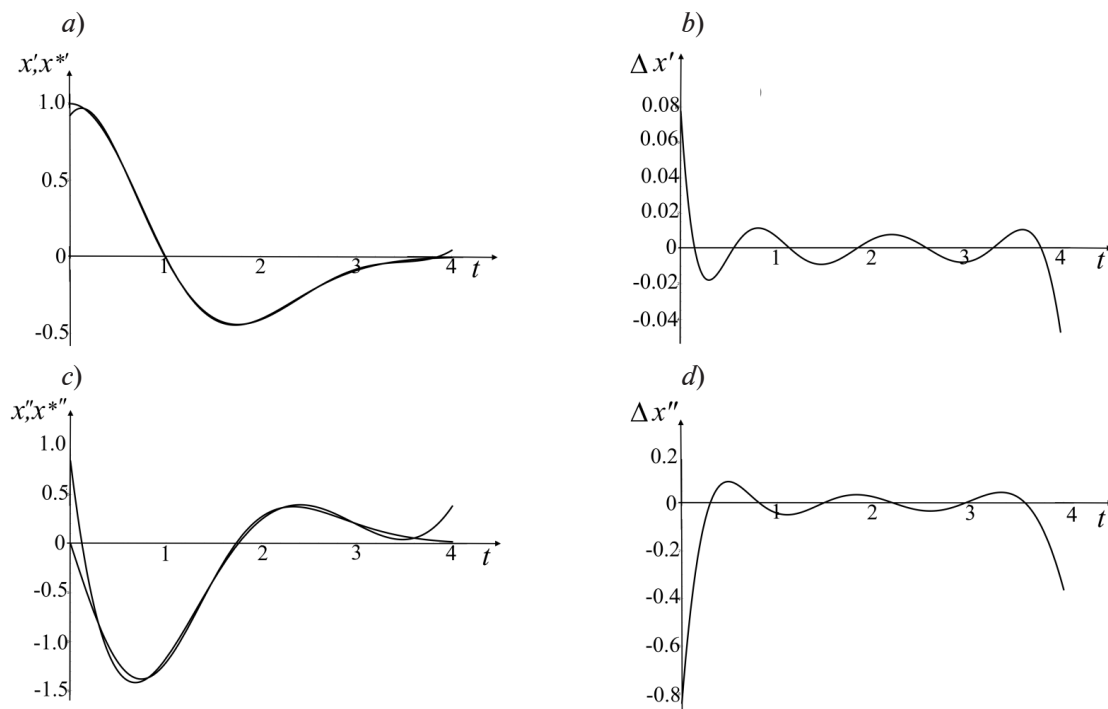
Fig. 4. First (*a*, *b*) and second (*c*, *d*) derivatives of approximate ($x(t)$) and exact ($x*(t)$) solutions of Eq. (3) (*a*, *c*) and error of derivatives for approximate solution (*b*, *d*). Results were obtained by the optimized Tau-method

Discussion

As mentioned in Remark 2 to Theorem 5, the result may differ from the optimal minimax polynomial if the proposed algorithm uses more than one auxiliary polynomial. To find the true optimal solution, it is necessary to consider a general variational problem, where the free parameters of the approximate solution are used to obtain the least deviating polynomial for the right-hand side of the integral equation.

However, the process of solving such a problem is poorly algorithmized. Substituting the true, least deviating polynomial in the right-hand side of the integral equation by the sum of Chebyshev polynomials makes it possible to reduce the general variational problem to simple algebraic calculations. Even if the error of the approximate solution obtained does not turn out to be the true minimax error, this error is still sufficiently small.

The undoubted advantage of the algorithm under consideration is that it allows to obtain approximate analytical solutions when the coefficients of the equation and/or the initial conditions and/or endpoints of the interval under consideration are algebraic expressions depending

on the parameters. This allows to investigate and optimize solutions without numerically solving differential equations for each set of parameters under consideration.

Conclusion

Based on the analysis carried out, we can formulate the following generalizing statements.

1. Minimization of differential residuals of an n-th order LODE or a system of first-order LODEs is not equivalent to minimization of errors of approximate solutions. The polynomial differential residuals in the right-hand sides of the equations used in the Lanczos method should be nth-order derivatives of Chebyshev polynomials and not Chebyshev polynomials themselves.

2. Using approximate initial conditions for approximate solutions gives the researcher more freedom in constructing approximate solutions and ensures greater accuracy. Optimal variations of the initial conditions follow from the analysis of integral residuals, which are linear combinations of scaled Chebyshev polynomials with abstract coefficients calculated subsequently from SLAE of the optimized Tau-method.

3. Derivatives of approximate solutions are not the best approximations to derivatives of exact solutions, even if approximate solutions turn out to be the best approximations to exact solutions. To obtain good approximations for derivatives of exact solutions, it is necessary to transform a linear differential equation with polynomial coefficients into a system of first-order linear differential equations and then apply the Lanczos method to this system. This approach also introduces more free coefficients for varying the approximate solution and, therefore, provides greater accuracy for the best approximate solution.

A separate publication will consider the potential offered by replacing a single differential equation with a system of differential equations in combination with the optimized Tau-method.

The proposed approach is an optimization of the original Lanczos Tau-method for the following reasons.

Firstly, the new method optimizes the error of the approximate solution, whereas the original Tau-method optimizes only the differential residual. However, the error of the approximate solution for high-order differential equations, calculated by multiple iterated integration of the minimum differential discrepancy, may turn out to be very far from the minimum achievable error if the differential residual is not identically zero. The same considerations hold true when some authors use orthogonal polynomials of other types to optimize differential residuals of differential equations.

Secondly, the proposed method introduces a controlled perturbation of the initial conditions. This gives the researcher more freedom to optimize the approximate solution, consequently yielding results with greater accuracy.

Thirdly, error-oriented analysis of integral residuals shows that equations with leading coefficients of polynomials should be considered using adjusted tau algorithms to obtain good accuracy for approximate solutions.

We intend to analyze the special case of the optimized Tau-method, focusing on differential equations with a leading coefficient of the polynomial in a future study.

Acknowledgments

REFERENCES

1. **Lanczos C.,** Trigonometric interpolation of empirical and analytical functions, Journal of Mathematics and Physics. 17 (1−4) (1938) 123−199.

2. **Lanczos C.,** Applied analysis. 1-st. Ed., Prentice Hall Inc., New York, USA, 1956.

3. **Goncharov V. L.,** Teoriya interpolirovaniya i priblizheniya funktsiy [Theory of interpolation and approximation of functions], State Publishing House of Technical and Theoretical Literature, Moscow-Leningrad, 1934 (in Russian).

4. **Achiezer N. I.,** Theory of approximation, 1-st. Ed., Frederick Ungar Publishing Co., New York, 1956.

5. **Golomb M.,** Lectures on theory of approximation, Argonne National Laboratory Publishing, Chicago, USA, 1962.

6. **Ortiz E. L.,** The Tau method, SIAM J. Numer. Anal. 6 (3) (1969) 480−492.

7. **Ortiz E. L.,** Step by step Tau method − Part I. Piecewise polynomial approximations, Comput. Math. Appl. 1 (3−4) (1975) 381−392.

8. **Gavina A., Matos J., Vasconcelos P. B.,** Improving the accuracy of Chebyshev Tau method for nonlinear differential problems, Math. Comput. Sci. 10 (2) (2016) 279−289.

9. **Ortiz E. L.,** A recursive method for the approximate expansion of functions in a series of polynomials, Comput. Phys. Commun. 4 (2) (1972) 151−156.

10. **Crisci M. R., Russo E.,** An extension of Ortiz′ recursive formulation of the Tau method to certain linear systems of ordinary differential equations, Math. Comput. 41 (163) (1983) 27−42.

11. **Freilich J. H., Ortiz E. L.,** Numerical solution of systems of ordinary differential equations with the Tau method: An error analysis, Math. Comput. 39 (160) (1982) 467−479.

12. **Namasivayam S., Ortiz E. L.,** Error analysis of the Tau method: dependence of the approximation error on the choice of perturbation term, Comput. Math. Appl. 25 (1) (1993) 89−104.

13. **Aliabadi M. H., Shamoard S.,** A matrix formulation of the Tau method for Fedholm and Volterra linear integro-diferential equations estimation, Korean J. Comput. & Appl. Math. 9 (May) (2002) 497−507.

14. **Shahmorad S.,** Numerical solution of the general form linear Fredholm−Volterra integro-differential equations by the Tau method with an error estimation, Appl. Math. Comput. 167 (2) (2005) 1418−1429.

15. **Gavina A., Matos J. M. A., Vasconcelos P. B.,** Solving nonholonomic systems with the Tau method, Math. Comput. Appl. 24 (4) (2019) 91−101.

16. **Provoost E., Michiels W.,** The Lanczos Tau framework for time-delay systems: Padé approximation and collocation revisited, SIAM J. Numer. Anal. 62 (6) (2024) 2529−2548.

17. **Varin V. P.,** Approximation of differential operators with boundary conditions, Comput. Math. Math. Phys. 63 (8) (2023) 1381−1400.

18. **Branquinho A., Dнаz J. E. F., Foulquié-Moreno A., Macas M.,** Classical multiple orthogonal polynomials for arbitrary number of weights and their explicit representation, Stud. Appl. Math. 154 (3) (2025) e70033.

19. **Lima N. J., Matos J. M. A., Vasconcelos P. B.,** Solving partial differential problems with Tau Toolbox, Math. Comput. Sci. 18 (8) (2024) 1−12.

20. **Vasconcelos P. B., Grammont L., Lima N. J.,** Low rank approximation in the computation of first kind integral equations with Tau Toolbox, Appl. Numer. Math. 205 (Nov) (2024) 1−15.

21. **Lima N., Matos J. A. O., Matos J. M. A., Vasconcelos P. B.,** A time-splitting Tau method for PDE′s: A contribution for the spectral Tau Toolbox library, Math. Comput. Sci. 16 (1) (2022) 6−11.

22. **Fernбndez L., Marcellбn F., Pérez T. E., Picar M. A.,** Sobolev orthogonal polynomials and spectral methods in boundary value problems, Appl. Numer. Math. 2024. Vol. 200 (June) (2024) 254−272.

23. **Grammont L., Kulkarni R. P., Vasconcelos P. B.,** Fast and accurate solvers for weakly singular integral equations, Numer. Algorithms. 92 (4) (2023) 2045−2070.

24. **Kalitkin N. N., Kolganov S. A.,** The construction of approximations satisfying the Chebyshev alternation, Keldish Institute preprints. (91) (2020).

25. **Zorkaltsev V., Gubiy E.,** Chebyshev approximations by least squares method, The Bulletin of Irkutsk State University. Series "Mathematics". 33 (2020) 3−19 (in Russian).

26. **Trubnikov Y. V., Chernyavsky M. M.,** On a numerical-analytical method for constructing extremal poly-nomials of a complex argument, Proc. Nat. Acad. Sci. of Belarus. Physics and Mathematics Series. 59 (1) (2023) 18−36 (in Russian).

27. **Gulevich D. R., Zalipaev V. V.,** Chislennyye metody v fizike i tekhnike [Numerical methods in physics and engineering], ITMO University, St. Petersburg, 2020 (in Russian).

28. **Belikova G. I., Brovkina E. A., Vager B. G., et al.,** Chislennyye metody [Numerical methods], Published by Russian State Hydrometeorological University, St. Petersburg, 2019 (in Russian).

29. **Belkheeva R. K., Sharyi S. P.,** Vychislitelnyye metody v primerakh [Computing techniques exemplified], Published by Novosibirsk State University, Novosibirsk, 2022 (in Russian).

30. **Berdnikov A., Solovyev K., Krasnova N., et al.,** Algorithm for constructing the Chebyshev-type polynomials and the Chebyshev-type approximations with a given weight, Proc. Int. Conf. on Electrical Engineering and Photonics (EExPolytech). Oct. 20−21, 2022, SPbPU, St. Petersburg (2022) 143−145 (in Russian).

31. **Berdnikov A. S., Solovyev K. V.,** A numerical algorithm for constructing polynomials deviating least from zero with a given weight, St. Petersburg State Polytechnic University Journal. Physics and Mathematics. 16 (2) (2023) 146−160 (in Russian).

32. **Berdnikov A. S., Masyukevich S. V.,** Numerical algorithm for minimax polynomial approximation of functions with a given weight, Nauchnoe Priborostroenie. 33 (3) (2023) 84−91.

33. **Hewitt E., Stromberg K. R.,** Real and abstract analysis: A modern treatment of the theory of functions of a real variable, Springer-Verlag, New-York, 1965.

34. **Paszkowski S.,** Numerical applications of Chebyshev polynomials and series, Państwowe Wydawnictwo Naukowe (PWN), Warsaw, 1975 (in Polish).

35. **Mason J. C., Handscomb D. C.,** Chebyshev polynomials, CRC Press LLC, Washington, 2003.

36. **Tricomi F. G.,** Differential equations, Blackie & Son Ltd., London, 1961.

СПИСОК ЛИТЕРАТУРЫ

1. **Lanczos C.** Trigonometric interpolation of empirical and analytical functions // Journal of Mathematics and Physics. 1938. Vol. 17. No. 1−4. Pp. 123−199.

2. **Lanczos C.** Applied analysis. First edition. New York, USA: Prentice Hall Inc., 1956. 539 p.

3. **Гончаров В. Л.** Теория интерполирования и приближения функций. Ленинград − Москва: Гос. издательство технико-теоретической литературы, 1934. 316 с.

4. **Ахиезер Н. И.** Лекции по теории аппроксимации. М.: Гостехиздат, 1947. 323 с.

5. **Golomb M.** Lectures on theory of approximation. Chicago, USA: Argonne National Laboratory Publishing, 1962. 289 p.

6. **Ortiz E. L.** The Tau method // SIAM Journal on Numerical Analysis. 1969. Vol. 6. No. 3. Pp. 480−492.

7. **Ortiz E. L.** Step by step Tau method − Part I. Piecewise polynomial approximations // Computers and Mathematics with Applications. 1975. Vol. 1. No. 3−4. Pp. 381−392.

8. **Gavina A., Matos J., Vasconcelos P. B.** Improving the accuracy of Chebyshev Tau method for non-linear differential problems // Mathematics in Computer Science. 2016. Vol. 10. No. 2. Pp. 279−289.

9. **Ortiz E. L.** A recursive method for the approximate expansion of functions in a series of polynomials // Computer Physics Communications. 1972. Vol. 4. No. 2. Pp. 151−156.

10. **Crisci M. R., Russo E.** An extension of Ortiz′ recursive formulation of the Tau method to certain linear systems of ordinary differential equations // Mathematics of Computation. 1983. Vol. 41. No. 163. Pp. 27−42.

11. **Freilich J. H., Ortiz E. L.** Numerical solution of systems of ordinary differential equations with the Tau method: An error analysis // Mathematics of Computation. 1982. Vol. 39. No. 160. Pp. 467−479.

12. **Namasivayam S., Ortiz E. L.** Error analysis of the Tau method: dependence of the approximation error on the choice of perturbation term // Computers & Mathematics with Applications. 1993. Vol. 25. No. 1. Pp. 89−104.

13. **Aliabadi M. H., Shamoard S.** A matrix formulation of the Tau method for Fedholm and Volterra linear integro-differential equations estimation // The Korean Journal of Computational & Applied Mathematics. 2002. Vol. 9. May. Pp. 497−507.

14. **Shahmorad S.** Numerical solution of the general form linear Fredholm−Volterra integro-differential equations by the Tau method with an error estimation // Applied Mathematics and Computation. 2005. Vol. 167. No. 2. No. Pp. 1418−1429.

15. **Gavina A., Matos J. M. A., Vasconcelos P. B.** Solving nonholonomic systems with the Tau method // Mathematical and Computational Applications. 2019. Vol. 24. No. 4. Pp. 91−101.

16. **Provoost E., Michiels W.** The Lanczos Tau framework for time-delay systems: Padé approximation and collocation revisited // SIAM Journal on Numerical Analysis. 2024. Vol. 62. No. 6. Pp. 2529−2548.

17. **Варин В. П.** Аппроксимация дифференциальных операторов с учетом граничных условий // Журнал вычислительной математики и математической физики. 2023. Т. 63. № 8. С. 1251−1271.

18. **Branquinho A., Dнаz J. E. F., Foulquié-Moreno A., Macas M.** Classical multiple orthogonal polynomials for arbitrary number of weights and their explicit representation // Studies in Applied Mathematics. 2025. Vol. 154. No. 3. P. e70033.

19. **Lima N. J., Matos J. M. A., Vasconcelos P. B.** Solving partial differential problems with Tau Toolbox // Mathematics in Computer Science. 2024. Vol. 18. No. 8. Pp. 1−12.

20. **Vasconcelos P. B., Grammont L., Lima N. J.** Low rank approximation in the computation of first kind integral equations with Tau Toolbox // Applied Numerical Mathematics. 2024. Vol. 205. November. Pp. 1−15.

21. **Lima N., Matos J. A. O., Matos J. M. A., Vasconcelos P. B.** A time-splitting Tau method for PDE′s: A contribution for the spectral Tau Toolbox library // Mathematics in Computer Science. 2022. Vol. 16. No. 1. Pp. 6−11.

22. **Fernбndez L., Marcellбn F., Pérez T. E., Picar M. A.** Sobolev orthogonal polynomials and spectral methods in boundary value problems // Applied Numerical Mathematics. 2024. Vol. 200. June. Pp. 254−272.

23. **Grammont L., Kulkarni R. P., Vasconcelos P. B.** Fast and accurate solvers for weakly singular

integral equations // Numerical Algorithms. 2023. Vol. 92. No. 4. Pp. 2045−2070.

24. **Калиткин Н. Н., Колганов С. А.** Построение аппроксимаций, удовлетворяющих чебышевскому альтернансу. Препринты ИПМ им. М. В. Келдыша. 33 .91 № .2020 с.

25. **Зоркальцев В. И., Губий Е. В.** Чебышевские приближения и аппроксимация методом наименьших квадратов // Известия Иркутского государственного университета. Серия ″Математика″. 2020. Т. 33. С. 3−19.

26. **Трубников Ю. В., Чернявский М. М.** О численно-аналитическом методе построения экстремальных полиномов комплексного аргумента // Известия Национальной академии наук Беларуси. Серия физико-математических наук. 2023. Т. 1 № .59. С. 36−18.

27. **Гулевич Д. Р., Залипаев В. В.** Численные методы в физике и технике. СПб.: Изд. Университета ИТМО, 211 .2020 с.

28. **Беликова Г. И., Бровкина Е. А., Вагер Б. Г., Витковская Л. В., Матвеев Ю. Л.** Численные методы. СПб.: РГГМУ, 174 .2019 с.

29. **Бельхеева Р. К., Шарый С. П.** Вычислительные методы в примерах. Новосибирск: ИПЦ НГУ, 2022. 90 с.

30. **Berdnikov A., Solovyev K., Krasnova N., Golovitski A., Syasko M.** Algorithm for constructing the Chebyshev-type polynomials and the Chebyshev-type approximations with a given weight // Proceedings of the Internatioonal Conference on Electrical Engineering and Photonics (EExPolytech). October 20−21., 2022. St. Petersburg: SPbPU, 2022. Pp. 143−145.

31. **Бердников А. С., Соловьев К. В.** Численный алгоритм для конструирования многочленов, наименее отклоняющихся от нуля с заданным весом // Научно-технические ведомости СПбГПУ. Физико-математические науки. 2023. Т. 16. № 2. С. 146−160.

32. **Бердников А. С., Масюкевич С. В.** Численный алгоритм для минимаксной полиномиальной аппроксимации функций с заданным весом // Научное приборостроение. 2023. Т. 33. № 3. С. 74−83.

33. **Hewitt E., Stromberg K. R.** Real and abstract analysis: A modern treatment of the theory of functions of a real variable. New-York: Springer-Verlag, 1965. 484 p.

34. **Пашковский С.** Вычислительные применения многочленов и рядов Чебышева. М.: ″Наука″, 1983. 384 с.

35. **Mason J. C., Handscomb D. C.** Chebyshev polynomials. London, New-York, Washington: CRC Press LLC, 2003. 335 p.

36. **Tricomi F. G.** Differential equations. London: Blackie & Son Ltd., 1961. 286 p.

THE AUTHORS

BULYANITSA Anton L.
Institute for Analytical Instrumentation of RAS;
Peter the Great St. Petersburg Polytechnic University
31−33 Ivan Chernykh St., St. Petersburg, 198095, Russia
antbulyan@yandex.ru
ORCID: 0000-0002-9235-8549

BERDNIKOV Alexander S.
Institute for Analytical Instrumentation of RAS
31−33 Ivan Chernykh St., St. Petersburg, 198095, Russia
asberd@yandex.ru
ORCID: 0000-0003-0985-5964

EVSTRAPOV Anatoly A.
Institute for Analytical Instrumentation of RAS
31−33 Ivan Chernykh St., St. Petersburg, 198095, Russia
an_evs@mail.ru
ORCID: 0000-0003-4495-8096

СВЕДЕНИЯ ОБ АВТОРАХ

БУЛЯНИЦА Антон Леонидович − *доктор физико-математических наук, ведущий научный сотрудник Института аналитического приборостроения Российской академии наук, профессор кафедры высшей математики Санкт-Петербургского политехнического университета Петра Великого.*
198095, Россия, г. Санкт-Петербург, ул. Ивана Черных, 31−33, лит. А.
antbulyan@yandex.ru
ORCID: 0000-0002-9235-8549

БЕРДНИКОВ Александр Сергеевич − *доктор физико-математических наук, главный научный сотрудник Института аналитического приборостроения Российской академии наук.*
198095, Россия, г. Санкт-Петербург, ул. Ивана Черных, 31−33, лит. А.
asberd@yandex.ru
ORCID: 0000-0003-0985-5964

ЕВСТРАПОВ Анатолий Александрович − *доктор технических наук, директор Института аналитического приборостроения Российской академии наук.*
198095, Россия, г. Санкт-Петербург, ул. Ивана Черных, 31−33, лит. А.
an_evs@mail.ru
ORCID: 0000-0003-4495-8096

EXPERIMENTAL TECHNIQUE AND DEVICES

A DETECTOR OF MICROMETEOROIDS AND SPACE DEBRIS PARTICLES BASED ON A FILM INDUCTANCE COIL

A. M. Telegin✉, *M. P. Kalaev*

Samara National Research University, Samara, Russia

✉ talex85@mail.ru

Abstract. In the paper, a model of a detector of high-speed microparticles (micrometeoroids and space debris) is proposed, made in the form of a round spiral film inductance coil. The design of the gauge ensures the creation of frequency resonance that occurs when the metal strip of the coil is broken. The obtained results of a laboratory and computer simulations of the detector showed that the film coil is suitable for recording high-speed microparticles larger than 100 μm on a spacecraft such as CubeSat. The fracture point of the inductance coil can be found by analyzing the shift of the resonant frequency of the amplitude-frequency characteristic. In this case, the reliable determination of the point becomes possible if the number of the broken turn is greater than 5.

Keywords: micrometeoroid, space debris, inductance coil, crater, spacecraft, laboratory simulation

ДАТЧИК МИКРОМЕТЕОРОИДОВ И ЧАСТИЦ КОСМИЧЕСКОГО МУСОРА НА ОСНОВЕ ПЛЕНОЧНОЙ КАТУШКИ ИНДУКТИВНОСТИ

А. М. Телегин✉, *М. П. Калаев*

Самарский национальный исследовательский университет имени академика С. П. Королёва,
г. Самара, Россия

✉ talex85@mail.ru

Аннотация. В работе предложена модель датчика высокоскоростных микрочастиц (микрометеороидов и частиц космического мусора) в виде круглой спиральной пленочной катушки индуктивности. Конструкция датчика обеспечивает создание частотного резонанса, возникающего при разрыве металлической полоски катушки. Полученные результаты компьютерного и лабораторного моделирования данной конструкции показали, что пленочная катушка пригодна для регистрации высокоскоростных микрочастиц размерами более 100 мкм на космических аппаратах типа CubeSat. Место разрыва металлической полоски катушки индуктивности можно определять с помощью анализа сдвига резонансной частоты амплитудно-частотной характеристики. При этом надежное определение места разрыва становится возможным, если номер разорванного витка больше 5.

Introduction

Spacecraft engineering must anticipate how various factors in the space environment influence the structural components and onboard electronics. To address this, ground-based laboratories are established, space experiments are conducted, and models of the behavior of materials in outer space are constructed. Besides various types of space radiation (protons, electrons, etc.), spacecraft are also bombarded by space debris and micrometeoroids. Typically, multilayer structures with specialized coatings (such as thermal control coatings, heat pipes, heat exchangers, optical glasses, solar panels, antennas, electric vacuum insulation, etc.) make up the elements of spacecraft directly exposed to these impacts. Even collisions with particles that do not penetrate these elements lead to degradation of their surfaces, gradually altering optical, electrical, and mechanical characteristics, ultimately compromising the spacecraft's performance. As lifespans of spacecraft are extended, detection of micrometeoroids and the ever-increasing amounts of man-debris, along with protection of spacecraft protection pose crucial challenges. Furthermore, the concentrations of high-speed man-made dust particles in near-Earth orbit have been growing in recent years [1−12].

Sensors based on different physical principles are used to control the distribution of microparticles (micrometeoroids and space debris particles) in near-Earth space [11−15]. Film-based detectors are of particular interest, allowing for large sensitive surface and relatively low mass [13−21].

In this paper, we consider the concept of a film detector for high-speed microparticles based on a spiral film inductor allowing to determine the impact sites of high-speed microparticles using spectral analysis of the data obtained. Only one measurement channel was used instead of a large number of multiplexers, as is customary in available equivalents [18].

Model of primary transducer (excluding parasitic parameters)

A film inductor made of conductive material deposited on a dielectric substrate is proposed as the primary transducer of the detector for high-speed microparticles (Fig. 1,*a*). The surface of the other side of the substrate is modified by metallization.

The inductance of such a circular spiral film inductor can be calculated by the following formula [22−28]:

$$L = 0.033937 \cdot \frac{a^2 \cdot n^2}{8 \cdot a + 11 \cdot c} \cdot K_g,$$

$$a = \frac{D_o + D_i}{4}, \; c = \frac{D_o - D_i}{2},$$

$$K_g = 0.570 - 0.145 \cdot \ln(W/h),$$

where L, nH, is the inductance of the inductor coil; n is the number of turns in the coil; D_i, D_o, μm, are its inner and outer diameters, respectively; h, μm, is the thickness of the dielectric substrate; W, μm, is the width of the strip; (some geometric parameters are shown in Fig. 1,*a*); K_g is a factor accounting for the presence of a ground plane.

The factor K_g decreases as it approaches the ground plane, so it was assumed to be equal to unity in [24].
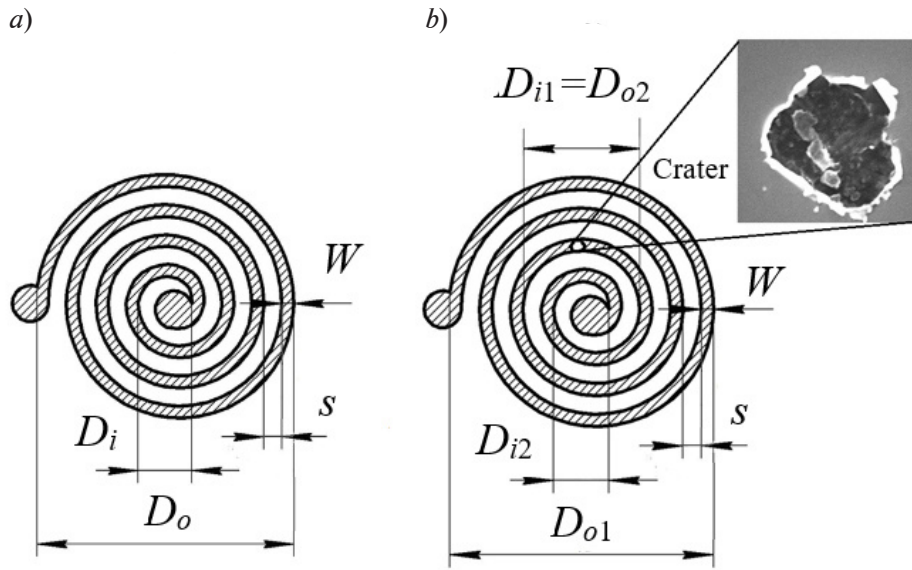
Fig. 1. Cross-sections of inductor coils without break (*a*)
and with break (*b*); their geometric parameters are shown
Inset: micrograph of bowl-shaped depression (crater)

When a high-speed microparticle collides with the metal strip, a crater forms, producing a break (Fig. 1,*b*). The size of the formed crater can be roughly estimated by the empirical models presented in [29]:

$$D/d = K_1 \cdot \rho_p^{0.333} \cdot V^{0.667},$$

where K_1 is a coefficient whose value depends on the nature of the materials of the metal strip and the microparticles; D, d, cm, are the diameters of the crater and microparticles, respectively; ρ_p, g/cm³, is the density of the incident microparticle; V, km/s, is the speed of the microparticle.

The break in the metal strip leads to the formation of an electrical capacitance series-connected to the metal strip (see Figs. 1 and 2). The nominal value of this capacitance can be calculated using model of a coplanar capacitor based on a microstrip line [30−33]:

$$C_g = \frac{1}{2} C_{even},$$

$$C_{even} = W \cdot \left(\frac{S}{W}\right)^{m_e} \cdot e^{K_e} \cdot \left(\frac{\varepsilon}{9.6}\right)^{0.9}$$

$$m_e = \frac{1.565}{(W/h)^{0.16}} - 1, \text{ for } 0.3 \leq \frac{S}{W} \leq 1,$$

$$K_e = 1.97 - \frac{0.03}{W/h}, \text{ for } 0.3 \leq \frac{S}{W} \leq 1.$$

where C_g, pF, is the capacitance of the broken strip; m_e, K_e, C_{even} are intermediate variables used for calculating the capacitance of the broken strip; S_g, μm, is the width of the break in the metal strip equal to the diameter of the crater from a high-speed collision; W, cm, is the width of the metal strip; h, mm, is the height of the dielectric substrate; ε is the dielectric constant of the material to which the strip is attached.
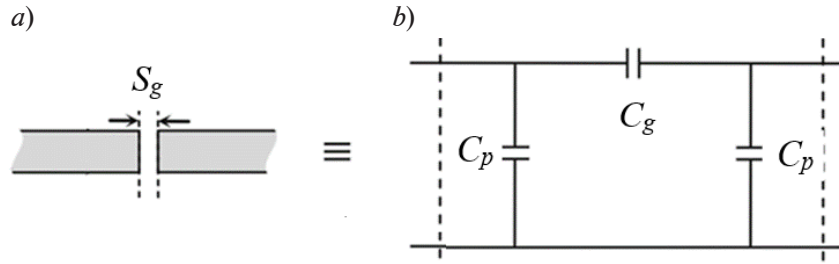
Fig. 2. Schematic model of coplanar capacitor formed from break
of the metal strip (see Fig. 1) (*a*) and its equivalent circuit (*b*):
S_g is the width of the strip; C_g is the capacitance of the broken strip; C_p is the parasitic capacitance
of the strip relative to metallization on the other side of the dielectric substrate
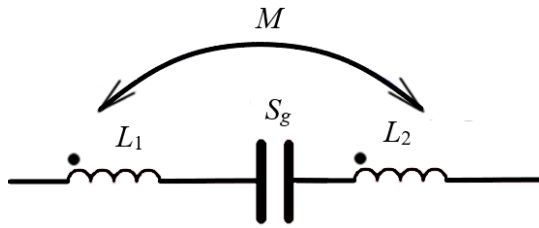
Fig. 3. Equivalent circuit of broken inductor coil:
inductances of the larger and smaller coils L_1, L_2;
their mutual inductance M; capacitance C_g (see
Fig. 2). Each bold dot indicates the point where
current flows into the inductor

Our preliminary calculations show that the capacitance of the coplanar capacitor is small compared with the turn-to-turn capacitance of the film inductor, therefore, C_g can be approximately estimated as the capacitance between two adjacent turns of the coil where break occurred (in accordance with the expressions given in [21, 34]).

Thus, a coil with a break (see Figs. 1, 2) can be represented as two inductively coupled coils, series-connected through an electrical capacitance (Fig. 3). The mutual inductance M can be estimated by the following analytical expression [25]:

$$M = \frac{\mu_0}{4\pi} N_1 \cdot N_2 \frac{D_{o1}}{(1-\theta)\cdot(\Delta-\delta)} \times$$

$$\times \left[\frac{A_3}{3}\left(\Delta^3 - \delta^3\right) \cdot \ln\left(\frac{1}{\theta}\right) + \frac{A_5}{10}\left(\Delta^5 - \delta^5\right)\cdot\left(\frac{1}{\theta^2}-1\right) + \frac{A_7}{28}\left(\Delta^7 - \delta^7\right)\cdot\left(\frac{1}{\theta^4}-1\right) \right],$$

where N_1, N_2 are the numbers of turns in the larger and smaller coils; D_{o1}, D_{i1}, cm, are the outer and inner diameters of the larger coil, respectively; d_{o1}, d_{i1}, cm, are the outer and inner diameters of the smaller coil, respectively (see Fig. 1,*b*); $\theta = D_{o2}/D_{o1}$; $\Delta = D_{i1}/D_{o1}$; $\delta = D_{i2}/D_{o1}$; $A_3 = 9.870$, $A_5 = 3.701$, $A_7 = 2.313$ are the coefficients taken from [25].
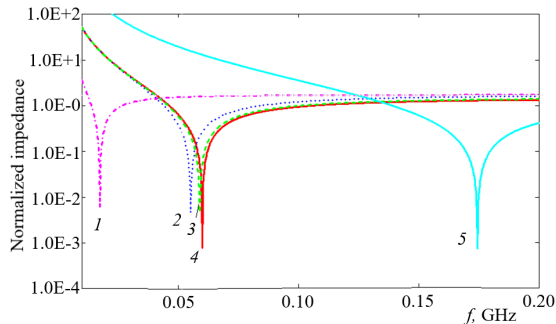
Fig. 4. Variation in normalized impedance
of broken inductor coil for different pairs
of parameters (ratio $k = N/N_{max}$ and
capacitance C_g, pF): 0.7, 0.005 (curve *1*); 0.7,
0.05 (*2*); 0.5, 0.05 (*3*); 0.9, 0.05 (*4*); 0.7, 0.005 (*5*)

The results of computer simulation carried out using the above analytical expressions are shown in Fig. 4. It was taken into account in the simulation that the outer diameter of the coil was taken equal to 10 cm (the dimensions were chosen so that the coil could be placed on the outer wall of a CubeSat spacecraft), the inner diameter of the spiral was 1 cm, the strip width was 250 μm and the number of turns was 90. The inductance of the coil was approximately $9.65\cdot10^{-5}$ H.

The simulation results showed that the total impedance of the broken coil at high frequencies tends to the impedance of an intact coil. The resonance frequencies are clearly detected in this case. They depend on the parameters of the inductor, the location of the break and the nominal value of the resulting capacitance.

Fig. 5. Equivalent circuit of broken coil
taking into account parasitic parameters:
parasitic turn-to-turn capacitance C_3, parasitic
coil resistance R
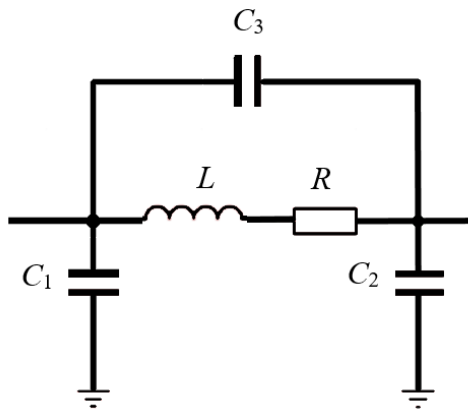
Model of primary transducer taking into account parasitic parameters

Each real coil has parasitic parameters: electrical capacitance and resistance, which can be estimated by the following expressions [22, 23] (Fig. 5):

$$R = \frac{K \cdot \pi \cdot a \cdot n \cdot R_{sh}}{W},$$

$$K = 1 + 0.333 \cdot \left(1 + \frac{S}{W}\right),$$

$$C_3 = 3.5 \cdot 10^{-5} \cdot D_0 + 0.06,$$

where R_{sh}, $\Omega/\square$, is the sheet resistance of the film; C_3, pF, is the parasitic turn-to-turn capacitance; S, μm, is the gap between the turns of the inductor coil; K is the correction factor accounting for current crowding in the corners of the conductor.

The simulation results for the dependence of the coil impedance on frequency (taking into account parasitic parameters) in Fig. 6 indicate that an additional resonance appears on the frequency response curve due to parasitic elements.
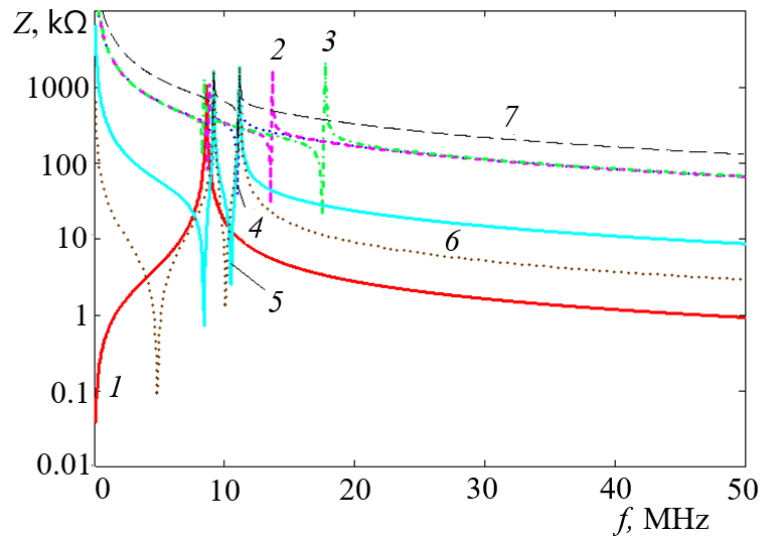
Fig. 6. Dependence of impedance on frequency (taking into account parasitic parameters)
for different pairs of parameters (ratio k and capacitance C_g, pF):
0.9, 0.05 (curve 2); 0.5, 0.05 (3); 0.7, 0.05 (4); 0.7, 0.5 (5); 0.7, 5.0 (6); 0.7, 0.025 (7);
curve 1 corresponds to inductance without break

Experimental results

A prototype of a circular inductor coil with a diameter of 100 mm was made for the experiments (Fig. 7); a close-up photograph of the break made by a scalpel cut is also shown. The width of the metal strip was about 200 μm, the width between the strips was about 250 μm. A LiteVNA64 vector network analyzer with a frequency range of 50 kHz−6.3 GHz was used to determine the amplitude and phase characteristics of the film detector. The analyzer, bundled with the NanoVNA-App software, was connected to a personal computer. The measurement results were saved to a database on the PC and then analyzed using the GNU Octave program.
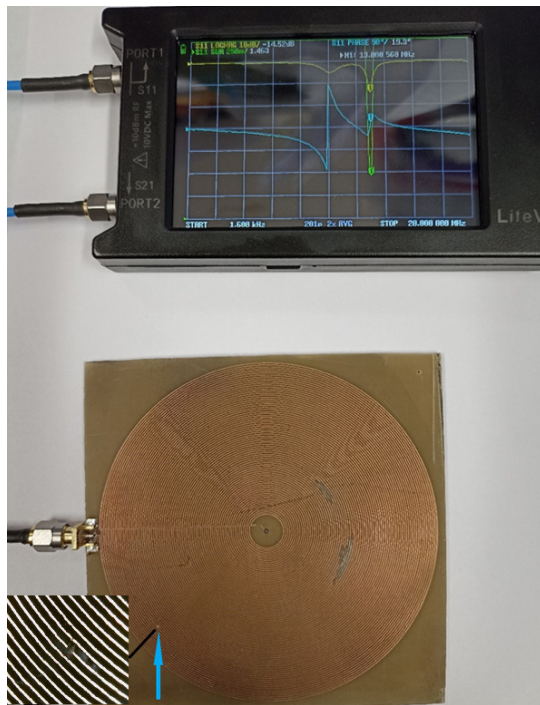
Fig. 7. Photographs of experimental waveform (top) and prototype detector (bottom) based on the inductor (the break point is marked by an arrow)

The screen shows curves of the magnitude of the total impedance, impedance phase and standing wave ratio (yellow, blue, and green lines, respectively).

Inset: enlarged region of the coil with the break

The obtained frequency response of the film inductor for different strip parameters is shown in Fig. 8. The turn numbering starts from the outer diameter of the coil. Importantly, multiple resonances are observed. Further analysis was performed only for the first two resonances.

Fig. 9 shows the experimental dependences of the position of the first (Res1) and second (Res2) resonance peaks on the position of the break point as well as the approximation of experimental data by power functions. It can be seen that the behavior of the experimental curves obtained is in good agreement with the results of computer simulation.

As it turned out, the dependence of the resonant frequency f of the detector on the positions of the break points are well approximated by a function of the form

$$f = k/N^{\alpha},$$

where N is the turn number (numbering starts from the outer diameter of the coil); k is a constant ($k_1 = 59.89$, $k_2 = 121.34$ for the first and second resonances, respectively); α is the exponent ($\alpha_1 = 0.589$, $\alpha_2 = 0.571$ for the first and second resonances, respectively). For small N (5−15), the resonant frequency shift reaches 1 MHz per turn, so that not only the radial position of the particle impact area, but also its sector (part of the arc length when the number N is not an integer) is determined with high accuracy. For large N (60−75), the resonant frequency shift is on the order of 20 kHz per turn, also allowing to determine the particle's impact sector, albeit with a lower accuracy.
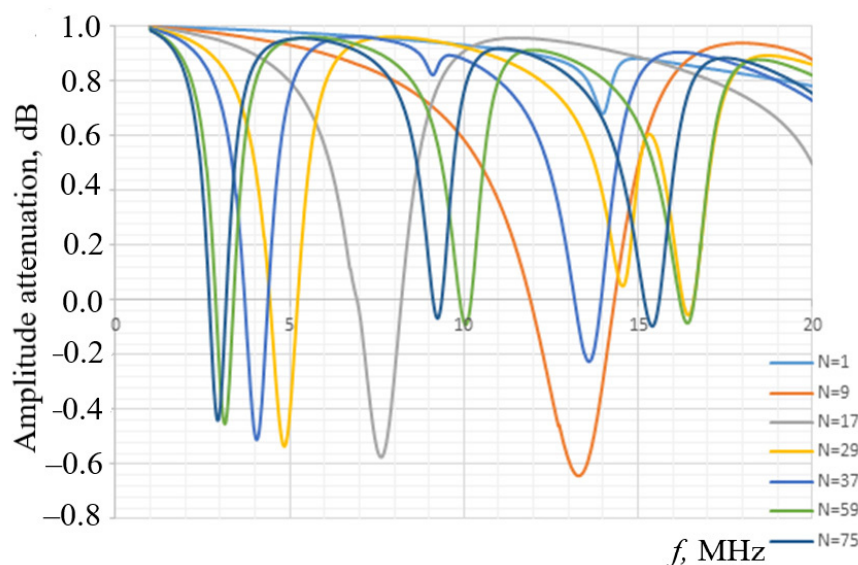
Fig. 8. Frequency response of film inductor with different broken turns
(N is the number of the broken turn)
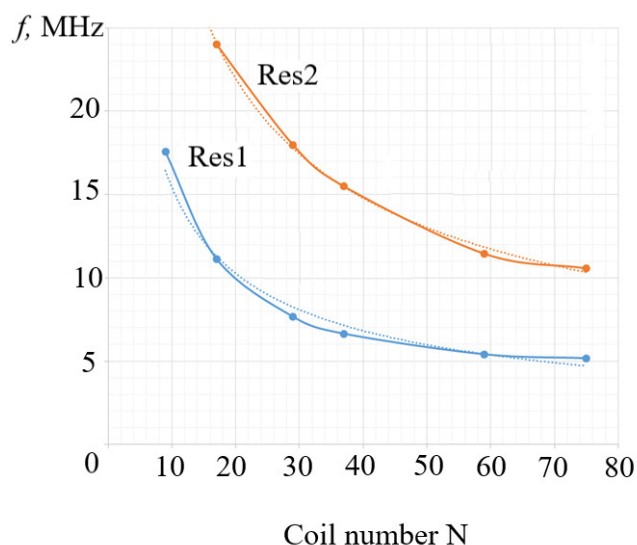
Fig. 9. Experimental (points) and approximating (lines) dependences
of resonant frequency of the detector on the positions of the break points
for the first (Res1) and second (Res2) resonances

Conclusion

In this paper, we propose to use a film inductor as a detector for incident high-speed micro-particles. This configuration eliminates the need for complex multiplexer arrays commonly used in sensors of this type. The presented results of computer and laboratory simulation of this configuration indicate that the film inductor is suitable for detection of high-speed microparticles with sizes from 100 μm in CubeSat spacecraft.

Analyzing the results, we found that the location of the break point in the metal strip of the inductor coil can be determined by analyzing the resonance frequency shift on the frequency response curve. It is possible to reliably determine the location of the break if the number of the broken turn is greater than 5.

REFERENCES

1. **Ivanov N. N., Dobritsa D. B., Yaschenko B. Y.,** A new way of automated dust control of the external atmosphere of a spacecraft during thermal-vacuum testing, Sol. Syst. Res. 54 (7) (2020) 662−667.

2. **Mironov V. V., Tolkach M. A.,** Velocity and distribution on velocity of meteoroids and space debris particles in near-Earth space, Kosmicheskaya Tekhnika i Tekhnologii [Space Technology and Engineering]. (1 (36)) (2022) 125−143 (in Russian).

3. **Durin C., Mandeville J. C., Perrin J. M.,** Active detection of micrometeoroids and space debris SODAD-2 experiment on SAC-D satellite, Adv. Space Res. 69 (10) (2022) 3856−3863.

4. **Dmitryuk S. V.,** Space debris threat: Fundamental & practical aspects, Magazine VKS. (2(99)) (2019) 56−59 (in Russian).

5. **Shustov B. M.,** About fundamental research on space debris problem, In book: Proc. of All-Russian Conf. "Space Debris: Fundamental and Practical Aspects of the Threat", Moscow, April 17−19 2019; Ser. "Mechanics, Management, Computer Science", L. M. Zelenyi, B. M. Shustov (Eds.). Space research Institute of the RAS, Moscow (2019) 7−14 (in Russian).

6. **Ipatov A. V., Vedeshin L. A., Gerasyutin S. A.,** Monitoring kosmicheskogo musora i perspektivy osvoeniya okolozemnogo kosmicheskogo prostranstva [Space debris monitoring and prospects for the exploration of near-Earth space], Zemlya i Vselennaya [The Earth and Universe]. (2 (356)) (2024) 91−108 (in Russian).

7. **Adushkin V. V., Kozlov S. I., Aksenov O. Y., et al.,** The small orbital debris population and its impact on space activities and ecological safety, Acta Astronaut. 176 (Nov) (2020) 591−597.

8. **Rodmann J., Miller A., Traud M., et al.,** Micrometeoroid impact risk assessment for interplanetary missions, Proc. 8th Eur. Conf. on Space Debris (virtual), Darmstadt, Germany, 20−23 April 2021, T. Flohrer, S. Lemmens, F. Schmitz (Eds.), publ. by the ESA Space Debris Office; May (2021) 1 − 5.

9. **Agapov V. M., et al.,** Kosmicheskij musor.: V 2 kn. Red. Raykunov G. G., Kn.1. Metody nablyudeniya i modeli kosmicheskogo musora [Space debris: In 2 books. Raykunov G. G. (Ed.), Book 1. Methods of observation and models of space debris], FIzmatlit Publishing, Moscow, 2014 (in Russian).

10. **Novikov L. S.,** Osnovy ekologii okolozemnogo kosmicheskogo prostranstva [Fundamentals of ecology of the near-Earth space], Universitetskaya kniga [University Book Publishing], 2006 (in Russian).

11. **Kalaev M. P., Rodina A. V., Telegin A. M.,** Investigation of changes in the characteristics of solar panels under the influence of space factors, Instrum. Exp. Tech. 65 (6) (2022) 970−975.

12. **Kalaev M. P., Telegin A. M., Voronov K. E., et al.,** Investigation of optical glass characteristics under the influence of space factors, Computer Optics. 43 (5) (2019) 803−809 (in Russian).

13. **Wang, W., Xue, W., Wu S., et al.,** High-speed micro-particle motion monitoring based on continuous single-frame multi-exposure technology, Materials. 15 (11) (2022) 3871.

14. **Barilaro L., Falsetti C., Olivieri L., et al.,** A conceptual study to characterize properties of space debris from hypervelocity impacts through thin film heat flux gauges, Proc. 2021 IEEE International Workshop on Metrology for AeroSpace (MetroAeroSpace-2021). IEEE Inc. (2021) 430−435.

15. **Gola Y., Kim D., Namilae S.,** Piezoresistive nanocomposites for sensing MMOD impact damage in inflatable space structures, Compos. Commun. 21 (Oct) (2020) 100375.

16. **Rose R., Koets M., Chocron S., Grimm R.,** Application of intelligent spacecraft structures for impact detection, Proc. 2022 IEEE Aerospace Conference (AERO). 5 −12 March 2022. Big Sky, MT, USA (2022) 1−7.

17. **Gbaguidi A., Madiyar F., Kim D., Namilae S.,** Multifunctional inkjet printed sensors for MMOD impact detection, Smart Mater. Struct. 29 (8) (2020) 085052.

18. **Hofmann D. C., Bordeenithikasem P., Zhu Y., et al.,** Design, fabrication, and hypervelocity impact testing of screen-printed flexible micrometeoroid and orbital debris impact sensors for long-duration spacecraft health monitoring, Aerosp. Sci. Technol. 139 (Aug) (2023) 108372.

19. **Faure P., Masuyama Sh., Nakamotoa H., et al.,** Space dust impacts detector development for the evaluation of ejecta, Proc. Eng. 58 (2013) 594−600.

20. **Semkin N. D., Telegin A. M.,** Shock-compressed metal-insulator-metal structures under the action of fast dust particles, Tech. Phys. 56 (7) (2011) 986−991.

21. **Telegin A. M.,** Modeling the transmission coefficient of a micrometeoroid and space debris particle sensor, Eng. Phys. (4) (2024) 37−44 (in Russian).

22. **Bahl I. J.,** Lumped elements for RF and microwave circuits, Artech House Microwave Library, Boston, London, 2003.

23. **Boreyko D. A., D'yachenko T. S., Tyumentsev A. I.,** Issledovanie parametrov katushek induktivnosti, vypolnennyh po LTCC tekhnologii [Study of the parameters of inductance coils made using LTCC technology], Tekhnika radiosvyazi [Radio Commun. Technol.] (17) (2012) 73−83 (in Russian).

24. **Wheeler H. A.,** Simple inductance formulas for radio coils, Proc. Instit. Radio Eng. 16 (10) (1928) 1398−1400.

25. **Kalantarov P. L., Tseitlin L. A.,** Raschet induktivnostej: Spravochnaya kniga [Calculation of inductances: Reference book], 3rd edition, Enerroatomizdat Publishing. Leningrad, 1986 (in Russian).

26. **Benhadda Y., Derkaoui M., Mendaz K., et al.,** Design for integrated planar spiral inductor for MEMS, Period. Polytech. Electr. Eng. Comput. Sci. 67 (4) (2023) 425−437.

27. **Hussain I., Woo D.-K.,** Simplified mutual inductance calculation of planar spiral coil for wireless power applications, Sensors. 22 (4) (2022) 1537.

28. **Futai N., Futai N., Matsumoto K., Shimoyama I**., A flexible micromachined planar spiral inductor for use as an artificial tactile mechanoreceptor, Sens. Actuators A: Phys. 111 (2) (2004) 293−303.

29. **Berthoud L., Mandeville J.-C.,** Empirical impact equations and marginal perforation, Proc. First Eur. Conf. on Space Debris, Darmstadt, Germany. 5−7 April 1993. ESA SD-01 (1993) 459−464.

30. **Awang Z.,** Microwave systems design, Springer Science & Business Media, Berlin/Heidelberg, 2013.

31. **Benedek P., Silvester P.,** Equivalent capacitances for microstrip gaps and steps, IEEE Trans. Microw. Theory Tech. 20 (11) (1972)729 −733.

32. **Garg R., Bahl I. J.,** Microstrip discontinuities, Int. J. Electron. 45 (1) (1978) 81−87.

33. **Qiao Q., Dai Y., Chen Z.,** Signal integrity analysis on discontinuous microstrip line, J. Phys. Conf. Ser. (ICAES-2012). 418 (2013) 012087.

34. **Clayton R. P.**, Analysis of multiconductor transmission lines, Wiley& Sons, Inc., Hoboken, New Jersey, USA, 2008.

СПИСОК ЛИТЕРАТУРЫ

1. **Ivanov N. N., Dobritsa D. B., Yaschenko B. Y.** A new way of automated dust control of the external atmosphere of a spacecraft during thermal-vacuum testing // Solar System Research. 2020. Vol. 54. No. 7. Pp. 662−667.

2. **Миронов В. В., Толкач М. А.** Скорость и распределение скорости метеороидов и частиц космического мусора в околоземном космическом пространстве // Космическая техника и технологии. 2022. № 1 (36). С. 125−143.

3. **Durin C., Mandeville J. C., Perrin J. M.** Active detection of micrometeoroids and space debris SODAD-2 experiment on SAC-D satellite // Advances in Space Research. 2022. Vol. 69. No. 10. Pp. 3856−3863.

4. **Дмитрюк С. В.** Космический мусор: прикладные аспекты угрозы // Воздушно-космическая сфера. 99) 2 № .2019). С. 59−56.

5. **Шустов Б. М.** О фундаментальных исследованиях по проблеме космического мусора // Сборник трудов Всероссийской научной конференции «Космический мусор: фундаментальные и практические аспекты угрозы». 19−17 апреля 2019 г. Сер. «Механика, управление и информатика». Под ред. Л. М. Зеленого, Б. М. Шустова. М.: ИКИ РАН, 2019. С. 7 −14.

6. **Ипатов А. В., Ведешин Л. А., Герасютин С. А.** Мониторинг космического мусора и перспективы освоения околоземного космического пространства // Земля и Вселенная. 2024. № 2 (356). С. 91−108.

7. **Adushkin V. V., Kozlov S. I., Aksenov O. Y., Veniaminov S. S., Tyurenkova V. V.** The small orbital debris population and its impact on space activities and ecological safety // Acta Astronautica. 2020. Vol. 176. Novenber. Pp. 591−597.

8. **Rodmann J., Miller A., Traud M., Bunte K. D., Millinger M.** Micrometeoroid impact risk assessment for interplanetary missions // Proceedings of the. 8th European Conference on Space Debris (virtual), Darmstadt, Germany, 20−23 April 2021, T. Flohrer, S. Lemmens, F. Schmitz (Eds.), published by the ESA Space Debris Office; May 2021. Pp. 1 − 5.

9. **Агапов В. М. и др.** Космический мусор: В 2 кн. Под науч. ред. Г. Г. Райкунова. Кн.1. Методы наблюдения и модели космического мусора. М.: Физматлит, 2014. 244 с.

10. **Новиков Л. С.** Основы экологии околоземного космического пространства. М.: Университетская книга, 84 .2006 с.

11. **Калаев М. П., Родина А. В., Телегин А. М.** Исследование изменения характеристик солнечных батарей при воздействии факторов космического пространства // Приборы и техника эксперимента. 6 № .2022. С. 105−99.

12. **Калаев М. П., Телегин А. М., Воронов К. Е., Лисян Ц., Цзилун Ц.** Исследование характеристик оптических стекол при воздействии факторов космического пространства // Компьютерная оптика. 2019. Т. 43. № 5. С. 803 −809.

13. **Wang, W., Xue, W., Wu S., Mu Z., Yi J., Tang A. J.** High-speed micro-particle motion monitoring based on continuous single-frame multi-exposure technology // Materials. 2022. Vol. 15. No. 11. P. 3871.

14. **Barilaro L., Falsetti C., Olivieri L., Giacomuzzo C., Francesconi A., Beard P., Camilleri R.** A conceptual study to characterize properties of space debris from hypervelocity impacts through thin film heat flux gauges// Proceedings of the 2021 IEEE International Workshop on Metrology for AeroSpace, (MetroAeroSpace- 2021). IEEE Inc. 2021. Pp. 430−435.

15. **Gola Y., Kim D., Namilae S.** Piezoresistive nanocomposites for sensing MMOD impact damage in inflatable space structures // Composites Communications. 2020. Vol. 21. October. P. 100375.

16. **Rose R., Koets M., Chocron S., Grimm R.** Application of intelligent spacecraft structures for impact detection // Proceedings of the 2022 IEEE Aerospace Conference (AERO). 5 −12 March 2022. Big Sky, MT, USA. 2022. Pp. 1−7.

17. **Gbaguidi A., Madiyar F., Kim D., Namilae S.** Multifunctional inkjet printed sensors for MMOD impact detection // Smart Materials and Structures. 2020. Vol. 29. No. 8. P. 085052.

18. **Hofmann D. C., Bordeenithikasem P., Zhu Y., Liu Y., Conrad N. J., Davis B. A., Christiansen E. L., Shakouri A., Mohammadi S.** Design, fabrication, and hypervelocity impact testing of screen-printed flexible micrometeoroid and orbital debris impact sensors for long-duration spacecraft health monitoring // Aerospace Science and Technology. 2023. Vol. 139. August. P. 108372.

19. **Faure P., Masuyama Sh., Nakamotoa H., Akahoshi Y., Yukihito Kitazawa Y., Koura T.** Space dust impacts detector development for the evaluation of ejecta // Procedia Engineering. 2013. Vol. 58. Pp. 594−600.

20. **Семкин Н. Д., Телегин А. М.** Ударно-сжатые структуры металл-диэлектрик-металл в условиях воздействия высокоскоростных пылевых частиц // Журнал технической физики. 2011. Т. 7 № .81. С. 93−88.

21. **Телегин А. М.** Моделирование коэффициента передачи датчика микрометеороидов и частиц космического мусора // Инженерная физика. 2024. № 4. С. 37−44.

22. **Bahl I. J.** Lumped elements for RF and microwave circuits. Boston, · London: Artech House Microwave Library, 2003. 488 p.

23. **Борейко Д. А., Дьяченко Т. С., Тюменцев А. И.** Исследование параметров катушек индуктивности, выполненных по LTCC технологии // Техника радиосвязи. 2012. № 17. С. 73−83.

24. **Wheeler H. A.** Simple inductance formulas for radio coils // Proceedings of the Institute of Radio Engineers. 1928. Vol. 16. No. 10. Pp. 1398−1400.

25. **Калантаров П. Л., Цейтлин Л. А.** Расчет индуктивностей: Справочная книга. 3-е изд., перераб. и доп. Ленинград: Энергоатомиздат, 1986. 488 с.

26. **Benhadda Y., Derkaoui M., Mendaz K., Kharbouch H., Spiter P.** Design for integrated planar spiral inductor for MEMS // Periodica Polytechnica Electrical Engineering and Computer Science. 2023. Vol. 67. No. 4. Pp. 425−437.

27. **Hussain I., Woo D.-K.** Simplified mutual inductance calculation of planar spiral coil for wireless power applications // Sensors. 2022. Vol. 22. No. 4. P. 1537.

28. **Futai N., Futai N., Matsumoto K., Shimoyama I**. A flexible micromachined planar spiral inductor for use as an artificial tactile mechanoreceptor // Sensors and Actuators A: Physical. 2004. Vol. 111. No. 2. Pp. 293−303.

29. **Berthoud L., Mandeville J.-C.** Empirical impact equations and marginal perforation // Proceedings of the First European Conference on Space Debris, Darmstadt, Germany. 5−7 April 1993. ESA SD-01. Pp. 459−464.

30. **Awang Z.** Microwave systems design. Berlin/Heidelberg: Springer Science & Business Media, 2013. 313 с.

31. **Benedek P., Silvester P.** Equivalent capacitances for microstrip gaps and steps // IEEE Transactions on Microwave Theory and Techniques. 1972. Vol. 20. No. 11. Pp.729 −733.

32. **Garg R., Bahl I. J.** Microstrip discontinuities // International Journal of Electronics. 1978. Vol. 45. No. 1. Pp. 81−87.

33. **Qiao Q., Dai Y., Chen Z.** Signal integrity analysis on discontinuous microstrip line // Journal of Physics: Conference Series. 7th International Conference on Applied Electrostatics (ICAES-2012). 2013. Vol. 418. P. 012087.

34. **Clayton R. P.** Analysis of multiconductor transmission lines. Hoboken, New Jersey, USA: Wiley& Sons, Inc., 2008. 821 p.

THE AUTHORS

TELEGIN Aleksey M.
Samara National Research University
34 Moscow HWy, Samara, 443086, Russia
talex85@mail.ru
ORCID: 0000-0002-1750-1536

KALAEV Mikhail P.
Samara National Research University
34 Moscow HWy, Samara, 443086, Russia
sgau5@yandex.ru
ORCID: 0009-0003-2601-4144

СВЕДЕНИЯ ОБ АВТОРАХ

ТЕЛЕГИН Алексей Михайлович — *кандидат физико-математических наук, доцент кафедры радиоэлектронных систем Самарского национального исследовательского университета имени академика С. П. Королёва.*
443086, Россия, г. Самара, Московское шоссе, 34
talex85@mail.ru
ORCID: 0000-0002-1750-1536

КАЛАЕВ Михаил Павлович — *кандидат технических наук, доцент кафедры радиоэлектронных систем Самарского национального исследовательского университета имени академика С. П. Королёва.*
443086, Россия, г. Самара, Московское шоссе, 34
sgau5@yandex.ru
ORCID: 0009-0003-2601-4144

PHYSICAL OPTICS

A DUAL-BEAM METHOD FOR STUDYING THE INHOMOGENEITY INDUCED BY LASER RADIATION IN A MAGNETIC FLUID

A. A. Alekseev[1]✉, I. V. Pleshakov[2,1], Yu. I. Kuzmin[2], Ya. A. Fofanov[3]

[1] Peter the Great St. Petersburg Polytechnic University, St. Petersburg, Russia;

[2] Ioffe Institute, St. Petersburg, Russia;

[3] Institute for Analytical Instrumentation RAS, St. Petersburg, Russia

✉ arseniy.alekseev98@gmail.com

Abstract. In the paper, a new method of experimental study based on the induction of a so-called thermal lens (TL) by the focused high-level laser radiation has been put forward for magnetic fluids. This TL is a region with a spatially changing refractive index, which occurs due to the redistribution of the nanoparticle concentration in the material and the thermal expansion of the carrier fluid. This region was illuminated by the low-level light emission of an auxiliary laser. The optical response of the medium was recorded as diffraction patterns formed from each of these two beams. The shape of the diffraction pattern in the auxiliary beam was shown to depend on the angle at which it was directed to the TL. The diffraction spot sizes were found to depend on the strength of the applied external magnetic field.

Keywords: magnetic fluid, laser radiation, thermal lens, light-induced inhomogeneity, diffraction pattern

ДВУХЛУЧЕВОЙ МЕТОД ИССЛЕДОВАНИЯ НЕОДНОРОДНОСТИ, ИНДУЦИРОВАННОЙ ЛАЗЕРНЫМ ИЗЛУЧЕНИЕМ В МАГНИТНОЙ ЖИДКОСТИ

А. А. Алексеев[1]✉, И. В. Плешаков[2,1], Ю. И. Кузьмин[2], Я. А. Фофанов[3]

[1] Санкт-Петербургский политехнический университет Петра Великого, Санкт-Петербург, Россия;

[2] Физико-технический институт им. А.Ф. Иоффе РАН, Санкт-Петербург, Россия;

[3] Институт аналитического приборостроения РАН, Санкт-Петербург, Россия

✉ arseniy.alekseev98@gmail.com

Аннотация. В статье предложен новый метод экспериментального исследования магнитной жидкости, основанный на эффекте индуцирования в ней так называемой тепловой линзы под действием высокоинтенсивного сфокусированного лазерного

излучения. Такая линза — это светоиндуцированная неоднородность, и она представляет собой область с пространственно-изменяющимся показателем преломления, которая формируется в результате перераспределения концентрации наночастиц в жидкой среде и теплового расширения жидкости-носителя. Указанная область просвечивается световым пучком вспомогательного лазера малой интенсивности. Оптический отклик среды регистрируется в виде дифракционных картин, образующихся от каждого из двух лазерных пучков. Установлено, что размеры дифракционных пятен зависят от напряженности приложенного внешнего магнитного поля.

Introduction

Magnetic fluids, which are colloids whose solid phase is a magnetically ordered material, find diverse different practical applications [1, 2]. They are also of interest for research: for example, recent studies considered the behavior of such fluids embedded in biological systems [3−5] and other complex media [6-8]. Optoelectronic devices (modulators, sensors, tunable filters, etc.) with an active medium based on magnetic fluids are considered in many works [9−12].

A key factor to take into account in exploiting the optical properties of these substances is that a high-intensity laser beam alters the concentration of magnetic nanoparticles. This effect can be attributed to several mechanisms, the primary one being thermal (see [13] and references therein). A change in concentration leads to a change in the refractive index n and the appearance of a lens-like inhomogeneity in the sample, the so-called thermal blooming or thermal lensing (TL), on which the light diffracts. This is in fact a type of self-diffraction. TL under high-intensity laser radiation is characteristic for many materials, in particular, it has been observed in magnetic fluids [14, 15].

The common technique for studying TL is focusing a laser beam in a medium, measuring the diffraction of the same beam on the inhomogeneity induced by it. The information obtained from such experiments is essential both for developing photonics devices and for understanding the nature of the processes occurring in such systems.

Since laser radiation induces TL and diffracts on it, its characteristics (power, beam shape, etc.) cannot be varied without it modifying the object studied.

In this paper, to study the effect of thermal lensing, we propose to use an auxiliary low-intensity laser illuminating the induced inhomogeneity at a certain angle. The advantage of this approach is independent probing of the studied object.

Experimental

Samples. The samples were made from a commercial magnetic fluid with a solid fraction consisting of magnetite nanoparticles with an average diameter of about 10 nm. The solvents were kerosene and water with added organic oils and stabilizers (surfactants that prevent aggregation). They were diluted with the appropriate carrier to concentrations $\varphi = 1−3$ vol.%. The fluid was placed in a cell with the thickness $d = 60$ μm.

Experimental setup. Fig. 1 shows a diagram of the experimental setup. The primary light source (a helium-neon laser) had a wavelength of 633 nm and a power of 17 MW. Its radiation was focused on the sample with a lens; according to estimates of focal spot size, the optical irradiance in it was 18 MW/m². Radiation from an auxiliary semiconductor laser with a wavelength of 660 nm
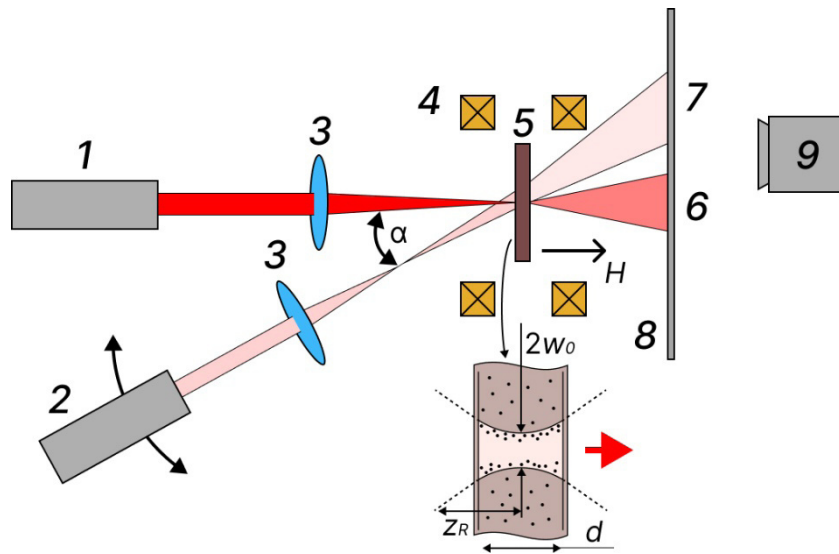
Fig. 1. Schematic of experimental setup: primary and auxiliary lasers *1, 2*, respectively;
focusing lenses *3*; electromagnet *4*; cell *5* with sample; diffraction spots *6, 7*
from primary and auxiliary beams, respectively; screen *8*,
digital CMOS (Complementary Metal-Oxide-Semiconductor) camera *9*
Inset: region of laser beam focused on the sample, with the waist parameters

and a power of 12 MW was focused onto the sample. The irradiance from this laser beam on the inhomogeneity induced by the primary laser did not exceed 4 kW/m^2 (by our estimate), i.e., it could not have any significant influence on it. Each of the two beams formed its own diffraction pattern on the translucent screen located behind the cell.

The cell with the magnetic fluid was placed in an electromagnet generating field with the strength H orthogonal to its plane, variable from zero to 60 kA/m.

The dimensions of the TL were estimated assuming its boundary is approximately defined by the caustic (see inset in Fig. 1); the parameters characterizing the laser beam waist were used: its diameter at the beam focus $2w_0$ and the Rayleigh length z_R. They were calculated using well-known formulas, equaling 35 and 900 μm, respectively, for the geometry of our optical circuit. Since the thickness of the cell d is much smaller than the Rayleigh length z_R, we assumed that the inhomogeneity had an approximately cylindrical shape with a diameter of about 35 μm and a length of 60 μm.

Results

Several series of diffraction patterns were obtained in the experiments under different conditions and for different samples (Fig. 2).

Pronounced diffraction patterns appearing as concentric rings were observed in both beams for the kerosene-based magnetic fluid (see Fig. 2,*a*), which were noticeably influenced by the application of the magnetic field (see Fig. 2,*b*). The spot in the auxiliary beam was elongated, and an increase in the angle α led to an increase in its ellipticity (see Fig. 2,*c*). The spot sizes in water-based samples were much smaller than in the kerosene-based samples (Fig. 2,d shows an image obtained at about three times the screen distance from the cell). It is evident that the diffraction rings are poorly resolved (the diffraction pattern from the auxiliary beam, located on the right in Fig. 2,*d*, is magnified by several times for clarity). For this reason, only the results obtained for kerosene-based samples are given below.

The size D of the diffraction patterns depended on the magnetic field strength H, while the variation in this size can be conveniently characterized by a normalized parameter

$$Q(H) = D(H)/D_0,$$

where $D(H)$, D_0 are the average diameters of the outer ring of the diffraction spot at field strength H and at $H = 0$, respectively.
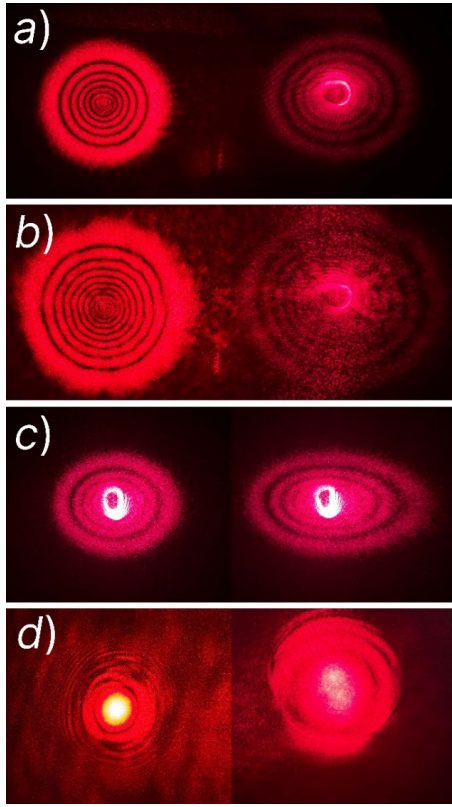
Fig. 2. Examples of diffraction patterns from different samples under different conditions: samples based on kerosene, φ = 2 vol.% (*a−c*) and water, φ = 3 vol.% (*d*); applied magnetic fields *H* = 0 (*a, c, d*) and *H* = 56 kA/m (*b*); images from primary (left) and auxiliary (on the right) beams are shown (*a,b,d*); angle α (see Fig. 1) was equal to 20°. The difference in Fig. 2,*c*: here both images are from auxiliary beams: at α = 35° on the left and at α = 55° on the right
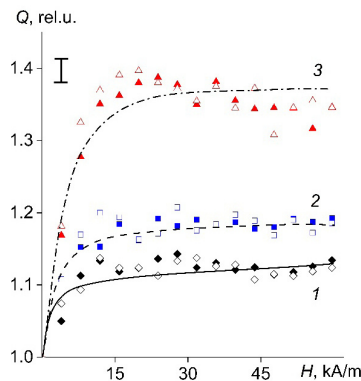
The dependences of Q on the magnetic field strength for some concentrations φ are shown in Fig. 3. The angle α was chosen small here so that the elliptical distortion of the response in the auxiliary beam was negligible. It can be seen that the shapes of the $Q(H)$ curves for the responses in the primary and auxiliary beams coincide. The concentration dependences $Q(φ)$ are shown in Fig. 4, illustrating the increase in the relative size of diffraction spots with increasing concentration.

Discussion

Analyzing the obtained experimental results, we can interpret them as follows. If a cylindrical inhomogeneity induced by radiation from the primary laser is placed in an additional radiation field from the auxiliary laser directed to the axis of the main laser at an angle, then another diffraction pattern similar to the primary one should appear on the screen; this is in fact exactly what is observed. The diffraction spot from the auxiliary beam becomes more elliptical with increasing angle α between the axes of the two lasers, which correlates with the elongation in the projection of the cylindrical inhomogeneity under side illumination, so that the number of resolved rings in the diffraction pattern decreases.

Since the size of the diffraction patterns is much smaller in the case of the water-based magnetic fluid, it is logical to assume that the characteristic size of TL in them should be estimated as larger than in kerosene-based samples. This assumption is consistent with the results obtained in [13], finding that such magnetic fluids tend to form large nanoparticle aggregates under laser radiation, significantly exceeding $2w_0$ (beam waist diameter).

Fig. 3. Dependences of relative sizes of diffraction spots on magnetic field strength in kerosene-based magnetic fluids at different concentrations φ, vol.%: 1.0 (curve *1*), 1.5 (*2*), 3.0 (*3*)

Data are shown for primary (shaded symbols) and auxiliary (unshaded symbols) laser beams at angle α = 20°
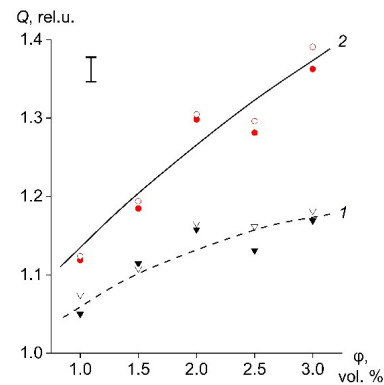
Fig. 4. Concentration dependences of relative sizes of diffraction spots in kerosene-based magnetic fluids at magnetic field strengths *H* = 4.0 kA/m (*1*) and 16 kA/m (*2*)

Data are shown for primary (shaded symbols) and auxiliary (unshaded symbols) laser beams

The behavior of optical responses in the magnetic field is qualitatively explained by the properties of magnetic fluids. It is known that chain-like aggregates arise in them under the influence of magnetic fields, with the diameters ranging from units to several tens of micrometers (for liquid media, where kerosene or water are solvents and the magnetic field strength H is more than 8 kA/m) [16, 17]. These sizes of the aggregates are comparable to the diameter $2w_0$, i.e., the inhomogeneity induced by laser radiation is commensurate with the magnetically induced aggregate. It is natural to assume that the shape of this object does not radically change upon application of the magnetic field. However, the spatial distribution of particles (and the refractive index n associated with their concentration [17]) in the object is transformed due to dipole interaction of magnetic moments aligned with the vector of the magnetic field. An increase in the divergence of the laser beam passing through the TL was observed in kerosene-based samples with increasing magnetic field strength, indicating a decrease in the size of the TL.

Evidently, the graphs of the functions $Q(H)$ for different concentrations φ are almost similar, reaching saturation at a magnetic field of about 15 kA/m (see Fig. 3). The value of the field strength at saturation we obtained differs from the values typical for magnetic fluids, however, it is in good agreement with the data on the dependence of the refractive index n on the field strength H [17]. The diffraction patterns of water-based magnetic fluids are almost independent of the magnetic field. This likely happens because the structure formed in the is larger and denser than in kerosene-based samples [13].

Conclusion

Based on our findings, we can conclude that using auxiliary laser beams to probe light-induced inhomogeneities in magnetic fluids can serve as an effective method for characterizing their physical properties. Its advantage is that inhomogeneities induced by high-intensity radiation can be probed independently using a weak laser beam.

Within the proposed approach, such inhomogeneities can be probed without altering the conditions under which they form, only tuning the auxiliary laser's illumination parameters.

REFERENCES

1. **Scherer C., Figueiredo Neto A. M.,** Ferrofluids: properties and applications, Braz. J. Phys. 35 (3A) (2005) 718−727.

2. **Oehlsen O., Cervantes-Rамнrez S. I., Cervantes-Avilés P., Medina-Velo I. A.,** Approaches on ferrofluid synthesis and applications: Current status and future perspectives, ACS Omega. 7 (4) (2022) 3134−3150.

3. **Socoliuc V., Avdeev M. V., Kuncser V., et al.,** Ferrofluids and bio-ferrofluids: Looking back and stepping forward, Nanoscale. 14 (13) (2022) 4786−4886.

4. **Monteseрнn M., Larumbe S., Martнnez A. V., et al.,** Recent advances in the development of magnetic nanoparticles for biomedical applications, J. Nanosci. Nanotechnol. 21 (5) (2021) 2705−2741.

5. **Imran M., Alam M. M., Khan A.,** Advanced biomedical applications of iron oxide nanostructures based ferrofluids, Nanotechnology. 32 (42) (2021) 422001.

6. **Yerin C., Belykh S.,** Magnetic emulsions as prospective magneto-optical media, IEEE Trans. Magn. 58 (2-1) (2022) 4600704.

7. **Pleshakov I. V., Alekseev A. A., Bibik E. E., et al.,** Magnetic nanoparticles in solid matrices: Formation and fixation of structures, induced by magnetic field, Nanosyst. Phys. Chem. Math. 14 (5) (2023) 544−548.

8. **Yerin K. V., Vivchar V. I.,** Transmission spectra of diluted and concentrated magnetite colloids in liquid dielectrics, J. Appl. Spectrosc. 90 (7) (2024) 1205−1211.

9. **Zhao Y., Zhang Y., Lv R.-Q., Wang Q.,** Novel optical devices based on the tunable refractive index of magnetic fluid and their characteristics, J. Magn. Magn. Mat. 323 (23) (2011) 2987−2996.

10. **Hao Z., Li Y., Pu Sh., et al.,** Ultrahigh-performance vector magnetic field sensor with wedge-shaped fiber tip based on surface plasmon resonance and magnetic fluid, Nanophotonics. 11 (15) (2022) 3519−3528.

11. **Han Sh., Pu Sh., Hao Z., et al.,** In-line temperature-compensated vector magnetic field sensor with side-polished fiber, Opt. Lett. 48 (17) (2023) 4504−4507.

12. **Dave V., Mehta R. V.,** Diffraction of laser light by a ferrocell and ferrofluid layers: A comparison, Optik. 311 (Sept) (2024) 171925.

13. **Pleshakov I. V., Alekseev A. A., Bibik E. E., et al.,** Effect of laser radiation on magnetite nanoparticles in deposited ferrofluid, Nanosyst. Phys. Chem. Math. 15 (3) (2024) 346−351.

14. **Du T., Yuan S., Luo W.,** Thermal lens coupled magneto-optical effect in a ferrofluid, Appl. Phys. Lett. 65 (14) (1994) 1844−1846.

15. **Sharma P., Alekhya V. V., Pathak S., et al.,** A novel experimental approach for direct observation of magnetic field induced structuration in ferrofluid, J. Magn. Magn. Mat. 534 (Sept) (2021) 168024.

16. **Prokof'ev A. V., Pleshakov I. V., Bibik E. E., Kuz'min Yu. I.,** An optical investigation of the geometric characteristics of aggregates formed by particles of magnetic fluid, Tech. Phys. Lett. 43 (2) (2017) 194−196.

17. **Horng H. E., Hong Ch.-Y., Yang S. Y., Yang H. C.,** Designing the refractive indices by using magnetic fluids, Appl. Phys. Lett. 82 (15) (2003) 2434−2436.

СПИСОК ЛИТЕРАТУРЫ

1. **Scherer C., Figueiredo Neto A. M.** Ferrofluids: properties and applications // Brazilian Journal of Physics. 2005. Vol. 35. No. 3A. Pp. 718−727.

2. **Oehlsen O., Cervantes-Ramнrez S. I., Cervantes-Avilés P., Medina-Velo I. A.** Approaches on ferrofluid synthesis and applications: Current status and future perspectives // ACS Omega. 2022. Vol. 7. No. 4. Pp. 3134−3150.

3. **Socoliuc V., Avdeev M. V., Kuncser V., Turcu R., Tombбcz E., Vékбs L.** Ferrofluids and bio-ferrofluids: Looking back and stepping forward // Nanoscale. 2022. Vol.14. No. 13. Pp. 4786−4886.

4. **Monteserнn M., Larumbe S., Martнnez A. V., Burgui S., Francisco M. L.** Recent advances in the development of magnetic nanoparticles for biomedical applications // Journal of Nanoscience and Nanotechnology. 2021. Vol. 21. No. 5. Pp. 2705−2741.

5. **Imran M., Alam M. M., Khan A.** Advanced biomedical applications of iron oxide nanostructures based ferrofluids // Nanotechnology. 2021. Vol. 32. No. 42. P. 422001.

6. **Yerin C., Belykh S.** Magnetic emulsions as prospective magneto-optical media // IEEE Transactions on Magnetics. 2022. Vol. 58. No. 2 (Part 1). P. 4600704.

7. **Pleshakov I. V., Alekseev A. A., Bibik E. E., Dudkin V. I., Kudryashova T. Yu., Karseeva E. K., Kostitsyna T. A., Medvedeva E. A.** Magnetic nanoparticles in solid matrices: Formation and fixation of structures, induced by magnetic field // Nanosystems: Physics, Chemistry, Mathematics. 2023. Vol. 14. No. 5. Pp. 544−548.

8. **Ерин К. В., Вивчарь В. И.** Спектры пропускания разбавленных и концентрированных коллоидов магнетита в жидких диэлектриках // Журнал прикладной спектроскопии. 2023. Т. 90. № 6. С. 843−849.

9. **Zhao Y., Zhang Y., Lv R.-Q., Wang Q.** Novel optical devices based on the tunable refractive index of magnetic fluid and their characteristics // Journal of Magnetism and Magnetic Materials. 2011. Vol. 323. No. 23. Pp. 2987−2996.

10. **Hao Z., Li Y., Pu Sh., Wang J., Chen F., Lahoubi M.** Ultrahigh-performance vector magnetic field sensor with wedge-shaped fiber tip based on surface plasmon resonance and magnetic fluid // Nanophotonics. 2022. Vol. 11. No. 15. Pp. 3519−3528.

11. **Han Sh., Pu Sh., Hao Z., et al.** In-line temperature-compensated vector magnetic field sensor with side-polished fiber // Optics Letters. 2023. Vol. 48. No. 17. Pp. 4504−4507.

12. **Dave V., Mehta R. V.** Diffraction of laser light by a ferrocell and ferrofluid layers: A comparison // Optik. 2024. Vol. 311. September. P. 171925.

13. **Pleshakov I. V., Alekseev A. A., Bibik E. E., Ilichev I. V., Prokof'ev A. V.** Effect of laser radiation on magnetite nanoparticles in deposited ferrofluid // Nanosystems: Physics, Chemistry, Mathematics. 2024. Vol. 15. No. 3. Pp. 346−351.

14. **Du T., Yuan S., Luo W.** Thermal lens coupled magneto-optical effect in a ferrofluid // Applied Physics Letters. 1994. Vol. 65. No.14. Pp. 1844−1846.

15. **Sharma P., Alekhya V. V., Pathak S., Jain K., Tomar P., Basheed G. A., Maurya K. K., Pant R. P.** A novel experimental approach for direct observation of magnetic field induced structuration in ferrofluid // Journal of Magnetism and Magnetic Materials. 2021. Vol. 534. 15 September. P. 168024.

16. **Прокофьев А. В., Плешаков И. В., Бибик Е. Е., Кузьмин Ю. И.** Оптическое исследование геометрических характеристик агрегатов, образованных частицами магнитной жидкости // Письма в Журнал технической физики. 2017. Т. 43. № 4. С. 26−31.

17. **Horng H. E., Hong Ch.-Y., Yang S. Y., Yang H. C.** Designing the refractive indices by using magnetic fluids // Applied Physics Letters. 2003. Vol. 82. No. 15. Pp. 2434−2436.

THE AUTHORS

ALEKSEEV Arseniy A.
Peter the Great St. Petersburg Polytechnic University
29 Politechnicheskaya St., St. Petersburg, 195251, Russia
arseniy.alekseev98@gmail.com
ORCID: 0009-0000-5368-6788

PLESHAKOV Ivan V.
Ioffe Institute of RAS
Peter the Great St. Petersburg Polytechnic University
26 Polytekhnicheskaya St., St. Petersburg, 194021, Russia
ivanple@yandex.ru
ORCID: 0000-0002-6707-6216

KUZMIN Yuri I.
Ioffe Institute of RAS
26 Polytekhnicheskaya St., St. Petersburg, 194021, Russia
iourk@yandex.ru
ORCID: 0000-0001-6052-8251

FOFANOV Yakov A.
Institute for Analytical Instrumentation of RAS
31-33, Ivan Chernykh St., St. Petersburg, 198095, Russia
yakinvest@yandex.ru
ORCID: 0009-0004-2565-8834

СВЕДЕНИЯ ОБ АВТОРАХ

АЛЕКСЕЕВ Арсений Александрович − *аспирант Высшей школы прикладной физики и космических технологий Санкт-Петербургского политехнического университета Петра Великого.*
195251, Россия, г. Санкт-Петербург, Политехническая ул., 29
arseniy.alekseev98@gmail.com
ORCID: 0009-0000-5368-6788

ПЛЕШАКОВ Иван Викторович − *доктор физико-математических наук, ведущий научный сотрудник Физико-технического института имени А. Ф. Иоффе РАН, профессор Высшей школы прикладной физики и космических технологий Санкт-Петербургского политехнического университета Петра Великого.*
194021, Россия, г. Санкт-Петербург, Политехническая ул., 26
ivanple@yandex.ru
ORCID: 0000-0002-6707-6216

КУЗЬМИН Юрий Игоревич − *кандидат физико-математических наук, старший научный сотрудник Физико-технического института имени А. Ф. Иоффе РАН.*
194021, Россия, г. Санкт-Петербург, Политехническая ул., 26
iourk@yandex.ru
ORCID: 0000-0001-6052-8251

ФОФАНОВ Яков Андреевич − *доктор физико-математических наук, главный научный сотрудник Института аналитического приборостроения РАН.*
198095, Россия, г. Санкт-Петербург, ул. Ивана Черных, 33-31, лит. А.
yakinvest@yandex.ru
ORCID: 0009-0004-2565-8834

PHYSICAL MATERIALS TECHNOLOGY

ELECTRICAL AND MECHANICAL PROPERTIES OF FLEXIBLE POLYMER COMPOSITE MATERIALS WITH VARIOUS CARBON FILLERS

D. N. Tonkov[1]✉, M. I. Kobylyatskaya[1], E. S. Vasilyeva[1],
V. E. Gasumyants[1,2], O. V. Tolochko[1,3]

[1] Peter the Great St. Petersburg Polytechnic University, St. Petersburg, Russia

[2] Herzen State Pedagogical University of Russia, St. Petersburg, Russia

[3] State Marine Technical University, St. Petersburg, Russia

✉ wtk_dima@mail.ru

Abstract. We studied the conductive and mechanical properties of polymer composites based on styrene butadiene rubber as a matrix and three different carbon fillers, namely graphite, graphene and carbon nanotubes. Based on the analysis of the resistivity dependences on the concentrations of various fillers, the values of percolation thresholds were determined. The sensitivity of the resistivity of all synthesized composites to the degree of their uniaxial stretching was investigated. The maximum values of the gauge factor were observed in composites with graphene filler. It was also found that in composites with carbon nanotubes as a filler, the deformations arising under applied stresses have an elastic character. After removing the tensile stresses, these composites completely relaxed to their initial size. Contrary to this, in composites with graphite and graphene, even minimal stresses caused the appearance of plastic deformations, and their complete relaxation did not occur after stress was removed.

Keywords: polymer composite, styrene-butadiene rubber, carbon, resistivity, percolation threshold, gauge factor, deformation

ЭЛЕКТРИЧЕСКИЕ И МЕХАНИЧЕСКИЕ СВОЙСТВА ГИБКИХ ПОЛИМЕРНЫХ КОМПОЗИЦИОННЫХ МАТЕРИАЛОВ С РАЗЛИЧНЫМИ УГЛЕРОДНЫМИ НАПОЛНИТЕЛЯМИ

Д. Н. Тонков[1]✉, М. И. Кобыляцкая[1], Е. С. Васильева[1],
В. Э. Гасумянц[1,2], О. В. Толочко[1,3]

[1] Санкт-Петербургский политехнический университет Петра Великого, Санкт-Петербург, Россия

[2] Российский государственный педагогический университет им. А. И. Герцена, Санкт-Петербург, Россия

[3] Санкт-Петербургский государственный морской технический университет, Санкт-Петербург, Россия

✉ wtk_dima@mail.ru

Аннотация. Исследованы проводящие и механические свойства полимерных композитов на основе бутадиен-стирольного каучука и трех различных углеродных наполнителей: графита, графена и углеродных нанотрубок (УНТ). На основании анализа концентрационных зависимостей удельного сопротивления определены значения порогов перколяции. Исследована чувствительность сопротивления композитов к степени их одноосного растяжения и обнаружено, что наибольшие значения коэффициента тензочувствительности наблюдаются в композитах с графеном. Показано, что в случае наполнителя из УНТ деформации, возникающие под действием приложенных напряжений, имеют упругий характер, а после снятия напряжения эти композиты полностью релаксируют к своему исходному размеру. В композитах с графитом и графеном возникают пластические деформации даже при минимальных напряжениях, а их полной релаксации не происходит.

Ключевые слова: полимерный композиционный материал, бутадиен-стирольный каучук, углеродный наполнитель, электропроводность, коэффициент тензочувствительности

Introduction

Polymer nanocomposite film materials show promise for applications in sensor devices for wearable electronics. These materials are characterized by a wide variety of structures, making it possible to achieve the necessary properties such as lightness, flexibility, wear and corrosion resistance, as well as to obtain products in diverse shapes. Devices based on polymer nanocomposites are miniature, so, while they are in constant contact with the body, they should be barely noticeably to the user. Therefore, development of new sensor materials can contribute to rapid progress in many fields, for example, in medicine to monitor human health [1], in sports to track the performance of athletes [2], in hazardous workplace environments to monitor the health status of workers, in the gaming industry to simulate immersive scenarios and in the fashion industry to create smart fabrics capable of adapting to external stimuli [3].

One of the promising applications for polymer nanocomposites is in flexible stretchable strain sensors [4, 5]. For this purpose, a conductive filler is introduced into the polymer matrix. Its particles form a conductive network, which partially collapses under deformation, leading to an increase in the resistance of the material. Composites containing metal fillers are characterized by low flexibility and elasticity; they are sensitive to strain only in a limited range [6], while polymer composites based on carbon fillers have significantly better parameters.

In view of this, research is underway to determine the properties of composites based on various polymers using graphite [7], graphene [8] or carbon nanotubes (CNTs) [9] as fillers. The properties of the obtained materials significantly depend on the technology used for synthesis, the type of polymer matrix and its concentrations of filler particles.

We developed a technology for synthesis of polymer composites based on styrene-butadiene rubber (SBR) as a matrix, as well as graphite, graphene and CNTs as fillers.

This paper presents a comparative study on the influence of concentrations of various carbon fillers on the conductive, piezoresistive, and mechanical properties of synthesized SBR-based composites.

Materials and methods

Preparation of samples. We used Sigma-Aldrich styrene butadiene rubber as a non-conductive polymer matrix, Super P Conductive Carbon Black graphite powder, graphene powder, and TUBALL single-walled carbon nanotubes as fillers.

To obtain a composite film, a weighed portion of the filler powder (graphite, graphene, or CNTs) was mixed in carbon tetrachloride (solvent) using a magnetic stirrer; the procedure was carried out in a sealed flask to prevent evaporation of the solvent and the ingress of air bubbles into the solution. Next, SBR polymer granules were introduced into this dispersion system at a concentration of 5.9 wt.% (relative to the solvent) and mixing continued until the polymer was completely dissolved. The resulting solution was poured into a PTFE mold and dried for 1 hour under a fume hood until completely dry. The composite film was then removed from the PTFE mold with tweezers.

To determine the percolation threshold and measure the mechanical and electrical properties depending on filler concentration, we synthesized samples with graphite and graphene concentrations from 13 wt.% to 33 wt.% and CNT concentrations from 0.25 wt.% to 2.5 wt.% (relative to the finished composite). The filler concentration was selected taking into account the average size and shape of its particles, using a model estimating the percolation threshold in a material of a given thickness.

Measurement procedure. The resistivity of all films obtained from synthesized composites, as well as its dependence on the degree of stretching of the samples, were measured by the four-probe van der Pauw method. The experiment was conducted by the following steps: the film sample was fixed in a measuring cell with a movable crosshead, after which electrical contacts were connected to it. During the stepwise movement of the movable crosshead, the sample was stretched to a certain length; the resistivity was measured after each step.

The mechanical properties of composite polymer films were investigated with the same setup, but without connecting the contacts. To measure the strength and relaxation ability of the material, the samples were repeatedly stretched, each time increasing the tension in increments of 10 mm. At the final time step of each stretching test, the sample was held for 5 seconds, then the tensile stress was abruptly removed and the length of the sample was measured with a caliper after 25 seconds. To measure the relaxation time, the samples were stretched by 400% of the initial length, and after the load was removed, the length of the sample was measured every 20 seconds until the relaxation effect disappeared.

Results and discussion

Study of percolation properties. To analyze changes in the conductive properties of composites under deformation, it is necessary to take into account the percolation threshold for particles of a conductive filler placed in a dielectric polymer matrix. The structural parameter of the composite that characterizes these properties is the degree of overlap of the particles [10]. A continuous conductive cluster is formed at a high concentration of particles, with the particles directly touching each other. As the concentration decreases, the arrangement of the particles becomes more

dispersed and the conduction mechanism changes to a hopping mechanism. A further decrease in particle concentration, taking into account their average size in one or more directions, significantly reduces the probability of charge carrier hopping and the conductivity of the composite abruptly tends to zero. The concentration of filler particles at which the composite stops conducting electric current is the percolation threshold.

Samples with filler concentrations at which hopping conductivity prevails are promising for subsequent use as active elements of sensing devices. The hopping probability (and hence the value of conductivity) exponentially depends on the distance between the conductive particles, which is why such composites have the greatest strain sensitivity.

For this reason, to obtain samples with high strain sensitivity, it is necessary to determine the value of the percolation threshold in synthesized composites for fillers with different structures and particle sizes. Fig. 1 shows experimentally obtained dependences of resistivity of the studied samples on the concentration of fillers: graphene, graphite and CNTs (at room temperature).
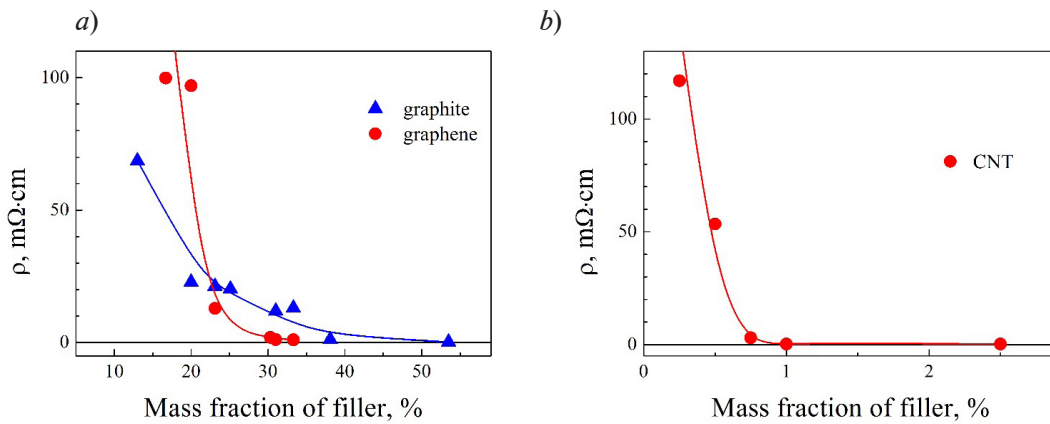
Fig. 1. Dependences of resistivity on filler concentration for composites containing graphene or graphite (*a*) and CNTs (*b*)

As can be seen from the above data, there is a sharp increase in resistivity for samples with graphite and graphene with about 37 wt.% and 30 wt.% concentrations, respectively. This may be due to the collapse of the percolating cluster and a transition of the cluster's conductivity to the hopping type. For a CNT-based composite, such a change in the conductive properties of the composite is observed at significantly lower concentrations of the filler (below 1 wt.%).

To clarify the conductivity mechanism, we plotted the dependences of $\ln(\rho)$ on $N^{-1/3}$ (where N is the concentration of particles) based on the obtained data. Filler particles in the matrix are considered as a set of nodes surrounded by closed surfaces of the same shape, randomly distributed in space. When the surfaces intersect, a conductive chain of nodes is formed, with the electron tunneling occurring between these nodes (the Miller−Abrahams model for nearest-neighbor hopping). The localization length of the wave function (hopping distance) can be determined from the slope of the dependence of $\ln(\rho)$ on $N^{-1/3}$ (see Fig. 2 for composites with graphite and graphene). Based on the calculations, we established a hopping distance of 5.4 Å for the composite with graphite, 1.1 Å for the composite with graphene and 60 Å for the composite with CNTs. Note that a similar calculation within the framework of the two-dimensional problem (circle approximation) yielded localization lengths of the order of 10^{-11} cm, which is physically unreasonable.

Fig. 2. Dependences of log resistivity for composites with graphite and graphene on $N^{-1/3}$ (N is the particle concentration)

Thus, to further calculate the percolation threshold, we use the three-dimensional model of the structure, although Monte Carlo simulations on the properties of a composite with graphene [11] considered graphene particles as two-dimensional circular nano-disks.

Our hypothesis is that flat graphene flakes coagulate, forming three-dimensional agglomerates during synthesis of the composite. For this reason, to interpret the results, we used the model proposed in [12] and schematically shown in Fig. 3. Here, spheres with small radius are agglomerates of conductive filler particles, spheres with large radius are non-conductive particles which are approximations of regions filled with a non-conductive matrix, and the circle in the inset connecting the filler particles is the tunneling space. As stated in [12], the percolation threshold depends on the ratio λ of the sizes of conductive and non-conductive particles:

$$\lambda = d_c/d_i,$$

where d_c, d_i are the sizes of conductive and non-conductive particles, respectively.

The higher the value of λ, the lower the percolation threshold. This model of the structure formed in the composite allows to explain the difference in the values of the percolation threshold subsequently found for composites with different fillers.
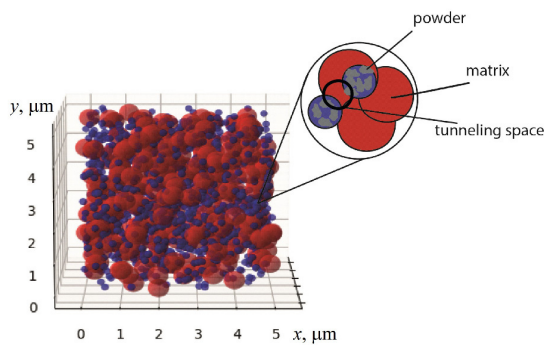
Fig. 3. Model of composite structure: spheres of small and large radii are, respectively, agglomerates of conductive and non-conductive particles (an approximation of regions filled with a non-conductive matrix). *Inset:* the tunneling space is shown by a circle with small radius connecting the filler particles (powder)
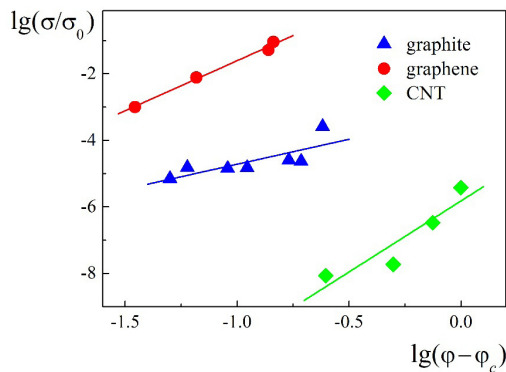
Fig. 4. Logarithmic dependences of normalized conductivity σ/σ_0 of composites with graphite, graphene and CNTs on logarithm of the difference in filler concentration φ and its value φ_c corresponding to the percolation threshold

To analyze the percolation model, we synthesized samples with different fillers with selected concentrations, considering their conductive properties in the absence of deformation.

The percolation threshold was determined graphically using the paired point method according to the well-known expression for conductivity σ (S):

$$\sigma = \sigma_0 \cdot (\varphi - \varphi_c)^t,$$

where φ, φ_c are the filler concentration and its value corresponding to the percolation threshold (wt.% relative to the final composite); t is the critical exponent (depending on the dimensionality of the structure); σ_0, S, is the conductivity of the filler [13].

Calculations were carried out based on data for the samples with filler concentrations at which a significant decrease in conductivities of composites is observed, i.e., a continuous cluster of conductive particles collapses.

Dependences of $\lg(\sigma/\sigma_0)$ on $\lg(\varphi - \varphi_c)$ were constructed to determine the critical exponent (Fig. 4).

Similar to [14], we simultaneously varied the values of φ_c and t to obtain an optimal linear relationship approximating the experimental data (see Fig. 4). The initially known range of possible values of the critical exponent t was used as a basis.

As a result, the critical exponent and the corresponding percolation threshold were determined for each of the composites. According to the calculation results, the values of the critical exponent were $t = 2.38$, 2.08 and 2.37 for composites with graphite, graphene and CNTs, respectively. These values generally correspond to the problem with spheres. Small deviations from the theoretical value may be associated with partial violation of dimensionality [13]. The obtained values of the

critical exponent correspond to certain percolation thresholds, amounting to 12.0% and 16.5% for composites with graphite and graphene, respectively. The slight difference in these values can be explained, as mentioned above, by the difference in the values of λ for composites with different fillers in accordance with the model in [12]. The percolation threshold for the CNT-based composite was 0.1%, i.e., it turned out to be significantly lower than the values obtained for composites with graphite and graphene. Note that the value we obtained is in good agreement with the literature data for CNT-based composites [15, 16]. Such a small value of the percolation threshold is clearly due to the structural properties of the filler, namely, a very high aspect ratio of CNTs, making it possible to form a continuous conductive cluster even at their low content in the composite.

Study of strain−resistance relationship of samples Next, the main functional property of the obtained composites was investigated: the sensitivity of their electrical resistance to the degree of stretching. Fig. 5 shows the variation in the resistivity of composites under uniaxial stretching in the deformed regions where they are conductive. Here, the relative elongation of the sample is plotted as a percentage along the abscissa: $\delta = \Delta L/L_0 \cdot 100\%$ (L_0 is the initial length of the sample, ΔL is the variation in its length during stretching). The resistivity of the sample ρ, normalized to its value ρ_0 in the absence of applied stress, is plotted along the ordinate.

As expected, the lower the filler concentration in the matrix, the lower the elongation at which the resistivity in the sample starts to change. A significant increase in filler concentration leads to a decrease in stretching sensitivity of the composite: such samples had to be stretched to a much longer length for a noticeable change in resistivity. This effect of filler concentration on the sensitivity to tensile strain can be explained by an increase in the distance between its particles, which turns out to be equivalent to a decrease in filler concentration in the context of electrical conductivity.

Furthermore, as pointed out in [17], stretching of the composite leads to a change in the critical exponent t, which in turn indicates a change in the dimensionality of the structure, and consequently, the value of the percolation threshold, since the latter depends on both the dimensionality of the structure and the size ratio of conductive and non-conductive particles (as mentioned above).

As can be seen from Fig. 5, at the minimum concentration of the introduced filler, the graphite composite (13 wt.%) turned out to be the most sensitive to stretching, which begins to sharply change its resistivity when stretched by 2−3%. The resistivity of the graphene composite at its minimum concentration (16 wt.%) changed with a relative elongation of 12%, and that of the composite with CNTs (0.25 wt.%) with an elongation of more than 40%. In addition, an increase in concentration for composites with graphite and graphene expands the range of applied stresses where the composite preserves its resistivity. This effect is less pronounced for composites with CNTs, which may be due to the characteristics of the formed structure, for example, the curvature of nanotubes inside the composite [18].

The values of the gauge factor were calculated for different types of composites:

$$\text{GF} = (\Delta\rho_{max}/\rho_0)/(\Delta L_{max}/L_0),$$

where ρ_0, L_0 are the resistivity and length of the sample before stretching; $\Delta\rho_{max}$, ΔL_{max} are the maximum values of changes in its resistance and length, respectively.

This factor characterizes the strain sensitivity of the composite's resistance and can be used to compare data obtained for different composites [19].

Table 1 shows the values of the gauge factor for different types and concentrations of fillers. As can be seen from the data, composites with graphene filler are characterized by the highest sensitivity to stretching. The maximum sensitivity for all types of fillers is observed for composites with moderate concentrations (24 wt.% for graphene and graphite and 0.50 wt.% for CNTs). Analyzing the data in Table 1, we can conclude that the gauge factor first increases and then decreases with an increase in filler concentration. A likely explanation for this is that an increase in this concentration leads to two different effects. On the one hand, the range of strains where the composite preserves conductive properties is expanded (see Fig. 5), which should lead to a decrease in the GF value. On the other hand, the resistivity of the composite decreases in the absence of deformation (see Fig. 1), which should lead to an increase in GF. As a result of the competition between these two effects, an optimal concentration exists for each filler type, at which the maximum value of the gauge factor is achieved.

a)

b)

c)
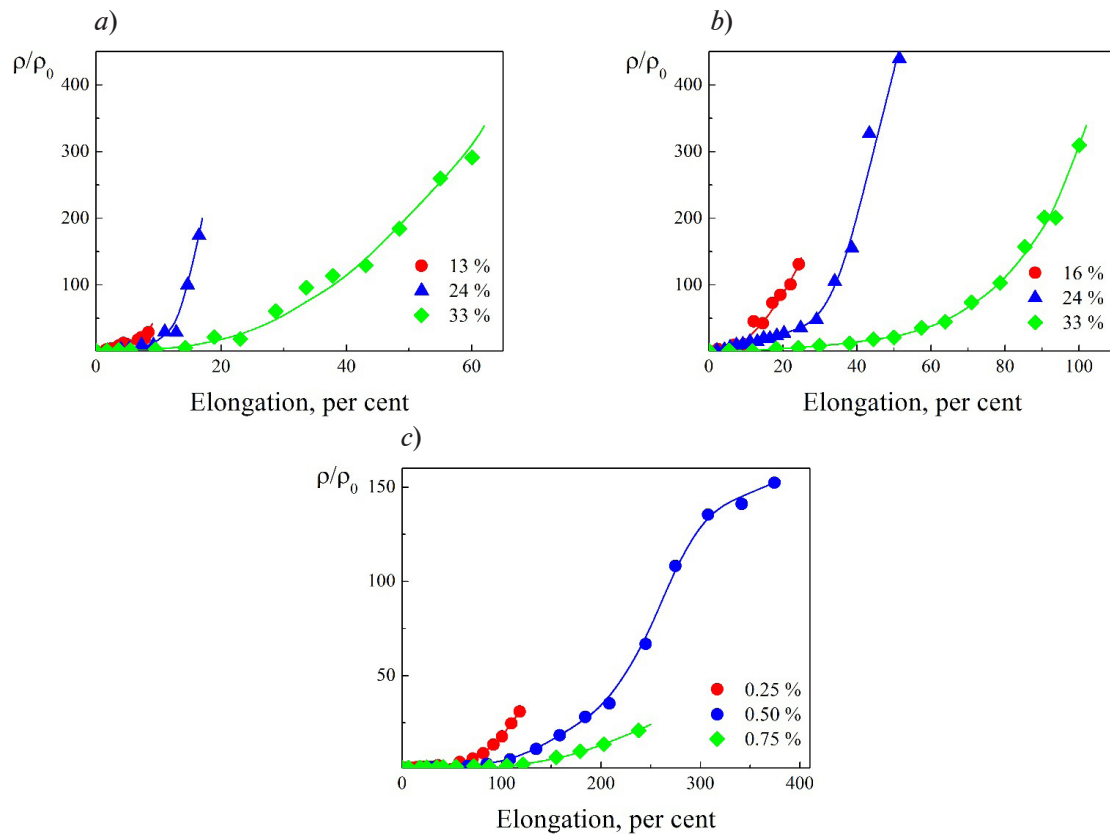
Fig. 5. Change in normalized resistivity of composite samples with graphite (*a*), graphene (*b*) and CNTs (*c*) in different concentrations, under stretching (elongation $\delta = \Delta L/L_0$)

Table 1

Gauge factor for samples of various composites subjected to stretching

Filler	Concentration, %	GF value
Graphene	16	534.7
	24	26661.0
	33	340.4
Graphite	13	224.3
	24	1005.0
	33	481.9
CNTs	0.25	25.3
	0.50	40.3
	0.75	8.4

Study of mechanical properties. As the first step in analysis of the mechanical properties of synthesized composites, we estimated their ultimate tensile strength, the nature of deformations developing in them under uniaxial static stretching and their relaxation properties.

First, the samples were repeatedly stretched in 10 mm increments until collapse. The length L of the sample was measured after each step (25 seconds after stress release). The obtained results are presented in Table 2 and in Fig. 6, showing the dependences of the ratio L/L_0 (L_0 is the initial length of the sample) on its relative elongation under stretching.

The data in Table 2 indicate that the maximum tensile strength in the case of the filler with CNTs is observed in the sample with the highest filler concentration, while the tensile strength in the graphene composite sample decreases gradually with increasing filler concentration. The ultimate tensile strength for the composite with graphite first increases with increasing filler concentration, then dropping abruptly.

An increase in filler concentration in the composite with CNTs expands the range of strain values at which the sample almost completely returns to its initial length (see Fig. 6,*c* and Table 2). This suggests that deformation within these strain ranges is purely elastic in nature. Increasing the CNT concentration in the composite improves its elastic properties, i.e., the higher the concentration, the fewer defects and residual strains the sample accumulates under uniaxial stretching.

The reason for this improvement may be related to both the three-dimensionality of the structure formed by introducing CNTs into the polymer matrix and the properties of individual particles of the filler itself. It is due to these characteristics that composites with CNTs can be considered the most promising for creating flexible sensor electronics devices. Residual strains arise in them only after reaching a certain critical strain value, which increases progressively with increasing filler concentration (see Fig. 6,*c* and the data in Table 2).

T a b l e 2

Mechanical properties of polymer composite sample under stretching

Filler	Concentration	Elastic strain range	Ultimate tensile strength
	%		
Graphene	16	–	565
	24		542
	33		401
Graphite	13	–	485
	24		708
	33		380
CNTs	0.25	150	585
	0.50	250	556
	0.75	440	659
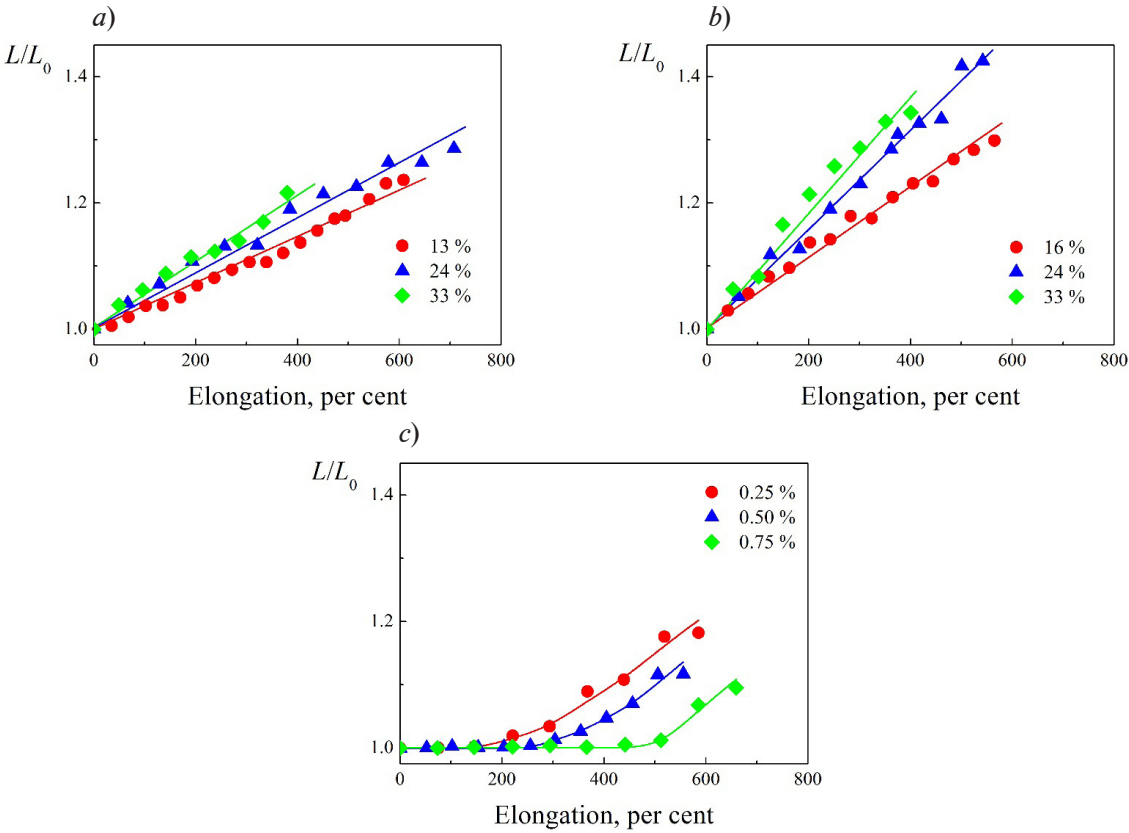
Fig. 6. Dependences of relative elongation L/L_0 of composite samples with graphite (*a*), graphene (*b*) and CNTs (*c*) in different concentrations on applied strain $\delta = \Delta L/L_0$ (measurements were carried out 25 seconds after each stress release)

In the case of composites with graphite or graphene fillers (see Fig. 6, *a*, *b*), the samples did not preserve their initial length even when minimal stresses were applied to them, which points to the emergence of irreversible plastic strains (along with elastic ones). Note that in both cases, the slope of the dependences in Fig. 6 increases progressively with increasing filler concentration, which indicates an increase in the proportion of residual strains, i.e., the effect of their accumulation during repeated stretching of the sample. There are two differences in the reaction of composites to repeated stretching for different types of fillers.

Firstly, the slope of the curves in Fig. 6 corresponding to composites with graphene is significantly greater than that for composites with graphite at the same (or similar) filler concentrations. This indicates that the proportion of residual strains is higher in the first case than in the second one. Secondly, a steeper increase in this slope is observed with increasing filler concentration for composites with graphene, i.e., the effect of accumulation of residual strains is more pronounced in this type of composites.

The results of the study on the relaxation properties of synthesized composites (for cases with CNT and graphene fillers) after 400% strain are shown in Fig. 7. Evidently, in the case of CNTs, samples that did not return to their initial length in 25 seconds after stress relief (at filler concentrations of 0.25 and 0.50%) exhibit almost complete relaxation within 60−80 seconds (see Fig. 7,*a*). In contrast, graphene composites do not return to their initial length (see Fig. 7,*b*) even 2−3 minutes after the load is removed. This result may be associated with jamming from flat filler particles inside polymer matrices during stretching. The sample with 33% graphene concentration undergoes virtually no relaxation; relaxation in the sample with 16% graphene concentration is weak and the sample with 24% graphene concentration exhibits the best relaxation properties, in terms of both the relaxation rate and degree.
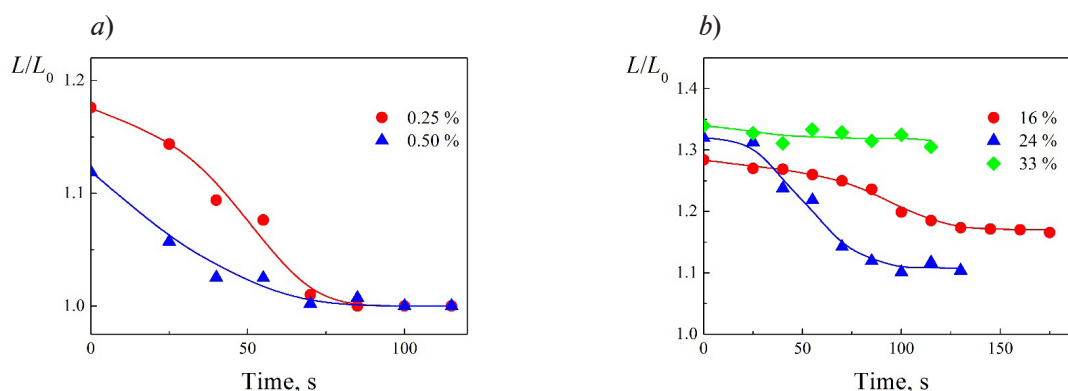
Fig. 7. Time evolution of relative elongation of composite samples with CNTs (*a*)
and graphene (*b*) in different concentrations after stress release

Therefore, the filler concentration of 24% is close to critical for this material: once it is reached, the mechanical properties of the composite stop improving and start deteriorating. Note that this result indirectly corresponds to the data obtained in [20], analyzing the properties of composites based on polyvinyl acetate with graphene filler, considering samples in a narrower range of graphene concentrations than in our study (up to its possible critical value). However, the study found that its gradual increase initially leads to a sharp improvement in the mechanical properties of the composite, but this improvement subsequently slows down.

Conclusion

In this paper, we considered the electrical and mechanical properties of composites based on styrene butadiene rubber (SBR) with three different types of carbon fillers (graphite, graphene and carbon nanotubes), varying their concentrations. Analyzing the dependences of resistivity of composites on filler concentration, we determined the dimensionality of the filler particles formed during synthesis (which turned out to be close to three-dimensional in all cases), as well as the percolation thresholds, amounting to 0.1 wt.% for the composite with CNTs, 12.0 wt.% for the composite with graphite and 16.5 wt.% for the composite with graphene.

It was found that an increase in the concentration of all fillers in the SBR matrix broadens the range of the applied uniaxial stresses where the composite slightly changes its resistivity. However, this effect was less pronounced for the CNT-based composite compared with graphite and graphene-based composites. Sequentially increasing the concentration of all fillers in the SBR matrix led first to an increase in sensitivity of composite resistance to stretching and then to its decrease. Consequently, the greatest sensitivity was observed in composites containing about 24 wt.% of graphite or graphene filler and in composites with 0.5 wt.% CNT. The highest sensitivity of resistance to stretching was found in the composite with 24 wt.% of graphene filler; its gauge factor reached 2661, which is due to a high conductivity of this composite in an undeformed state and a narrow stress range where it preserves resistance.

Studies of mechanical properties of the obtained composites revealed that the ultimate tensile strength of graphene composites decreases with increasing filler concentration, that of CNT composites increases and that of graphite composites first increases and then sharply decreases. Furthermore, an increase in the CNT concentration in the composite expands the range of uniaxial strain over which the deformation remains elastic. In contrast, even the application of minimal stresses in composites with graphene and graphite leads to the emergence of plastic deformation. The proportion of this plastic deformation increases with repeated stretching of the sample as filler concentration is increased; this increase is more significant in the case of graphene compared with graphite. Composites with graphene exhibit the maximum values of the gauge factor, while composites with CNTs exhibit the best relaxation properties.

Thus, our studies and analysis indicate that composites with graphene are the most promising materials for further development of flexible sensor electronics devices from the standpoint of strain sensitivity of resistance, while CNT-based composites exhibit the best mechanical properties. Further research is necessary to optimize both the electrical and mechanical properties of polymer composites based on carbon fillers.

REFERENCES

1. **Bonato P.,** Advances in wearable technology and applications in physical medicine and rehabilitation, J. NeuroEng. Rehabil. 2 (1) (2005) 2.

2. **Aroganam G., Manivannan N., Harrison D.,** Review on wearable technology sensors used in consumer sport applications, Sensors. 19 (9) (2019) 1983.

3. **Wilson S., Laing R.,** Wearable technology: Present and future, Integrating Design with Sustainable Technology, In book: Proc. 91st World Conf. of the Textile Institute, Vol. 1. Manchester: Textile Institute Press (2018) 266−280.

4. **Ma L., Lu W.,** Carbon nanotube film based flexible bi-directional strain sensor for large deformation, Mater. Lett. 260 (1 Febr) (2020) 126959.

5. **Ren J., Wang C., Zhang X., et al.,** Environmentally-friendly conductive cotton fabric as flexible strain sensor based on hot press reduced graphene oxide, Carbon. 111 (Jan) (2017) 622−630.

6. **Takei K., Takahashi T., Ho J. C., et al.,** Nanowire active-matrix circuitry for low-voltage macroscale artificial skin, Nat. Mater. 9 (10) (2010) 821−826.

7. **Xia Y., Zhang Q., Wu X. E., et al.,** Practical and durable flexible strain sensors based on conductive carbon black and silicone blends for large scale motion monitoring applications, Sensors. 19 (20) (2019) 4553.

8. **Shi G., Zhao Z., Pai J. H., et al.,** Highly sensitive, wearable, durable strain sensors and stretchable conductors using graphene/silicon rubber composites, Adv. Func. Mater. 26 (42) (2016) 7614−7625.

9. **Dalmas F., Dendievel R., Chazeau L., et al.,** Carbon nanotube-filled polymer composites. Numerical simulation of electrical conductivity in three-dimensional entangled fibrous networks, Acta Mater. 54 (11) (2006) 2923−2931.

10. **Hu N., Karube Y., Arai M., et al.,** Investigation on sensitivity of a polymer/carbon nanotube composite strain sensor, Carbon. 48 (3) (2010) 680−687.

11. **Fang C., Zhang J., Chen X., Wen G. J.,** Calculating the electrical conductivity of graphene nanoplatelet polymer composites by a Monte Carlo method, Nanomaterials. 10 (6) (2020) 1129.

12. **He D., Ekere N. N.,** Effect of particle size ratio on the conducting percolation threshold of granular conductive-insulating composites, J. Phys. D: Appl. Phys. 37 (13) (2004) 1848.

13. **Mora A., Verma P., Kumar S.,** Electrical conductivity of CNT/polymer composites: 3D printing, measurements and modeling // Compos. B. Eng. 183 (15 Febr) (2020) 107600.

14. **Kilbride B. E., Coleman J. N., Fraysse J., et al.,** Experimental observation of scaling laws for alternating current and direct current conductivity in polymer-carbon nanotube composite thin films, J. Appl. Phys. 92 (7) (2022) 4024−4030.

15. **Berezkin V. I., Popov V. V.,** Percolation transition in carbon composite on the basis of fullerenes and exfoliated graphite, Phys. Solid State. 60 (1) (2018) 207−211.

16. **Spitalsky Z., Tasis D., Papagelis K., Galiotis C.,** Carbon nanotube-polymer composites: Chemistry, processing, mechanical and electrical properties, Prog. Polym. Sci. 35 (3) (2010) 357−401.

17. **Chen Y., Li Y., Xu D., Zhai W.,** Fabrication of stretchable, flexible conductive thermoplastic polyurethane/graphene composites via foaming, RSC Adv. 5 (100) (2015) 82034−82041.

18. **Hu N., Masuda Z., Yan C., et al.,** The electrical properties of polymer nanocomposites with carbon nanotube fillers, Nanotechnology. 19 (21) (2008) 215701.

19. **Yang H., Yao X., Zheng Z., et al.,** Highly sensitive and stretchable graphene-silicone rubber composites for strain sensing. Compos. Sci. Technol. 167 (20 Oct) (2018) 371−378.

20. **Zhao X., Zhang Q., Chen D.,** Enhanced mechanical properties of graphene-based poly (vinyl alcohol) composites, Macromolecules. 43 (3) (2010) 2357−2363.

СПИСОК ЛИТЕРАТУРЫ

1. **Bonato P.** Advances in wearable technology and applications in physical medicine and rehabilitation // Journal of NeuroEngineering and Rehabilitation. 2005. Vol. 2. No. 1. P. 2 (4 p.).

2. **Aroganam G., Manivannan N., Harrison D.** Review on wearable technology sensors used in consumer sport applications // Sensors. 2019. Vol. 19. No. 9. P. 1983.

3. **Wilson S., Laing R.** Wearable technology: Present and future // Integrating Design with Sustainable Technology: Proceeding of the 91st World Conference of the Textile Institute, Vol. 1. Manchester: Textile Institute Press, 2018. P. 266−280.

4. **Ma L., Lu W.** Carbon nanotube film based flexible bi-directional strain sensor for large deformation // Materials Letters. 2020. Vol. 260. 1 February. P. 126959.

5. **Ren J., Wang C., Zhang X., Carey T., Chen K., Yin Y., Torrisi F.** Environmentally-friendly conductive cotton fabric as flexible strain sensor based on hot press reduced graphene oxide // Carbon. 2017. Vol. 111. January. Pp. 622−630.

6. **Takei K., Takahashi T., Ho J. C., Ko H., Gillies A. G., Leu P. W., Fearing R. S., Javey A.** Nanowire active-matrix circuitry for low-voltage macroscale artificial skin // Nature Materials. 2010. Vol. 9. No. 10. Pp. 821−826.

7. **Xia Y., Zhang Q., Wu X. E., Kirk T. V., Chen X. D**. Practical and durable flexible strain sensors based on conductive carbon black and silicone blends for large scale motion monitoring applications // Sensors. 2019. Vol. 19. No. 20. P. 4553.

8. **Shi G., Zhao Z., Pai J. H., Lee I., Zhang L., Stevenson C., Ishara K., Zhang R., Zhu H., Ma J.** Highly sensitive, wearable, durable strain sensors and stretchable conductors using graphene/silicon rubber composites // Advanced Functional Materials. 2016. Vol. 26. No. 42. Pp. 7614−7625.

9. **Dalmas F., Dendievel R., Chazeau L., Cavaille J.-Y., Gauthier C.** Carbon nanotube-filled polymer composites. Numerical simulation of electrical conductivity in three-dimensional entangled fibrous networks // Acta Materialia. 2006. Vol. 54. No. 11. Pp. 2923−2931.

10. **Hu N., Karube Y., Arai M., Watanabe T., Yan C., Li Y., Liu Y., Fukunaga H.** Investigation on sensitivity of a polymer/carbon nanotube composite strain sensor // Carbon. 2010. Vol. 48. No. 3. Pp. 680−687.

11. **Fang C., Zhang J., Chen X., Wen G. J.** Calculating the electrical conductivity of graphene nanoplatelet polymer composites by a Monte Carlo method // Nanomaterials. 2020. Vol. 10. No. 6. P. 1129.

12. **He D., Ekere N. N.** Effect of particle size ratio on the conducting percolation threshold of granular conductive-insulating composites // Journal of Physics D: Applied Physics. 2004. Vol. 37. No. 13. P. 1848.

13. **Mora A., Verma P., Kumar S.** Electrical conductivity of CNT/polymer composites: 3D printing, measurements and modeling // Composites. Part B: Engineering. 2020. Vol. 183. 15 February. P. 107600.

14. **Kilbride B. E., Coleman J. N., Fraysse J., Fournet P., Cadek M., Drury F., Hatzler S. B., Roth S., Blau W. J.** Experimental observation of scaling laws for alternating current and direct current conductivity in polymer-carbon nanotube composite thin films // Journal of Applied Physics. 2022. Vol. 92. No. 7. Pp. 4024−4030.

15. **Березкин В. И., Попов В. В.** Перколяционный переход в углеродном композите на основе фуллеренов и терморасширенного графита // Физика твердого тела. 2018. Т. 60. № 1. С. 202−206.

16. **Spitalsky Z., Tasis D., Papagelis K., Galiotis C.** Carbon nanotube−polymer composites: Chemistry, processing, mechanical and electrical properties // Progress in Polymer Science. 2010. Vol. 35. No. 3. Pp. 357−401.

17. **Chen Y., Li Y., Xu D., Zhai W.** Fabrication of stretchable, flexible conductive thermoplastic polyurethane/graphene composites via foaming // RSC Advances. 2015. Vol. 5. No. 100. Pp. 82034−82041.

18. **Hu N., Masuda Z., Yan C., Yamamoto G., Fukunaga H., Hashida T.** The electrical properties of polymer nanocomposites with carbon nanotube fillers // Nanotechnology. 2008. Vol. 19. No. 21. P. 215701.

19. **Yang H., Yao X. F., Zheng Z., Gong L. H., Yuan L., Yuan Y. N., Liu Y. H.** Highly sensitive and stretchable graphene-silicone rubber composites for strain sensing // Composite Science and Technology. 2018. Vol. 167. 20 October. Pp. 371−377.

20. **Zhao X., Zhang Q., Chen D.** Enhanced mechanical properties of graphene-based poly (vinyl alcohol) composites // Macromolecules. 2010. Vol. 43. No. 3. Pp. 2357−2363.

THE AUTHORS

TONKOV Dmitry N.
Peter the Great St. Petersburg Polytechnic University
29 Politechnicheskaya St., St. Petersburg, 195251, Russia
wtk_dima@mail.ru
ORCID: 0000-0003-1528-669X

KOBYLYATSKAYA Mariya I.
Peter the Great St. Petersburg Polytechnic University
29 Politechnicheskaya St., St. Petersburg, 195251, Russia
koby-masha@yandex.ru
ORCID: 0009-0004-3109-2830

VASILYEVA Ekaterina S.
Peter the Great St. Petersburg Polytechnic University
29 Politechnicheskaya St., St. Petersburg, 195251, Russia
vasilyeva_es@spbstu.ru
ORCID: 0009-0008-2967-8487

GASUMYANTS Vitaliy E.
Peter the Great St. Petersburg Polytechnic University;
Herzen State Pedagogical University of Russia
29 Politechnicheskaya St., St. Petersburg, 195251, Russia
vgasum@yandex.ru
ORCID: 0000-0002-5306-6738

TOLOCHKO Oleg V.
Peter the Great St. Petersburg Polytechnic University;
State Marine Technical University
29 Politechnicheskaya St., St. Petersburg, 195251, Russia
ol_tol@hotmail.com
ORCID: 0000-0001-9623-4001

СВЕДЕНИЯ ОБ АВТОРАХ

ТОНКОВ Дмитрий Николаевич — *старший преподаватель кафедры физики Института физики и математики Санкт-Петербургского политехнического университета Петра Великого.*
195251, Россия, г. Санкт-Петербург, Политехническая ул., 29
wtk_dima@mail.ru
ORCID: 0000-0003-1528-669X

КОБЫЛЯЦКАЯ Мария Игоревна — *аспирантка* Высшей школы физики и технологий материалов Санкт-Петербургского политехнического университета Петра Великого.
195251, Россия, г. Санкт-Петербург, Политехническая ул., 29
koby-masha@yandex.ru
ORCID: 0009-0004-3109-2830

ВАСИЛЬЕВА Екатерина Сергеевна — *кандидат технических наук, доцент Высшей школы физики и технологий материалов Санкт-Петербургского политехнического университета Петра Великого.*
195251, Россия, г. Санкт-Петербург, Политехническая ул., 29
vasilyeva_es@spbstu.ru
ORCID: 0009-0008-2967-8487

ГАСУМЯНЦ Виталий Эдуардович – доктор *физико-математических наук, профессор Высшей инженерно-физической школы Санкт-Петербургского политехнического университета Петра Великого*; *профессор кафедры физической электроники Российского государственного педагогического университета имени А.И. Герцена*.

195251, Россия, г. Санкт-Петербург, Политехническая ул., 29

vgasum@yandex.ru

ORCID: 0000-0002-5306-6738

ТОЛОЧКО Олег Викторович – *доктор технических наук, профессор Высшей школы физики и технологий материалов Санкт-Петербургского политехнического университета Петра Великого*; *профессор кафедры материаловедения и технологии материалов Санкт-Петербургского государственного морского технического университета*.

195251, Россия, г. Санкт-Петербург, Политехническая ул., 29

ol_tol@hotmail.com

ORCID: 0000-0001-9623-4001

NUCLEAR PHYSICS

AN ANALYSIS OF THE FEATURES OF CHARGED HADRON PRODUCTION IN COLLISIONS OF BISMUTH NUCLEI AT AN ENERGY OF 9.2 GEV USING THE BLAST-WAVE MODEL

D. M. Larionova✉, *Ya. A. Berdnikov, D.O. Kotov*

Peter the Great St. Petersburg Polytechnic University, St. Petersburg, Russia

✉ dlar@bk.ru

Abstract. The paper presents charged hadron invariant spectra obtained in Bi+Bi collisions at an energy of 9.2 GeV on the basis of simulation performed using the UrQMD hybrid generator and the MPDroot package. The spectra were analyzed in the framework of statistical and Blast-Wave models, resulting in the values of temperatures and baryonic chemical potentials corresponding to the stages of kinetic and chemical freeze-out in Bi+Bi collisions. The results were discussed in the context of the phase diagram of nuclear matter.

АНАЛИЗ ОСОБЕННОСТЕЙ РОЖДЕНИЯ ЗАРЯЖЕННЫХ АДРОНОВ В СТОЛКНОВЕНИЯХ ЯДЕР ВИСМУТА ПРИ ЭНЕРГИИ 9,2 ГЭВ С ПОМОЩЬЮ МОДЕЛИ BLAST-WAVE

Д. М. Ларионова✉, *Я. А. Бердников, Д. О. Котов*

Санкт-Петербургский политехнический университет Петра Великого, Санкт-Петербург, Россия

✉ dashalario@gmail.com

Аннотация. В работе представлены инвариантные спектры по поперечной массе для заряженных адронов в столкновениях ядер висмута (Bi + Bi) при энергии 9,2 ГэВ, полученные путем моделирования с использованием гибридного генератора UrQMD и пакета MPDroot. Проведен анализ спектров в рамках статистической и Blast-Wave моделей, в результате которого получены значения температуры и барионных химических потенциалов, соответствующих стадиям кинетического и химического вымораживания в столкновениях Bi + Bi. Полученные результаты рассмотрены в контексте фазовой диаграммы ядерной материи.

Introduction

The Multi-Purpose Detector (MPD) [1] is one of the two experimental facilities at the NICA (Nuclotron-based Ion Collider fAcility) [2], the flagship project of the Joint Institute for Nuclear Research (Dubna, Moscow Region, Russia).

The main objectives of the MPD experiment are to study the boundary of the phase transition and to find a critical point in the phase diagram of nuclear matter by analyzing particle production in heavy ion collisions in the energy range $\sqrt{S_{NN}} = 4-11$ GeV [3].

The phase boundary of nuclear matter determines the transition of hadron matter to quark-gluon plasma (QGP) [4, 5] with an increase in temperature T and/or the baryonic chemical potential μ_B. The formation of the QGP and the corresponding phase transition in nucleus-nucleus collisions were experimentally confirmed at energies exceeding 100 GeV [4−6], which corresponds to temperatures of about 200 MeV and $\mu_B \approx 10$ MeV achieved in the collision. Nevertheless, study of the rest of the phase diagram and the search for QGP signatures in nuclear collisions at lower energies (below or around 100 GeV) remain major challenges.

To identify the potential signatures of a phase transition in nucleus-nucleus collisions at NICA energies, it is necessary to determine the available range of temperature T and baryonic chemical potential μ_B. The values of T and μ_B can be estimated by analyzing the characteristics of charged hadron production using the statistical model and the Blast-Wave model [7, 8] based on the approach of relativistic hydrodynamics.

This paper presents the invariant spectra for transverse mass m_T measured for charged hadrons ($\pi^\pm$, $K^\pm$, p, $\bar{p}$) in collisions of bismuth nuclei (Bi+Bi) at $\sqrt{S_{NN}} = 9.2$ GeV; these results were obtained based on simulation data using the UrQMD hybrid generator [9] and the MPDroot package [1] reproducing the operation of the detector system at the MPD experiment.

Analysis of the obtained spectra is carried out within the framework of the statistical model and the Blast-Wave model. The results are considered in the context of the phase diagram of nuclear matter.

Evolution of nucleus-nucleus collisions

The process of evolution of relativistic collisions can be divided into four main stages:

initial stage,

thermalization and collective flow,

chemical freeze-out,

kinetic freeze-out [10].

Initial stage corresponds to primary interaction of colliding nuclei, accompanied by the exchange of gluons and quarks. This process leads to rapid heating of the system and potential production of QGP (if the values of T_{QGP} and μ_B necessary for the phase transition are reached).

Second stage. As a result of subsequent interactions between the particles, the system is thermalized, after which collective flow begins.

Third stage. Chemical freeze-out occurs when the particle system expands to a state where inelastic reactions altering its composition cease and the final particle ratios are established.

According to the statistical model, after the onset of chemical freeze-out, the antiproton to proton yield ratio is determined by the value of the baryonic chemical potential μ_B [11]:

$$\frac{\overline{p}}{p} = \exp\left(-\frac{2\mu}{T}\right) \Leftrightarrow \mu = T \cdot \frac{\ln\left(\overline{p}/p\right)}{2} \Leftrightarrow T = -\frac{2\mu}{\ln\left(\overline{p}/p\right)}. \tag{1}$$

Fourth stage. After chemical freeze-out starts, the particle system continues to expand and cool. When the mean free path of the particles becomes larger than the size of the system, elastic collisions stop, fixing the momentum distribution of the particles, which corresponds to the onset of kinetic freeze-out.

Phenomenological models such as Blast-Wave are used to study the characteristics of kinetic freeze-out [7, 8]. This model is based on the relativistic hydrodynamic approach and describes the collective motion of particles in an expanding system.

Blast-Wave model. The basis of the model is that heated matter has a high temperature, distributed nonuniformly: the temperature in the center of the particle system is higher than at its periphery, which creates a pressure gradient. According to the equations of hydrodynamics, matter flows outward from the center, forming a blast wave.

According to the Blast-Wave model, all hadrons are produced from quarks and gluons simultaneously, so consequently they acquire the same average velocity of radial flow. In this case, the expansion of the hadron system is described in terms of relativistic hydrodynamics.

The invariant spectra for the transverse mass $m_T = \sqrt{p_T^2 + m_0^2}$ can be described by the following formula within the Blast-Wave model:

$$\frac{dN}{m_T dm_T} = C\int_0^R rdr m_T I_0\left(\frac{p_T \sinh\rho}{T_0}\right) K_1\left(\frac{p_T \cosh\rho}{T_0}\right), \tag{2}$$

where C is the normalization constant; β_T is the average velocity of radial flow; T_0 is the kinetic freeze-out temperature; R is the maximum radius of the expanding system during the freeze-out stage; I_0, K_1 are the modified Bessel functions; $\rho(r)$ is the transverse acceleration depending on the particle coordinate,

$$\rho(r) = \tanh^{-1}(\beta_T) \cdot r / R.$$

C, β_T, T_0 are the free parameters of the model.

Measurement procedure

We used simulation data from 15,000,000 Bi+Bi collisions at $\sqrt{S_{NN}}$ = 9.2 GeV; the data were obtained using the MPDroot package [1]. The latter uses the hybrid UrQMD event generator [9] including a hydrodynamic approach; in addition, MPDroot allows reproducing the response of the detector subsystems of the MPD experiment via the Geant4 package [12, 13].

Detection of charged hadrons in MPD is carried out by analyzing, firstly, the energy losses of particles measured in the TPC (Time Projection Chamber), and secondly, the time of flight of the particles measured by the ToF (Time-of-Flight) detector. The details of the simulation and the particle detection procedure can be found in [3, 14].

Analysis of characteristics of charged hadron production

Determination of kinetic freeze-out parameters. Fig. 1 shows the invariant m_T spectra measured for charged hadrons at different centrality bins in Bi+Bi collisions at $\sqrt{S_{NN}}$ = 9.2 GeV. The lines show the fit of the obtained spectra by the corresponding function of the Blast-Wave model (see Eq. (2)).

Fitting of the invariant m_T spectra of different particles with the Blast-Wave function was carried out in the following ranges.

Charged hadron type   Approximation range, GeV
π^+, π^- .... 0.50−1.00
K^+, $\overline{p}$ .... 0.12−1.00
K^- .... 0.40−1.00
p .... 0.20−1.00
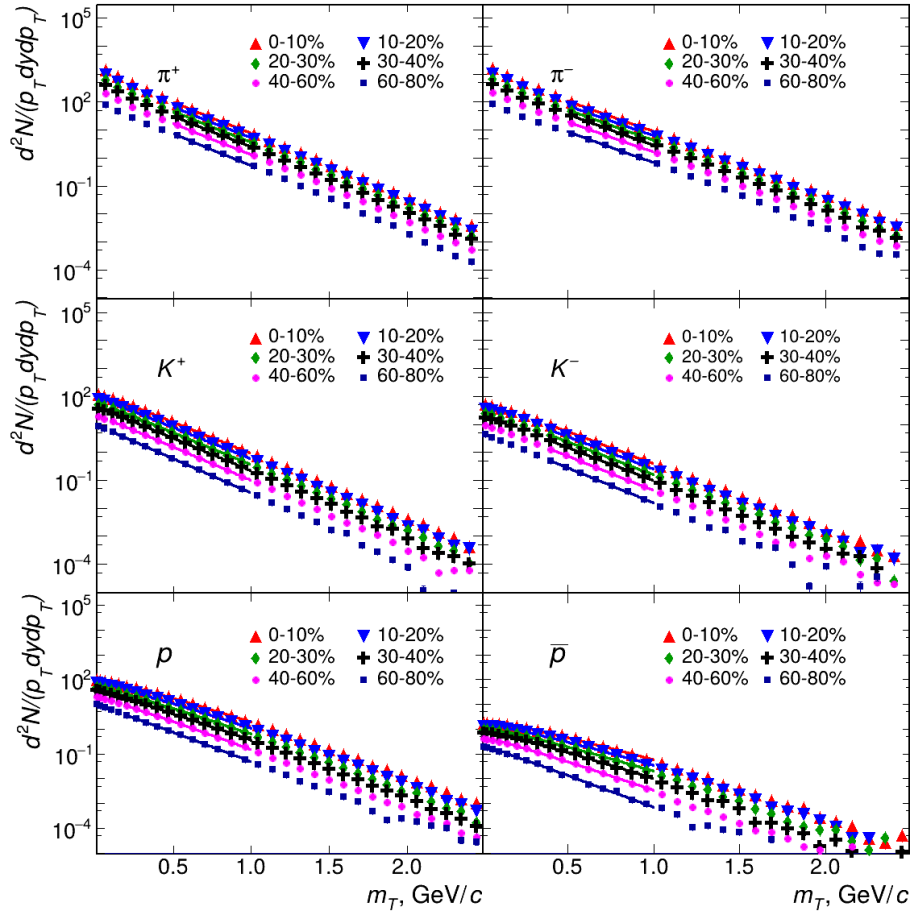
Fig. 1. Invariant transverse mass spectra measured for $\pi^{\pm}$, $K^{\pm}$, p, $\bar{p}$ particles
at different centrality bins in Bi+Bi collisions at energy $\sqrt{S_{NN}} = 9.2$ GeV.
Fits to the spectra with the corresponding function of the Blast-Wave model (see Eq. (2))
are shown by straight lines

The fitting ranges were chosen so as to achieve the best agreement with the simulation data. It was found that the difference between the simulation data and the Blast-Wave function did not exceed 1%.

Since the Blast-Wave function is integral, the free fitting parameters (C, T_0, β_T) are sensitive to variation in the fitting range, the choice of initial parameter values and the constraints imposed on the parameter values. The impact of these factors was taken into account by estimating the systematic uncertainties.

For this purpose, the fitting parameters (given below) were varied by $\pm 10\%$. These were the following conditions:

range bounds;

initial parameter values;

constraints on parameter values.

The final values of systematic uncertainties were determined by the quadrature sum of the percentage differences between the final values of the parameters and those obtained under different fitting conditions.

Fig. 2 shows the final values of the parameters T_0 and β_T obtained by fitting of invariant m_T with the Blast-Wave function for different types of charged hadrons ($\pi^{\pm}$, $K^{\pm}$, p, $\bar{p}$) depending on centrality of Bi+Bi collisions. Systematic uncertainties are represented by boxes.

We found that the kinetic freeze-out temperature T_0 shows no significant dependence on either the collision centrality or the type of charged hadrons. The average value of the kinetic freeze-out temperature $T_0 = 109$ MeV (red dashed line in Fig. 2,a).
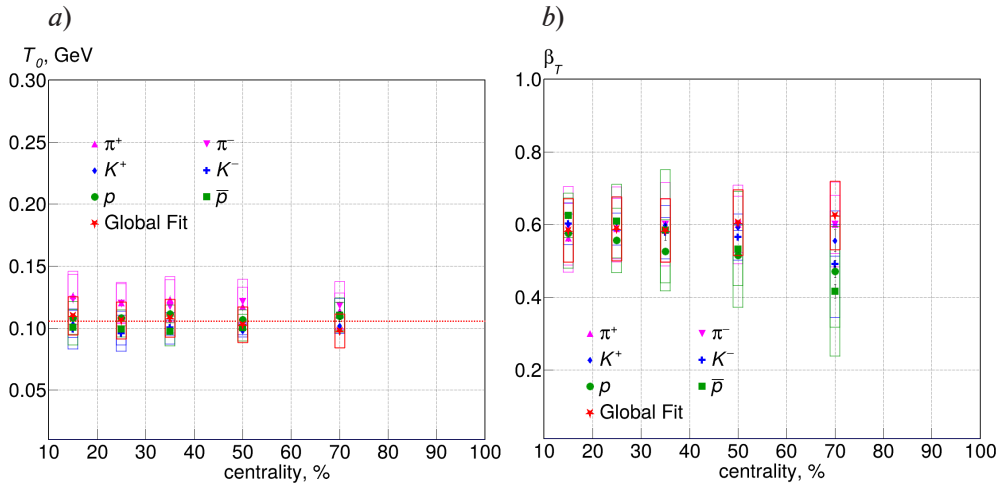
Fig. 2. Kinetic freeze-out temperature T_0 (*a*) and average velocity β_T of radial flow of particle system (*b*) depending on centrality of Bi+Bi collisions. The bars correspond to systematic uncertainty in determining the values of T_0 and β_T
The average value of $T_0 = 109$ MeV (red horizontal dashed line)

The average velocities β_T of radial particle flow show a decreasing trend with a decrease in the overlap of colliding nuclei (this corresponds to an increase in centrality as a percentage). Nevertheless, the decrease in β_T values in peripheral collisions, compared with the central ones, is insignificant taking into account systematic uncertainty.

Determination of phase transition parameters. The values of the baryonic chemical potential and temperature corresponding to the phase transition are estimated by calculating the antiproton to proton yield ratios ($\bar{p}/p$).

The values of ($\bar{p}/p$) measured in different centrality bins of Bi+Bi collisions are shown in Fig. 3,*a*. Evidently, they do not show a significant dependence on the collision centrality and the transverse momentum p_T. The average value of the ratio ($\bar{p}/p$) = 0.025 (shown by a red horizontal red dashed line) was used for further calculations.

According to calculations within the framework of quantum chromodynamics, the phase transition boundary can be expressed by the following formula [15]:

$$T_{QGP} = \frac{\sqrt{3/34}}{\pi}\sqrt{\sqrt{340\pi^2(220)^4 + 55\mu^4} - 15\mu^2}. \tag{3}$$

The baryonic chemical potential μ can be expressed in terms of temperature and the $\bar{p}/p$ ratio by Eq. (1). Thus, the temperature and the baryonic chemical potential corresponding to the phase transition can be found as the intersection point of the curve expressed by Eq. (3) and the straight line given by Eq. (1).

The following values of T_{QGP} and μ_B were obtained, corresponding to the phase transition in Bi+Bi collisions at NICA energies:

$$T_{QGP} = 131 \text{ MeV}, \ \mu_B = 247 \text{ MeV}.$$

Visualization of the obtained results on the phase diagram. Fig. 3,*b* shows the phase diagram of nuclear matter. The red line indicates the phase boundary calculated by Eq. (3). The lines correspond to the temperatures in terms of the baryonic chemical potential and the value found for $\bar{p}/p$ = 0.025 (see Eq. (2). The purple line in Fig. 3,b expresses the dependence $T(\mu_B,\bar{p}/p)$, obtained using the value $\bar{p}/p$ = 0.025 corresponding to Bi+Bi collisions at $\sqrt{S_{NN}}$ = 9.2 GeV.

Using Eq. (2), we additionally calculated the value of the baryonic chemical potential μ_B corresponding to the kinetic freeze-out temperature in Bi+Bi collisions at $\sqrt{S_{NN}}$ = 9.2 GeV (the temperature was determined earlier using the Blast-Wave model). The found value of μ_B = 205 MeV.

The kinetic freeze-out and phase transition temperatures corresponding to the energy of the PHENIX experiment ($\sqrt{S_{NN}}$ = 200 GeV) are given for comparison. The dependence $T(\mu_B,\bar{p}/p)$ as

a)

b)
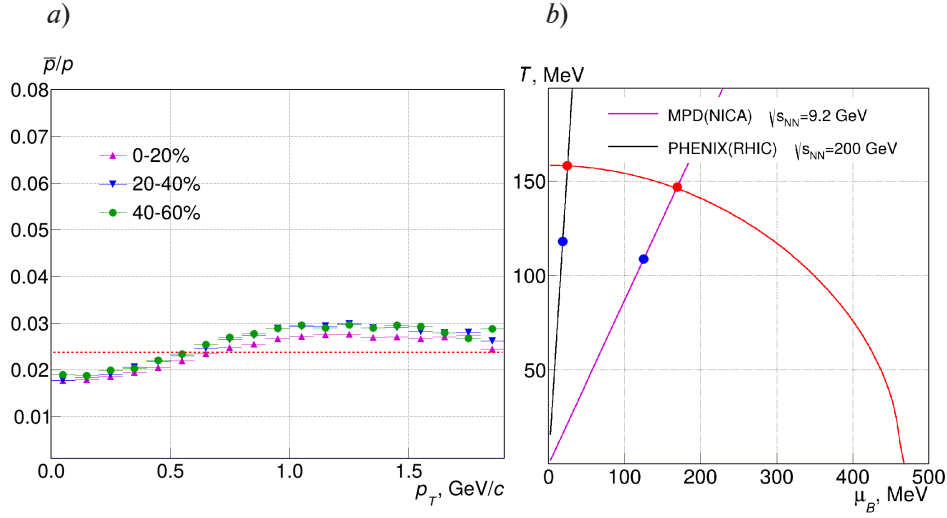
Fig. 3. Antiproton to proton yield ratios $\bar{p}/p$ as functions of transverse momentum, measured in different centrality bins (%) of Bi+Bi collisions at $\sqrt{S_{NN}}$ = 9.2 GeV (*a*) and corresponding phase diagram of nuclear matter (dependence of temperature on baryonic chemical potential) (*b*)

a straight line (shown in Fig. 3,*b* in black) is obtained taking into account the value of $\bar{p}/p$ = 0.79 measured in the PHENIX experiment at $\sqrt{S_{NN}}$ = 200 GeV.

The blue dots in Fig. 3,*b* mark the values of the temperature and the baryonic chemical potential of the particle system during a collision at the kinetic freeze-out stage, and the red ones mark these values at the phase transition stage.

Conclusion

We report on the transverse mass spectra of charged hadrons $\pi^{\pm}$, $K^{\pm}$, p, $\bar{p}$ obtained in simulations of Bi+Bi collisions at $\sqrt{S_{NN}}$ = 9.2 GeV using the hybrid UrQMD generator and the MPDroot package.

Analyzing the obtained spectra of charged hadrons within the Blast-Wave model, we found the values of the kinetic freeze-out temperature T_0 and the average velocity β_T of the particle system's radial flow depending on collision centrality.

Calculating the antiproton to proton yield ratios allowed to determine the temperatures T_0 and T_{QGP}, as well as the baryonic chemical potential μ_B corresponding to the kinetic freeze-out and phase transition. The following parameter values were obtained:

$$T_0 \approx 109 \text{ MeV}, \mu_B \approx 205 \text{ MeV for kinetic freeze-out;}$$

$$T_{QGP} \approx 131 \text{ MeV}, \mu_B \approx 247 \text{ MeV for phase transition.}$$

The presented results make it possible to estimate the accessible range of values for the temperature T and the baryonic chemical potential μ_B, which is important for potential signatures of the phase transition in nucleon-nucleon collisions at NICA energies.

REFERENCES

1. **Abraamyan Kh. U., Afanasyev S. V., Alfeev V. S., et al.** (MPD Collaboration), The MPD detector at the NICA heavy-ion collider at JINR, Nucl. Instrum. Methods Phys. Res. Sec. A. 628 (1) (2011) 99−102.

2. **Kekelidze V. D., Lednicky R., Matveev V. A., et al.,** Three stages of the NICA accelerator complex, Eur. Phys. J. A. 52 (8) (2016) 211.

3. **Abgaryan V., Acevedo Kado R., Afanasyev S. V., et al.** (MPD Collaboration), Status and initial physics performance studies of the MPD experiment at NICA, Eur. Phys. J. A. 58 (7) (2022) 140.

4. **Adcox K., Adler S. S., Afanasyev S., et al.** (PHENIX Collaboration), Formation of dense partonic matter in relativistic nucleus-nucleus collisions at RHIC: Experimental evaluation by the PHENIX collaboration, Nucl. Phys. A. 757 (1−2) (2005) 184−283.

5. **Rafelski J.,** Melting hadrons, boiling quarks, Eur. Phys. J. A. 51 (9) (2015) 114.

6. **Adams J., Aggarwal M. M., Ahammed Z., et al.** (STAR Collaboration), Experimental and theoretical challenges in the search for the quark gluon plasma: The STAR Collaboration's critical assessment of the evidence from RHIC collisions, Nucl. Phys. A. 757 (1−2) (2005) 102−183.

7. **Schnedermann E., Sollfrank J., Heinz U. W.,** Fireball spectra (Chapter), In book: Gutbrod H. H., Rafelski J. (Eds). Particle production in highly excited matter, NATO Science Ser. B: Phys. Vol. 303. Springer, Boston, MA, USA (1993) 175−206.

8. **Schnedermann E., Sollfrank J., Heinz U. W.,** Thermal phenomenology of hadrons from 200 A GeV S+S collisions, Phys. Rev. C. 48 (5) (1993) 2462.

9. **Petersen H., Steinheimer J., Burau G., et al.,** Fully integrated transport approach to heavy ion reactions with an intermediate hydrodynamic stage, Phys. Rev. C. 78 (4) (2008) 044901.

10. **Bjorken J. D.,** Highly relativistic nucleus-nucleus collisions: The central rapidity region, Phys. Rev. D. 27 (1) (1983) 140.

11. **Oganiessian Yu. Ts. (Ed.),** Vvedeniye v fiziku tyazhelykh ionov [Introduction to heavy-ion physics], MIFI Publishing, Moscow, 2008 (in Russian).

12. **Agostinelli S., Allison J., Amako K., et al.** Geant4 − a simulation toolkit, Nucl. Instrum. Methods Phys. Res. A. 506 (3) (2003) 250−303.

13. **Allison J., K. Amako K., Apostolakis J, et al.** Recent developments in Geant4, Nucl. Instrum. Methods Phys. Res. A. 835 (1 Nov) (2016) 186−225.

14. **Mudrokh A.,** Prospects of the MPD detector for measuring the spectra of identified hadrons in Bi+Bi collisions at energy $\sqrt{s_{NN}}$ = 9.2 CeV, Phys. Particl. Nucl. 55 (4) (2024) 937−977.

15. **Aoki Y., Endrydi G., Fodor Z., et al.,** The order of the quantum chromodynamics transition predicted by the standard model of particle physics, Nature. 443 (7112) (2006) 675−678.

СПИСОК ЛИТЕРАТУРЫ

1. **Abraamyan Kh. U., Afanasyev S. V., Alfeev V. S., et al.** (MPD Collaboration). The MPD detector at the NICA heavy-ion collider at JINR // Nuclear Instruments and Methods in Physics Research. Sec. A. 2011. Vol. 628. No. 1. Pp. 99−102.

2. **Kekelidze V. D., Lednicky R., Matveev V. A., Meshkov I. N., Sorin A. S., Trubnikov G. V.** Three stages of the NICA accelerator complex // The European Physical Journal A. 2016. Vol. 52. No. 8. P. 211.

3. **Abgaryan V., Acevedo Kado R., Afanasyev S. V., et al.** (MPD Collaboration). Status and initial physics performance studies of the MPD experiment at NICA // The European Physical Journal A. 2022. Vol. 58. No. 7. P. 140.

4. **Adcox K., Adler S. S., Afanasyev S., et al.** (PHENIX Collaboration). Formation of dense partonic matter in relativistic nucleus-nucleus collisions at RHIC: Experimental evaluation by the PHENIX collaboration // Nuclear Physics A. 2005. Vol. 757. No. 1−2. Pp. 184−283.

5. **Rafelski J.** Melting hadrons, boiling quarks // The European Physical Journal A. 2015. Vol. 51. No. 9. P. 114.

6. **Adams J., Aggarwal M. M., Ahammed Z., et al.** (STAR Collaboration). Experimental and theoretical challenges in the search for the quark gluon plasma: The STAR Collaboration's critical assessment of the evidence from RHIC collisions // Nuclear Physics A. 2005. Vol. 757. No. 1−2. Pp. 102−183.

7. **Schnedermann E., Sollfrank J., Heinz U. W.** Fireball spectra (Chapter) // Gutbrod H. H.,

Rafelski J. (Eds). Particle production in highly excited matter. NATO Science Book Series B: Physics. Vol. 303. Boston, MA, USA: Springer, 1993. Pp. 175−206.

8. **Schnedermann E., Sollfrank J., Heinz U. W.** Thermal phenomenology of hadrons from 200A GeV S+S collisions // Physical Review C. 1993. Vol. 48. No. 5. P. 2462.

9. **Petersen H., Steinheimer J., Burau G., Bleicher M., Stцcker H.** Fully integrated transport approach to heavy ion reactions with an intermediate hydrodynamic stage // Physical Review C. 2008. Vol. 78. No. 4. P. 044901.

10. **Bjorken J. D.** Highly relativistic nucleus-nucleus collisions: The central rapidity region // Physical Review D. 1983. Vol. 27. No. 1. P. 140.

11. Введение в физику тяжелых ионов. Под ред. Ю. Ц. Оганесяна. М.: Изд-во МИФИ, 2008. 424 с.

12. **Agostinelli S., Allison J., Amako K., et al.** Geant4 − a simulation toolkit // Nuclear Instruments and Methods in Physics Research. Sec. A. 2003. Vol. 506. No. 3. Pp. 250−303.

13. **Allison J., K. Amako K., Apostolakis J, et al.** Recent developments in Geant4 // Nuclear Instruments and Methods in Physics Research. Sec. A. 2016. Vol. 835. 1 November. Pp. 186−225.

14. **Мудрох А.** Перспективы детектора MPD по измерению спектров идентифицированных адронов в (Bi + Bi)-столкновениях при энергии $\sqrt{s_{NN}} = 9{,}2$ ГэВ // Физика элементарных частиц и атомного ядра. 2024. Т. 55. № 4. С. 1128−1135.

15. **Aoki Y., Endrydi G., Fodor Z., Katz S. D., Szabo K. K.** The order of the quantum chromodynamics transition predicted by the standard model of particle physics // Nature. 2006. Vol. 443. No. 7112. Pp 675−678.

THE AUTHORS

LARIONOVA Daria M.
Peter the Great St. Petersburg Polytechnic University
29 Politechnicheskaya St., St. Petersburg, 195251, Russia
dlar@bk.ru

BERDNIKOV Yaroslav A.
Peter the Great St. Petersburg Polytechnic University
29 Politechnicheskaya St., St. Petersburg, 195251, Russia
berdnikov@spbstu.ru

KOTOV Dmitry O.
Peter the Great St. Petersburg Polytechnic University
29 Politechnicheskaya St., St. Petersburg, 195251, Russia
dmitriy.kotov@gmail.com

СВЕДЕНИЯ ОБ АВТОРАХ

ЛАРИОНОВА Дарья Максимовна − *кандидат физико-математических наук, ассистент Высшей школы фундаментальных физических исследований Санкт-Петербургского политехнического университета Петра Великого.*
195251, Россия, г. Санкт-Петербург, Политехническая ул., 29
dashalario@gmail.com
ORCID: 0009-0007-7019-5586

БЕРДНИКОВ Ярослав Александрович − *доктор физико-математических наук, профессор Высшей школы фундаментальных физических исследований Санкт-Петербургского политехнического университета Петра Великого.*
195251, Россия, г. Санкт-Петербург, Политехническая ул., 29
berdnikov@spbstu.ru
ORCID: 0000-0003-0309-5917

КОТОВ Дмитрий Олегович – *кандидат физико-математических наук, доцент **Высшей школы фундаментальных физических исследований Санкт-Петербургского политехнического университета Петра Великого**.*
195251, Россия, г. Санкт-Петербург, Политехническая ул., 29
dmitriy.kotov@gmail.com
ORCID: 0000-0002-3395-0454

DIRECT PHOTON ASYMMETRIES IN THE LONGITUDINALLY POLARIZED PROTON-PROTON COLLISIONS AT ENERGIES FROM 9 TO 27 GEV

A. A. Lobanov✉, *Ya. A. Berdnikov*

Peter the Great St. Petersburg Polytechnic University, St. Petersburg, Russia

✉ lobanov2.aa@edu.spbstu.ru

Abstract. This paper presents the development of the Generative Adversarial Network (GAN) model to study the properties of direct photons produced in proton-proton collisions. The study aims to extend the capabilities of our model (developed previously) by introducing the initial collision energy parameter $\sqrt{s_{NN}}$ in the range from 9 to 27 GeV. The model has been trained on the data generated using PYTHIA8 and tested both at training energies and at intermediate energy values. Special attention was paid to the ability of the model to preserve kinematic dependencies and to reproduce the double longitudinal spin asymmetry A_{LL}. The results proved the possibility of using the GAN to interpolate the characteristics of direct photons in terms of collision energy.

Keywords: asymmetries, direct photons, neural network, generative-adversarial network

Citation: Lobanov A. A., Berdnikov, Ya. A., Direct photon asymmetries in the longitudinally polarized proton-proton collisions at energies from 9 to 27 GeV, St. Petersburg State Polytechnical University Journal. Physics and Mathematics. 18 (3) (2025) 91−97. DOI: https://doi.org/10.18721/JPM.18308

АСИММЕТРИИ ПРЯМЫХ ФОТОНОВ В ПРОДОЛЬНО-ПОЛЯРИЗОВАННЫХ ПРОТОН-ПРОТОННЫХ СТОЛКНОВЕНИЯХ ПРИ ЭНЕРГИЯХ 9 – 27 ГЭВ

А. А. Лобанов✉, *Я. А. Бердников*

Санкт-Петербургский политехнический университет Петра Великого, Санкт-Петербург, Россия

✉ lobanov2.aa@edu.spbstu.ru

Аннотация. В работе представлено развитие модели генеративно-состязательной сети (ГСС) для изучения характеристик прямых фотонов, образующихся при столкновениях протонов. Исследование направлено на расширение возможностей ранее разработанной нами модели путем введения параметра начальной энергии столкновения $\sqrt{s_{NN}}$ в диапазоне 27 − 9 ГэВ. Модель обучена на данных, сгенерированных с помощью PYTHIA8, и протестирована как при энергиях обучения, так и при промежуточных значениях энергии. Особое внимание уделено способности модели сохранять кинематические зависимости и воспроизводить двойную продольную спиновую асимметрию A_{LL}. Результаты доказали возможность использования ГСС для интерполяции характеристик прямых фотонов по энергии столкновения.

Introduction

Study of the proton structure and the formation of its spin remains one of the key challenges in modern physics [1]. Various experimental facilities are constructed to solve this problem, among them, in particular, the SPD experiment at the NICA collider currently under construction at the Joint Institute for Nuclear Research (Dubna, Russia) [1].

Gluons play a major role to the total spin of the proton [1], described by gluon helicity functions $\Delta g(x)$, integrated to obtain the total contribution to proton spin. An effective approach to obtaining the values of $\Delta g(x)$ is to measure the double longitudinal spin asymmetry (DLSA) A_{LL} occurring in collisions of longitudinally polarized protons [1].

DLSA can be measured for various particles, including charged and neutral pions [2], as well as (J/ψ) mesons [3]. A particular interest lies in the direct photons produced in electromagnetic interactions of proton partons, in particular, in the Compton scattering reaction $gq(\bar{q}) \to \gamma q$ [4]. The advantage of direct photon measurement is in the simpler theoretical description that does not require hadronization models.

Despite this advantage, direct photon measurements are fraught with difficulties, including small sample size and problems with isolating direct photons against the background of photons from decay of secondary particles, for example, the decay of the π^0 mesons [4].

An approach using a generative adversarial network (GAN) was proposed in a previous paper to solve the problem of small samples [5]. It was proved that the GAN can faithfully reproduce the characteristics of direct photons produced in collisions of longitudinally polarized protons, allowing to calculate the asymmetries.

This paper develops the proposed approach to expand the capabilities of our GAN model [5].

For this purpose, we introduce the parameter of the initial collision energy $\sqrt{s_{NN}}$, which should provide results for arbitrary energies in a given range. Such an interpolation should provide improved accuracy in determining the values of $\Delta g(x)$, consequently yielding better estimates for the contribution of gluons to the proton spin.

Computational procedure

To verify that the GAN could be expanded to predict direct photon production at different energies $\sqrt{s_{NN}}$ and in the absence of experimental data, the model was trained on pre-generated simulation data. The PYTHIA8 program was used as a Monte Carlo generator [5, 6].

The main parameters of the Pythia8 program used in this study were as follows [5]:

PromptPhoton: qg2qgamma = on,

PromptPhoton: qqbar2ggamma = on,

MultipartonInteractions: pT0Ref = 2.2,

NNPDF31_nlo_as_0118 [7] (for unpolarized events),

NNPDFpol11_100 [8] (for polarized events).

The energy range of 9−27 GeV was considered for the initial collision energy $\sqrt{s_{NN}}$. The choice of the range was dictated by the experimental conditions of the SPD at the NICA facility [4]. To

train the model, samples were generated at $\sqrt{s_{NN}}$ = 9, 15, 21, and 27 GeV for collisions of both unpolarized and polarized protons (the term 'events' is used throughout the paper). The size of each sample was 500,000 events (collisions).

Similar to the procedure adopted in the previous paper [5], the z-components of the momentum $p_{z\,q1}$ of the first and $p_{z\,q2}$ of the second partons, as well as the p_x-, p_y- and p_z-components of the momentum of the produced direct photon were extracted from the generated samples. Instead of the components $p_{z\,q1}$ and $p_{z\,q2}$, we used their transformed versions $T(p_{z\,q1})$ and $T(p_{z\,q2})$ to train the GAN, in accordance with the results from [5].

The GAN loss function remained unchanged and was a least square function [5]. The number of epochs for training was increased to 2,000. The batch size was also increased to 2,000. The gradient descent optimizer was replaced by Adam with the following parameter values:

The training step of $2 \cdot 10^{-4}$ was taken for the generator and discriminator, the forgetting factors β_1 = 0.9 and β_2 = 0.5 for the gradients and the second moments of the gradients, respectively [9].

The architecture of the generator is based on the results of our previous work [5]. A 128-dimensional vector whose elements are normally distributed is fed to the input of the generator. The initial energy $\sqrt{s_{NN}}$ and the polarization type of the event are used as conditional variables. Conditional variables are combined with a 128-dimensional vector so that the generator can adapt its output to different generation scenarios. The number of hidden layers was increased to 8. Each hidden layer has 512 neurons and a Leaky ReLU activation function with a dropout of 0.2 [10]. Next, the ResidualAdd procedure was applied to each hidden layer [11] to make the training process with a large number of hidden layers more stable. The ResidualAdd procedure is that the output of each layer after the activation function is summed with the output of the previous layer. This approach allows to mitigate the gradient vanishing problem in deep neural networks [11]. The output of the generator contains 5 generated values:

$$T(p_{z\,q1}),\ T(p_{z\,q2}),\ p_x,\ p_y,\ p_z.$$

The discriminator has almost the same architecture as the generator. The input of the discriminator is fed 6 values generated by the generator, along with conditional variables. The parameters of the hidden layers of the discriminator repeat the parameters of the hidden layers of the generator with one exception: Spectral Normalization is applied to each hidden layer [12]. The output from the discriminator contains one neuron reflecting the degree of confidence of the discriminator that the input is real data as opposed to those obtained using the generator.

Simulation results

To illustrate the performance of the GAN at different initial $\sqrt{s_{NN}}$, only a part of the complete set of parameters is shown below; these are p_{zq1} and $p_T = \sqrt{p_x^2 + p_y^2}$, as well as the DLSA values.

The remaining values are not shown because their distributions are similar.

Fig. 1,a shows the distributions of the parton momentum $p_{z\,q1}$ in collisions of unpolarized protons. The simulation results obtained by PYTHIA8 and the GAN predictions were compared for $\sqrt{s_{NN}}$ of 9, 15, 21 and 27 GeV, at which the model was trained, as well as for intermediate energies of 12, 18, 24 and 30 GeV. Each subsequent distribution in the graphs in Fig. 1 was shifted by 10 GeV for clarity (to separate the distributions). Analyzing the graphs, we can see that the GAN model provides good predictive accuracy for both the energies at which the training was performed and the interpolated values.

A similar picture is observed in Fig. 1,b, showing the distributions of the transverse momentum p_T for photons in collisions of polarized protons. Notably, the model preserves the prediction accuracy in this case.

Fig. 2 shows the dependences of asymmetries A_{LL} on the momentum fraction $x_T = \dfrac{2p_T}{\sqrt{s_{NN}}}$ of direct photons, calculated from GAN predictions and PYTHIA8 simulations. It follows from this figure that GAN predictions yield A_{LL} values coinciding with the PYTHIA8 values (with an accuracy up to the uncertainty) over the entire range of initial energies $\sqrt{s_{NN}}$.
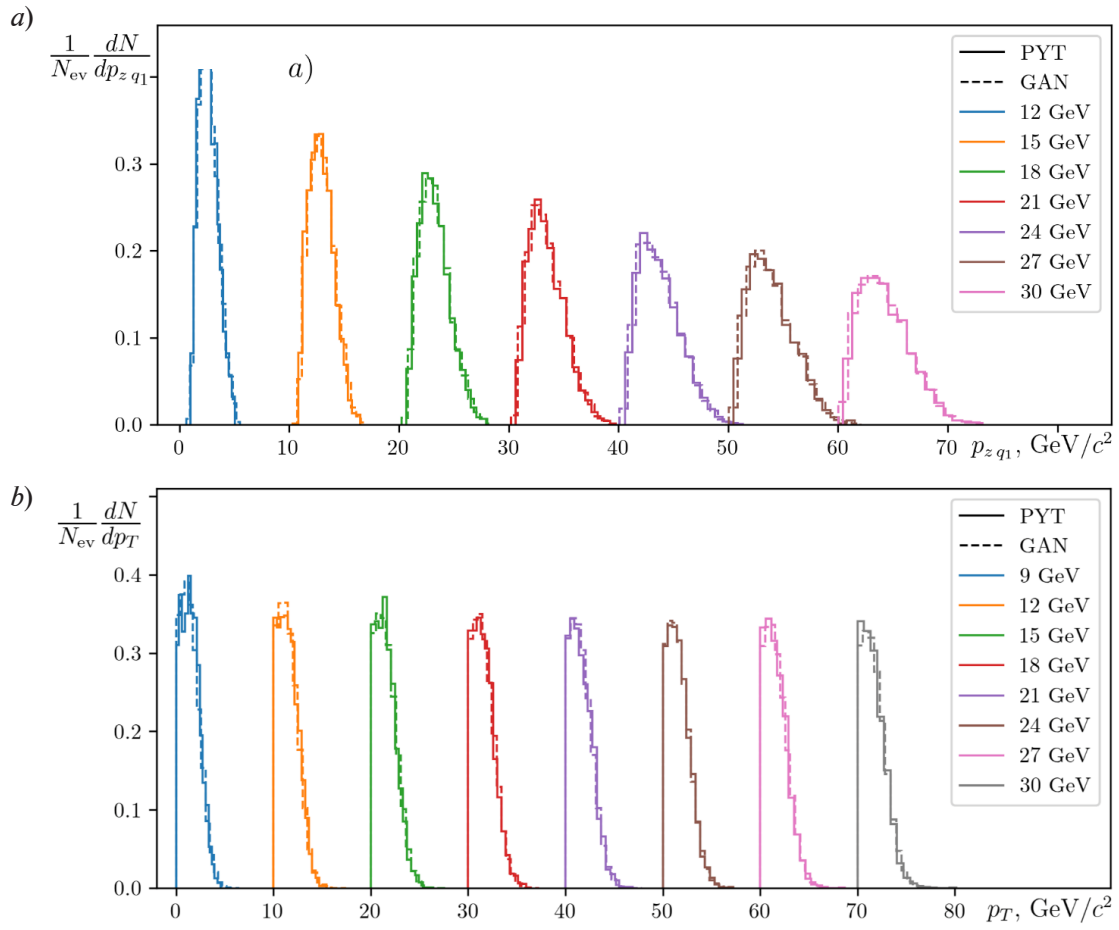
Fig. 1. Comparison of GAN predictions (solid lines) and simulations (dashed lines) for momentum distributions of partons $p_{z\,q_1}$ (*a*) and direct photons p_T (*b*) in collisions of unpolarized (*a*) and polarized (*b*) protons at different initial $\sqrt{s_{NN}}$ (see the legends: the energies are given in GeV; odd values were obtained during training and even values were interpolated). Number of events N_{ev} = 500,000; the PYTHIA8 program was used for simulation
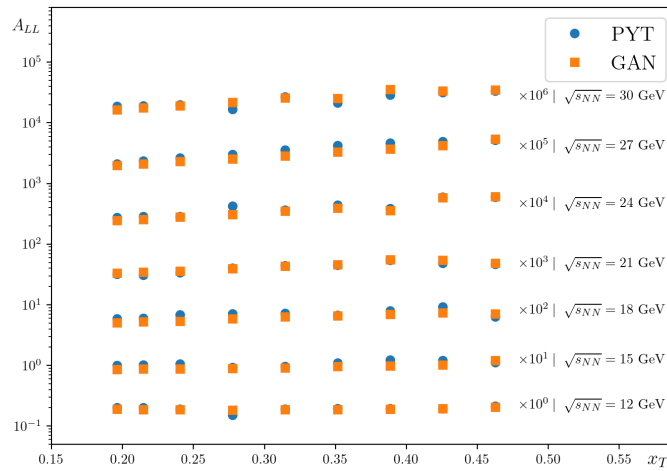
Fig. 2. Asymmetry A_{LL} as function of momentum fraciton x_T of direct photons in collisions of longitudinally polarized protons, at different initial energies of $\sqrt{s_{NN}}$ in the range of 12−30 GeV. The data were obtained using GAN and PYTHIA8 (orange squares and blue circles, respectively) The error bars are comparable in size to the data points

Conclusion

This paper continues to developed the generative adversarial network (GAN) developed earlier for predicting the characteristics of direct photon production in proton collisions. The model's predictive capabilities were expanded to extracting the characteristics of direct photon at various initial energies $\sqrt{s_{NN}}$ in the range of $9-27$ GeV.

We confirmed that the model predicts the results of proton collisions with high accuracy both for the energies at which the training was performed and at intermediate values. From this, we can conclude that the model is capable of interpolating the given parameters based on the initial energies $\sqrt{s_{NN}}$. The accuracy of the predictions is preserved collisions of both unpolarized and longitudinally polarized protons ($p^{\rightarrow}p^{\rightarrow(\leftarrow)}$).

In addition, we established that the GAN model preserves the kinematic dependences between the generated parameters, allowing to calculate the values of double longitudinal spin asymmetry A_{LL}. The A_{LL} values can also be obtained at any energies $\sqrt{s_{NN}}$ in the considered range of $9-30$ GeV.

REFERENCES

1. **Arbuzov A., Bacchetta A., Butenschoen M., et al.,** On the physics potential to study the gluon content of proton and deuteron at NICA SPD, Prog. Part. Nucl. Phys. 119 (July) (2021) 103858.

2. **Acharya U., Adare A., Aidala C., et al.** (PHENIX Collaboration), Measurement of charged pion double spin asymmetries at midrapidity in longitudinally polarized $p + p$ collisions at $\sqrt{s} = 510$ GeV, Phys. Rev. D. 102 (3) (2020) 032001.

3. **Adare A., Aidala C., Ajitanand N. N., et al.** (PHENIX Collaboration), Measurements of double-helicity asymmetries in inclusive J/ψ production in longitudinally polarized $p + p$ collisions at $\sqrt{s} = 510$ GeV, Phys. Rev. D. 94 (11) (2016) 112008.

4. **Guskov A. and on behalf of the SPD working group,** Physics with prompt photons at SPD, J. Phys.: Conf. Ser. 1435 (2020) 012035.

5. **Lobanov A. A., Berdnikov Ya. A.,** Direct photon asymmetries in the longitudinally polarized proton-proton collisions at an energy of 27 GeV, St. Petersburg State Polytechnical University Journal. Physics and Mathematics. 18 (1) (2025) 142−148 (in Russian).

6. **Sjöstrand T., Mrenna S., Skands P.** A brief introduction to PYTHIA 8.1 Comput. Phys. Commun. 178 (11) (2008) 852−867.

7. **Ball R. D., Bertone V., Carrazza S., et al.,** Parton distributions from high-precision collider data, Eur. Phys. J. C. 77 (04 Oct.) (2017) 663.

8. **Nocera E. R., Ball R. D., Forte S., et al.,** A first unbiased global determination of polarized PDFs and their uncertainties, Nucl. Phys. B. 887 (Oct) (2014) 276−308.

9. **Imran Khan M. J., Ismail R. A., Syed Qamrun N. A.,** Optimization algorithm for wide and deep neural network, Knowl. Eng. Data Sci. 2 (1) (2019) 41−46.

10. **Sharma O.,** A new activation function for deep neural network, Proc. Int. Conf. on Machine Learning, Big Data, Cloud and Parallel Computing (COMITCon); IEEE, Faridabad, India, Febr. 14−16 (2019) 84−86.

11. **Fengxiang H., Liu T., Tao D.,** Why ResNet works? Residuals Generalize. arXiv: 1904.01367, 2019. https://doi.org/10.48550/arXiv.1904.01367.

12. **Miyato T., Kataoka T., Koyama M., Yoshida Y.,** Spectral normalization for Generative Adversarial Networks, arXiv: 1802.05 957/v1, 2018. https://doi.org/10.48550/arXiv.1802.05957.

СПИСОК ЛИТЕРАТУРЫ

1. **Arbuzov A., Bacchetta A., Butenschoen M., et al.** On the physics potential to study the gluon content of proton and deuteron at NICA SPD // Progress in Particle and Nuclear Physics. 2021. Vol. 119. July. P. 103858.

2. **Acharya U., Adare A., Aidala C., et al.** (PHENIX Collaboration). Measurement of charged pion double spin asymmetries at midrapidity in longitudinally polarized $p + p$ collisions at $\sqrt{s} = 510$ GeV // Physical Review D. 2020. Vol. 102. No. 3. P. 032001.

3. **Adare A., Aidala C., Ajitanand N. N., et al.** (PHENIX Collaboration), Measurements of double-helicity asymmetries in inclusive J/ψ production in longitudinally polarized $p + p$ collisions at $\sqrt{s} = 510$ GeV // Physical Review D. 2016. Vol. 94. No. 11. P. 112008.

4. **Guskov A. and on behalf of the SPD working group.** Physics with prompt photons at SPD // Journal of Physics: Conference Series. 2020. Vol. 1435. P. 012035.

5. **Лобанов А. А., Бердников Я. А.** Асимметрии прямых фотонов в продольно-поляризованных протон-протонных столкновениях при энергии 27 ГэВ // Научно-технические ведомости СПбГПУ. Физико-математические науки. 2025. Т. 18. № 1. С. 142−148.

6. **Sjöstrand T., Mrenna S., Skands P.** A brief introduction to PYTHIA 8.1 // Computer Physics Communications. 2008. Vol. 178. No. 11. Pp. 852−867.

7. **Ball R. D., Bertone V., Carrazza S., et al.** Parton distributions from high-precision collider data // The European Physical Journal C. 2017. Vol. 77. 04 October. P. 663.

8. **Nocera E. R., Ball R. D., Forte S., Ridolfi G., Rojo J.** A first unbiased global determination of polarized PDFs and their uncertainties // Nuclear Physics B. 2014. Vol. 887. October. Pp. 276−308.

9. **Imran Khan M. J., Ismail R. A., Syed Qamrun N. A.** Optimization algorithm for wide and deep neural network // Knowledge Engineering and Data Science. 2019. Vol. 2. No. 1. Pp. 41−46.

10. **Sharma O.** A new activation function for deep neural network // Proceedings of the International Conference on Machine Learning, Big Data, Cloud and Parallel Computing (COMITCon); IEEE, Faridabad, India, February 14−16, 2019. Pp. 84−86.

11. **Fengxiang H., Liu T., Tao D.** Why ResNet works? Residuals Generalize. arXiv: 1904.01367, 2019. https://doi.org/10.48550/arXiv.1904.01367.

12. **Miyato T., Kataoka T., Koyama M., Yoshida Y.** Spectral normalization for Generative Adversarial Networks. arXiv: 1802.05 957/v1, 2018. https://doi.org/10.48550/arXiv.1802.05957.

THE AUTHORS

LOBANOV Andrey A.
Peter the Great St. Petersburg Polytechnic University
29 Politechnicheskaya St., St. Petersburg, 195251, Russia
lobanov2.aa@edu.spbstu.ru
ORCID: 0000-0002-8910-4775

BERDNIKOV Yaroslav A.
Peter the Great St. Petersburg Polytechnic University
29 Politechnicheskaya St., St. Petersburg, 195251, Russia
berdnikov@spbstu.ru
ORCID: 0000-0003-0309-5917

СВЕДЕНИЯ ОБ АВТОРАХ

ЛОБАНОВ Андрей Александрович — *студент Физико-механического института Санкт-Петербургского политехнического университета Петра Великого.*
195251, Россия, г. Санкт-Петербург, Политехническая ул., 29
lobanov2.aa@edu.spbstu.ru
ORCID: 0000-0002-8910-4775

БЕРДНИКОВ Ярослав Александрович — *доктор физико-математических наук, профессор Высшей школы фундаментальных физических исследований Санкт-Петербургского политехнического университета Петра Великого.*
195251, Россия, г. Санкт-Петербург, Политехническая ул., 29
berdnikov@spbstu.ru
ORCID: 0000-0003-0309-5917

A COMPARATIVE ANALYSIS OF HADRON CREATION IN DEUTERON-DEUTERON INTERACTIONS AT ENERGIES OF 13.5 AND 27.0 GEV

D. S. Shapaev✉, Ya. A. Berdnikov

Peter the Great St. Petersburg Polytechnic University, St. Petersburg, Russia

✉ dima.shapaev@yandex.ru

Abstract. This paper presents the results of nuclear modification factors for hadrons in deuteron-deuteron collisions at energies of $\sqrt{s_{NN}} = 13.5$ GeV and $\sqrt{s_{NN}} = 27.0$ GeV. We have applied the widely-used nuclear-modified parton distribution functions and parton distribution functions for free nucleons to determine nuclear modification factors (NMFs) of J/ψ, $D^{\pm}$ and π^0 mesons. The obtained results showed the NMFs values of J/ψ and π^0 ones to remain close to unity over the entire transverse momentum range from 0.5 to 4.5 GeV/c. The NMFs values of $D^{\pm}$ ones decreased sharply with increasing the transverse momentum at $\sqrt{s_{NN}} = 13.5$ GeV, but they remained close to unity at $\sqrt{s_{NN}} = 27.0$ GeV.

Keywords: nuclear modification factor, SPD, NICA, parton distribution function, hadron

СРАВНИТЕЛЬНЫЙ АНАЛИЗ ОСОБЕННОСТЕЙ РОЖДЕНИЯ АДРОНОВ В ДЕЙТРОН-ДЕЙТРОННЫХ ВЗАИМОДЕЙСТВИЯХ ПРИ ЭНЕРГИЯХ 13,5 И 27,0 ГЭВ

Д. С. Шапаев✉, Я. А. Бердников

Санкт-Петербургский политехнический университет Петра Великого, Санкт-Петербург, Россия

✉ dima.shapaev@yandex.ru

Аннотация. В статье представлены результаты исследования факторов ядерной модификации адронов в столкновениях ядер дейтерия при значениях энергии $\sqrt{s_{NN}} = 13,5$ ГэВ и $\sqrt{s_{NN}} = 27,0$ ГэВ. Проведено сравнение полученных факторов ядерной модификации (J/ψ)-, $D^{\pm}$- и π^0-мезонов с использованием функций партонного распределения свободных нуклонов и ядерно-модифицированных функций партонного распределения. Полученные результаты показали, что факторы ядерной модификации (J/ψ)- и π^0-мезонов остаются близкими к единице на всем исследуемом диапазоне 0,5−4,5 ГэВ/c поперечного импульса. Значения факторов ядерной модификации $D^{\pm}$-мезонов резко снижаются при увеличении поперечного импульса при энергии $\sqrt{s_{NN}} = 13,5$ ГэВ, тогда как при энергии $\sqrt{s_{NN}} = 27,0$ ГэВ значения остаются близкими к единице.

Introduction

Measurement of production of $D^{\pm}$, (J/ψ), π^0 mesons in proton-proton $(p+p)$ interactions at $\sqrt{s_{pp}} = 27.0$ GeV and deuteron-deuteron $(d+d)$ interactions at energy $\sqrt{s_{NN}} = 13.5$ GeV/nucleon [1] is one of the intended goals in the planned SPD experiment [2] at the NICA collider [3].

The main mechanism behind the production of $D^{\pm}$ and (J/ψ) mesons at the given energies is the fusion of a gluon pair (gg), leading to the production of a quark-antiquark pair $(c\bar{c})$ [4].

As follows from Fig. 1,*a*, a quark-antiquark pair $(c\bar{c})$ can produce a (J/ψ) meson during hadronization. The scheme for production of $D^{\pm}$ mesons is shown in Fig. 1,*b*: $c\bar{d} \to D^+$, $\bar{c}d \to D^-$.

The (J/ψ) mesons can be detected through weak muon decay modes within the framework of the SPD project [4]:

$$J/\psi \to \mu^+\mu^-.$$

$D^{\pm}$ mesons are to be detected in the following decay channels [4]:

$$D^+ \to \pi^+ K^- \pi^+ \, (\text{BF} = 0.094),$$

$$D^- \to \pi^- K^+ \pi^- \, (\text{BF} = 0.094).$$

Thus, study of the processes associated with the production of $D^{\pm}$ and (J/ψ) mesons yields information about the properties and role of gluons in proton-proton and deuteron-deuteron interactions (as well as in the nucleon-nucleon interactions). In particular, information about gluon distribution functions in nucleons and nuclei can be extracted.
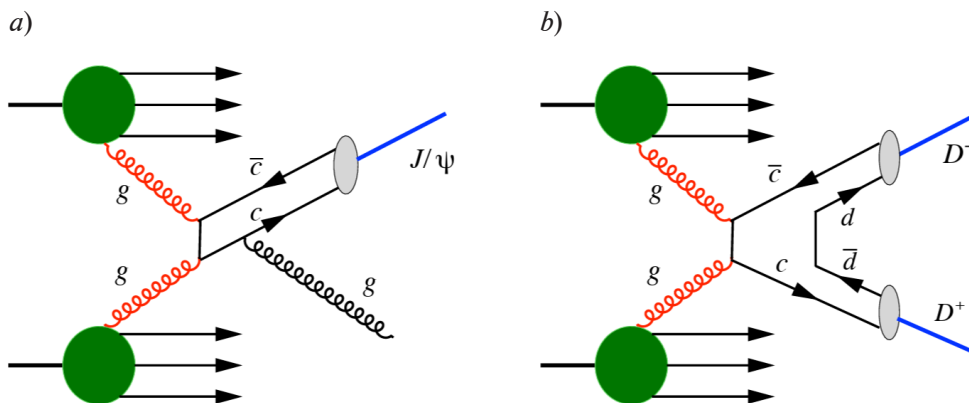
Fig. 1 [4]. Feynman diagrams for production of (J/ψ) meson (*a*) and $D^{\pm}$ mesons (*b*)
Production occurs through fusion of a gluon pair (gg),
leading to the production of a quark-antiquark pair $(c\bar{c})$

Measurements of the yields of neutral pions consisting of $u\bar{u}$ and $d\bar{d}$ quarks can help verify and refine the existing models describing the production of these particles. Comparing the yields of neutral pions with heavier particles, such as $D^{\pm}$ and J/ψ mesons can provide insights into the role of heavy quarks in high-energy collisions of nucleons and nuclei.

Parton distribution functions (PDFs) are commonly used in studies of hadron production. The PDF $f_i(x, Q^2)$ is used to describe the probability of finding the ith parton in the hadron; x is the parton parameter determining the fraction of the nucleon momentum carried by the parton; Q^2 is a quantity following the expression

$$Q^2 = -q^2,$$

where q^2 is the four-momentum of the virtual particle [5].

The range of large x is of particular interest, as there is a significant discrepancy between the theoretical predictions for the gluon distribution function in the deuteron and the gluon distribution function in the nucleon [4].

Nuclear-modified parton distribution functions (nPDFs) were obtained to analyze the nucleon-nucleus and nucleus-nucleus collisions [6]. The fundamental difference between these functions and PDFs taken for free nucleons is that they take into account the nucleonic composition of nuclei and interactions between nucleons in the nucleus.

According to the factorization theorem [7], the differential cross section for the production of the hadron H can be represented as follows in the collinear approximation:

$$E_H \frac{d^3\sigma}{dp_H^3} = \sum_{a,b,c} f_a \otimes f_b \otimes d\hat{\sigma}_{ab}^c \otimes D_c^H,$$

where f_a, f_b are the PDFs; $d\hat{\sigma}_{ab}^c$ is the cross section of the hard parton subprocess; a, b, c are the interacting partons; D_c^H is the fragmentation function.

Different PDFs influence the cross section for hadron production, provided that the same fragmentation functions are applied to each particle.

The goal of this study is to determine the characteristics of the production of hadrons in collisions of deuterium nuclei ($d+d$).

The nPDFs (with nuclear modifications) and PDFs (for free nucleons) were used to simulate ($d+d$) collisions.

Computational procedure

Hadron yields in ($d+d$) collisions at $\sqrt{s_{NN}}$ = 13.5 and 27.0 GeV were analyzed in this paper based on the simulation data we obtained using the Pythia8 software package [8].

The simulations were run using two types of functions:

parton distribution functions obtained for free nucleons (PDFs);

nuclear-modified (in this case in the deuteron) parton distribution functions (nPDFs).

Because the collision energy of deuteron beams is much higher than the binding energy of nucleons in the deuteron (2.23 MeV), a model of unbound (free) nucleons can be used for the deuteron, using PDFs for free nucleons within the parton model. Collisions of deuteron beams can be represented via PDFs as collision of each nucleon of one deuteron nucleus with each nucleon of another deuteron nucleus. There are four possible combinations of nucleon-nucleon collisions: pp, pn, np, nn. Since the total cross sections of these interactions are approximately similar [9], these interactions can be reasonable assumed to be equally probable without significant loss of accuracy.

It was found in our previous paper [10] that different combinations of interacting nucleons making up the deuterium nucleus produce different numbers of direct photons. However, this dependence should not be observed during the formation of (J/ψ) and $D^{\pm}$ mesons, since the probabilities of their formation do not depend on the electric charge of the quark. The cross section for the production of the quark-antiquark pair due to gluon-gluon interaction is proportional to the square of the strong interaction constant [4].

An alternative approach to the study of deuteron beam collisions are nPDFs obtained for deuterons [11−13]. A variety of functions is used because they originate from different experimental

data, which may cause discrepancies in the results obtained. For this reason, we selected three different nPDFs to ensure the reliability and comparability of the data.

Since the Pythia8 program allows using only one PDF in the calculations, we used the weight w to speed up the calculation of all the nPDFs we selected (the formula for calculating it is given in [14]):

$$w = \frac{x_1 f_i^{p/d}(x_1;Q^2)}{x_1 f_i^{p}(x_1;Q^2)} \cdot \frac{x_2 f_i^{p/d}(x_2;Q^2)}{x_2 f_i^{p}(x_2;Q^2)}, \qquad (1)$$

where $x_1 f_i^{p/d}(x_1,Q^2)$, $x_2 f_i^{p/d}(x_2,Q^2)$ are the nPDFs for deuterons in the first and second nuclei; $x_1 f_i^{d}(x_1,Q^2)$, $x_2 f_i^{p}(x_2,Q^2)$ are the PDFs obtained for free protons in the first and second nuclei.

This weight w characterizes the ratio of the probabilities of detecting the parton for two different PDFs with the same values of variables x and Q^2. Thus, using a weight in the calculations makes it possible to obtain hadron spectra for both PDFs and nPDFs within a single simulation run.

Due to the low probability that (J/ψ) and $D^{\pm}$ mesons are produced in $(d+d)$ collisions, we used custom settings in Pythia8 to increase the production statistics of (J/ψ) and $D^{\pm}$ mesons (see the Appendix). Importantly, the proposed modifications do not have any effect on the physical interpretation of the results obtained.

The PDFs are taken from the LHAPDF6 software package [14] connected directly to the Pythia8 collision generator. Computer analysis included application of the following PDFs (the numbers are highlighted in bold, see also the captions to the figures).

For PDFs: nNNPDF30_nlo_as_0118_p [11] **(FI),** TUJU21_nlo_1_1 [12] **(FII)**, nCTEQ15HIX_FullNuc_1_1 [13] **(FIII)**;

for nPDFs: nNNPDF30_nlo_as_0118_A2_Z1 [11] **(FIV),** TUJU21_nlo_2_1 [12] **(FV),** nCTEQ15HIX_FullNuc_2_1 [13] **(FVI).**

The nuclear modification factor (NMF) R_{dd} was used to quantify the differences in the hadron spectra obtained from $(d+d)$ collisions using nPDFs and PDFs.

The value of R_{dd} can be calculated by the following relation [15]:

$$R_{dd} = \frac{1}{N_{coll}} \cdot \frac{d^2 N_{dd}/dp_T dy}{d^2 N_{pp}/dp_T dy}, \qquad (2)$$

The numerator of Eq. (2) contains the invariant spectrum of hadrons obtained in collisions of deuterium nuclei in the ranges of rapidity dy and transverse momentum dp_T. This spectrum is normalized by the number of binary nucleon-nucleon collisions N_{coll} (for $d+d$). The denominator in Eq. (2) contains the invariant spectrum of hadrons measured in $(p+p)$ interactions for the same ranges of rapidity and transverse momentum.

The rapidity range ($|y| < 3$) in this paper is taken from [16].

Results and discussion

Fig. 2 shows the values of R_{dd} for hadrons as a function of transverse momentum p_T at $\sqrt{s_{NN}} = 13.5$ GeV and $\sqrt{s_{NN}} = 27.0$ GeV in the rapidity range $|y| < 3$ using different PDFs (see functions FI−FIII).

Fig. 3 shows the values of R_{dd} for hadrons as a function of transverse momentum p_T at $\sqrt{s_{NN}} = 13.5$ GeV and $\sqrt{s_{NN}} = 27.0$ GeV in the rapidity range $|y| < 3$ using different nPDFs (see functions FIV−FVI).

It can be seen from Fig. 2 and Fig. 3 that the NMFs for $D^{\pm}$, (J/ψ) and π^0 mesons, calculated using nPDFs and PDFs, have similar values over the entire p_T range under consideration. Nevertheless, small differences in the values of R_{dd} obtained by the functions FII and FV may indicate the presence of nuclear phenomena influencing the particle production process.

The results for NMFs R_{dd} obtained using the remaining functions (FI, FIII, FIV, FVI) do not exceed unity, which predicts the absence of possible nuclear phenomena during the production of (J/ψ) and π^0 mesons in deuteron-deuteron collisions.
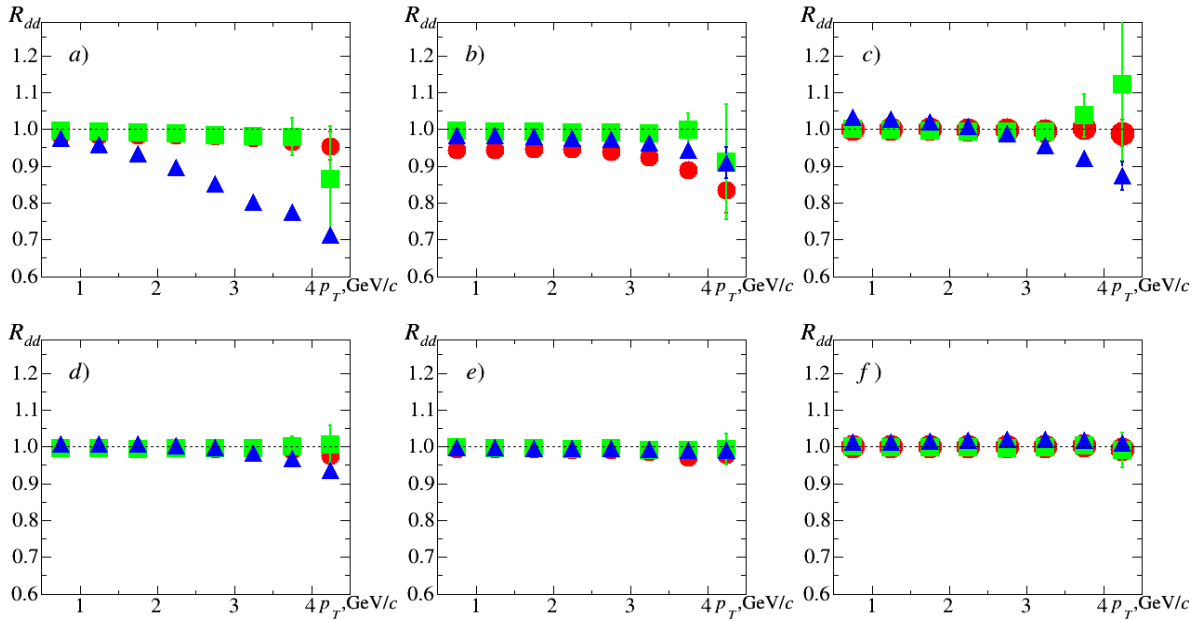
Fig. 2. Dependences of NMFs for mesons J/ψ ($\bullet$), $D^\pm$ ($\blacktriangle$), π^0 ($\blacksquare$) on transverse momentum
(see Eq. (2)) in $(d+d)$ collisions at $\sqrt{s_{NN}} = 13.5$ GeV ($a-c$) and $\sqrt{s_{NN}} = 27.0$ GeV ($d-f$),
in the rapidity range $|y| < 3$, using different PDFs: FI(a, d); FII(b, e); FIII(c, f);
numbering of the functions is given in the text
The vertical bars correspond to statistical uncertainties
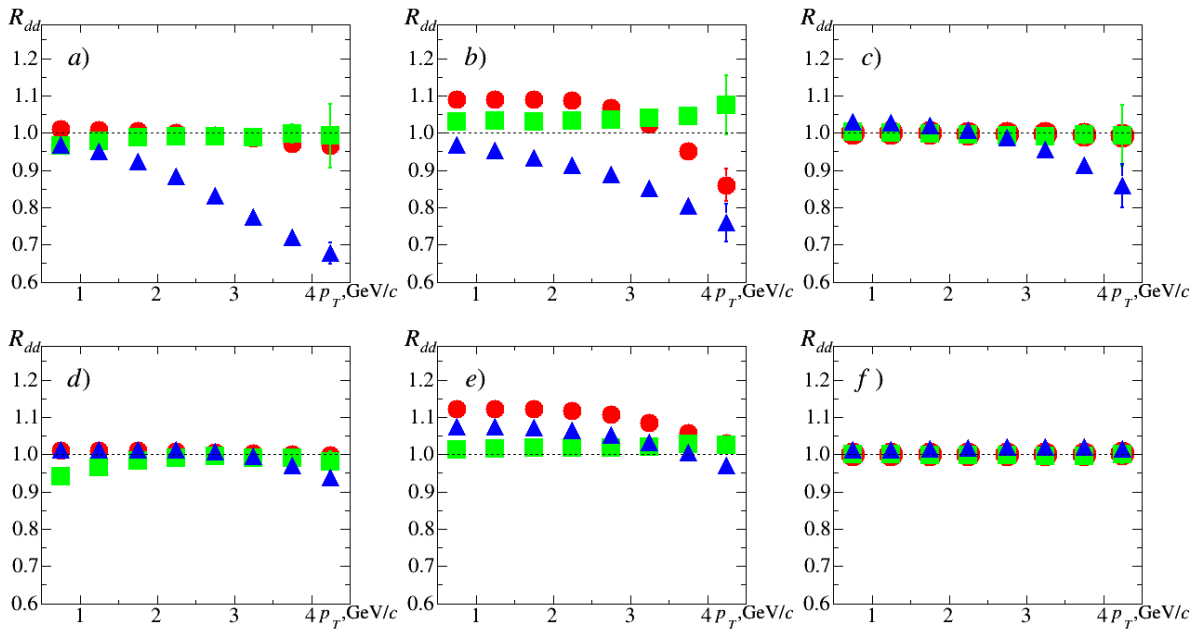
Fig. 3. Dependences similar to those in Fig. 2, at $\sqrt{s_{NN}} = 13.5$ GeV ($a-c$)
and $\sqrt{s_{NN}} = 27.0$ GeV ($d-f$), for the remaining nPDFs: FIV (a, d); FV(b, e); FVI (c, f)

We should also note that the values of R_{dd} for $D^\pm$ mesons decrease with increasing p_T at $\sqrt{s_{NN}} = 13.5$ GeV, in contrast to collisions at $\sqrt{s_{NN}} = 27.0$ GeV, where the values of R_{dd} remain close to unity. The reason for this behavior of the dependences requires additional research.

Conclusion

We calculated the nuclear modification factors of $D^{\pm}$, (J/ψ) and π^0 mesons in $(d+d)$ interactions at $\sqrt{s_{NN}} = 13.5$ and $\sqrt{s_{NN}} = 27.0$ GeV energies depending on the transverse momentum p_T in the rapidity range $|y| < 3$ s using PDFs (FI−FIII) and nPDFs (FIV−FVI).

Applying the weight (see Eq. (1)) for hadron spectra allowed to speed up the computations.

We established that using either PDFs or nPDFs yields very slight differences in the values of R_{dd} for hadrons.

We found that the ratios of the invariant spectra for (J/ψ) and π^0 mesons in $(d+d)$ and $(p+p)$ collisions differ insignificantly at the studied energies for all selected sets of PDFs and nPDFs. The invariant spectra of $D^{\pm}$ mesons in $(d+d)$ interactions at $\sqrt{s_{NN}} = 13.5$ GeV are decreased compared to the invariant spectra in $(p+p)$ interactions with an increase in the transverse momentum p_T.

Appendix

Parameter settings of the Monte Carlo event generator in Pythia8 for increasing meson production

Parameter	Position	Parameter	Position
For (J/ψ) mesons		*For $D^{\pm}$ mesons*	
Charmonium:all	on	HardQCD:gg2ccbar	on
PhaseSpace:pTHatMin	0.1	HardQCD:qqbar2ccbar	on
PhaseSpace:pTHatMax	10.0	PhaseSpace:mHatMin	0.0
PhaseSpace:pTHatMinDiverge	0.5	PhaseSpace:pTHatMinDiverge	0.5
BeamRemnants:primordialKT	on	BeamRemnants:primordialKT	on
BeamRemnants:primordialKTsoft	0.9	BeamRemnants:primordialKTsoft	1.1
BeamRemnants:primordialKThard	1.8	BeamRemnants:primordialKThard	1.8
BeamRemnants:halfScaleForKT	2.0	BeamRemnants:halfScaleForKT	2.0
BeamRemnants:halfMassForKT	4.0	BeamRemnants:halfMassForKT	4.0
BeamRemnants:reducedKTatHighY	0.5	BeamRemnants:reducedKTatHighY	0.7
BeamRemnants:primordialKTremnant	0.4	BeamRemnants:primordialKTremnant	0.4
443:onMode	off		
443:onIfAll	13–13		

REFERENCES

1. **Savin I., Efremov A., Peshekhonov D., et al.,** Spin physics experiments at NICA-SPD with polarized proton and deuteron beams, EPJ Web Conf. 85 (23 Jan) (2015) 02039.

2. **Ladygin V. P.,** Spin physics detector at NICA, JPS Conf. Proc., Proc. 24th Int. Spin Symp. (SPIN-2021), 37 (2022) 011012.

3. **Trubnikov G., Butenko A., Golovatyuk V., et al.,** NICA heavy-ion collider at JINR (Dubna). Status of accelerator complex and first physics at NICA, J. Phys.: Conf. Ser. 2586 (1) (2023) 012013.

4. **Arbuzov A., Bacchetta A., Butenschoen M., et al.** (SPD Collaboration), On the physics potential to study the gluon content of proton and deuteron at NICA SPD, Prog. Part. Nucl. Phys. 119 (July) (2021) 103858.

5. **Ethier J. J., Nocera E. R.,** Parton distributions in nucleons and nuclei, Annu. Rev. Nucl. Part. Sci. 70 (1) (2020) 43−76.

6. **Eskola K. J.,** Global analysis of nuclear PDFs − latest developments, Nucl. Phys. A. 910−911 (Aug) (2013) 163−170.

7. **De Florian D., Sassot R., Stratmann M.,** Global analysis of fragmentation functions for pions and kaons and their uncertainties, Phys. Rev. D. 75 (11) (2007) 114010.

8. **Bierlich C., Chakraborty S., Desai N., et al.,** A comprehensive guide to the physics and usage of PYTHIA 8.3, SciPost Phys. (2022). Advance online publication. https://inspirehep.net/literature/2056998.

9. **Murthy P. V. R., Ayre C. A., Gustafson H. R., et al.,** Neutron total cross sections on nuclei at Fermilab energies, Nucl. Phys. B. 92 (3) (1975) 269−308.

10. **Shapaev D. S., Berdnikov Ya. A.,** The creation of direct photons during interactions of deuterium nuclei at energies of 13.5 GeV and 27.0 GeV, St. Petersburg State Polytechnical University Journal. Physics and Mathematics. 17 (4) (2024) 138−146 (in Russian).

11. **Khalek R. A., Gauld R., Giani T., et al.,** nNNPDF3.0: evidence for a modified partonic structure in heavy nuclei, Eur. Phys. J. C. 82 (6) (2022) 507.

12. **Helenius I., Walt M., Vogelsang W.,** NNLO nuclear parton distribution functions with electroweak-boson production data from the LHC, Phys. Rev. D. 105 (9) (2022) 094031.

13. **Segarra E. P., Ježo T., Accardi A., et al.,** Extending nuclear PDF analyses into the high-x, low-Q^2 region, Phys. Rev. D. 103 (11) (2021) 114015.

14. **Buckley A., Ferrando J., Lloyd S., et al.,** LHAPDF6: parton density access in the LHC precision era, Eur. Phys. J. C. 75 (3) (2015) 132.

15. **Rezaeian A. H., Schaefer A.,** Hadrons and direct photon production in *pp* and *pA* collisions at the LHC and saturation effects, Phys. Rev. D. 81 (11) (2010) 114032.

16. **Saleev V. A., Shipilova A. V.,** Double longitudinal-spin asymmetries in direct photon production at NICA, Phys. Part. Nuclei. Lett. 20 (3) (2023) 400−403.

СПИСОК ЛИТЕРАТУРЫ

1. **Savin I., Efremov A., Peshekhonov D., Kovalenko A., Teryaev O., Shevchenko O., Nagajcev A., Guskov A., Kukhtinand V., Toplilin N.** Spin physics experiments at NICA-SPD with polarized proton and deuteron beams // EPJ Web of Conferences. 2015. Vol. 85. 23 January. P. 02039.

2. **Ladygin V. P.** Spin physics detector at NICA // JPS Conference Proceedings. Proceedings of the 24th International Spin Symposium (SPIN-2021). 2022. Vol. 37. P. 011012.

3. **Trubnikov G., Butenko A., Golovatyuk V., Guskov A., Kapishin M., Kekelidze V., Lednicky R., Meshkov I., Sorin A.** NICA heavy-ion collider at JINR (Dubna). Status of accelerator complex and first physics at NICA // Journal of Physics: Conference Series. 2023. Vol. 2586. No. 1. P. 012013.

4. **Arbuzov A., Bacchetta A., Butenschoen M., et al.** (SPD Collaboration). On the physics potential to study the gluon content of proton and deuteron at NICA SPD // Progress in Particle and Nuclear Physics. 2021. Vol. 119. July. P. 103858.

5. **Ethier J. J., Nocera E. R.** Parton distributions in nucleons and nuclei // Annual Review of Nuclear and Particle Science. 2020. Vol. 70. No. 1. Pp. 43−76.

6. **Eskola K. J.** Global analysis of nuclear PDFs − latest developments // Nuclear Physics A. 2013. Vol. 910−911. August. Pp. 163−170.

7. **De Florian D., Sassot R., Stratmann M.** Global analysis of fragmentation functions for pions and kaons and their uncertainties // Physical Review D. 2007. Vol. 75. No. 11. P. 114010.

8. **Bierlich C., Chakraborty S., Desai N., et al.** A comprehensive guide to the physics and usage of PYTHIA 8.3 // SciPost Physics. 2022. Advance online publication. https://inspirehep.net/literature/2056998.

9. **Murthy P. V. R., Ayre C. A., Gustafson H. R., Jones L. W., Longo M. J.** Neutron total cross sections on nuclei at Fermilab energies // Nuclear Physics B. 1975. Vol. 92. No. 3. Pp. 269−308.

10. **Шапаев Д. С., Бердников Я. А.** Рождение прямых фотонов во взаимодействиях ядер дейтерия при энергиях 13,5 и 27,0 ГэВ // Научно-технические ведомости СПбГПУ. Физико-математические науки. 2025. Т. 17. № 4. С. 138−146.

11. **Khalek R. A., Gauld R., Giani T., Nocera E. R., Rabemananjara T. R., Rojo J.** nNNPDF3.0: evidence for a modified partonic structure in heavy nuclei // European Physics Journal C. 2022. Vol. 82. No. 6. P. 507.

12. **Helenius I., Walt M., Vogelsang W.** NNLO nuclear parton distribution functions with electroweak-boson production data from the LHC // Physical Review D. 2022. Vol. 105. No. 9. P. 094031.

13. **Segarra E. P., Ježo T., Accardi A., et al.** Extending nuclear PDF analyses into the high-x, low-Q^2 region // Physical Review D. 2021. Vol. 103. No. 11. P. 114015.

14. **Buckley A., Ferrando J., Lloyd S., Nordstrцm K., Page B., Rьfenacht M., Schцnherr M., Watt G.** LHAPDF6: parton density access in the LHC precision era // European Physics Journal C. 2015. Vol. 75. No. 3. P. 132.

15. **Rezaeian A. H., Schaefer A.** Hadrons and direct photon production in pp and pA collisions at the LHC and saturation effects // Physical Review D. 2010. Vol. 81. No. 11. P. 114032.

16. **Салеев В. А., Шипилова А. В.** Двойные продольные спиновые асимметрии в прямом рождении фотонов на коллайдере NICA // Письма в журнал «Физика элементарных частиц и атомного ядра». 2023. Т. 20. № 3 (248). С. 417−421.

THE AUTHORS

SHAPAEV Dmitry S.
Peter the Great St. Petersburg Polytechnic University
29 Politechnicheskaya St., St. Petersburg, 195251, Russia
dima.shapaev@yandex.ru
ORCID: 0009-0006-8542-4401

BERDNIKOV Yaroslav A.
Peter the Great St. Petersburg Polytechnic University
29 Politechnicheskaya St., St. Petersburg, 195251, Russia
berdnikov@spbstu.ru
ORCID: 0000-0003-0309-5917

СВЕДЕНИЯ ОБ АВТОРАХ

ШАПАЕВ Дмитрий Сергеевич — *студент Физико-механического института Санкт-Петербургского политехнического университета Петра Великого.*
195251, Россия, г. Санкт-Петербург, Политехническая ул., 29
dima.shapaev@yandex.ru
ORCID: 0009-0006-8542-4401

БЕРДНИКОВ Ярослав Александрович — *доктор физико-математических наук, профессор Высшей школы фундаментальных физических исследований Санкт-Петербургского политехнического университета Петра Великого.*
195251, Россия, г. Санкт-Петербург, Политехническая ул., 29
berdnikov@spbstu.ru
ORCID: 0000-0003-0309-5917

Theoretical physics

INTEGRALS OF MOTION OF A RELATIVISTIC PARTICLE IN 1 + 1 DIMENSIONS WITH COUPLED PARAMETERS

N. S. Akintsov [1], A. P. Nevecheria [2] ✉, V. Yu. Kozhevnikov [3], G. F. Kopytov [4], T. Cao [5]

[1] Nantong University, Nantong, People's Republic of China;

[2] Kuban State University, Krasnodar, Russia;

[3] Institute of High Current Electronics, Siberian Branch, RAS (IHCE SB RAS), Tomsk, Russia;

[4] Moscow State University of Technology and Management, Moscow, Russia;

[5] Dalian University of Technology, Dalian, People's Republic of China

✉ artiom1989@mail.ru

Abstract. The eigenfunctions and eigenvalues of the integrals of motion γ and θ have been studied. An invariant form of motion was obtained for the derivatives of γ and θ, with respect to the proper time and velocity of a relativistic particle (RP). The integrals γ and θ were shown to be mutually expressible. Inverse values $1/E$ and $1/P$ were introduced for the energy and momentum of a free RP. A one-to-one correspondence of the RP energy and momentum was obtained. The properties of the γ integral expressed in terms of $1/E$ and $1/P$ were determined as a functional dependence $\gamma = \gamma(1/E, 1/P)$. Forms of the motion equations depending on the γ and θ integrals were obtained using Lagrangian and Hamiltonian formalism. Based on the latter, a generalized integral of motion describing all types of motions in 1+1 dimensions was derived. Mutually expressive differential forms of RP motion were introduced.

Keywords: integral of motion, special relativity, Lagrangian and Hamiltonian formalisms

ИНТЕГРАЛЫ ДВИЖЕНИЯ РЕЛЯТИВИСТСКОЙ ЧАСТИЦЫ В ИЗМЕРЕНИЯХ 1 + 1 СО СВЯЗАННЫМИ ПАРАМЕТРАМИ

Н. С. Акинцов [1], **А. П. Невечеря** [2] ✉, **В. Ю. Кожевников** [3],
Г. Ф. Копытов [4], **Т. Цо** [5]

[1] Наньтунский университет, г. Наньтун, Китайская Народная Республика;

[2] Кубанский государственный университет, г. Краснодар, Россия;

[3] Институт сильноточной электроники Сибирского отделения РАН, г. Томск, Россия;

[4] Московский государственный университет технологий и управления
имени К. Г. Разумовского, Москва, Россия;

[5] Даляньский технологический университет, г. Далянь, Китайская Народная Республика

✉ artiom1989@mail.ru

Аннотация. В работе исследованы собственные функции и собственные значения от интегралов движения γ и быстроты θ. Для производных от γ и θ получена форма движения относительно собственного времени и скорости частицы. Показано, что интегралы движения являются взаимно-выражаемыми. Введены обратные значения для энергии $E_g = 1/E$ и импульса $P_g = 1/P$ свободной релятивистской частицы. Найдены свойства интеграла движения γ, который выражается через обратный импульс P_g и обратную энергию E_g как функциональная зависимость $\gamma = \gamma(E_g, P_g)$. С использованием формализма Лагранжа и Гамильтона получены уравнения движения $L' = L'(q, Q)$ и $H' = H'(\theta)$. На основе Гамильтонова формализма выведен обобщенный интеграл движения $\gamma = \gamma(\theta)$. Введены взаимно-выражающиеся дифференциальные формы движения релятивистской частицы.

Ключевые слова: интеграл движения, специальная теория относительности, Лагранжев и Гамильтонов формализмы

Introduction

The classical integral of motion of a relativistic particle γ_0 has the invariant form

$$\gamma_0 = \frac{mc(1-f\mathbf{n}\boldsymbol{\beta})}{\sqrt{1-\beta^2}} = mc\exp(-f\theta), \; \mathbf{n}\boldsymbol{\beta} = \frac{\mathbf{n}\mathbf{V}}{c} = \tanh\theta, \; \gamma = \frac{\gamma_0}{mc} = \exp(-f\theta), \tag{1}$$

where $\mathbf{V}$ is the particle velocity, c is the light speed, m is the particle mass, $f = \pm 1$.

For analytical and numerical calculations in Refs. [1 − 8], the integral of motion is understood as a constant (γ = const), however, this case is satisfied only for a constant particle velocity ($\boldsymbol{\beta}$ = const). Ignoring the nonlinear functional dependence $\gamma = \gamma(\mathbf{r}, t)$, for finding the trajectory of a charged particle $\mathbf{R}(\mathbf{r}, t)$ in the field of an electromagnetic wave

$$\mathbf{R}(\mathbf{r},t) = \int \frac{\mathbf{p_E}}{\gamma}dt + \boldsymbol{\chi} = \int \frac{q\mathbf{E}(\mathbf{r},t)}{\omega\gamma}dt + \boldsymbol{\chi}, \tag{2}$$

where $\mathbf{p}_E$ is the momentum of particle oscillation in the field of an electromagnetic wave, $\mathbf{p}_E = q\mathbf{E}(\mathbf{r}, t)/\omega$; $\mathbf{E}(\mathbf{r}, t)$ is the electric field strength of the wave; q is the particle charge; ω is the particle oscillation frequency; $\boldsymbol{\chi}$ is a certain constant that determines the initial phase of the wave; $\mathbf{r}$ is the particle position at time t.

In many papers (see, for example, Refs. [1 − 8]), as a rule, integration is performed over the space-time coordinate $\xi = t - \mathbf{n}\mathbf{r}/c$ and supposing that γ = const. In this case, there are no relativistic effects of particle acceleration.

The angular integral of motion θ is defined from Hamiltonian mechanics

$$\frac{\partial H'}{\partial \theta} = \sqrt{Q_\xi^+ Q_\xi^- - 1} = P = \mathbf{n}\mathbf{P}, \tag{3}$$

where $H' = H/(mc^2) = \sqrt{Q_\xi^+ Q_\xi^-}$ is the Hamiltonian of a freely moving particle,

$Q_\xi^+ = \dfrac{1}{1-\mathbf{n}\boldsymbol{\beta}}, Q_\xi^- = \dfrac{1}{1+\mathbf{n}\boldsymbol{\beta}}$, $\mathbf{n}$ is the normal vector, and $H'(\beta = 0) = 1$ [9, 10].

As is known, the integral angle or the so-called angular integral of motion is expressed from Eq. (3) and has the following form:

$$\theta = \cosh^{-1}\left(\sqrt{Q_\xi^+ Q_\xi^-}\right), \tag{4}$$

where $E = \sqrt{Q_\xi^+ Q_\xi^-}$ is the dimensionless particle energy, $E \geq 0$.

From Eqs. (3) and (4) it can be seen that the energy and momentum of the system take the following values:

$$E = \sqrt{Q_\xi^+ Q_\xi^-} = \cosh\theta, \; \mathbf{n}\mathbf{P} = \sqrt{Q_\xi^+ Q_\xi^- - 1} = \sinh\theta, \tag{5}$$

which express the laws of conservation of energy and momentum for the particle

$$E^2 = P^2 + 1, \tag{6}$$

where

$$E = \varepsilon/mc^2 = \sqrt{Q_\xi^+ Q_\xi^-} = \frac{1}{\sqrt{1-\beta^2}}, \mathbf{P} = \mathbf{p}/mc = \mathbf{n}\sqrt{Q_\xi^+ Q_\xi^- - 1}. \tag{7}$$

From Eqs. (4) − (7) and Ref. [10], for θ, $\mathbf{r}$, t, and γ, we have the following functional relationship:

$$\theta = \theta(\mathbf{r}, t, \gamma). \tag{8}$$

Using the functional dependence (8), it is easy to show that the trajectory of the relativistic particle (see Eq. (3)) can be represented as a function of the integral angle θ:

$$\mathbf{R}(\theta) = \int \frac{\mathbf{p_E}(\theta)}{\gamma(\theta)}d\theta + \boldsymbol{\chi} = \int \frac{q\mathbf{E}(\theta)}{\omega\gamma(\theta)}d\theta + \boldsymbol{\chi}. \tag{9}$$

From Eq. (8) we also have a mutually functional dependence with the space-time coordinate $\xi = \xi(\theta)$.

It is of interest to study in this paper the mutually functional dependence of the laws of conservation of energy and momentum of a particle in a mutually invariant form depending on $\theta = \theta(\gamma)$ and $\gamma = \gamma(\theta)$, that is

$$E^2 = P^2 + 2\gamma E - \gamma^2, \tag{10}$$

where $\gamma^{-1} = 2E - \gamma$.

From the rapid development of such areas as the double special theory of relativity and grav-itomagnetism [11 − 16], it follows that it is necessary to introduce differential forms, which in the future will help to give a more extensive answer to such a question as: "Do we observe the violation of the Lorentz invariant form in gamma-ray bursts?"

The purpose of this work is to search for new forms of the of motion and to study the mutual functional relationship between integrals. Based on the Hamiltonian and Lagrange formalisms, successively derive generalized formulas that are applicable to the motion of a particle in any con-figuration of electromagnetic fields. Thus, in Refs. [17 − 19], the effectiveness of using Lorentz coordinates in terms of rapidity has been demonstrated $\xi = \xi(\theta)$. In Ref. [20], Lorentz coordi-nates with associated parameters were applied to describe the dynamics of a charged particle in the field of a plane wave and in the field of a one-dimensional Gaussian laser beam.

The method of coupled parameters was first introduced in relativistic hydrodynamics [21], where these parameters were defined as physical quantities of a hydrodynamic system, such as pressure, volume, and entropy, depending on a single parameter, such as temperature. In the special theory of relativity, the method of coupled parameters has been applied in Refs. [10, 17 − 20] based on eigenfunctions and eigenvalues, where it has been demonstrated that the chosen parameters being related to the invariance of the obtained results across different reference frames.

In this work, we will also show that the use of integrals of motion with coupled parameters and their eigenvalues can describe the dynamics of a particle more efficiently than its presentation in the orthogonal form [22]. Further, based on the task, on the eigenfunctions and eigenvalues, we will find the eigenvalues of the integrals of motion γ and θ from the operators of differentiation

with respect to time $\hat{t} = \dfrac{d}{dt}$, velocity $\hat{\beta} = \dfrac{d}{d\beta}$ and angular displacement $\hat{\theta} = \dfrac{d}{d\theta}$.

This work presents an approach that allows transitioning from certain eigenfunctions in the special theory of relativity with associated parameters to eigenvalues in various representations of the integrals of motion, which facilitate working with these eigenvalues.

A problem for eigenfunctions and eigenvalues from γ

We introduce the direct integral of motion from $\xi = t - \mathbf{nr}/c$ as a derivative with respect to time t:

$$\frac{d\xi}{dt} = Q_t = 1 - f\mathbf{n\beta}, \tag{11}$$

where

$$Q_t^+ = 1 - \mathbf{n\beta}, \; Q_t^- = 1 + \mathbf{n\beta}, \tag{12}$$

conjugate expressions.

The relationship between Q_t^+, Q_t^- and Q_t is expressed by the following relationships:

$$Q_t^+ = 1 - f(1 - Q_t), Q_t^- = 1 + f(1 - Q_t), Q_t^+ + Q_t^- = 2. \tag{13}$$

Using Eqs. (7), (11), and (12), we represent the integral of motion (1) in the following form:

$$\gamma = \frac{Q_t}{\sqrt{Q_t^+ Q_t^-}} = Q_t \sqrt{Q_\xi^+ Q_\xi^-} = Q_t E. \tag{14}$$

Eigenfunctions and eigenvalues from the integral of motion γ (14) are obtained by differenti-ating with respect to time t, that is,

$$\frac{d\gamma}{dt} = \frac{dQ_t}{dt}E + Q_t\frac{dE}{dt}, \tag{15}$$

where

$$\frac{dQ_t}{dt} = -f\left(1-Q_t\right)^2 = -f\left(1-Q_t^+Q_t^-\right) \tag{16}$$

is the function from Ref. [10].

The expression $\frac{dQ_t}{dt}E$ has the form in the closed Lorentz group, viz.

$$\frac{dQ_t}{dt}E = -f\left(1-Q_t^+Q_t^-\right)\sqrt{Q_\xi^+Q_\xi^-} = -f\left(\sqrt{Q_\xi^+Q_\xi^-} - \sqrt{Q_t^+Q_t^-}\right). \tag{17}$$

Under the closed Lorentz group, we will understand when all relations in the equations are closed, that is, they have a connection $Q_t^+Q_t^-$ or $Q_\xi^+Q_\xi^-$.

Under the open Lorentz group, we will understand when there is one "free" integral of motion Q_t or Q_ξ in the equations. It is possible to choose an invariant form. For example, for the integral of motion (see Eq. (14)) we have

$$\gamma^+ \equiv Q_t^+E \equiv E - \mathbf{nP} \equiv \mathrm{inv}, \ \gamma^- \equiv Q_t^-E \equiv E + \mathbf{nP} \equiv \mathrm{inv}. \tag{18}$$

The time derivative of the energy has the form [10]

$$\frac{dE}{dt} = P^3 \equiv \mathbf{nP}P^2. \tag{19}$$

The particle velocity can also be represented in the following form:

$$\boldsymbol{\beta} = f\mathbf{n}(1-Q_t). \tag{20}$$

Expanding $\frac{dQ_t}{dt}E$ from Eq. (15) in an open group, we get

$$\frac{dQ_t}{dt}E = -f\boldsymbol{\beta}\mathbf{P}, \tag{21}$$

$$\frac{d\gamma}{dt} = -f\boldsymbol{\beta}\mathbf{P} + Q_tP^3, \tag{22}$$

$$Q_t\mathbf{P} = \boldsymbol{\beta}\gamma = \mathbf{n}\boldsymbol{\beta}\gamma, \tag{23}$$

$$\frac{d\gamma}{dt} = -f\boldsymbol{\beta}\mathbf{P} + \boldsymbol{\beta}\gamma P^2 = -f\boldsymbol{\beta}\mathbf{P}\left(1-f\gamma P\right). \tag{24}$$

In Eq. (24) on the right side, multiplying and dividing by γ we get the function $f_t(\gamma)$,

$$\frac{d\gamma}{dt} = f_t\left(\gamma\right)\gamma, \tag{25}$$

$$f_t\left(\gamma\right) = \frac{-f\boldsymbol{\beta}\mathbf{P}\left(1-f\gamma P\right)}{\gamma} = -\frac{f\boldsymbol{\beta}\mathbf{P}}{\gamma} + \mathbf{n}\boldsymbol{\beta}P^2. \tag{26}$$

Representations $\boldsymbol{\beta}\mathbf{P}$ in the open Lorentz group have the form

$$\boldsymbol{\beta}\mathbf{P} = f\mathbf{n}(1-Q_t)f\mathbf{n}(Q_\xi-1)\gamma = \gamma(Q_\xi+Q_t-2). \tag{27}$$

Due to the invariance in Eq. (26), for $\mathbf{n}\boldsymbol{\beta}P^2$ can be represented compactly $\mathbf{n}\boldsymbol{\beta}$ in an open group, and P^2 in a closed group,

$$\boldsymbol{\beta} = f\mathbf{n}(1-Q_t), \ P^2 = Q_i^+Q_i^- - 1. \tag{28}$$

Representation $f_t(\gamma)$ in $f_t(\gamma^+)$. The representation of $\mathbf{n}\boldsymbol{\beta}P^2$ from Eq. (26) for the case $f = +1$ has the form

111

$$\beta^+ = \mathbf{n}\left(1 - Q_t^+\right), \tag{29}$$

$$\mathbf{n}\beta^+ P^2 = \left(1 - Q_t^+\right)\left(Q_\xi^+ Q_\xi^- - 1\right) = P^2 - Q_\xi^- + Q_t^+. \tag{30}$$

Substituting Eqs. (27) and (28) into Eq. (26), and passing from representations $f_t(\gamma)$ to $f_t(\gamma^+)$, we obtain

$$f_t\left(\gamma^+\right) = -\left(Q_\xi^+ + Q_t^+ - 2\right) + P^2 - Q_\xi^- + Q_t^+, \tag{31}$$

$$f_t(\gamma^+) = -P^2. \tag{32}$$

From Eqs. (31) and (32) we also have the form

$$f_t\left(\gamma^+\right) = -\frac{Q_\xi^+ + Q_\xi^-}{2} + 1. \tag{33}$$

Representation $f_t(\gamma)$ in $f_t(\gamma^-)$. The representation of $\mathbf{n}\beta P^2$ from Eq. (26) for the case $f = -1$ has the form

$$\beta^- = -\mathbf{n}\left(1 - Q_t^-\right), \tag{34}$$

$$\mathbf{n}\beta^- P^2 = -\left(1 - Q_t^-\right)\left(Q_\xi^+ Q_\xi^- - 1\right) = -P^2 + Q_t^- P^2, \tag{35}$$

$$Q_t^- P^2 = Q_t^-\left(Q_i^+ Q_i^- - 1\right) = Q_i^+ - Q_t^-, \tag{36}$$

$$\mathbf{n}\beta^- P^2 = -\left(1 - Q_t^-\right)\left(Q_\xi^+ Q_\xi^- - 1\right) = -P^2 + Q_\xi^+ - Q_t^-, \tag{37}$$

$$f_t\left(\gamma^-\right) = \frac{-f\beta\mathbf{P}\left(1 - f\gamma P\right)}{\gamma} = Q_\xi^- + Q_t^- - 2 - P^2 + Q_\xi^+ - Q_t^-, \tag{38}$$

$$f_t\left(\gamma^-\right) = Q_\xi^+ + Q_\xi^- - 2 - P^2, \tag{39}$$

$$f_t(\gamma^-) = P^2. \tag{40}$$

From Eqs. (39) and (40) there is also the following form:

$$f_t\left(\gamma^-\right) = \frac{Q_\xi^+ + Q_\xi^-}{2} - 1. \tag{41}$$

Summarizing the obtained results — Eqs. (32) and (40), we have that

$$f_t(\gamma) = -fP^2. \tag{42}$$

Representation γ in γ^+ and γ^-. The representation of γ^+ and γ^- in the closed Lorentz group has the form

$$\gamma + \gamma - = 1. \tag{43}$$

Differentiating Eq. (43) with respect to time, we obtain

$$\frac{d\left(\gamma^+ \gamma^-\right)}{dt} = 0, \text{ or } \frac{d\gamma^+}{dt}\gamma^- + \frac{d\gamma^-}{dt}\gamma^+ = 0. \tag{44}$$

The eigenfunction and eigenvalue problems for γ^+ and γ^- have the forms

$$\frac{d\gamma^+}{dt} = f_t\left(\gamma^+\right)\gamma^+, \frac{d\gamma^-}{dt} = f_t\left(\gamma^-\right)\gamma^-, \tag{45}$$

where $f_t(\gamma^+)$ and $f_t(\gamma^-)$ are eigenfunctions γ^+ and γ^- in time t.

Substituting Eq. (45) in Eq. (44) we obtain

$$f_t(\gamma^+) + f_t(\gamma^-) = 0. \tag{46}$$

112

Representation of γ^+ and γ^- in differential form with respect to Q_ξ^+ and Q_ξ^-. Using the relations $Q_t^+ + Q_t^- = 2$ and $Q_t Q_\xi = 1$, we represent γ^+ and γ^- in the form

$$\gamma^+ = \sqrt{2Q_\xi^- - 1}, \ \gamma^- = \sqrt{2Q_\xi^+ - 1},$$

$$\gamma^- = \frac{1}{\sqrt{2Q_\xi^- - 1}}, \ \gamma^+ = \frac{1}{\sqrt{2Q_\xi^+ - 1}}. \tag{47}$$

In differential form, γ^+ and γ^- with respect to Q_ξ^- and Q_ξ^+, have the following form:

$$\frac{d\gamma^+}{dQ_\xi^-} = \gamma^-, \ \frac{d\gamma^-}{dQ_\xi^+} = \gamma^+, \ \frac{d\gamma^-}{dQ_\xi^-} = -\left(\gamma^-\right)^3, \ \frac{d\gamma^+}{dQ_\xi^+} = -\left(\gamma^+\right)^3. \tag{48}$$

The fulfillment of properties of Eq. (48) can be easily verified by differentiating $\gamma^+ \gamma^- = 1$, with respect to Q_ξ^- or Q_ξ^+.

The representation of $\dfrac{dQ_\xi^+}{dQ_\xi^-}$ and $\dfrac{dQ_\xi^-}{dQ_\xi^+}$ in differential form is as follows:

$$\frac{dQ_\xi^+}{dQ_\xi^-} = -\left(\gamma^-\right)^4, \ \frac{dQ_\xi^-}{dQ_\xi^+} = -\left(\gamma^+\right)^4. \tag{49}$$

Energy and momentum in γ^+ and γ^- have the following relationships:

$$\gamma^+ + \gamma^- = 2E = 2Q_{\xi\gamma}, \tag{50}$$

$$\gamma^- - \gamma^+ = 2\mathbf{nP} = 2f(Q_\xi - 1)\gamma. \tag{51}$$

Expanding Eq. (51), we obtain a following equation for $f = +1$:

$$\gamma^- - \gamma^+ = 2Q_\xi^+ \gamma^+ - 2\gamma^+; \tag{52}$$

for $f = -1$ we have

$$\gamma^- - \gamma^+ = -2Q_\xi^- \gamma^- + 2\gamma^-. \tag{53}$$

Representation of functions $f_t(\gamma^+)$ and $f_t(\gamma^-)$ in γ^+ and γ^-. Let us represent the functions $f_t(\gamma^-)$ from Eq. (41) and $f_t(\gamma^+)$ from Eq. (33) using the invariant forms

$$Q_\xi^+ = \frac{\left(\gamma^-\right)^2}{2} + \frac{1}{2} \ \text{and} \ Q_\xi^- = \frac{\left(\gamma^+\right)^2}{2} + \frac{1}{2},$$

in the representation γ^+ and γ^-, which have the form

$$f_t\left(\gamma^+\right) = -\frac{\left(\gamma^+\right)^2 + \left(\gamma^-\right)^2}{4} - \frac{1}{2}, \tag{54}$$

$$f_t\left(\gamma^-\right) = \frac{\left(\gamma^+\right)^2 + \left(\gamma^-\right)^2}{4} + \frac{1}{2}. \tag{55}$$

Adding and subtracting Eqs. (54) and (55), we have

$$f_t(\gamma^+) + f_t(\gamma^-) = 0, \tag{56}$$

$$f_t\left(\gamma^-\right) - f_t\left(\gamma^+\right) = \frac{\left(\gamma^+\right)^2 + \left(\gamma^-\right)^2}{2} + 1, \tag{57}$$

Alternately multiplying Eqs. (56) and (57) by $(\gamma^+)^2$ and $(\gamma^-)2$, we obtain a mutually invariant form of eigenvalues:

$$f_t(\gamma^+)(\gamma^+)^2 + f_t(\gamma^-)(\gamma^+)^2 = 0, f_t(\gamma^+)(\gamma^-)^2 + f_t(\gamma^-)(\gamma^-)^2 = 0, \tag{58}$$

$$\left[f_t\left(\gamma^-\right)-f_t\left(\gamma^+\right)\right]\left(\gamma^+\right)^2 = \frac{\left(\gamma^+\right)^4+1}{2}+\left(\gamma^+\right)^2, \tag{59}$$

$$\left[f_t\left(\gamma^-\right)-f_t\left(\gamma^+\right)\right]\left(\gamma^-\right)^2 = \frac{1+\left(\gamma^-\right)^4}{2}+\left(\gamma^-\right)^2. \tag{60}$$

The invariance property of the energy and momentum of a particle expressed in terms of the integral of motion γ and Q_ξ. To write the invariance property as

$$f_t(\gamma^-) + f_t(\gamma^+) = P^2 - P^2 = 0, \tag{61}$$

and

$$P^2 = P^2, \tag{62}$$

let us represent P as an open Lorentz group in the form

$$(P^+)^2 = (P^-)^2, \tag{63}$$

where the invariance property holds $2P = 2P^+ = 2P- = \gamma^- - \gamma^+ \equiv$ inv.

The momentum P of the particle is represented in the following form:

$$\mathrm{P} = f(Q_\xi - 1)\gamma = \beta Q_\xi \gamma = \beta E = -f(Q_t - 1)Q_\xi \gamma. \tag{64}$$

Substituting the values of the pulse in the open group $P^+ = \left(Q_\xi^+ - 1\right)\gamma^+$ and $P^- = -\left(Q_\xi^- - 1\right)\gamma^-$ in Eq. (63), we obtain

$$\left[\left(Q_\xi^+ - 1\right)\gamma^+\right]^2 = \left[\left(Q_\xi^- - 1\right)\gamma^-\right]^2, \tag{65}$$

$$\left(Q_\xi^+ - 1\right)^2\left(\gamma^+\right)^2 = \left(Q_\xi^- - 1\right)^2\left(\gamma^-\right)^2, \tag{66}$$

$$\left[\left(Q_\xi^+\right)^2 - 2Q_\xi^+ + 1\right]\left(\gamma^+\right)^2 = \left[\left(Q_\xi^-\right)^2 - 2Q_\xi^- + 1\right]\left(\gamma^-\right)^2. \tag{67}$$

Using the invariance property of the energy $E = Q_\xi \gamma = Q_\xi^+ \gamma^+ = Q_\xi^- \gamma^-$, in Eq. (67) we have

$$\left(-2Q_\xi^+ + 1\right)\left(\gamma^+\right)^2 = \left(-2Q_\xi^- + 1\right)\left(\gamma^-\right)^2. \tag{68}$$

Substituting properties $Q_\xi^- = Q_\xi^+\left(\gamma^+\right)^2$ and $Q_\xi^+ = Q_\xi^-\left(\gamma^-\right)^2$ in Eq. (68), we derive an invariant form

$$2\left(Q_\xi^+ - Q_\xi^-\right) = \left(\gamma^-\right)^2 - \left(\gamma^+\right)^2 = \left(\gamma^+ + \gamma^-\right)\left(\gamma^- - \gamma^+\right). \tag{69}$$

From the difference Q_ξ^+ and Q_ξ^-, we obtain

$$Q_\xi^+ - Q_\xi^- = 2\mathbf{n}\boldsymbol{\beta}Q_\xi^+ Q_\xi^+. \tag{70}$$

From the invariance property of the velocities $\boldsymbol{\beta} = \boldsymbol{\beta}^- = \boldsymbol{\beta}^+$, we have the conservation law

$$Q_\xi^+ + Q_\xi^+ = 2Q_\xi^+ Q_\xi^+, \tag{71}$$

also for $\boldsymbol{\beta}^-$

$$Q_\xi^+ - Q_\xi^- = -2Q_\xi^+ Q_\xi^+ + 2Q_\xi^+, \tag{72}$$

as well for $\boldsymbol{\beta}^+$

$$Q_\xi^+ - Q_\xi^- = 2Q_\xi^+ Q_\xi^+ - 2Q_\xi^-. \tag{73}$$

Substituting the values of the energy

$$E^2 = Q_\xi^+ Q_\xi^- = \frac{\left(\gamma^-\right)^2 + \left(\gamma^+\right)^2 + 2}{4}$$

in Eqs. (72) and (73), we obtain

$$Q_\xi^+ - Q_\xi^- = -\frac{\left(\gamma^-\right)^2 + \left(\gamma^+\right)^2 + 2}{2} + 2Q_\xi^+, \tag{74}$$

$$Q_\xi^+ - Q_\xi^- = \frac{\left(\gamma^-\right)^2 + \left(\gamma^+\right)^2 + 2}{2} - 2Q_\xi^-. \tag{75}$$

Substituting Eq. (74) into Eq. (69), we have the form

$$-\left(\gamma^-\right)^2 - \left(\gamma^+\right)^2 - 2 + 4Q_\xi^+ = \left(\gamma^-\right)^2 - \left(\gamma^+\right)^2. \tag{76}$$

Similarly, substituting Eq. (75) into Eq. (69), we obtain

$$\left(\gamma^-\right)^2 + \left(\gamma^+\right)^2 + 2 - 4Q_\xi^- = \left(\gamma^-\right)^2 - \left(\gamma^+\right)^2. \tag{77}$$

Adding Eqs. (76) and (77), we have the value of the invariant form

$$2Q_\xi^+ - 2Q_\xi^- = \left(\gamma^-\right)^2 - \left(\gamma^+\right)^2, \tag{78}$$

Subtracting Eq. (76) from Eq. (77), we have

$$\frac{1}{2}\left[\left(\gamma^-\right)^2 + \left(\gamma^+\right)^2\right] + 1 = Q_\xi^+ + Q_\xi^-. \tag{79}$$

Invariant forms of the integrals γ^+ and γ^- of particle motion. The invariant form of the integrals of motion $(\gamma^-)^2$ and $(\gamma^+)^2$ has the following form:

$$\left(\gamma^-\right)^2 + \left(\gamma^+\right)^2 = \left[\left(Q_t^+\right)^2 + \left(Q_t^-\right)^2\right]E^2 = 2\frac{1+\beta^2}{1-\beta^2} = 2\left(Q_\xi^+ + Q_\xi^+\right) - 2, \tag{80}$$

$$\left(\gamma^-\right)^2 - \left(\gamma^+\right)^2 = 2\left(Q_\xi^+ - Q_\xi^-\right) = 4\mathbf{n}\beta Q_\xi^+ Q_\xi^- = 2\mathbf{n}\beta\left(Q_\xi^+ + Q_\xi^-\right) = \frac{4\mathbf{n}\beta}{1-\beta^2}. \tag{81}$$

We introduce invariant functions that have the form

$$g = \frac{1+\beta^2}{1-\beta^2} = \frac{\left(\gamma^-\right)^2 + \left(\gamma^+\right)^2}{2}, \ h = \frac{\left(\gamma^-\right)^2 - \left(\gamma^+\right)^2}{4} = \frac{\mathbf{n}\beta}{1-\beta^2}. \tag{82}$$

The functions g and h belong to the same class: their partial derivatives with respect to β are their eigenvalues and reflect the closure property of the Lorentz group:

$$\frac{dg}{d\beta} = 4hQ_\xi^+ Q_\xi^- = 4hE^2, \frac{dh}{d\beta} = gQ_\xi^+ Q_\xi^- = gE^2. \tag{83}$$

Taking the derivatives of the integrals of motion γ^- and γ^+ (see Eq. (18)) with respect to $\boldsymbol{\beta}$, we obtain

$$\mathbf{n}\frac{d\gamma^-}{d\beta} = \frac{\gamma^+}{\left(Q_t^+\right)^2} = \frac{\left(\gamma^+\right)^2}{\left(Q_t^+\right)^2}\gamma^- = f_\beta\left(\gamma^-\right)\gamma^-, \ f_\beta\left(\gamma^-\right) = \frac{\left(\gamma^+\right)^2}{\left(Q_t^+\right)^2} = E^2. \tag{84}$$

Similarly, for γ^+ we have

$$\mathbf{n}\frac{d\gamma^+}{d\beta} = f\left(\gamma_\beta^+\right)\gamma^+, f\left(\gamma_\beta^+\right) = -E^2. \tag{85}$$

As can be seen, for Eqs. (84) and (85) the following properties of the invariant form hold:

$$f_\beta(\gamma^+) + f_\beta(\gamma^-) = 0, \tag{86}$$

$$\mathbf{n}\frac{d\gamma^+}{d\beta} + \mathbf{n}\frac{d\gamma^-}{d\beta} = f_\beta\left(\gamma^-\right)\left(\gamma^- - \gamma^+\right) = 2\mathbf{n}PE^2, \tag{87}$$

$$\mathbf{n}\frac{d\gamma^-}{d\beta} - \mathbf{n}\frac{d\gamma^+}{d\beta} = f_\beta\left(\gamma^-\right)\left(\gamma^- + \gamma^+\right) = 2E^3. \tag{88}$$

From properties (5), (6), and (7) of the invariance of the energy E and momentum $\mathbf{P}$ with respect to β, we have

$$\frac{d\mathbf{P}}{d\beta} = E^3, \frac{dE}{d\beta} = \beta E^3 = \mathbf{P}E^2. \tag{89}$$

Taking the derivative of the integrals of motion (18), we obtain the invariant form

$$\frac{dE}{d\beta} + \mathbf{n}\frac{d\mathbf{P}}{d\beta} = \frac{d\gamma^-}{d\beta}, \tag{90}$$

and substituting the values (89), (85) into Eq. (90) we obtain that the integrals of motion γ^- and γ^+ are invariant with respect to differentiation with respect to β.

From properties (5), (6) and (7) of the invariance of energy and momentum with respect to time t, we obtain:

$$\mathbf{n}\frac{d\mathbf{P}}{dt} = P^2E. \tag{91}$$

Differentiating Eq. (18) with respect to time t and substituting the values (91), (45) and (19), we obtain the mutually invariant form (18). The fulfillment of the invariant form of Eqs. (19), (89) and (91) is also easy to check by differentiating the conservation law (6) with respect to time t or velocity β.

Reverse energy of a relativistic particle. We introduce the inverse energy function as

$$E_g = \frac{1}{E} = \frac{1}{Q_\xi\gamma} = \frac{Q_t}{\gamma} = \sqrt{Q_t^+ Q_t^-}. \tag{92}$$

The invariant form of the inverse energy has the form

$$E_g = \frac{Q_t}{\gamma} = Q_t^+ \gamma^- = Q_t^- \gamma^+ = \sqrt{Q_t^+ Q_t^-}. \tag{93}$$

From the properties obtained above, we introduce invariant relations using the reciprocal energy of the particle:

$$EE_g = 1. \tag{94}$$

$$P^2 E_g^- = \left(Q_\xi^+ Q_\xi^- - 1\right)Q_t^- \gamma^+ = Q_\xi^+ \gamma^+ - Q_t^- \gamma^+. \tag{95}$$

$$P^2 E_g^+ = \left(Q_\xi^+ Q_\xi^- - 1\right)Q_t^+ \gamma^- = Q_\xi^- \gamma^- - Q_t^+ \gamma^-, \tag{96}$$

$$\mathbf{P}E_g = f\mathbf{n}\left(Q_\xi - 1\right)\gamma\frac{Q_t}{\gamma} = f\mathbf{n}\left(Q_\xi - 1\right)Q_t = f\mathbf{n}\left(1 - Q_t\right) = \beta. \tag{97}$$

$$\mathbf{P}^+ E_g^+ = \beta^+ = \mathbf{P}^- E_g^- = \beta^-, \tag{98}$$

$$\mathbf{P}^+ E_g^- = \mathbf{n}\left(1 - Q_t^+\right) = \beta^+, P^- E_g^+ = -\left(1 - Q_t^-\right) = \beta^-. \tag{99}$$

Pseudopotential energy of a relativistic particle. We introduce the pseudopotential energy function as

$$E_p = Q_t \gamma = Q_t^2 E. \tag{100}$$

$$EE_p = \gamma^2, \tag{101}$$

$$E^+ E_p^+ = E^- E_p^+ = \left(\gamma^+\right)^2, \tag{102}$$

$$E^+ E_p^- = E^- E_p^- = \left(\gamma^-\right)^2. \tag{103}$$

Reverse momentum of a relativistic particle. The reverse momentum of a particle has the form

$$\mathbf{nP}_g = \frac{1}{\mathbf{nP}} = \frac{Q_t}{\mathbf{n\beta\gamma}}, \tag{104}$$

and

$$\mathbf{nP}_g = \frac{1}{\mathbf{nP}} = \frac{Q_t}{\mathbf{n\beta\gamma}} = \frac{Q_t^+ \gamma^-}{\mathbf{n\beta}} = \frac{Q_t^- \gamma^+}{\mathbf{n\beta}}, \tag{105}$$

where $\mathbf{n\beta} = \mathbf{n\beta}^- = \mathbf{n\beta}^+$.

Decomposition into a spectrum in terms of γ^+ and γ^- of the squared momentum $\mathbf{P}^2$ and squared energy E^2 of the particle. The connections of the integrals of the motion of the particle γ^+ and γ^- through the energy of the particle has the form

$$\gamma^+ + \gamma^- = 2E. \tag{106}$$

Squaring Eq. (106) we obtain

$$\frac{\left(\gamma^+\right)^2 + \left(\gamma^-\right)^2}{4} + \frac{1}{2} = E^2. \tag{107}$$

Subtracting one from both sides of the equation, we have

$$\frac{\left(\gamma^+\right)^2 + \left(\gamma^-\right)^2}{4} - \frac{1}{2} = E^2 - 1 = P^2. \tag{108}$$

Using the invariant property of integrals of motion

$$Q_\xi^+ Q_\xi^- = \frac{\left(\gamma^+\right)^2 + \left(\gamma^-\right)^2}{4} + \frac{1}{2}, \tag{109}$$

we have

$$P^2 = Q_\xi^+ Q_\xi^- - 1 = (E-1)(E+1), \tag{110}$$

and

$$\left(1 - Q_\xi^+\right)\left(Q_\xi^- - 1\right) = (E-1)(E+1). \tag{111}$$

Adding $\gamma^+ \gamma^- = 1$ to the left side of Eq. (111), we obtain

$$\left(\gamma^+ - Q_\xi^+ \gamma^+\right)\left(Q_\xi^- \gamma^- - \gamma^-\right) = (E-1)(E+1), \tag{112}$$

and using the invariance property

$$E = Q_\xi \gamma = Q_\xi^+ \gamma^+ = Q_\xi^- \gamma^-,$$

we have

$$(\gamma^+ - E)(E - \gamma^-) = (E-1)(E+1). \tag{113}$$

Revealing Eq. (113), we obtain a representation of the square momentum of the particle:

$$\frac{\gamma^+ E + E\gamma^-}{2} = E^2 = P^2 + 1. \tag{114}$$

Dividing Eq. (114) by energy, we have

$$\frac{\gamma^+ + \gamma^-}{2} = E. \tag{115}$$

Substituting into the left part of Eq. (115) the values of the invariant form of the energy of the particle

$$E = Q_\xi \gamma = Q_\xi^+ \gamma^+,$$

we obtain

$$\frac{\left(\gamma^+\right)^2 + 1}{2} = Q_\xi^-. \tag{116}$$

Similarly, substituting the values of the invariant form of the particle energy

$$E = Q_\xi \gamma = Q_\xi^- \gamma^-$$

into the left part of Eq. (115), we obtain

$$\frac{\left(\gamma^-\right)^2 + 1}{2} = Q_\xi^+, \tag{117}$$

Adding Eqs. (116) and (117), we have the following form:

$$\frac{\left(\gamma^+\right)^2 + \left(\gamma^-\right)^2}{2} + 1 = Q_\xi^+ + Q_\xi^-, \tag{118}$$

and

$$\frac{\left(\gamma^+\right)^2 + \left(\gamma^-\right)^2}{2} = 2Q_\xi^+ Q_\xi^- - 1 = P^2 + E^2. \tag{119}$$

Subtracting Eq. (117) from Eq. (116), we obtain

$$\frac{\left(\gamma^-\right)^2 - \left(\gamma^+\right)^2}{2} = Q_\xi^+ - Q_\xi^- = 2\mathbf{n\beta} Q_\xi^+ Q_\xi^- = 2\mathbf{n\beta} E^2, \tag{120}$$

Expressing $2\mathbf{n\beta}$, we obtain

$$2\mathbf{n\beta} = Q_t^- - Q_t^+ = \frac{\left(Q_t^-\right)^2}{2} - \frac{\left(Q_t^+\right)^2}{2} = \frac{\left(Q_t^- - Q_t^+\right)\left(Q_t^+ + Q_t^-\right)}{2}. \tag{121}$$

Converting Eq. (119), we obtain the value of the square of the particle energy:

$$E^2 = Q_\xi^+ Q_\xi^- = \frac{\left(\gamma^+\right)^2 + \left(\gamma^-\right)^2}{2} + \frac{1}{2}. \tag{122}$$

Similarly, for the value of the square of the particle momentum, we obtain

$$P^2 = Q_\xi^+ Q_\xi^- - 1 = \frac{\left(\gamma^+\right)^2 + \left(\gamma^-\right)^2}{2} - \frac{1}{2}. \tag{123}$$

Using the relations between the integrals of motion

$$Q_\xi^+ + Q_\xi^- = 2Q_\xi^+ Q_\xi^-, \ Q_t^+ + Q_t^- = 2, \tag{124}$$

it is easy to collect the particle momentum from the invariant forms of the integrals of motion Q_t and Q_ξ:

$$Q_\xi^+ + Q_\xi^- - \left(Q_t^+ + Q_t^-\right) = 2Q_\xi^+ Q_\xi^- - 2 = 2P^2. \tag{125}$$

Multiplying P^2 from Eq. (125) by $2\mathbf{n\beta} = Q_t^- - Q_t^+$, we obtain

$$Q_\xi^+ - Q_t^- - Q_\xi^- + Q_t^+ = 2\mathbf{n\beta}P^2. \tag{126}$$

Adding and subtracting Eqs. (125) and (126), we have

$$Q_t^- P^2 = Q_\xi^+ - Q_t^-, \; Q_t^+ P^2 = Q_\xi^- - Q_t^+. \tag{127}$$

The relation for the particle energy has the following invariant relations:

$$Q_t^- E^2 = Q_\xi^+, \; Q_t^+ E^2 = Q_\xi^-. \tag{128}$$

Representation of integrals of motion as a function $\gamma = \gamma\,(Q_t\,,\,\mathbf{P},\,E,\,\mathbf{P}_g,\,E_g)$. From the problems on eigenfunctions and eigenvalues from the above paragraphs, it is convenient to represent the integrals of motion γ^+ and γ^- as invariant functions

$$\gamma = \left(1 - Q_t\right)^2 EP_g^2 - fQ_t\mathbf{nP}, \tag{129}$$

$$\gamma = E_g - fQ_t\mathbf{nP}. \tag{130}$$

The γ values (129) and (130) are expressed in terms of a one-to-one correspondence:

$$E_g + f\mathbf{nP}_g = f\frac{E_g\mathbf{nP}_g}{\gamma}, \tag{131}$$

$$\gamma^{-1} = E + f\mathbf{nP}. \tag{132}$$

Angular integral of motion θ

The functional dependencies $\gamma = \gamma(Q_t)$ and $Q_t = Q_t(\gamma)$ have been introduced above. We now define the integral angle, or angular integral of motion, as a function $\gamma = \gamma(\theta)$.

The integrals of motion from Eq. (18) with the application of Eq. (5) take the form

$$\gamma^+ = \cosh\theta - \sinh\theta = \exp(-\theta), \; \gamma^- = \cosh\theta + \sinh\theta = \exp(\theta). \tag{133}$$

Generalizing the Eqs. (133), the integral of motion γ has the following relation with the angular integral of motion θ

$$\gamma = \cosh\theta - f\sinh\theta = \exp(-f\theta). \tag{134}$$

Substituting the integral of motion (134) in the invariant form of the particle energy $E = Q_\xi\gamma$, we obtain

$$Q_t = 1 - f\tanh\theta, \tag{135}$$

where in Eq. (135) Q_t^+ and Q_t^- take the forms

$$Q_t^+ = 1 - \tanh\theta, \; Q_t^- = 1 + \tanh\theta. \tag{136}$$

It is easy to show from Eq. (135) that the particle velocity has the form

$$\mathbf{n\beta} = \tanh\theta. \tag{137}$$

Substituting the particle energy and momentum values of the from Eq. (5), it can be seen that

$$\mathbf{n\beta} = \frac{\sqrt{E^2 - 1}}{E}, \; \beta = \frac{\mathbf{P}}{\sqrt{P^2 + 1}}, \tag{138}$$

thus, the functions $\mathbf{\beta} = \mathbf{\beta}(\mathbf{P}, E)$, $\mathbf{P} = \mathbf{P}(\mathbf{\beta})$ and $E = E(\mathbf{\beta})$ have a mutual functional dependence.

Multiplying Q_t^+ and Q_t^- from Eq. (136), we have

$$Q_t^+ Q_t^- = 1 - \tanh^2 \theta, \quad Q_\xi^+ Q_\xi^- = \cosh^2 \theta. \tag{139}$$

Expressing from Eq. (135) Q_ξ, we obtain

$$Q_\xi = 0.5 \cdot [\exp(2f\theta) + 1], \tag{140}$$

where

$$Q_\xi^+ = \frac{1}{2}\big[\exp(2\theta) + 1\big], \quad Q_\xi^- = \frac{1}{2}\big[\exp(-2\theta) + 1\big]. \tag{141}$$

From (140) we obtain the invariant form of the integral of motion γ:

$$(\gamma^{-f})2 = 2Q_\xi - 1 = \exp(2f\theta), \quad \gamma^{-f} = \exp(f\theta), \tag{142}$$

where the choice of $f = +1$ or $f = -1$ is determined by the principle of relativity.

Representation of the space-time characteristics depending on the integral of motion θ. By representing the integral of motion (134) as a function differentiable with respect to θ, we obtain the eigenvalue of the function γ:

$$\gamma' = -f\exp(-f\theta) = -f\gamma. \tag{143}$$

From the representations of the principle of the particle motion for the space-time Lorentz coordinate, we have

$$\xi = t - f\,\frac{\mathbf{nr}}{c}, \tag{144}$$

where

$$t = 1 - \frac{f}{(1 - Q_t)}, \quad \mathbf{nr} = \frac{1}{2}\ln\big[(1 - Q_t)^2\big]; \tag{145}$$

using Eq. (135) we can be sure that the angular integral of motion has the following dependence:

$$t = 1 - \coth\theta, \quad \mathbf{nr} = 0.5\ln(\tanh^2\theta). \tag{146}$$

Differentiating Eq. (146) with respect to θ, we obtain

$$\frac{dt}{d\theta} = \frac{1}{\sinh^2\theta}, \quad \mathbf{n}\frac{d\mathbf{r}}{d\theta} = \frac{1}{\cosh\theta\sinh\theta}, \tag{147}$$

where

$$\mathbf{n\beta} = \mathbf{n}\frac{d\mathbf{r}}{d\theta}\frac{d\theta}{dt} = \tanh\theta, \tag{148}$$

the value from Eq. (137).

Differentiating ξ from Eq. (144) with respect to θ, we obtain

$$\frac{d\xi}{d\theta} = \frac{\gamma}{\sinh^2\theta\cosh\theta} = \frac{\gamma}{P^2 E} = \frac{Q_t}{\sinh^2\theta} = \frac{Q_t}{P^2}. \tag{149}$$

Using the differential form from Eq. (147) $\zeta = P^2 = \sinh 2\theta$, we have

$$\frac{d\xi}{dt} = \frac{d\xi}{d\theta}\frac{d\theta}{dt} = \frac{d\xi}{d\theta}\dot\theta = Q_t. \tag{150}$$

Lagrangian and Hamiltonian formalisms for a free particle in the representation θ. The Lagrangian depending on θ and $\zeta = \dfrac{d\theta}{dt}$ has the following representations:

$$L' = \frac{L}{mc} = -\sqrt{Q_t^+ Q_t^-} = -\frac{Q_t}{\gamma} = -\frac{1}{\cosh\theta} = -\frac{1}{\sqrt{\zeta + 1}}. \tag{151}$$

The derivatives of the differential forms of θ and ζ from Eq. (151) have the form

$$\frac{\partial L'}{\partial \theta} = \frac{\sinh \theta}{\cosh^2 \theta} = \frac{\mathbf{n}\boldsymbol{\beta}}{E},$$ (152)

$$\frac{\partial L'}{\partial \zeta} = \frac{1}{2(\zeta+1)^{\frac{3}{2}}} = \frac{1}{2\cosh^3 \theta} = \frac{1}{2E^3},$$ (153)

$$\frac{d}{dt}\left(\frac{\partial L'}{\partial \zeta}\right) = -\frac{3}{2}\frac{P^3}{E^4}.$$ (154)

The Lagrangian function of the integral of motion Q_t and the coordinate $q = -f\mathbf{nr}/c$ from Eq. (146) has the following form in the representation θ:

$$\frac{\partial L'}{\partial Q_t} = -\frac{1-Q_t}{\sqrt{Q_t^+ Q_t^-}} = -f \sinh \theta = -f\mathbf{nP},$$ (155)

$$\frac{d}{dt}\left(\frac{\partial L'}{\partial Q_t}\right) = -f\left(\sqrt{Q_\xi^+ Q_\xi^-} - \sqrt{Q_t^+ Q_t^-}\right) = -f \tanh \theta \sinh \theta = -f\boldsymbol{\beta}\mathbf{P},$$ (156)

$$\frac{\partial L'}{\partial q} = -f\left(\sqrt{Q_\xi^+ Q_\xi^-} - \sqrt{Q_t^+ Q_t^-}\right) = -f \tanh \theta \sinh \theta = -f\boldsymbol{\beta}\mathbf{P}.$$ (157)

It follows from Eqs. (155) and (157) that

$$\frac{\partial Q_t}{\partial q} = \mathbf{n}\boldsymbol{\beta}.$$ (158)

Also, from Eq. (135), we have a partial differential form

$$\frac{\partial \theta}{\partial Q_t} = -f \cosh^2 \theta.$$ (159)

From Eqs. (158) and (159) we have the following differential form:

$$\frac{\partial \theta}{\partial q} = -f \cosh \theta \sinh \theta.$$ (160)

The Lagrange equation of the second kind as a function $L' = L'(q, t, Q_t, \theta, \zeta)$ has the following form:

$$\frac{d}{dt}\left(\frac{\partial L'}{\partial \zeta}\right)\frac{\partial \zeta}{\partial \theta} + \frac{d}{dt}\left(\frac{\partial \zeta}{\partial Q_t}\right)\frac{\partial L'}{\partial \theta} - \frac{\partial L'}{\partial \theta}\frac{\partial Q_t}{\partial q} = 0.$$ (161)

From Eqs. (134), (140) and (50) we have that the Hamiltonian of a free particle is

$$H' = Q_\xi \gamma = E = \cosh \theta.$$ (162)

Substituting Eqs. (162) and (3) into the integral of motion (134), we obtain a generalized integral of motion in the form

$$\gamma = H' - f\frac{\partial H'}{\partial \theta}.$$ (163)

Due to the fact that γ^+ and γ^- are invariants of motion different in direction and from the principle of relativity, we obtain

$$\gamma^+ = H' - \frac{\partial H'}{\partial \theta}, \; \gamma^- = H' + \frac{\partial H'}{\partial \theta},$$ (164)

$$\gamma^+ \gamma^- = \left(H'\right)^2 - \left(\frac{\partial H'}{\partial \theta}\right)^2 = 1,$$ (165)

where Eq. (165) expresses the law of conservation of energy in Hamiltonian form.

Using Lagrangian and Hamiltonian formalisms, it is convenient to introduce the following equation describing the conservation law by ζ:

$$2\frac{\partial H'}{\partial \zeta} + L' = 0. \tag{166}$$

The classical action function for a particle that has no charge has the form [23]

$$\frac{\partial S'}{\partial t} = -\sqrt{Q_t^+ Q_t^-} = L'. \tag{167}$$

As is known, in the Hamilton − Jacobi equation [23], when substituting Eq. (167), we have the following form:

$$H' + \frac{\partial S'}{\partial t} = Q_\xi \gamma - \frac{Q_t}{\gamma} = \cosh\theta - \frac{1}{\cosh\theta} = \hat{H}', \tag{168}$$

where $\hat{H}$ is the displacement Hamiltonian.

Differentiating Eq. (168) with respect to θ, we have

$$\frac{\partial \hat{H}'}{\partial \theta} = \sinh(\theta) + \frac{\tanh(\theta)}{\cosh(\theta)} = \mathbf{nP} + \frac{\mathbf{n\beta}}{E} = \frac{\partial L'}{\partial \theta} - f\frac{\partial L'}{\partial Q_t}, \tag{169}$$

and

$$\frac{\partial \hat{H}'}{\partial \theta} - \frac{\partial L'}{\partial \theta} = \mathbf{nP}. \tag{170}$$

Representing Eq. (168) as a function $\hat{H} = \hat{H}(\zeta)$, we obtain

$$\hat{H}' = \sqrt{\zeta+1} - \frac{1}{\sqrt{\zeta+1}} = \frac{\zeta}{\sqrt{\zeta+1}} = \frac{P^2}{\sqrt{P^2+1}} = \mathbf{\beta P}. \tag{171}$$

Differentiating Eq. (171) with respect to ζ, we have

$$\frac{\partial \hat{H}'}{\partial \zeta} = \frac{\zeta+2}{2(\zeta+1)^{\frac{3}{2}}} = \frac{\cosh^2\theta+1}{2\cosh^3\theta} = \frac{\partial L'}{\partial \zeta} - \frac{L}{2}. \tag{172}$$

The relationship between derivatives (169) and (172) has the following form:

$$\sinh(2\theta)\frac{\partial \hat{H}'}{\partial \zeta} = \frac{\partial \hat{H}'}{\partial \theta}, \tag{173}$$

where

$$\sinh(2\theta) = \frac{\partial \zeta}{\partial \theta} = -f\frac{1}{2}\frac{\partial \theta}{\partial q}. \tag{174}$$

Thus, it is established mutually expressible between $\gamma = \gamma(\theta)$ and $\theta = \theta(\gamma)$, where the explicit relationship θ depending on γ has the form

$$\theta = \arctan h\left[f\left(\frac{1-\gamma^2}{1+\gamma^2}\right)\right]. \tag{175}$$

Conclusions

In this work, based on the integrals of motion $\gamma = \gamma(\mathbf{r}, t, Q_t, \theta)$ and $\theta = \theta(\mathbf{r}, t, Q_t, \gamma)$, new relativistic forms have been obtained, which can be used to analyze the motion of particles, both in electromagnetic and gravitational fields.

From the problem on eigenfunctions and eigenvalues, the integral of motion was shown to have a relativistic invariant form, when taking the derivative with respect to time t and velocity $\mathbf{\beta}$. A mutually invariant relationship between $\gamma = \gamma(\theta)$ and $\theta = \theta(\gamma)$ was derived.

The generalized integral of motion $\gamma = \gamma(\theta)$ from Eq. (163) was obtained using the Hamiltonian formalism.

Thus, in the future, to analyze the motion of a relativistic particle in electromagnetic fields, not only the invariant form γ from Eq. (1) should be taken into account, but also the contribution of the scalar φ and vector A potentials, that is, the integral of motion should be considered as a function of $\gamma = \gamma(Q_t, \mathbf{A}, \varphi)$.

Relations of mutually invariant differential forms with generalized forms of motion were obtained. The Lagrange equation of the second kind was derived as a function of $L' = L'(q, t, Q_t, \theta, \zeta)$. The Lagrangian formalism showed the mutual correspondence between $L' = L'(q, Q_t)$ and $L' = L'(\theta, \zeta)$.

The functions of reverse energy and reverse momentum, the functions of pseudopotential energy and pseudopotential momentum were introduced. Their connection with the integral of motion γ was shown.

Using these conclusions, it is further interesting to generalize such problems as the motion of a charged particle in electromagnetic fields of various configurations in the presence of stationary and variable electric and magnetic fields and to study relativistic effects that occur when particles are accelerated and decelerated by electromagnetic fields. Our findings will be also useful in the future for the development of such areas as double special relativity and gravitomagnetism.

Acknowledgments

REFERENCES

1. **Qian, B.-L.,** Relativistic motion of a charged particle in a superposition of circularly polarized plane electromagnetic waves and a uniform magnetic field, Phys. Plasmas. 7 (2) (2000) 537−543.

2. **Kong L.-B., Liu P.-K.,** Analytical solution for relativistic charged particle motion in a circularly polarized electromagnetic wave, Phys. Plasmas. 14 (6) (2007) 063101.

3. **Andreev S. N., Makarov V. P., Rukhadze A. A.,** On the motion of a charged particle in a plane monochromatic electromagnetic wave, Kvant. Elektron. 39 (1) (2009) 68−72.

4. **Volodin B. A., Ponomarev I. V., Khapaev A. M.,** On electron motion in the Redmond field, Soviet Phys. J. 27 (3) (1984) 113.

5. **Galkin A. L., Korobkin V. V., Romanovskii M. Yu., Shiryaev O. B.,** Relativistic motion and radiation of an electron in the field of an intense laser pulse, Kvant. Elektron. 37 (10) (2007) 903−909.

6. **Akintsov N. S., Nevecheria A. P.,** Acceleration of a charged particle in the Redmond field, AIP Adv. 12 (3) (2022) 035212.

7. **Borovskiy A. V., Galkin A. L.,** Electron emission from the focus of the Gaussian pulse, Laser Phys. 32 (8) (2022) 084008.

8. Buts V. A., Zagorodny A. G., New cyclotron resonances and features of charged-particle dynamics in the presence of an intense electromagnetic wave, Phys. Plasmas. 28 (2) (2021) 022311.

9. **Landau L. D., Lifshitz E. M.,** Course of theoretical physics. Vol. 2. The classical theory of fields, Pergamon Press, Oxford, UK, 1975.

10. **Akintsov N. S., Nevecheria A. P., Martinov A. A.,** The motion of an uncharged relativistic particle: an analysis of its integrable motion integrals dynamics, St. Petersburg State Polytechnical University Journal. Physics and Mathematics. 16 (2) (2023) 132−145.

11. **Aoisio R., Galante A., Grillo A., et al.,** A note on DSR-like approach to space−time, Phys. Lett. B. 610 (1−2) (2005) 101−106.

12. **Amelino-Camelia G.,** Testable scenario for relativity with minimum length, Phys. Lett. B. 510 (1−4) (2001) 255−263.

13. **Pavlopoulos T. G.,** Are we observing Lorentz violation in gamma ray bursts? Phys. Lett. B. 625 (1−2) (2005) 13−18.

14. **Amelino-Camelia G.,** Special treatment, Nature. 418 (6893) (2002) 34−35.

15. **Amelino-Camelia G.,** Doubly-special relativity: fact, myths and some key open issues, Symmetry. 2 (1) (2010) 230−271.

16. **Addazi A., Alvarez-Muniz J., Alves Batista R., et. al.,** Quantum gravity phenomenology at the dawn of the multi-messenger era − A review, Progr. Part. Nucl. Phys. 125 (July) (2022) 103948.

17. **Akintsov N. S., Nevecheria A. P., Kopytov G. F., Yang Y.,** Lagrangian and Hamiltonian formalisms for relativistic mechanics with Lorentz-invariant evolution parameters in $1 + 1$ dimensions, Symmetry. 15 (9) (2023) 1691.

18. **Akintsov N. S., Kopytov G. F., Nevecheria A. P., Yang Y.,** Lorentz-invariant forms of motion of classical relativistic particles in 3+1 dimensions, Izv. Vuzov. Fiz. 66 (8) (2023) 41−49.

19. **Akintsov N. S., Nevecheria A. P., Kopytov G. F., et. al.,** Special relativity in terms of hyperbolic functions with coupled parameters in 3+1 dimensions, Symmetry. 16(3) (2024) 357.

20. **Akintsov N., Nevecheria A., Kopytov G.,** Modulated laser-induced acceleration of a relativistic charged particle, Indian J. Phys. 98 (3) (2024) 1123−1137.

21. **Milekhin G. A.,** Hydrodynamic theory of multiple production of particles in collisions between fast nucleons and nuclei, Sov. Phys. JETP. 8 (5) (1959) 829−837.

22. **Khadka C. B.,** Formulation of the Lorentz transformation equations in the three dimensions of space, St. Petersburg State Polytechnical University Journal. Physics and Mathematics. 17 (2) (2024) 160−173.

23. **Landau L. D., Lifshitz E. M.,** Course of theoretical physics. Vol. 1. Mechanics, Butterworth-Heinemann, London, UK, 1976.

СПИСОК ЛИТЕРАТУРЫ

1. **Qian B.-L.** Relativistic motion of a charged particle in a superposition of circularly polarized plane electromagnetic waves and a uniform magnetic field // Physics of Plasmas. 2000. Vol. 7. No. 2. Pp. 537−543.

2. **Kong L.-B., Liu P.-K.** Analytical solution for relativistic charged particle motion in a circularly polarized electromagnetic wave // Physics of Plasmas. 2007. Vol. 14. No. 6. P. 063101.

3. **Андреев С. Н., Макаров В. П., Рухадзе А. А.** О движении заряженной частицы в плоской монохроматической электромагнитной волне // Квантовая электроника. 2009. Т. 39. № 1. С. 68−72.

4. **Володин Б. А., Пономарев И. В., Хапаев А. М.** К вопросу о движении электрона в поле Редмонда // Известия высших учебных заведений. Физика. 1984. № 3. С. 113−115.

5. **Галкин А. Л., Коробкин В. В., Романовский М. Ю., Ширяев О. Б.** Релятивистское движение и излучение электрона в поле интенсивного лазерного импульса // Квантовая электроника. 2007. Т. 37. № 10. С. 903−909.

6. **Akintsov N. S., Nevecheria A. P.** Acceleration of a charged particle in the Redmond field // AIP Advances. 2022. Vol. 12. No. 3. P. 035212.

7. **Borovskiy A. V., Galkin A. L.** Electron emission from the focus of the Gaussian pulse // Laser Physics. 2022. Vol. 32. No. 8. P. 084008.

8. **Buts V. A., Zagorodny A. G.** New cyclotron resonances and features of charged-particle dynamics in the presence of an intense electromagnetic wave // Physics of Plasmas. 2021. Vol. 28. No. 2. P. 022311.

9. **Ландау Л. Д., Лифшиц Е. М.** Теоретическая физика в 10 тт. Т. 2. Теория поля. М.: Наука, 1967. 458 с.

10. **Akintsov N. S., Nevecheria A. P., Martinov A. A.** The motion of an uncharged relativistic particle: an analysis of its integrable motion integrals dynamics // St. Petersburg State Polytechnical University Journal. Physics and Mathematics. 2023. Vol. 16. No. 2. Pp. 132−145.

11. **Aoisio R., Galante A., Grillo A., Luzio E., Mendez F.** A note on DSR-like approach to space−time // Physics Letters B. 2005. Vol. 610. No. 1−2. Pp. 101−106.

12. **Amelino-Camelia G.** Testable scenario for relativity with minimum length // Physics Letters B. 2001. Vol. 510. No. 1−4. Pp. 255−263.

13. **Pavlopoulos T. G.** Are we observing Lorentz violation in gamma ray bursts? // Physics Letters B. 2005. Vol. 625. No. 1−2. Pp. 13−18.

14. **Amelino-Camelia G.** Special treatment // Nature.2002. Vol. 418. No. 6893. Pp. 34−35.

15. **Amelino-Camelia G.** Doubly-special relativity: fact, myths and some key open issues // Symmetry. 2010. Vol. 2. No. 1. Pp. 230−271.

16. **Addazi A., Alvarez-Muniz J., Alves Batista R., et. al.** Quantum gravity phenomenology at the dawn of the multi-messenger era − A review // Progress in Particle and Nuclear Physics. 2022. Vol. 125. July. P. 103948.

17. **Akintsov N. S., Nevecheria A. P., Kopytov G. F., Yang Y.** Lagrangian and Hamiltonian formalisms for relativistic mechanics with Lorentz-invariant evolution parameters in 1 + 1 dimensions // Symmetry. 2023. Vol. 15. No. 9. P. 1691.

18. **Акинцов Н. С., Копытов Г. Ф., Невечеря А. П., Ян Ю.** Лоренц-инвариантные формы движения классической релятивистской частицы в 3+1-измерениях // Известия вузов. Физика. 2023. Т. 66. № 8. С. 41−49.

19. **Akintsov N. S., Nevecheria A. P., Kopytov G. F., Yang Y., Cao T.** Special relativity in terms of hyperbolic functions with coupled parameters in 3+1 dimensions // Symmetry. 2024. Vol. 16. No. 3. P. 357.

20. **Akintsov N., Nevecheria A., Kopytov G.** Modulated laser-induced acceleration of a relativistic charged particle // Indian Journal of Physics. 2024. Vol. 98. No. 3. Pp. 1123−1137.

21. **Milekhin G. A.** Hydrodynamic theory of multiple production of particles in collisions between fast nucleons and nuclei, Sov. Phys. JETP. 1959. Vol. 8. No. 5. Pp. 829−837.

22. **Khadka C. B.** Formulation of the Lorentz transformation equations in the three dimensions of space // St. Petersburg State Polytechnical University Journal: Physics and Mathematics. 2024. Vol. 17. No. 2. Pp. 160−173.

23. **Ландау Л. Д., Лифшиц Е. М.** Теоретическая физика. В 10 тт. Т. 1. Механика. М.: Наука. Гл. ред. физ.-мат. лит-ры, 1988. 216 с.

THE AUTHORS

AKINTSOV Nikolai S.
Nantong University, Ocean University of China
40 Qing Nian Dong Lu, Chongchuan Qu, Nantong Shi, Jiangsu Sheng,
Nantong University, Nantong, 226019, People's Republic of China
akintsov777@mail.ru
ORCID: 0000-0002-1040-1292

NEVECHERIA Artem P.
Kuban State University
149 Stavropolskaya St., Krasnodar, 350040, Russia
artiom1989@mail.ru
ORCID: 0000-0001-6736-4691

KOZHEVNIKOV Vasily Yu.
Institute of High Current Electronics, Siberian Branch of RAS
2/3 Akademichesky Ave., Tomsk, 634055, Russia
Vasily.Y.Kozhevnikov@ieee.org
ORCID: 0000-0001-7499-0578

KOPYTOV Gennadij F.
Moscow State University of Technology and Management
73 Zemlyanoy Val St., Moscow, 109004, Russia
rektorat@mgutm.ru
ORCID: 0000-0003-1378-576X

CAO Tun
Dalian University of Technology
2 Linggong Road, Dalian City, 116024, People's Republic of China
caotun1806@dlut.edu.cn
ORCID: 0000-0003-3536-0092

СВЕДЕНИЯ ОБ АВТОРАХ

АКИНЦОВ Николай Сергеевич — *кандидат физико-математических наук, научный исследователь (постдокторант) Наньтунского университета, научный сотрудник Китайского океанологического университета, г. Наньтун, Китайская Народная Республика.*
226019, People's Republic of China, 40 Qing Nian Dong Lu, Chongchuan
Qu, Nantong Shi, Jiangsu Sheng, Nantong University, Nantong
akintsov777@mail.ru
ORCID: 0000-0002-1040-1292

НЕВЕЧЕРЯ Артём Павлович — *преподаватель кафедры математических и компьютерных методов Кубанского государственного университета, г. Краснодар, Россия.*
350040, Россия, г. Краснодар, Ставропольская ул., 149
artiom1989@mail.ru
ORCID: 0000-0001-6736-4691

КОЖЕВНИКОВ Василий Юрьевич — *доктор физико-математических наук, ведущий научный сотрудник лаборатории теоретической и математической физики Института сильноточной электроники Сибирского отделения РАН (ИСЭ СО РАН).*
634055, Россия, г. Томск, Академический пр., 2/3
Vasily.Y.Kozhevnikov@ieee.org
ORCID: 0000-0001-7499-0578

КОПЫТОВ Геннадий Филиппович — *доктор физико-математических наук, заведующий кафедрой физики Московского государственного университета технологий и управления имени К. Г. Разумовского, Москва, Россия.*
109004, Россия, г. Москва, ул. Земляной Вал, 73.
rektorat@mgutm.ru
ORCID: 0000-0003-1378-576X

ЦАО Тун — *PhD, профессор кафедры биомедицинской инженерии Даляньского технологического университета, г. Далянь, Китайская Народная Республика.*
116024, Китайская Народная Республика., провинция Ляонин, г. Далянь,
Р-н Ганьцзинцзы, ул. Лингун, 2,
caotun1806@dlut.edu.cn
ORCID: 0000-0003-3536-0092

MECHANICS

ACTIVE CONTROL OF BENDING VIBRATIONS OF TIMOSHENKO BEAMS USING STATE OBSERVERS

A. V. Fedotov✉, *A. K. Belyaev*

Institute for Problems of Mechanical Engineering of RAS, St. Petersburg, Russia

✉ alvafed@yandex.ru

Abstract. When describing bending vibrations of elastic beams, the transition from the Bernoulli − Euler model to the Timoshenko model leads to a complication in the dynamic behavior of the beam and to the emergence of new dynamic effects and a new spectrum of vibration modes. The aim of this study is to test control approaches developed for Bernoulli − Euler beams, for thicker beams described by the Timoshenko model, and to study the influence of beam thickness on the efficiency of such approaches. For this purpose, the problem of active damping of forced bending vibrations of simply supported metal beams has been studied numerically using control systems with state observers, where point forces or moments serve as control inputs. It was shown that the proposed approach remained effective for the vibration control problem of Timoshenko beams at lower modes over a wide thickness range of the considered beams.

Keywords: Bernoulli − Euler beam, Timoshenko beam, active vibration control, state observer

АКТИВНОЕ ГАШЕНИЕ ИЗГИБНЫХ КОЛЕБАНИЙ БАЛОК ТИМОШЕНКО С ИСПОЛЬЗОВАНИЕМ НАБЛЮДАТЕЛЕЙ СОСТОЯНИЯ

А. В. Федотов✉, *А. К. Беляев*

Институт проблем машиноведения РАН, Санкт-Петербург, Россия

✉ alvafed@yandex.ru

Аннотация. При описании изгибных колебаний упругих балок переход от модели Бернулли − Эйлера к модели Тимошенко ведет к усложнению динамического поведения балки, появлению новых эффектов и новых форм колебаний. Цель работы − протестировать подходы к управлению, разработанные для балок Бернулли − Эйлера, в применении к более толстым балкам, которые описываются моделью Тимошенко, и исследовать влияние толщины балок на эффективность таких подходов. Для этого проведен численный анализ задачи активного гашения вынужденных колебаний шарнирно-опертых металлических балок с помощью систем управления с наблюдателями состояния, где в качестве управляющих воздействий выступают сосредоточенные силы или моменты. Показано, что для задачи гашения колебаний балки Тимошенко по низшим формам предложенный подход остается эффективным для широкого диапазона значений толщины рассматриваемых балок.

Introduction

While the Bernoulli−Euler model well describes the bending vibrations in thin beams, more complex models are required to describe the dynamics of relatively thick beams. The Timoshenko model differs from the Bernoulli−Euler model by accounting for the shear in beam cross-sections: this means that these cross-sections are not necessarily perpendicular to the beam centerline (the cross-sections remain flat in both models). Additionally, the Timoshenko model accounts for rotational inertia of the beam cross-sections. There are also intermediate models accounting for only one of these two effects (shear or rotational inertia of the cross-sections), but they are inferior to the Timoshenko model in accuracy and are used much less frequently.

The transition from the Bernoulli−Euler model to the Timoshenko model in the problem of free bending vibrations in beams expectedly transforms the solution, complicating it. First, the existing eigenmodes and eigenfrequencies of vibrations are slightly modified: the eigenmodes gain a shear component, while the frequencies are shifted to the left (toward decreasing). Secondly, a completely new part of the spectrum of eigenfrequencies and eigenmodes appears: these are the modes in which shear deformations prevail over bending ones. Thus, the behavior of the beams changes not only quantitatively, but also qualitatively.

Evidently, the influence of these factors becomes more pronounced with increasing thickness of the given beam; also growing with increasing vibration frequency, since the Timoshenko model specifically provides a better description of high-frequency dynamics compared to the Bernoulli−Euler model. Therefore, it is more correct to use the Timoshenko model in problems on high-frequency dynamics of beams, for example, in simulations of damping of elastic waves, [1, 2].

The Bernoulli−Euler model is often used to describe the behavior of thin beams in problems where active vibration suppression is considered not as blocking of elastic waves but as damping of certain vibration modes [3] (in particular, this model was selected in several of our earlier studies [4, 5]). The natural questions, then, are how an increase in beam thickness influences the efficiency of control in such problems and at what point this influence becomes significant.

To find answers to these questions, it is necessary to make a transition to the Timoshenko model, considering several cases with beams of different thicknesses.

Several studies confirmed that effective active damping of Timoshenko beam vibrations can be achieved with piezoelectric sensors and actuators using both the proportional control law [6] and state observers [7]. However, these studies did not compare the efficiency of control systems (CS) for beams of different thicknesses. It was shown in [8] that using the control law synthesized for the Bernoulli−Euler beam to dampen the vibrations of the Timoshenko beam can lead to instability of a closed system.

Thus, the influence of the factors inherent to the Timoshenko model on the operation of systems for controlling beam vibrations remains an important issue.

This paper continues the research carried out in [4, 5], reporting on the control of vibrations in elastic beams using observers was.

The goal of this study consists in numerical analysis of the influence of contributors in the Timoshenko model appearing with an increase in beam thickness on the efficiency of control systems for active damping of beam vibrations using observers.

In this study, the thickness of the beam varies over a wide range of values: from 1/250 to 1/10 of the length of the beam. The control inputs considered are either concentrated forces (in this

case, the transverse displacements of the beam in the corresponding cross-sections are fed to the input of the control system) or concentrated moments (in this case, the rotation angles of the corresponding cross-sections of the beam are measured).

Optimization methods involving formulation and solution of matrix Riccati equations are widely used to synthesize optimal control systems with an observer. However, this approach to synthesis of CS cannot be directly applied in this study, since the size of the elements of the observation and control matrices in the problem considered is limited not by the factors adopted within the framework of this approach, but by others.

These limiting factors in the standard formulation of the optimization problem are the dependence of the quality functional on the magnitude of the control inputs (for the control matrix) and the measurement noise (for the observation matrix). On the contrary, the limiting factor in this study is the excitation of higher modes by the CS which are not controlled, because of the phase shift in control inputs due to a delay in the control loop (the so-called spillover effect). Accounting for this particular factor as the main one is dictated by our experience in cnducting experimental studies on active damping of metal beam vibrations in a metal beam [9].

An alternative approach to optimal synthesis of CS is the Linear Matrix Inequalities (LMI) method, however, the given problems are not directly reduced to LMI for the case of control with an observer, so this method is also ineffective in this study. In view of this circumstance, the synthesis of CS in the study was carried out by the Nelder−Mead numerical optimization method.

Peculiarities of the Timoshenko beam model

The Bernoulli−Euler beam model is widely used to describe the bending vibrations in thin beams. This model is based on the assumption that the cross-sections of the beam always remain perpendicular to its centerline (i.e., there is no cross-section shear). Thus, the state of the beam under bending deformation is fully described by the transverse displacement function of the beam centerline depending on the longitudinal coordinate. Furthermore, this model does not account for the rotational inertia of the beam cross-sections.

A model describing bending vibrations in thicker beams was proposed by Stepan Timoshenko in 1921 [10]. This model accounts for both the shear deformation and the rotational inertia of the beam cross-sections. Thus, the Timoshenko model uses two functions of the longitudinal coordinate to fully describe the dynamics of the beam: the transverse displacement w and the rotation angle of the cross-section φ. The equations of bending vibrations of the beam for the model under consideration can be written as follows (for simplicity, we assume that the beam has a constant cross-section):

$$\begin{cases} \rho A \ddot{w} + \kappa A G \left(\varphi' - w'' \right) = q, \\ \rho I \ddot{\varphi} + \kappa A G \left(\varphi - w' \right) - E I \varphi'' = m, \end{cases} \tag{1}$$

where ρ is the bulk density of the beam material; A and I are the area and moment of inertia of the beam cross-sections; E and G are Young's modulus and shear modulus of the beam material; κ is the dimensionless Timoshenko shear coefficient (depends on the shape of the beam section and is commonly taken equal to 5/6 for a rectangular cross-section); q, m are the distributed transverse force and the bending moment applied to the beam.

The two second-order equations above can be combined into one fourth-order equation for the beam's transverse displacement w:

$$EI \frac{d^4 w}{dx^4} + \rho A \ddot{w} - \rho I \left(1 + \frac{E}{\kappa G} \right) \ddot{w}'' + \frac{\rho^2 I}{\kappa G} \frac{d^4 w}{dt^4} = q + \frac{\rho I}{\kappa A G} \ddot{q} - \frac{EI}{\kappa A G} q'' - m'. \tag{2}$$

If the shear stiffness of the beam $\kappa A G$ tends to infinity and we neglect the rotational inertia of the beam cross-sections ρI, the distinctive effects of the Timoshenko model disappear, and Eq. (2) is reduced to an equation describing the bending vibrations of the Bernoulli−Euler beam.

The solution to the problem of free beam vibrations is significantly transformed with the transition from the Bernoulli−Euler beam model to the Timoshenko model. Details of the solution

to this problem for the Timoshenko model are discussed in [11, 12]; in particular, a simply supported beam and its set of eigenfrequencies and eigenmodes are considered.

A similar formulation of the problem is used in this study. The complete solution is rather cumbersome, so here we will briefly provide only basic information about it.

The solution to the problem of free vibrations in a Bernoulli−Euler beam is an infinite series (spectrum) of eigenfrequencies and their corresponding eigenmodes. The frequency spectrum has a lower bound (the first eigenfrequency), but there is no upper bound. The Timoshenko model is the more complex form of the Bernoulli−Euler model, so the solution for it contains all the same elements, i.e., frequencies and modes, but with a certain correction: the frequencies decrease slightly, and the modes acquire a shear component; in addition, the model adds new solutions: frequencies and their corresponding modes.

Thus, a new frequency spectrum is added, and this spectrum also has a lower bound, the transition frequency:

$$\Omega^* = \sqrt{\frac{\kappa A G}{\rho I}}. \tag{3}$$

The presence of an eigenmode corresponding to the given frequency depends on the boundary conditions. In the case of a simply supported beam, this mode exists and represents the rotation of all beam cross-sections by the same angle (i.e., constant shear deformation along the length of the beam) in the absence of transverse displacement. The new part of the spectrum originating from the transition frequency includes vibration modes for which shear deformations prevail over bending ones. The frequencies in this region of the spectrum also grow to infinity with an increase in the sequence number.

Problem statement

The goal of the study is to synthesize CS with observers and numerically compare their efficiency for active damping of forced bending vibrations in Timoshenko beams with different thicknesses.

A schematic of the beam with applied input for two configurations of control elements considered is shown in Fig. 1. A 1 m long simply supported aluminum beam with a rectangular cross-section is subjected to an external perturbation, which is a concentrated bending moment M_0 applied to the beam at a distance of 0.4 m from the left end. The study considers three cases of beams with different cross-sections: 4×25 mm, 20×25 mm and 10×10 cm.
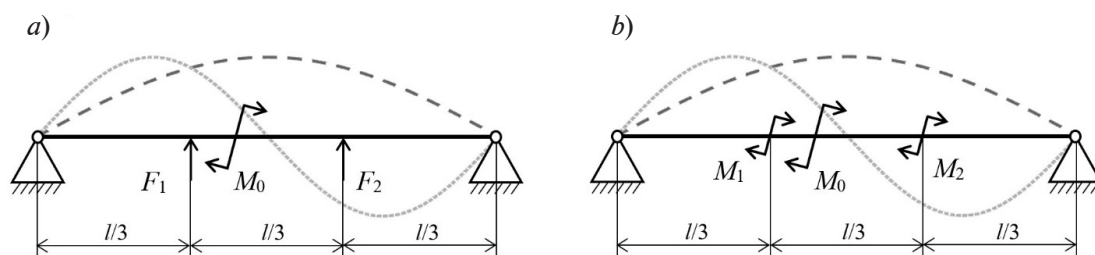
Fig. 1. Schematics of control object with applied control inputs:
concentrated forces F_1 and F_2 (a), concentrated moments M_1 and M_2 (b);
beam length l, external bending moment M_0

The paper considers two configurations of the CS.

Case A. The sensors measure the transverse displacement in two cross-sections of the beam, dividing it into three equal parts, and the control input consists of concentrated transverse forces applied in the same cross-sections.

Case B. The control system is designed differently from case A in that the it is the rotation angles of these cross-sections that are measured and the input is applied as concentrated bending moments.

Control is aimed at dampening forced vibrations at the two lowest resonant frequencies of the beam. The vibration modes corresponding to these frequencies (more precisely, their components in the form of transverse displacement, since there are also other components in the form of rotation angles) are also shown in Fig. 1.

In this paper, we consider CS with observers, widely used for feedback control in the case when the state of an object cannot be directly measured and an adequate model of the object is known. A detailed mathematical description of this method with respect to the problems considered in this paper can be found in our earlier works [4, 5]. To set each such CS, it is necessary to define the observation and control matrices; the Nelder−Mead optimization method built into the computing package used was selected for this purpose in our study. Then the results generated by the synthesized systems for beams of different thicknesses are compared.

Modeling of object without control

Before constructing CS, it is necessary to model the object itself. This section is dedicated to modeling of beams without control. It consists of the expansion in terms of the beam's vibration eigenmodes, calculated together with the eigenfrequencies using the Timoshenko beam model.

First of all, we should verify that the mathematical model of beam behavior used is correct, subsequently determining the number of eigenmodes in the model sufficient to adequately describe the required dynamics. For this purpose, the frequency response obtained for this model as an eigenmode expansion were compared with the frequency response obtained for beams with the same parameters by finite element analysis.

Three-node beam elements were used in all FE models. The beam was divided into 200 elements with a length of 5 mm, each model contained a total of 401 nodes.
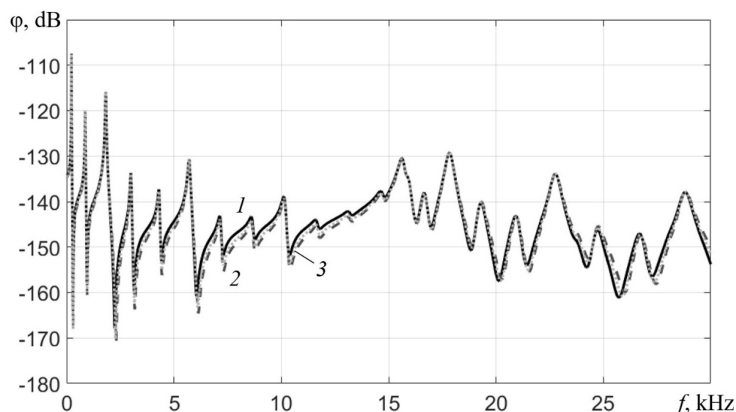
Fig. 2. Comparison of the frequency response for moment versus rotation angle in beam III (10 cm thick) obtained for two models: FE (curve *1*) and models with eigenmode expansion (curves *2*, *3*), taking into account 41 (*2*) and 71 (*3*) modes

Fig. 2 shows the frequency response of beam III (the thickest one, with the thickness of 10 cm), calculated by applying the first (left) concentrated control moment to the beam and measuring the rotation angle in the same cross-section (obtained by both methods). Two solutions are given for two numbers of eigenmodes taken into account for the second of these models:

configuration *A* consists of 25 traditional modes (their equivalents are included in the Bernoulli−Euler beam model), one transitional mode, and 15 shear-dominated forms from the new spectrum of the Timoshenko model;

configuration *B* consists of 45 traditional modes, one transitional mode and 25 shear mode.

The ordinate axis on the frequency response curves here and below has a logarithmic scale, therefore, the quantities plotted along this axis (transverse displacement or rotation angle) are measured in decibels (dB).

As evident from Fig. 2, there is a good agreement between the two models considered, and the proposed number of modes taken into account (45 + 1 + 25) turns out to be sufficient for an adequate description of beam dynamics within the framework of the problem solved in a wide frequency range. A similar comparison was carried out for two other beam configurations (I and II), with the following numbers of modes taken into account in the simulations selected for them:

45 + 1 + 25 for beam II (same as for beam III),
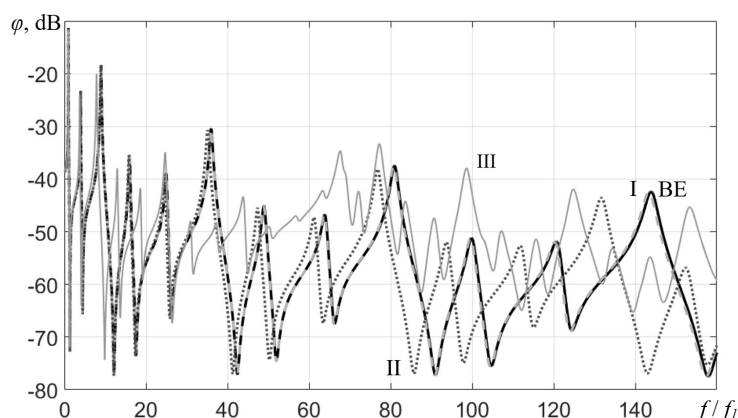
45 for beam I (traditional vibration modes).

Fig. 3. Comparison of frequency response for moment versus rotation angle φ in Timoshenko beams I–III taking into account scaling (curve numbers correspond to beam numbers): beam I taking into account 45 modes; beams II and III both taking into account 71 modes; Bernoulli–Euler beam model taking into account 45 modes (BE curve)

The frequency f is normalized by the frequency of the first resonance f_1 for each of the beams

The comparison shows that the eigenmode expansion of the Timoshenko beam model used in the study is correct.

It should be noted here that with the beam dimensions adopted (length of 1 m, thickness of 10 cm), the finite element beam model itself, like the Timoshenko model, may not be entirely accurate due to the warping of the beam cross-sections. Investigation of this circumstance is beyond the scope of this work, since our goal was to compare the Timoshenko and Bernoulli–Euler models, and the thickness-to-length ratio (1:10) of beam III was chosen as the limit for the correct use of the Timoshenko model.

When an adequate model of the object is selected, it becomes possible to compare the frequency response for beams of different thicknesses. Such a comparison is of particular interest, since it is the differences between these frequencies that will have the key influence on the synthesis process and the efficiency of CS constructed for each of the beams.

Fig. 3 shows a comparison of the frequency characteristics obtained for the first control moment acting on the beam, measuring the rotation angle in the same section for each of the beams. To compare these characteristics in the same graph, it is necessary to coordinate their scale on both axes. The frequencies along the abscissa axis were normalized by the frequency of the first resonance of each beam, since this value increases exactly by n times with an increase in the thickness of the Bernoulli–Euler beam by n times. The rotation angles of the cross-section (ordinate axis) were also normalized, since the vibration amplitude of the Bernoulli–Euler beam decreases by n^3 times with an increase in its thickness of beam by n times and by n times with an increase in width. Moreover, the vibration amplitude of the beam decreases inversely with an increase in beam width, and the width of beam III, as mentioned earlier, is 4 times the width of beams I and II. For this reason, the values of the rotation angles in this graph were multiplied by 125 for beam II, and by 62,500 for beam III (the ordinate axis in Fig. 3 also has a logarithmic scale, and the logarithm of the angle was calculated after multiplying it by a multiplying factor).

Fig. 3 also shows the reference characteristic corresponding to the Bernoulli–Euler beam model (its BE curve nearly coincides with the curve for beam I).

Importantly, if this particular model were used for beams of different thicknesses, then all the curves on the graph would have coincided with the reference one. Furthermore, all synthesis results and efficiency indicators of CS for different beams would also have been the same with an accuracy up to the similarity coefficients. Therefore, the graph shown in Fig. 3 illustrates precisely the influence of the Timoshenko beam model, becoming more pronounced with increasing beam thickness.

Let us analyze how the influence of the Tymoshenko model manifests on the graph. A comparison of the curves for beams I and II shows that the resonant frequencies are shifted to the left (towards a decrease) and this shift increases with increasing frequency. This is even more pronounced for beam III, where a new factor is also noticeable: a significant change in the structure of the solution to the right of a certain boundary. This boundary is located in the vicinity of the transition frequency (mentioned earlier in the section on the characteristics of the Timoshenko model): for beam III, it exceeds the first eigenfrequency by about 68 times. A new part is added to the spectrum present in the Bernoulli–Euler model starting from this transition

frequency: modes with a predominant shear component. This feature is not observed on the graph for beams I and II, since for them the value of the transition frequency significantly (by several orders of magnitude) exceeds the value of the first eigenfrequency, therefore not falling within the considered range.

Synthesis of control systems

Consider the operation of CS with state observers used to actively dampen beam vibrations in this study. Only the basic equations are given here; a more detailed description of this method as applied to the problems considered in this paper can be found in [4, 5].

We assume that n lower vibration modes must be taken into account for satisfactory description of the dynamics of an object. We introduce the state vector q^n:

$$q^n = \begin{pmatrix} q_1 & \dots & q_n & \dot{q}_1 & \dots & \dot{q}_n \end{pmatrix}^T, \tag{4}$$

where q_i is the generalized coordinate corresponding to the ith mode of the beam's vibrations; $\dot{q}_i$ is the generalized velocity.

In this case, the object's behavior can be described by the following equations:

$$\dot{q}^n = Aq^n + Bu + Dd, \tag{5}$$

$$y = Cq^n, \tag{6}$$

where d is the vector of external perturbations; y, u are the vectors of measured signals and control inputs; A, B, C are the matrices defining the behavior of the object and its interaction with drives (actuators) and sensors.

We assume that observation and control are carried out for k lowest vibration modes of the object ($k \leq n$). The observer's objective is to evaluate the state vector q^k corresponding to these modes:

$$q^k = \begin{pmatrix} q_1 & \dots & q_k & \dot{q}_1 & \dots & \dot{q}_k \end{pmatrix}^T. \tag{7}$$

The observer forms an estimate of this vector $\hat{q}$ using the known matrices $A^{(1)}$, $B^{(1)}$, $C^{(1)}$ describing the dynamics of the k lowest modes of the object and this estimate is then used to define the vector of control inputs:

$$\dot{\hat{q}} = A^{(1)}\hat{q} + B^{(1)}u + L\left(y - C^{(1)}\hat{q}\right), \tag{8}$$

$$u = -R\hat{q}, \tag{9}$$

where L, R are the observation and control matrices that must be set correctly (so that the control objective is achieved).

Within framework of this study, we consider the matrices $A^{(1)}$, $B^{(1)}$ and $C^{(1)}$ to be known (they are obtained from matrices A, B and C by eliminating unnecessary columns and rows), so only the matrices L and R are to be determined to define the CS. Observation and control in the given problem are carried out for two modes using two sensors and two actuators. Since observation and control of these modes are carried out separately, the matrices L and R can be set as follows [5]:

$$L_{4\times2} = \begin{bmatrix} K^L_{2\times2} \\ K^{Ld}_{2\times2} \end{bmatrix} T_{2\times2}, \quad R_{2\times4} = F_{2\times2}\begin{bmatrix} K^R_{2\times2} & K^{Rd}_{2\times2} \end{bmatrix}, \tag{10}$$

where K^L, K^{Ld}, K^R, K^{Rd} are 2×2 diagonal matrices; T, F are modal matrices (mode analyzer and synthesizer) [4, 5, 9], determining how each control loop uses each sensor and actuator in its operation.

Since the sensors and actuators are located symmetrically on the beam, and the beam's eigenmodes are symmetrical or antisymmetric, the modal matrices in this study have a specific form, presented below. In the case when the transverse displacement is measured and the control input is applied as concentrated forces, they can be set as follows:

133

$$T^{(1)} = \begin{bmatrix} 0.5 & 0.5 \\ 0.5 & -0.5 \end{bmatrix}, \; F^{(1)} = \begin{bmatrix} 1 & 1 \\ 1 & -1 \end{bmatrix}. \tag{11}$$

In the case when the rotation angles are measured, and the control inputs are concentrated moments, the modal matrices take the form:

$$T^{(2)} = \begin{bmatrix} 0.5 & -0.5 \\ 0.5 & 0.5 \end{bmatrix}, \; F^{(2)} = \begin{bmatrix} 1 & 1 \\ -1 & 1 \end{bmatrix}. \tag{12}$$

Thus, taking into account the structure of the matrices K^L, K^{Ld}, K^R and K^{Rd} to be set (they are diagonal and have the size of 2×2), it is necessary to optimally select 8 parameters to fully define the CS in the case of simultaneous damping of two vibration modes. If the objective of the CS is to dampen only one of the resonances, then only 4 parameters should be determined.

The optimization problem for the given number of parameters was solved by the Nelder−Meade optimization method. The objective function for damping of a single mode was the height of the corresponding resonant peak on the frequency response of the beam with the control switched on. If both modes were to be damped, the objective function was set as the sum of the heights of both resonant peaks. In addition, a penalty was added to this function in case of violation of stability margins in the closed system.

The Nyquist criterion was used for stability analysis, modified for the case of two inputs and two outputs of the control system (it is described in detail in [13]). The aspects of numerical simulation of a closed system with observers are discussed in [4]. It contains, in particular, a formulation of the problem where a link simulating a delay with the transfer function $R^{del}(s)$ is introduced into the control loop:

$$R^{del}(s) = \frac{1}{1 + \tau s}, \tag{13}$$

where τ is the time constant and s is the complex variable.

This exact formulation is used in this study. To preserve the similarity of the problem formulations for different beams, a specific time constant is selected in each formulation:

$$\tau_I = 0.005 \text{ s}, \; \tau_{II} = \frac{1}{5}\tau_I = 0.001 \text{ s}, \; \tau_{III} = \frac{1}{25}\tau_I = 0.0002 \text{ s}, \tag{14}$$

where τ_i is the time constant for controlling the oscillations of the ith beam.

Example. As an example, consider the one of the synthesized systems, namely, the system for beam II (cross-section of 20x25 mm), measuring angles and controlling moments while simultaneously damping the first and second vibration modes of the beam. The diagonal matrices defining observation and control were obtained in the following form:

$$\begin{cases} K^L = \begin{bmatrix} -81.63 & 0 \\ 0 & -63.24 \end{bmatrix}, & K^{Ld} = \begin{bmatrix} 76.01 & 0 \\ 0 & 79.78 \end{bmatrix} \cdot 10^3, \\ K^R = \begin{bmatrix} -53.93 & 0 \\ 0 & 13.82 \end{bmatrix} \cdot 10^2, & K^{Rd} = \begin{bmatrix} 37.25 & 0 \\ 0 & -149.3 \end{bmatrix}. \end{cases} \tag{15}$$

Fig. 4 shows a Nyquist plot for the resulting system (the general view and an enlarged fragment of the vicinity of the origin). The stability margins for all synthesized CS were set such that the system's Nyquist plot did not intersect a circle with 0.5 radius centered at (− 1.0) (this corresponds to an amplitude margin of 6 dB and a phase margin of 29°). Evidently, all stability requirements are satisfied for this CS.
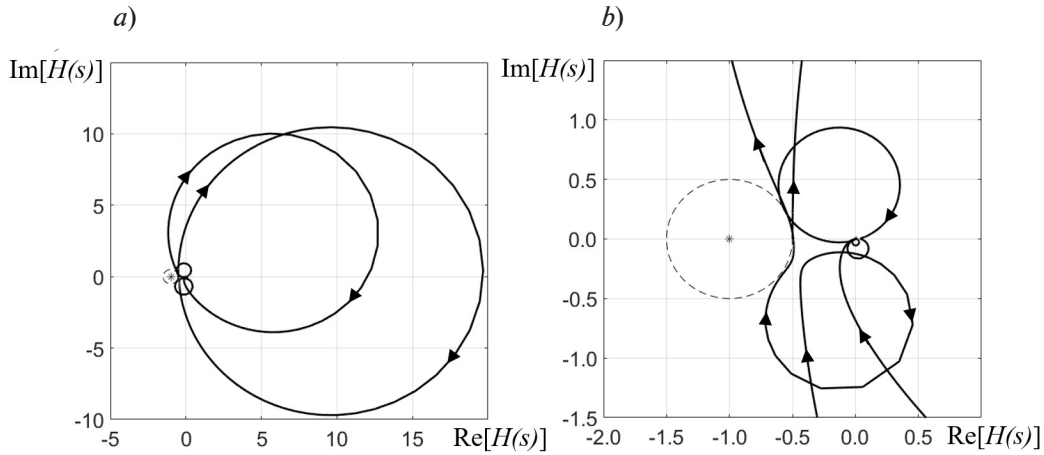
Fig. 4. Example of a Nyquist plot for one of the synthesized control systems:
general view (*a*), enlarged fragment (*b*)

Comparison of results obtained from different CS

This section provides an overview of the results obtained from all synthesized CS for beams of different thicknesses.

As already noted, to determine the efficiency of control, the values of the height *y* of the first and second resonant peaks on the frequency response of the beam with control were analyzed against the height of these peaks in the absence of control. The choice of the frequency response curve itself should be explained: we considered the total energy of steady-state vibrations of the beam exposed to a harmonically varying external perturbation in the form of a concentrated moment, depending on the frequency of the applied input. This quantity was calculated by the following formula for each value of the frequency ω:

$$E(\omega) = \sum_{i=1}^{n} \omega^2 Q_i^2(\omega),$$ (16)

where Q_i is the steady-state amplitude of the *i*th generalized coordinate of the vibration mode, n is the number of generalized coordinates (beam vibration modes) in the model.

As with all frequency characteristics in this study, the amplitude of the quantity considered here was expressed in decibels (dB).

Expression (16) corresponds to the total energy of beam vibrations, since all vibration modes (with transverse displacement $X_i(x)$ and rotation $_i(x)$ components) are normalized as:

$$w(x,t) = \sum_{i=1}^{n} X_i(x) q_i(t), \ \varphi(x,t) = \sum_{i=1}^{n} \Phi_i(x) q_i(t)$$ (17)

$$\int_0^l \left(\rho A X_i(x) X_j(x) + \rho I \Phi_i(x) \Phi_j(x) \right) dx = \delta_{ij}$$ (18)

where δ_{ij} is the Kronecker symbol.

The control results for all systems are summarized in Table. A decrease in amplitude at the first (Res1) and second (Res2) resonances as a result of control is observed for all three beams, cases of control using both concentrated forces and moments are considered. Vibration damping was carried out either for only one of the modes, or simultaneously for both modes for each formulation. The best results for each beam and each of the resonances are highlighted in bold.

Fig. 5 shows the frequency response of beams with and without control for CS simultaneously operating at both resonances. To compare the results obtained for different beams on the same graph, the frequency response was scaled along both axes as done in Fig. 3.

Table

**Decrease in beam vibration amplitudes at resonance
for different control systems**

Beam	Control method	Damping scenario	Amplitude decrease, dB, at resonance	
			Res1 (Δy_1)	Res2 (Δy_2)
I (*1, 4a, 4b*)	Forces	Separately	**35.47**	29.4
		Together	34.05	**29.5**
	Moments	Separately	31.18	25.91
		Together	30.16	24.78
II (*2, 5a, 5b*)	Forces	Separately	35.44	29.73
		Together	33.79	**29.73**
	Moments	Separately	31.14	25.93
		Together	30.16	24.77
III (*3, 6a, 6b*)	Forces	Separately	35.03	27.9
		Together	34.16	**27.9**
	Moments	Separately	30.59	25.21
		Together	29.79	23.97

N o t e . The numbers of the curves in Fig. 5 corresponding to each beam are given in parentheses in the left column.

Analyzing the data in Table and Fig. 5, we can conclude that the CS obtained make it possible to efficiently dampen the forced vibrations of the beam at both the first and second resonances. The main conclusion is that the efficiency of the synthesized CS only changes insignificantly as the beam thickness increases over a wide range. This means that the considered control method allows to efficiently control the vibrations in not only thin but also relatively thick beams. A noticeable trend is that the damping efficiency decreases slightly with increasing thickness of the beam both at each resonance in the case of separate damping and as the sum of parameters at both resonances in the case of simultaneous damping. This effect is almost unnoticeable for the results for beams I and II compared but manifests clearly for beam III. A possible explanation for this result is that the frequency response curves are virtually identical at low frequencies for beams I and II in the absence of control, while the resonant peaks on the frequency response curve of beam III shift to the left with increasing frequency, compared with the frequency response of
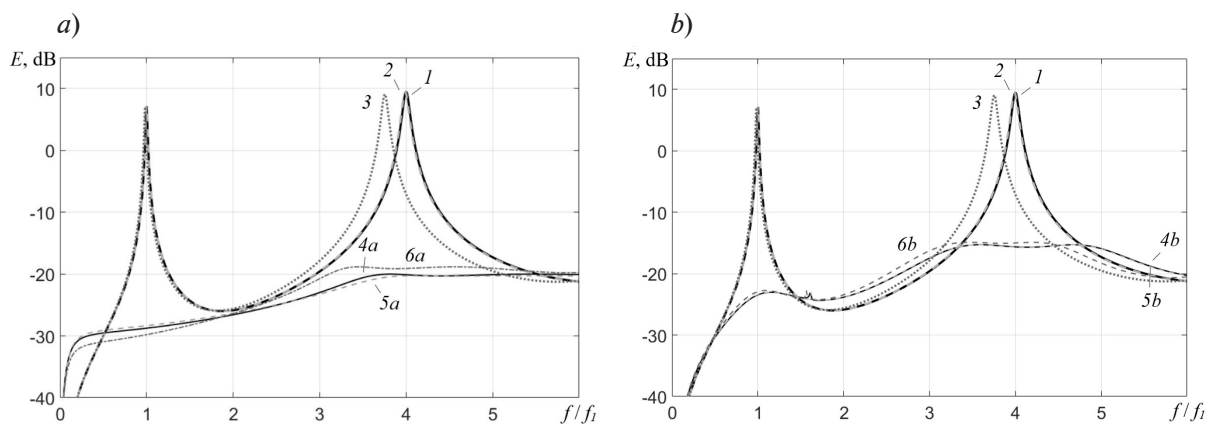

Fig. 5. Frequency response for beams I− III (*a, b*) without control (curves *1−3*),
with force-based control (curves *4a−6a*)
and with moment-based control (curves *4b−6b*) (see Table)

thinner beams; accordingly, the gains in the CS are more noticeably limited by the deterioration in stability at higher frequencies and the efficiency of the CS decreases.

Notably, the observed difference is caused not so much by the influence of the new part of the frequency spectrum and the corresponding shear modes found in the solution to the problem on the Timoshenko beam vibrations, but rather by the 'deformation' of its scaled frequency response near the lower resonant frequencies with increasing beam thickness (this effect can also be observed in Fig. 3). The influence of the new part of the spectrum is small, since the transition frequency bounding this part of the spectrum from below for all the beams considered significantly exceeds the cutoff frequency of the open system for all synthesized CS (even in the case of beam III, the first quantity is about an order of magnitude higher than the second and the difference is even more significant for the remaining beams).

In addition, the presented results show that control using displacements and concentrated forces is carried out far more efficiently than with systems using rotation angles and concentrated moments. This is explained by the fact that the resonant amplitudes on the force−displacement curve of the beam (without control) decrease significantly faster with increasing frequency than on moment−rotation angle curve, i.e., the influence of control for the first systems is more pronounced at lower frequencies than at higher ones, therefore, the damping efficiency at lower frequencies increases, and the decrease in stability at high frequencies decreases.

Another observation concerns the results given in Table: as a rule, the vibrations at the first and second resonances are dampened individually somewhat more efficiently than together, this effect is characteristic of CS both with and without observers, as discussed in our earlier studies [4, 5]. An explanation for this result is that when two loops are switched on simultaneously in the CS, the degree of stability of the closed system decreases, so the gain coefficients must be reduced, consequently decreasing the efficiency of the CS.

Conclusion

The paper considers the problem of active damping of forced vibrations in metal beams using control systems with state observers. We analyzed the influence of beam thickness on control efficiency. For this purpose, the problem was solved numerically using the Timoshenko beam model for different beam thicknesses, varying over a wide range. The study focuses specifically on the effects of the Timoshenko model, since the Bernoulli−Euler model would yield identical results for the dynamics of beams with different thicknesses.

We found that the proposed CS remain efficient for all the beams considered in the case of damping beam vibrations at lower resonances. Only a slight decrease in vibration damping efficiency was observed with a significant increase in beam thickness; a reasonable explanation was given for this effect.

The following directions are of the greatest interest for future studies:

modeling of beam vibration control using specific piezoelectric sensors and actuators,

damping of beam vibrations at higher resonant frequencies,

variation of the object model in the observer, including the expansion of the number of beam eigenmodes included in this model.

Other promising directions are accounting for cross-section warping for thick beams and measurement noise during synthesis of the control system, as well as analysis of various quality functionals for optimization of the parameters of the control system. It is also of interest to solve the problem on damping of elastic waves in the Timoshenko beam.

REFERENCES

1. **Carvalho M. O. M., Zindeluk M.,** Active control of waves in a Timoshenko beam, Int. J. Solid. Struct. 38 (10−13) (2001) 1749−1764.

2. **Mei C.,** Hybrid wave/mode active control of bending vibrations in beams based on the advanced Timoshenko theory, J. Sound Vib. 322 (1−2) (2009) 29−38.

3. **Selivanov A., Fridman E.,** Disturbance attenuation in the Euler−Bernoulli beam with viscous and Kelvin − Voigt damping via piezoelectric actuators, Proc. 62nd IEEE Conf. Decision and Control (CDO), Dec. 13−15, 2023, Marina Bay Sands, Singapore (2023) 1961−1966.

4. **Fedotov A. V., Belyaev A. K., Polyanskiy V. A.,** Numerical study of the efficiency of modal filter method and observer method for implementation of modal control of vibrations of elastic systems, St. Petersburg State Polytechnical University Journal. Physics and Mathematics. 16 (3) (2023) 160−176 (in Russian).

5. **Fedotov A. V.,** A comparison of approaches to specifying the modal matrices in the modal control of elastic systems with and without observers, St. Petersburg State Polytechnical University Journal. Physics and Mathematics. 17 (1) (2024) 114−129. (in Russian).

6. **Yildirim K., Kucuk I.,** Active piezoelectric vibration control for a Timoshenko beam, J. Frank. Inst. 353 (1) (2016) 95−107.

7. **Li X., Agarwal R. K., Shue S.-P.,** Active control of Timoshenko beam vibrations using piezoelectric material, Proc. 40th Struct. Struct. Dyn. Mater. Conf. Exhibit, 12−15 Apr. 1999, St. Lous, MO, USA (1999) 894−902.

8. **Aldraihem O. J., Wetherhold R. C., Singh T.,** Distributed control of laminated beams: Timoshenko theory vs. Euler − Bernoulli theory, J. Intel. Mat. Syst. Struct. 8 (2) (1997) 149−157.

9. **Belyaev A. K., Fedotov A. V., Irschik H., et al.,** Experimental study of local and modal approaches to active vibration control of elastic systems, Struct. Control Health Monit. 25 (8) (2018) e2105.

10. **Timoshenko S. P.,** LXVI. On the correction for shear of the differential equation for transverse vibrations of prismatic bars, Lond., Edinb., Dubl. Phil. Mag. (Ser. 6). 41 (245) (1921) 744−746.

11. **Cazzani A., Stochino F., Turco E.,** On the whole spectrum of Timoshenko beams. Part I: a theoretical revisitation, Zeit. angew. Math. Phys. 67 (24) (2016) 1−30.

12. **Cazzani A., Stochino F., Turco E.** On the whole spectrum of Timoshenko beams. Part II: further applications, Zeit. angew. Math. Phys. 67 (25) (2016) 1−22.

13. **Fedotov A. V.,** The damping of the distributed system vibrations using piezoelectric transducers: simulation, St. Petersburg Polytechnical State University Journal. Physics and Mathematics. 12 (1) (2019) 142−155. (in Russian).

СПИСОК ЛИТЕРАТУРЫ

1. **Carvalho M. O. M., Zindeluk M.** Active control of waves in a Timoshenko beam // International Journal of Solids and Structures. 2001. Vol. 38. No. 10−13. Pp. 1749−1764.

2. **Mei C.** Hybrid wave/mode active control of bending vibrations in beams based on the advanced Timoshenko theory // Journal of Sound and Vibration. 2009. Vol. 322. No. 1−2. Pp. 29−38.

3. **Selivanov A., Fridman E.** Disturbance attenuation in the Euler−Bernoulli beam with viscous and Kelvin − Voigt damping via piezoelectric actuators // Proceedings of the 62nd IEEE Conference on Decision and Control (CDO). December 13−15, 2023. Marina Bay Sands, Singapore, Pp. 1961−1966.

4. **Федотов А. В., Беляев А. К., Полянский В. А.** Численное исследование эффективности метода модальных фильтров и метода наблюдателей при реализации модального управления колебаниями упругих систем // Научно-технические ведомости СПбГПУ. Физико-математические науки. 2023. Т. 16. № 3. С. 160−176.

5. **Федотов А. В.** Сравнение подходов к заданию модальных матриц при модальном управлении упругими системами с наблюдателями и без них // Научно-технические ведомости СПбГПУ. Физико-математические науки. 2024. Т. 17. № 1. С. 114−129.

6. **Yildirim K., Kucuk I.** Active piezoelectric vibration control for a Timoshenko beam // Journal of the Franklin Institute. 2016. Vol. 353. No. 1. Pp. 95−107.

7. **Li X., Agarwal R. K., Shue S.-P.** Active control of Timoshenko beam vibrations using piezoelectric material // Proceedings of the 40th Structures, Structural Dynamics, and Materials Conference and Exhibit. 12−15 April 1999, St. Lous, MO, USA. Pp. 894−902.

8. **Aldraihem O. J., Wetherhold R. C., Singh T.** Distributed control of laminated beams: Timoshenko theory vs. Euler–Bernoulli theory // Journal of Intelligent Material Systems and Structures. 1997. Vol. 8. No. 2. Pp. 149–157.

9. **Belyaev A. K., Fedotov A. V., Irschik H., Nader M., Polyanskiy V. A., Smirnova N. A.** Experimental study of local and modal approaches to active vibration control of elastic systems // Structural Control and Health Monitoring. 2018. Vol. 25. No. 8. P. e2105.

10. **Timoshenko S. P.** LXVI. On the correction for shear of the differential equation for transverse vibrations of prismatic bars // The London, Edinburg and Dublin Philosophical Magazine (Series 6). 1921. Vol. 41. No. 245. Pp. 744–746.

11. **Cazzani A., Stochino F., Turco E.** On the whole spectrum of Timoshenko beams. Part I: a theoretical revisitation // Zeitschrift fьr angewandte Mathematik und Physik. 2016. Vol. 67. No. 24. Pp. 1–30.

12. **Cazzani A., Stochino F., Turco E.** On the whole spectrum of Timoshenko beams. Part II: further applications // Zeitschrift fьr angewandte Mathematik und Physik. 2016. Vol. 67. No. 25. Pp. 1–22.

13. **Федотов А. В.** Численное моделирование гашения колебаний распределенной системы с помощью пьезоэлементов // Научно-технические ведомости СПбГПУ. Физико-математические науки. 2019. Т. 12. № 1. С. 142–155.

THE AUTHORS

FEDOTOV Aleksandr V.
Institute for Problems of Mechanical Engineering of RAS
61 Bolshoi Ave., V. Isl., St. Petersburg, 199178, Russia
alvafed@yandex.ru
ORCID: 0000-0001-6028-7566

BELYAEV Alexander K.
Institute for Problems of Mechanical Engineering of RAS
61 Bolshoi Ave., V. Isl., St. Petersburg, 199178, Russia
13augen@mail.ru
ORCID: 0000-0002-5934-8138

СВЕДЕНИЯ ОБ АВТОРАХ

ФЕДОТОВ Александр Васильевич – *кандидат технических наук, старший научный сотрудник лаборатории мехатроники Института проблем машиноведения РАН.*

199178, Россия, г. Санкт-Петербург, Большой проспект В. О., 61.

alvafed@yandex.ru

ORCID: 0000-0001-6028-7566

Беляев Александр Константинович – *член-корреспондент Российской академии наук, доктор физико-математических наук, главный научный сотрудник, заведующий лабораторией мехатроники Института проблем машиноведения РАН.*

199178, Россия, г. Санкт-Петербург, Большой проспект В. О., 61.

13augen@mail.ru

ORCID: 0000-0002-5934-8138

MECHANICS

A SOLUTION TO THE PROBLEM OF ELASTICITY CAUSED BY MASS TRANSPORT IN THE PRESENCE OF IMPERFECT CONTACTS AT THE INTERNAL INTERFACES OF A TWO-PHASE MATERIAL

K. P. Frolova[1]✉, *N. M. Bessonov*[1], *E. N. Vilchevskaya*[2]

[1] Institute for Problems in Mechanical Engineering RAS, St. Petersburg, Russia;

[2] Technical University of Berlin, Berlin, Germany

✉ fkp@ipme.ru

Abstract. The paper studies the influence of imperfect contacts (IC) at the phase interfaces of a micro-heterogeneous material on the macroscopic transport of impurity and the stress-strain state caused by its accumulation. Two types of IC are considered: segregation, which involves the accumulation of impurity that disrupts the continuity of concentration, and the formation of bypass paths for accelerated diffusion, which disrupts the continuity of the normal component of the flux. Modeling the coupled processes of mass transport and changes in the stress-strain state of the medium consists of two stages. In the first stage, the effective diffusion permeability of the material is determined using micromechanical methods. In the second stage, the macroscopic elasticity problem caused by mass transport is solved. The analysis is carried out using the example of a long cylinder, which is a two-phase material at the micro-level, consisting of a matrix and less permeable prolate spheroidal inhomogeneities with an arbitrary distribution of orientations.

Keywords: diffusion, elasticity due to mass transport, effective properties, imperfect contact, phase interface, two-phase material

РЕШЕНИЕ ЗАДАЧИ МАССОУПРУГОСТИ ПРИ НАЛИЧИИ НЕИДЕАЛЬНЫХ КОНТАКТОВ НА ВНУТРЕННИХ ГРАНИЦАХ ДВУХФАЗНОГО МАТЕРИАЛА

К. П. Фролова[1]✉, Н. М. Бессонов[1], Е. Н. Вильчевская[2]

[1] Институт проблем машиноведения РАН, Санкт-Петербург, Россия;

[2] Берлинский технический университет, г. Берлин, Германия

✉ fkp@ipme.ru

Аннотация. В работе исследовано влияние неидеальных контактов (НК) на границах раздела фаз неоднородного (на микроуровне) материала на транспорт примеси и на напряженно-деформированное состояние среды (на макроуровне), вызванное ее накоплением. Рассмотрены два типа НК: сегрегация (оседание примеси), когда нарушается непрерывность концентрации, и образование обходных путей ускоренной диффузии, когда нарушается непрерывность нормальной компоненты потока. Моделирование связанных процессов массопереноса и изменения напряженно-деформированного состояния среды включает два этапа. На первом определяется эффективная диффузионная проницаемость материала с помощью методов микромеханики. На втором этапе решается задача массоупругости на макроуровне. Анализ проведен на примере длинного цилиндра, представленного как двухфазный материал, состоящий из матрицы и менее проницаемых сфероидальных неоднородностей, имеющих вытянутую форму и произвольно распределенных по ориентациям. Показано, что тип НК и способ его учета могут оказывать существенное влияние на распределение примеси в образце и на величину внутреннего давления.

Ключевые слова: диффузия, массоупругость, эффективные свойства, неидеальный контакт, граница раздела фаз, двухфазный материал

Introduction

As more new materials are created and their range of applications expands, new challenges arise, associated with describing the state of objects under thermomechanical loads, taking into account the influence of various characteristics of the internal structure. Simulations of the behavior of materials that are inhomogeneous at the meso-level can be divided into two stages: at the first stage, effective properties are determined using micromechanical methods, and at the second stage, the problem is solved at the macro-level.

As a rule, calculations of the effective properties assume that the fields are continuous at the phase interfaces in the material [1]. However, this hypothesis may prove invalid in some cases. In particular, in the context of the problem on determining the diffusion properties, segregation (impurity deposition) [2] cannot be described if the concentration field is assumed to be continuous [3]. Cracking, grain refinement, etc., can lead to the formation of additional bypasses of accelerated diffusion [4], which, in turn, contradicts the assumption of continuity of the normal component of the flux.

Any disruption of field continuity means the presence of imperfect contact (IC) [5]. ICs of the above types have been taken into account in a number of studies describing various processes. For example, the diffusion process was considered in [6−8] taking into account segregation in a material consisting of a matrix and isolated inhomogeneities. The model introduced a parameter equal to the ratio of concentrations on the outer and inner sides of the phase interface (the segregation parameter). Thermal processes in two-phase materials containing isolated inhomogeneities were considered in [9−11] taking into account various types of imperfect contact. It was assumed that the inhomogeneities have a coating with extreme properties (it is an insulator or superconductor). We carried out generalization and comparison of different approaches to simulation of imperfect contacts in [12].

The presence of imperfect contacts that must be taken into account to determine the effective diffusion permeability can directly affect both the impurity distribution in the macroscopic sample and its stress−strain state, as the latter can change as a result of impurity accumulation. We analyzed the effect of segregation on diffusion and mass elasticity in [13]. Impurity deposition at the phase interface between matrix and inhomogeneity was modeled only by setting the segregation parameter.

This study focuses on analysis of the influence of two types of imperfect contacts (segregation and the formation of additional bypasses of accelerated diffusion). These contacts are investigated by different approaches: determining a jump in the field and considering an inhomogeneity with a thin coating of extreme properties.

The analysis is presented for a two-phase material consisting of a matrix and less conductive, arbitrarily oriented inhomogeneities shaped like prolate spheroids. This microstructure is typical, in particular, for polycrystals used in simulation of grains with inhomogeneities and grain boundaries with the matrix [7]. Hydrogen-assisted degradation is a major issue in polycrystals, as the accumulation of hydrogen leads to fracture of metals [14, 15].

Simulation stages

Coupled processes of mass transfer and change in the stress−strain state of the material in the presence of two types of imperfect contacts at the phase interface (segregation and formation of additional bypasses for accelerated diffusion) on a smaller scale is modeled in two stages. At the first stage, the effective diffusion permeability of the material is determined taking into account its internal structure; at the second stage, the coupled problem of mass transport and elasticity is solved, taking into account the macroscopic properties found.

To determine the effective diffusion permeability $\mathbf{D}^{eff}$, we limit ourselves to considering linear macroisotropic material, i.e.,

$$\mathbf{D}^{eff} = D^{eff}\mathbf{I}$$

($\mathbf{I}$ is a unit tensor); this material consists of an isotropic matrix with the permeability $\mathbf{D}_0 = D_0\mathbf{I}$ and isotropic inhomogeneities with permeability $\mathbf{D}_1 = D_1\mathbf{I}$, shaped as prolate spheroids with an arbitrary orientation distribution.

Consider different types of imperfect contacts at the phase interface. Segregation is modeled by taking into account the discontinuity of the concentration field c. The additional bypasses of accelerated diffusion are modeled by taking into account the normal component of the flux J_n.

We solve the initial boundary-value quasi-static problem of elasticity caused by mass transport for a long cylinder with radius r_0. We assume that stresses and strains arise in the cylinder solely due to accumulation of diffusing species with a constant concentration maintained on the lateral surface. We consider two cases: with and without taking into account the phenomenon of pressure-induced diffusion, where the pressure gradient gives rise to an additional diffusion flux.

Next, we present a mathematical formulation of the problem for each simulation stage, discussing the methods for solving it.

Determination of effective material properties

These properties of the material are obtained from the solution to the homogenization problem for a representative volume V, which is a material point of the continuum at the macro-level [9]. The macroscopic diffusion permeability tensor $\mathbf{D}^{eff}$ relates the volume-averaged flux $\mathbf{J}$ and the concentration gradient c, in accordance with classical Fick's law:

143

$$<\mathbf{J}>_V = -\mathbf{D}^{eff} \cdot <\nabla c>_V.$$ (1)

It is assumed that the conservation law is fulfilled at each point of the representative volume:

$$\nabla \cdot \mathbf{J}(\mathbf{x}) = 0,$$ (2)

where $\mathbf{x}$ is the radius vector, and the flux is linearly related to the concentration gradient by the formula

$$\mathbf{J}(\mathbf{x}) = -\mathbf{D}(\mathbf{x}) \cdot \nabla c(\mathbf{x}),$$ (3)

where $\mathbf{D}(\mathbf{x})$ is the diffusion permeability tensor of the material at point $\mathbf{x}$.

It is convenient to define a homogeneous Hill condition on the boundary Σ of the representative volume:

$$c(\mathbf{x})\big|_\Sigma = \mathbf{G}_0 \cdot \mathbf{x}.$$ (4)

The presence of imperfect contacts is taken into account either by setting the field jump at the interface between matrix ($+$) and the inhomogeneity ($-$), or by considering inhomogeneities with a thin coating with extreme properties. In the latter case, it is first assumed that the inhomogeneity is represented by confocal ellipsoids whose semi-axes b_1, b_2, b_3 and a_1, a_2, a_3 are related as

$$b_i^2 = a_i^2 + \xi \ (i = 1, 2, 3), \ \xi = \text{const},$$

while the properties of the layer D_s formed by two ellipsoids are finite.

Then the passage to the limit is carried out at $\xi \to 0$ and either at $D_s \to 0$, or at $D_s \to \infty$, depending on the type of imperfect contact [10, 11].

As a result, the presence of segregation can be taken into account in the model either by setting the parameter s_c such that the concentration jump is defined as

$$[c] = (s_c - 1)c(\mathbf{x})\big|_{\mathbf{x} \to \Gamma_-},$$ (5)

(Γ is the interface of the inhomogeneity with the external normal $\mathbf{n}_\Gamma$), or by setting the dimensionless parameter β of the equivalent surface resistance, expressed as follows for spheroidal inhomogeneities

$$\beta = \frac{1 + 2\gamma^2}{2\gamma S} \frac{D_1}{a^2} \lim_{\xi \to 0, D_s \to 0} \frac{\xi}{D_s},$$ (6)

where γ is the ratio of the spheroid semi-axes, $\gamma = a_3/a$; S is the surface area of the spheroid divided by $(4/3)\pi a^2$.

Similarly, the formation of additional bypasses of accelerated diffusion is taken into account either by setting the parameter s_f,

$$[J_n] = (s_f - 1)\mathbf{n}_\Gamma \cdot \mathbf{J}(\mathbf{x})\big|_{\mathbf{x} \to \Gamma_-},$$ (7)

characterizing a jump in the normal component of the flux, or by setting a dimensionless equivalent surface permeability λ, which, in the case of spheroids, takes the form

$$\lambda = \frac{1 + 2\gamma^2}{2\gamma S} \frac{1}{D_1 a^2} \lim_{\xi \to 0, D_s \to \infty} \xi D_s.$$ (8)

The problem of determining the effective properties consists of two stages. At the first stage, the problem of isolated inhomogeneity in an infinite matrix is solved. At the second stage, a homogenization scheme is used to account for the presence of multiple inhomogeneities.

Based on the solution to the problem of isolated inhomogeneity, we can obtain an expression for the tensor characterizing the contribution of inhomogeneity to the required property [1].

The tensor **H** characterizing the contribution to the diffusion permeability can be obtained from the representation of the average flux as

$$<\mathbf{J}>_V = -\left(\mathbf{D}_0 + \frac{V_1}{V}\mathbf{H}\right)\cdot\mathbf{G}_0. \tag{9}$$

Expression (9) takes into account that the average concentration gradient does not depend on the microstructure and is completely determined by boundary condition (4):

$$<\nabla c>_V = \mathbf{G}_0.$$

The sum of the contribution tensors is a microstructural parameter that can be used to express the macroscopic characteristics of a material. Expressions for the tensors corresponding to the contributions of ellipsoidal and, in particular, spheroidal inhomogeneities were obtained and analyzed in [8−12]. The presence of various imperfect contacts was taken into account in two ways: by setting the field jump and by considering the inhomogeneity with a coating with extreme properties.

Let us give the final expressions for the contribution tensors of spheroids taking into account various factors:

$$\mathbf{H}^{s_c} = D_0\left[\frac{D_1 - s_c D_0}{f_0 D_1 + (1-f_0)s_c D_0}\boldsymbol{\theta} + \sum_{i=1}^{3}\frac{D_1 - s_c D_0}{(1-2f_0)D_1 + 2f_0 s_c D_0}\mathbf{nn}\right] \tag{10}$$

accounting for the discontinuity of the concentration field using the parameter s_c;

$$\mathbf{H}^\beta = D_0\left[\frac{D_1 - D_0 - f_0 D_0\beta\dfrac{S}{\gamma}}{f_0 D_1 + (1-f_0)D_0 + (1-f_0)D_0\beta\dfrac{S}{\gamma}(f_0 - F_\theta)}\boldsymbol{\theta} + \right.$$

$$\left. + \frac{D_1 - D_0 - (1-2f_0)D_0\beta\dfrac{S}{\gamma}}{(1-2f_0)D_1 + 2f_0 D_0 + 2f_0 D_0\beta\dfrac{S}{\gamma}(1-2f_0 - F_n)}\mathbf{nn}\right] \tag{11}$$

accounting for the discontinuity of the concentration field using the dimensionless equivalent surface resistance β;

$$\mathbf{H}^{s_f} = D_0\left[\frac{s_f D_1 - D_0}{f_0 s_f D_1 + D_0(1-f_0)}\boldsymbol{\theta} + \frac{s_f D_1 - D_0}{(1-2f_0)s_f D_1 + 2f_0 D_0}\mathbf{nn}\right] \tag{12}$$

accounting for the discontinuity of the normal component of the flux using the parameter s_f;

$$\mathbf{H}^\lambda = D_0\left[\frac{D_1 - D_0 + \lambda D_1\dfrac{S}{\gamma}(1-f_0)}{f_0 D_1 + (1-f_0)D_0 + f_0\lambda D_1\dfrac{S}{\gamma}(1-f_0 + F_\theta)}\boldsymbol{\theta} + \right.$$

$$\left. + \frac{D_1 - D_0 + 2f_0\lambda D_1\dfrac{S}{\gamma}}{(1-2f_0)D_1 + 2f_0 D_0 + (1-2f_0)\lambda D_1\dfrac{S}{\gamma}(2f_0 + F_n)}nn\right] \tag{13}$$

accounting for the discontinuity of the normal component of the flux using the dimensionless equivalent surface diffusion permeability λ.

The following notations are used in Eqs. (10)−(13): $\mathbf{n}$ is the unit vector along the symmetry axis of the spheroid; $\boldsymbol{\theta} = \mathbf{I} - \mathbf{nn}$; F_n, F_θ are functions of the parameter γ for which the equalities hold true:

$$F_n = \frac{f_0\left(1+2\gamma^2\right)-\gamma^2}{1+2\gamma^2}, \; F_\theta = -2F_n,$$

where

$$f_0\left(\gamma\right) = \frac{1-g\left(\gamma\right)}{2\left(1-\gamma^{-2}\right)}, \; g = g\left(\gamma\right) = \begin{cases} \dfrac{1}{\gamma\sqrt{1-\gamma^2}} \arctan \dfrac{\sqrt{1-\gamma^2}}{\gamma}, \; \gamma \le 1 \\[4mm] \dfrac{1}{2\gamma\sqrt{\gamma^2-1}} \ln\left(\dfrac{\gamma+\sqrt{\gamma^2-1}}{\gamma-\sqrt{\gamma^2-1}}\right), \; \gamma \ge 1. \end{cases}$$

To determine the effective properties of a material with multiple inhomogeneities, we use the Mori−Tanaka method [1, 16], giving physically consistent results for both small and large volume fractions of inclusions. We analyzed this method along with several others for materials with imperfect contacts earlier in [8]. Let us outline the main points of the method and present the results for effective diffusion permeability.

Within the framework of the Mori−Tanaka method, inhomogeneities are treated as isolated and the interaction between them is taken into account by placing them in an effective field averaged over the matrix rather than in the initial field $\mathbf{G}_0$ satisfying expression (4):

$$\mathbf{G}^{eff} = \left\langle \nabla c \right\rangle_{V_0}. \tag{14}$$

The very presence of an imperfect contact as well as its type and the approach to account for it directly influence the effective field. Note that for the Mori−Tanaka method to be applied, we need to take into account the discontinuity of the concentration field/normal component of the flux at two stages: when we solve the problem of the isolated inhomogeneity and when we use the homogenization scheme, since the parameters responsible for imperfect contact appear not only in expressions for contribution tensors [8]. Indeed, taking into account various factors, the effective diffusion permeability of a material with spheroidal inhomogeneities is defined as follows in terms of the contribution tensors:

$$\mathbf{D}^{eff} = \mathbf{D}_0 + \frac{1}{V}\sum_i V_i \mathbf{H}_i^{s_c} \cdot \left[\left(1-p\right)\mathbf{I} + \left(\frac{1}{s_c}\mathbf{D}_1 - \mathbf{D}_0\right)^{-1} \cdot \frac{1}{V}\sum_i V_i \mathbf{H}_i^{s_c}\right]^{-1} \tag{15}$$

accounting for imperfect contact using the parameter s_c;

$$\mathbf{D}^{eff} = \mathbf{D}_0 + \frac{1}{V}\sum_i V_i \mathbf{H}_i^{\beta} \cdot \Big[\left(1-p\right)\mathbf{I} + \frac{1}{V}\sum_i V_i \times$$

$$\times \left(\frac{1+\beta\dfrac{S}{\gamma}f_0}{D_1-D_0-D_0\beta\dfrac{S}{\gamma}f_0} H_{11_i}^{\beta}\boldsymbol{\theta}_i + \frac{1+\beta\dfrac{S}{\gamma}\left(1-2f_0\right)}{D_1-D_0-D_0\beta\dfrac{S}{\gamma}\left(1-2f_0\right)} H_{33_i}^{\beta}\mathbf{n}_i\mathbf{n}_i\right)\Big]^{-1} \tag{16}$$

accounting for the imperfect contact using the parameter β, here the tensors corresponding to the contributions of individual inhomogeneities are represented in coordinate form as $\mathbf{H}^{\beta} = H_{11}^{\beta}\left(\mathbf{I}-\mathbf{nn}\right) + H_{33}^{\beta}\mathbf{nn}$;

$$\mathbf{D}^{eff} = \mathbf{D}_0 + \frac{1}{V}\sum_i V_i \mathbf{H}_i^{s_f} \cdot \left[(1-p)\mathbf{I} + \left(s_f \mathbf{D}_1 - \mathbf{D}_0\right)^{-1} \cdot \frac{1}{V}\sum_i V_i \mathbf{H}_i^{s_f} \right]^{-1} \qquad (17)$$

accounting for imperfect contact using the parameter s_f;

$$\mathbf{D}^{eff} = \mathbf{D}_0 + \frac{1}{V}\sum_i V_i \mathbf{H}_i^{\lambda} \cdot \left[(1-p)\mathbf{I} + \frac{1}{V}\sum_i V_i \times \right.$$

$$\left. \times \left(\frac{1}{D_1 - D_0 + D_1\lambda\dfrac{S}{\gamma}(1-f_0)} H_{11_i}^{\lambda}\boldsymbol{\theta}_i + \frac{1}{D_1 - D_0 + 2D_1\lambda\dfrac{S}{\gamma}f_0} H_{33_i}^{\lambda}\mathbf{n}_i\mathbf{n}_i \right)_j \right]^{-1} \qquad (18)$$

accounting for imperfect contact using the parameter λ.

In the case when the inhomogeneities have the same properties and the same shape (while their sizes may generally be different), the summation operation in expressions (15)−(18) can be replaced by averaging over the orientations of the inhomogeneities.

$$1 \Big/ V\sum_i V_i \dots = p\langle \dots \rangle,$$

which is reduced to averaging the tensor $\boldsymbol{\theta}$ and the dyadic $\mathbf{nn}$ in expressions (10)−(13) for the contribution tensors.

Consequently, we obtain the following final formulas for calculating the effective diffusion permeability of macroisotropic material consisting of isotropic phases (taking into account the arbitrary orientation distribution of inhomogeneities and, accordingly, equality $\langle \mathbf{nn} \rangle = (1/3)\mathbf{I}$ holding true):

$$\frac{D^{eff}}{D_0} = 1 + \frac{pA_{s_c}}{(1-p) + \dfrac{pA_{s_c}}{(\alpha/s_c - 1)}}, \quad A_{s_c} = \frac{2\dfrac{H_{11}^{s_c}}{D_0} + \dfrac{H_{33}^{s_c}}{D_0}}{3} \qquad (19)$$

accounting for imperfect contact using the parameter s_c (the dimensionless parameter $\alpha = D_1/D_0$ is introduced here);

$$\frac{D^{eff}}{D_0} = 1 + \frac{pA_{\beta}}{(1-p) + pB_{\beta}}, \quad A_{\beta} = \frac{2\dfrac{H_{11}^{\beta}}{D_0} + \dfrac{H_{33}^{\beta}}{D_0}}{3},$$

$$B_{\beta} = \frac{2}{3}\frac{1+\beta\dfrac{S}{\gamma}f_0}{\alpha - 1 - \beta\dfrac{S}{\gamma}f_0}\frac{H_{11}^{\beta}}{D_0} + \frac{1}{3}\frac{1+\beta\dfrac{S}{\gamma}(1-2f_0)}{\alpha - 1 - \beta\dfrac{S}{\gamma}(1-2f_0)}\frac{H_{33}^{\beta}}{D_0} \qquad (20)$$

accounting for imperfect contact using the parameter β;

$$\frac{D^{eff}}{D_0} = 1 + \frac{pA_{s_f}}{(1-p) + \dfrac{pA_{s_f}}{(\alpha s_f - 1)}}, \quad A_{s_f} = \frac{2\dfrac{H_{11}^{s_f}}{D_0} + \dfrac{H_{33}^{s_f}}{D_0}}{3} \qquad (21)$$

accounting for imperfect contact using the parameter s_f;

147

$$\frac{D^{eff}}{D_0} = 1 + \frac{pA_\lambda}{(1-p)+pB_\lambda}, \ A = \frac{2\,H_{11}^\lambda\big/D_0 + H_{33}^\lambda\big/D_0}{3},$$

$$B_\lambda = \frac{2}{3}\frac{1}{\alpha - 1 + \alpha K\dfrac{S}{\gamma}(1-f_0)}\frac{H_{11}^\lambda}{D_0} + \frac{1}{3}\frac{1}{\alpha - 1 + 2\alpha K\dfrac{S}{\gamma}f_0}\frac{H_{33}^\lambda}{D_0}$$

(22)

accounting for imperfect contact using the parameter λ.

Solution to coupled problem of mass transport and elasticity

Now let us describe the diffusion process at the macro-level. The diffusion equation has the following local form:

$$\frac{\partial c}{\partial t} = -\nabla \cdot \mathbf{J},$$

(23)

where t is the time.

The diffusion flux $\mathbf{J}$ can generally be driven by both a concentration gradient c and a pressure gradient P (pressure-induced diffusion; $P = -\mathrm{tr}\sigma$, where σ is the stress tensor):

$$\mathbf{J} = -D^{eff}\left(\nabla c + Ac\nabla P\right),$$

(24)

where $A = M\alpha_V/(3\rho RT)$ (M is the molar mass, α_V is the volumetric coefficient of thermal expansion, ρ is the density, R is the universal gas constant, T is the temperature).

Along with the case when the flux is given by expression (24), let us consider classical Fick's law:

$$\mathbf{J} = -D^{eff}\nabla c.$$

(25)

The presence of imperfect contacts at the meso-level is taken into account here in the coefficient D^{eff}, determined from one of the formulas (19)−(22) depending on the type of imperfect contact and the model used.

The stress−strain state of the material satisfies the equilibrium equation

$$\nabla \cdot \boldsymbol{\sigma} = 0.$$

(26)

As a rule, the accumulation of diffusing species leads only to volumetric expansion of the material. In this case, the constitutive relations between stress and strain ε are given by the Duhamel−Neumann equations:

$$\boldsymbol{\sigma} = -P\mathbf{I} + 2\mu\,\mathrm{dev}\,\boldsymbol{\varepsilon}, \ P = -K\left(\mathrm{tr}\,\boldsymbol{\varepsilon} - \alpha_V\left(c - c_0\right)\right)\mathbf{I},$$

(27)

where c_0 is the reference concentration; K and μ are the bulk modulus and the shear modulus, respectively.

Strains in linear material are defined in terms of the displacement gradient as $\boldsymbol{\varepsilon} = \left(\nabla\mathbf{u}\right)^s$.

Example problem for long cylinder. Now let us consider an initial boundary-value problem for a long cylinder. We write a system of equations in a cylindrical coordinate system (r,φ,z); the unit basis vectors are denoted, respectively, as $\mathbf{e}_r$, $\mathbf{e}_\varphi$, $\mathbf{e}_z$.

A constant concentration c_1 is maintained on the lateral surface of the cylinder, and this surface is free from loading:

$$c\big|_{r=r_0} = c_1, \ \mathbf{e}_r \cdot \boldsymbol{\sigma}\big|_{r=r_0} = 0.$$

(28)

The following conditions are satisfied in the center of the cylinder:

$$\frac{\partial c}{\partial r}\bigg|_{r=0} = 0, \ \mathbf{u}\cdot\mathbf{e}_r\big|_{r=0} < \infty.$$

(29)

The following integral equilibrium condition holds true in accordance with Saint-Venant's principle and the plane section hypothesis:

$$\int_0^{r_0} \mathbf{e}_z \cdot \boldsymbol{\sigma} r\, dr = 0. \tag{30}$$

Assuming axial symmetry, the solution to the problem takes the following form:

$$\mathbf{u} = u_r(r)\mathbf{e}_r + u_z(z)\mathbf{e}_z, \quad \frac{\partial u_z}{\partial z} = \varepsilon = \text{const}, \; c = c(r). \tag{31}$$

The initial concentration distribution is assumed to be zero:

$$c\big|_{t=0} = c_0 = 0. \tag{32}$$

In accordance with expression (27) and taking into account assumptions (31), the nonzero components of the stress tensor take the following form:

$$\sigma_{rr} = -P + \frac{4\mu}{3}\left[\frac{\partial u_r}{\partial r} - \frac{1}{2}\left(\frac{u_r}{r} + \varepsilon\right)\right],$$

$$\sigma_{\varphi\varphi} = -P + \frac{4\mu}{3}\left[\frac{u_r}{r} - \frac{1}{2}\left(\varepsilon + \frac{\partial u_r}{\partial r}\right)\right], \tag{33}$$

$$\sigma_{zz} = -P + \frac{4\mu}{3}\left[\varepsilon - \frac{1}{2}\left(\frac{\partial u_r}{\partial r} + \frac{u_r}{r}\right)\right],$$

and the pressure P takes the form

$$P = -K\left(\frac{\partial u_r}{\partial r} + \frac{u_r}{r} + \varepsilon - \alpha_V c\right). \tag{34}$$

Let us turn to the dimensionless formulation of the problem, introducing the following scales:
radius of the cylinder r_0 for the radial coordinate r and the radial displacement u_r;
quantity $4\mu/3$ for the components of the stress tensor σ_{ii} and pressure P;
concentration c_1 maintained on the lateral surface for the concentration c.
The scale for time t is denoted as T.
Then the final system of equations, supplemented by initial and boundary conditions, takes the following form (the notations are preserved for dimensionless quantities):

$$\begin{cases} \dfrac{\partial}{\partial r}\left[\dfrac{\partial u_r}{\partial r} + \dfrac{u_r}{r} - P\right] = 0, \\[2mm] P = -k\left(\dfrac{\partial u_r}{\partial r} + \dfrac{u_r}{r} + \varepsilon - \alpha_V c\right), \\[2mm] u_r\big|_{r=0} < \infty, \quad \left(-P + \left[\dfrac{\partial u_r}{\partial r} - \dfrac{1}{2}\left(\dfrac{u_r}{r} + \varepsilon\right)\right]\right)\Bigg|_{r=1} = 0, \\[2mm] \displaystyle\int_0^1 \left(-P + \left[\varepsilon - \dfrac{1}{2}\left(\dfrac{\partial u_r}{\partial r} + \dfrac{u_r}{r}\right)\right]\right) r\, dr = 0, \\[2mm] r\dfrac{\partial c}{\partial t} = F\dfrac{\partial}{\partial r}\left[r\left(\dfrac{\partial c}{\partial r} + A_k c \dfrac{\partial P}{\partial r}\right)\right] \\[2mm] c\big|_{r=1} = 1, \quad \dfrac{\partial c}{\partial r}\bigg|_{r=0} = 0, \quad c\big|_{t=0} = 0, \end{cases} \tag{35}$$

where the dimensionless coefficients $k = 3K/4\mu$, $A_k = 4\mu/3A$ are introduced; F is the diffusion Fourier number, $F = D^{eff}T/r_0^2$.

Note that the presence of imperfect contacts in the dimensionless formulation of the problem is taken into account only in the diffusion Fourier number, since it includes the effective diffusion permeability. For a fixed time scale and the same cylinder radius, varying the parameter F means varying D^{eff}.

System of equations (35) was solved numerically using the implicit finite difference method. A one-dimensional spatial mesh was introduced along the r axis, concentration and radial displacements were set in nodes, stresses (including pressure) and strains were set in cells.

Analysis of results

Consider the influence of imperfect contacts on the solution to the coupled problem of mass transport and elasticity. Let us consider several models in this case. First, let us find a solution with and without taking into account pressure-induced diffusion. Secondly, let us consider two types of imperfect contacts: I and II.

I. Segregation occurs.

II. Additional bypasses of accelerated diffusion arise in the material.

We use two approaches to account for imperfect contact within the framework of each model.

1. The field jump is defined as a ratio of the quantities from the outer and inner sides of inhomogeneity boundary.

2. An inhomogeneity with a thin coating of extreme properties is introduced.

Let us compare the results obtained with those for the case of perfect contacts at the matrix/inhomogeneity interface. To compare the approaches, let us express the parameters s_c and s_f in terms of the equivalent surface resistance β and permeability λ, respectively:

$$s_c = 1 + \beta, \quad s_f = 1 + 2\lambda; \tag{36}$$

then both approaches to accounting for imperfect contacts produce the same results in the case of spherical inhomogeneities.

The analysis is carried out for the example of a material consisting of a matrix and arbitrarily oriented prolate spheroidal inhomogeneities with a ratio of semi-axis lengths $\gamma = 10$; we adopt the ratio of diffusion permeabilities $\alpha = D_1/D_0 = 0.2$.

Let us first present the results for effective properties of the material with imperfect contacts. The effect of segregation is illustrated in Fig. 1.

As can be seen from Fig. 1, the diffusion permeability decreases with an increase in the volume fraction of inhomogeneities p, while the presence of imperfect contact leads to a more pronounced change in the property (see Fig. 1,*a*). Fig. 1,*b* shows the dependences of effective permeability on parameter β at fixed volume fraction of inhomogeneities $p = 0.9$. It can be seen that the difference
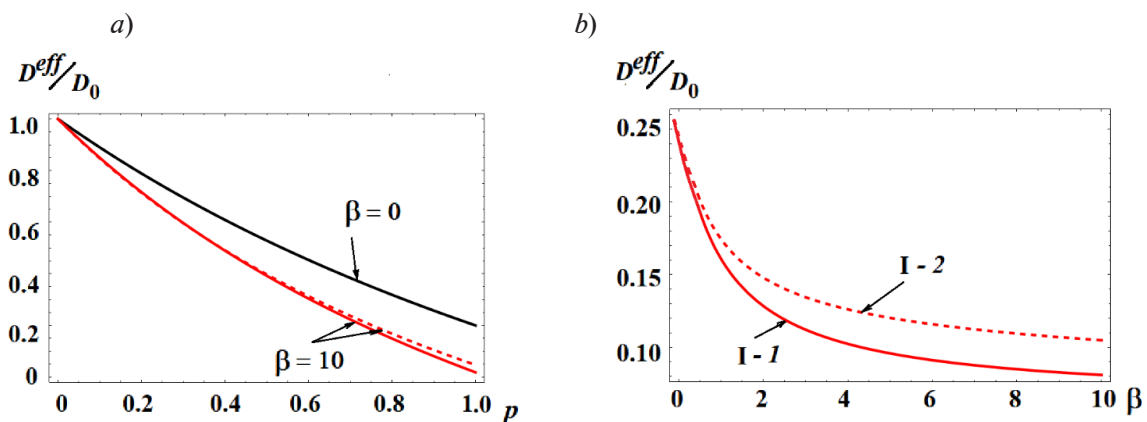

Fig. 1. Dependences of effective diffusion coefficient on volume fraction of inhomogeneities p for two values of parameter β (*a*) and on parameter β (*b*) for the case of segregation (I), simulated by approaches *1* and *2* (solid and dashed lines, respectively), see also the explanations in the text

between approaches to accounting for imperfect contact increases with increasing β. The difference remains insignificant with the selected characteristics of the structure.

The influence of the presence of bypasses for accelerated diffusion is shown in Fig. 2. Evidently, the presence of imperfect contact at the phase interface increases the diffusion permeability, compared with the case of its absence. Depending on the value of the parameter λ, the diffusion permeability can either decrease with an increase in the volume fraction of inhomogeneities, or increase, which is explained by the simultaneous influence of two competing factors, the presence of less conductive inhomogeneities in the matrix and bypasses of accelerated diffusion. Evidently, an increase in the parameter λ entails an increase in the difference between approaches to accounting for imperfect contact.
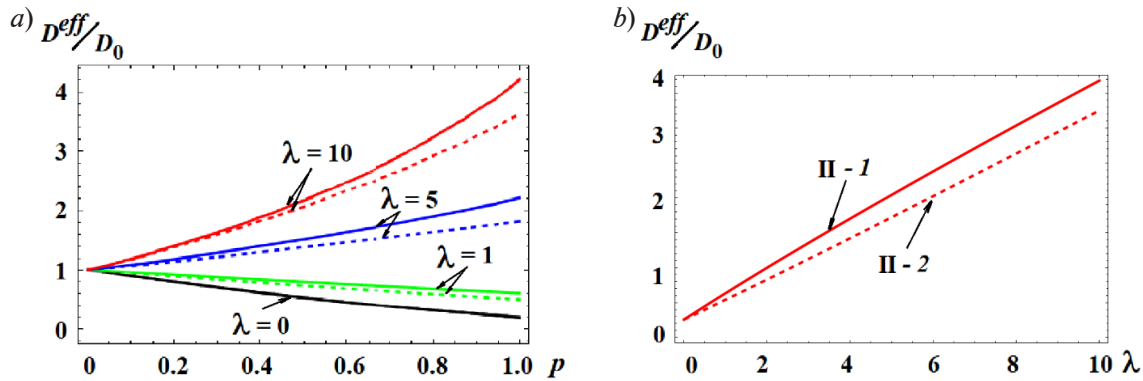

Fig. 2. Dependences of effective diffusion coefficient on volume fraction of inhomogeneities p at 4 values of parameter λ (*a*) and parameter λ (*b*) for the case of bypasses for accelerated diffusion (II), simulated by approaches *1* and *2* (solid and dashed lines, respectively), see also the explanations in the text

We solve the coupled problem of mass transport and elasticity with the following parameter values: $k = 1.6$, $A = 49.3$, $\alpha_V = 4.5 \cdot 10^{-6}$ (typical parameters for aluminum). The presence of imperfect contacts influences the value of the effective diffusion permeability and, consequently, the diffusion Fourier number F. Consider the values of D^{eff}/D_0 obtained at $p = 0.9$ and, depending on the type of imperfect contact, at $\beta = 10$ or $\lambda = 10$ (see column 3 in Table). Note that the ratios of the diffusion Fourier numbers corresponding to different values of the effective diffusion permeability are more important for analysis than the absolute values of F. We introduce the notation F_0

Table

Diffusion characteristics of material: calculation results

Model		Parameter value	
IC type	Approach to accounting for IC	D^{eff}/D_0	F_i
Without accounting for IC		0.26	$F_0 = 2.25 \cdot 10^{-4}$
I	*1*	0.08	$F_1 = 0.3\,F_0$
I	*2*	0.10	$F_2 = 0.4\,F_0$
II	*1*	3.68	$F_3 = 14.2\,F_0$
II	*2*	3.25	$F_4 = 12.5\,F_0$

N o t a t i o n s : D^{eff}/D_0 is the dimensionless effective diffusion permeability; F_i is the diffusion Fourier number; IC is the imperfect contact. The numbers I, II, *1*, *2* are explained in the text.

N o t e . The calculations were carried out for the material consisting of a matrix and arbitrarily oriented, prolate spheroidal inhomogeneities with a ratio of semi-axis lengths $\gamma = 10$.

151

for the Fourier number corresponding to the value of D^{eff}/D_0 obtained without taking into account imperfect contacts ($s_c = s_f = 1$, $\beta = \lambda = 0$). The value of F_0 is calculated at $D^{eff} = 1 \cdot 10^{-12}$ m²/s (typical parameter for aluminum), $r_0 = 0.004$ m, $T = 3600$ s = 1 h. The values of the diffusion Fourier number are given in Table (last column).

The concentration profiles and pressure dependences on the radius (cylindrical coordinate system) at different values of diffusion Fourier number at time $t = 100$ are shown in Fig. 3. Note that the results obtained without and with taking into account pressure-induced diffusion coincided with the given material parameters (the value of parameter A_k is small, so the pressure gradient multiplied by it turns out to be much smaller than the concentration gradient).
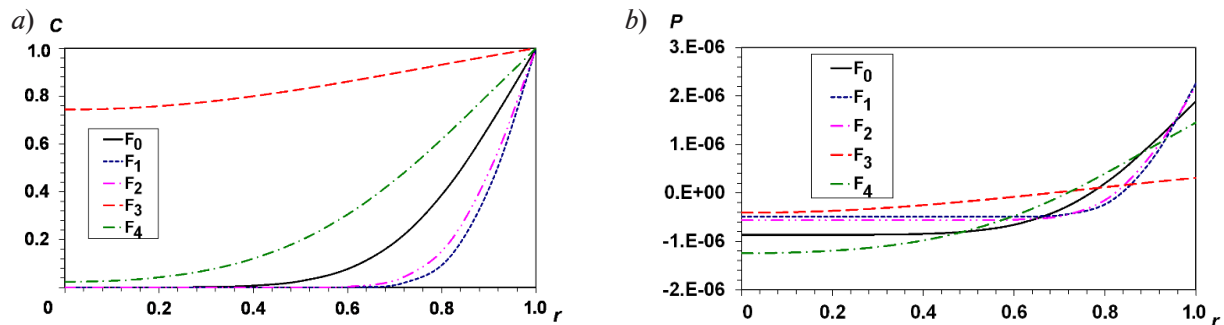

Fig. 3. Dependences of concentration (*a*) and pressure (*b*) on radius
(coordinate along the polar axis) at different values of diffusion Fourier number
(see Table) at time $t = 100$

Fig. 3 shows that the presence of imperfect contacts and the approach to accounting for them for has a significant influence on the concentration of diffusing species in the material and on its distribution. In particular, the presence of segregation for which a decrease in the diffusion rate is observed can considerably reduce the concentration of impurities in the material. The concentration gradient increases, which leads to more pronounced pressure drops. Such a variation in pressure, in turn, can be critical in problems of hydrogen degradation where local characteristics are important. The presence of bypasses for accelerated diffusion can lead to a significant increase in the concentration in the material, directly influencing its behavior in case of aggressive environments. The approach where the field jump is set as the ratio of the field values from the outer and inner sides of the inhomogeneity interface (both in the case of segregation and in the case of additional bypasses of accelerated diffusion) affects the result to a greater extent. The difference between models II-*1* and II-*2* used to simulate the discontinuity of the normal component of the flux is particularly significant.

The effect of pressure-induced diffusion was studied separately and is shown in Fig. 4. This effect occurs at higher values of the thermal expansion coefficient than the characteristic value for aluminum. In particular, the graphs in Fig. 4 are plotted for $\alpha_V = 0.2$. For clarity, the figure
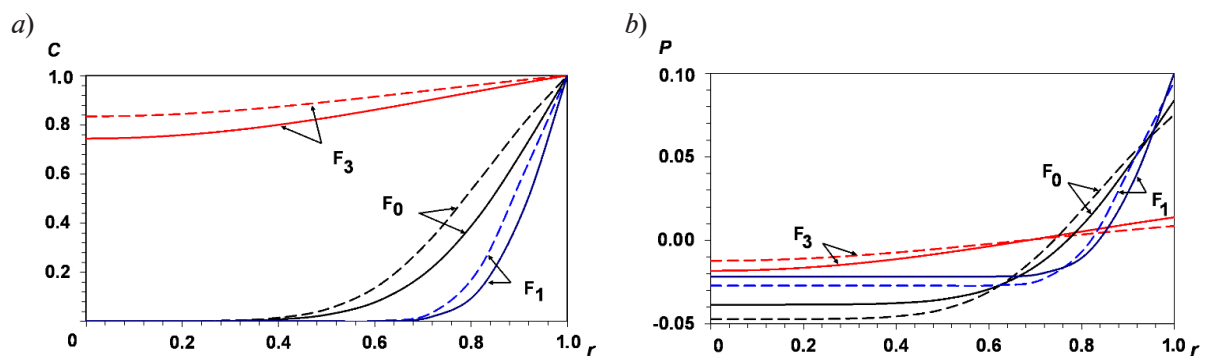

Fig. 4. Dependences of concentration (*a*) and pressure (*b*) of diffusing species on radius (coordinate
along the polar axis) at different values of diffusion Fourier number (see Table), taking into
account (dashed lines) and without taking into account (solid lines) pressure-induced diffusion

shows the results obtained at three values of F_0 from Table: at the value obtained without taking into account imperfect contacts as well as at the maximum and minimum values from the considered range. Fig. 4 shows that the presence of pressure-induced diffusion leads to an increase in the concentration of the diffusing species in the material, a decrease in both the concentration gradient and the pressure difference in all cases.

Thus, the presence, type, and approach to accounting for imperfect contacts influences the distribution of diffusing species in the material and its stress−strain state.

Conclusion

We obtained a solution to the coupled problem (in particular, to the one-way coupled problem) of diffusion and elasticity, describing the material's elastic behavior due to impurity accumulation taking into account the presence of imperfect contacts at the phase interface. Two types of imperfect contacts were considered: the presence of segregation (leading to discontinuity of the concentration field) and the presence of additional bypasses of accelerated diffusion (leading to discontinuity of the normal component of the flux). Each type of imperfect contact was taken into account within the framework of two approaches: by setting the ratio of the field magnitudes from the outer and inner sides of the inhomogeneity interface and by considering an inhomogeneity with a thin coating of extreme properties.

The microstructure was taken into account at the stage when the effective properties of the material were determined by the Mori−Tanaka homogenization method based on tensors describing the contributions to diffusion permeability.

The analysis was carried out for an axisymmetric sample made of two-phase material with arbitrarily oriented prolate spheroidal inhomogeneities characterized by lower diffusion permeability than the matrix.

It was established that the type of imperfect contact and the approach to accounting for it can have a significant effect on the distribution of impurities in the sample and on the internal pressure. This can be crucial, for example, in the case of saturation of metals with harmful impurities.

Thus, to improve the accuracy of stress−strain analysis, it is necessary to take into account the specifics of impurity transport and the presence of defects, so that the assumption of continuity of fields at the phase interfaces may have to be consequently abandoned.

REFERENCES

1. **Kachanov M., Sevostianov I.,** Micromechanics of materials, with applications (Book Ser. "Solid Mechanics and its Applications". Vol. 249), Springer, Berlin, Germany, 2018.

2. **Zhang X, Qiao L, Zhang H, Wang P.,** Influence of impurity gas seeding into deuterium plasma on the surface modification, sputtering erosion and deuterium retention in W and W-La$_2$O$_3$ alloy, Int. J. Hydr. Energy. 48 (6) (2023) 2075−2089.

3. **Zhang Y., Liu L.,** On diffusion in heterogeneous media, Am. J. Sci. 312 (9) (2012) 1028−1047.

4. **Chepak-Gizbrekht M. V., Knyazeva A. G.,** Two-dimensional model of grain boundary diffusion and oxidation, PNPU Mechanics Bulletin. (1) (2022) 156−166 (in Russian)

5. **Pham D. C., Nguyen T. K.,** General imperfect interface model for spherical−circular inclusion composites, Acta Mech. 235 (4) (2024) 2211−2229.

6. **Belova I. V., Murch G. E.,** Calculation of the effective conductivity and diffusivity in composite solid electrolytes, J. Phys. Chem. Solids. 66 (5) (2005) 722−728.

7. **Knyazeva A. G., Grabovetskaya G. P., Mishin I. P., Sevostianov I.,** On the micromechanical modelling of the effective diffusion coefficient of a polycrystalline material, Philos. Mag. 95 (19) (2015) 2046−2066.

8. **Frolova K. P., Vilchevskaya E. N.,** Effective diffusivity of transversely isotropic material with embedded pores, Mater. Phys. Mech. 47 (6) (2021) 937−950.

9. **Markov K. Z.,** Elementary micromechanics of heterogeneous media. Heterogeneous media: micromechanics modeling methods and simulations, Birkhдuser, Boston, MA, USA, 2000.

10. **Levin V., Markov M.,** Effective thermal conductivity of micro-inhomogeneous media containing imperfectly bonded ellipsoidal inclusions, Int. J. Eng. Sci. 109 (Dec) (2016) 202−215.

11. **Markov M., Levin V., Markova I.,** Determination of effective electromagnetic parameters of concentrated suspensions of ellipsoidal particles using Generalized Differential Effective Medium approximation, Phys. A: Stat. 492 (15 Febr) (2018) 113−122.

12. **Frolova K. P., Vilchevskaya E. N.,** Comparison of approaches to accounting for imperfect contacts when determining the effective permeability of material, St. Petersburg Polytechnical State University Journal. Physics and Mathematics. 16 (4) (2023) 146−159 (in Russian).

13. **Frolova K. P., Bessonov N. M., Vilchevskaya E. N.,** Diffusion in media with spheroidal pores, In book: V. A. Polyanskiy, A. K. Belyaev (Eds.). Mechanics and Control of Solids and Structures (Book Series: Advanced Structures Materials. Vol. 164), Springer Int. Publ., Cham, Switzerland (2022) 209−225.

14. **Sun Y., Cheng Y. F.,** Hydrogen-induced degradation of high-strength steel pipeline welds: A critical review, Eng. Fail. Anal. 133 (March) (2022) 105985.

15. **Sedova Y. S., Polyanskiy V. A., Belyaev A. K., Yakovlev Y. A.,** Modeling the skin effect, associated with hydrogen charging of samples, within the framework of the HEDE mechanism of cracking, Mater. Phys. Mech. 51 (6) (2023) 152−159.

16. **Mori T., Tanaka K.,** Average stress in matrix and average elastic energy of materials with misfitting inclusions, Acta Metall. 21 (5) (1973) 571−574.

СПИСОК ЛИТЕРАТУРЫ

1. **Kachanov M., Sevostianov I.** Micromechanics of materials, with applications (Book Series "Solid Mechanics and its Applications". Vol. 249). Berlin, Germany: Springer, 2018. 712 p.

2. **Zhang X, Qiao L, Zhang H, Wang P.** Influence of impurity gas seeding into deuterium plasma on the surface modification, sputtering erosion and deuterium retention in W and W-La$_2$O$_3$ alloy // International Journal of Hydrogen Energy. 2023. Vol. 48. No. 6. Pp. 2075−2089.

3. **Zhang Y., Liu L.** On diffusion in heterogeneous media // American Journal of Science. 2012. Vol. 312. No. 9. Pp. 1028−1047.

4. **Чепак-Гизбрехт М. В., Князева А. Г.** Двумерная модель зернограничной диффузии и окисления // Вестник Пермского национального исследовательского политехнического университета. Механика. 2022. № 1. С. 156−166.

5. **Pham D. C., Nguyen T. K.** General imperfect interface model for spherical−circular inclusion composites // Acta Mechanica. 2024. Vol. 235. No. 4. Pp. 2211−2229.

6. **Belova I. V., Murch G. E.** Calculation of the effective conductivity and diffusivity in composite solid electrolytes // Journal of Physics and Chemistry of Solids. 2005. Vol. 66. No. 5. Pp. 722−728.

7. **Knyazeva A. G., Grabovetskaya G. P., Mishin I. P., Sevostianov I.** On the micromechanical modelling of the effective diffusion coefficient of a polycrystalline material // Philosophical Magazine. 2015. Vol. 95. No. 19. Pp. 2046−2066.

8. **Frolova K. P., Vilchevskaya E. N.** Effective diffusivity of transversely isotropic material with embedded pores // Materials Physics and Mechanics. 2021. Vol. 47. No. 6. Pp. 937−950.

9. **Markov K. Z.** Elementary micromechanics of heterogeneous media. Heterogeneous media: micromechanics modeling methods and simulations. Boston, USA: Birkhдuser, MA, 2000. 162 p.

10. **Levin V., Markov M.** Effective thermal conductivity of micro-inhomogeneous media containing imperfectly bonded ellipsoidal inclusions // International Journal of Engineering Science. 2016. Vol. 109. December. Pp. 202−215.

11. **Markov M., Levin V., Markova I**. Determination of effective electromagnetic parameters of concentrated suspensions of ellipsoidal particles using Generalized Differential Effective Medium approximation // Physica A: Statistical Mechanics and its Applications. 2018. Vol. 492. 15 February. Pp. 113−122.

12. **Фролова К. П., Вильчевская Е. Н.** Сравнение подходов к учету неидеальных контактов при определении эффективной проницаемости материала // Научно-технические ведомости Санкт-Петербургского государственного политехнического университета. Физико-математические науки. 2023. Т. 16. №. 4. С. 146−159.

13. **Frolova K. P., Bessonov N. M., Vilchevskaya E. N.** Diffusion in media with spheroidal pores // V. A. Polyanskiy, A. K. Belyaev (Eds.). Mechanics and Control of Solids and Structures (Book Series: Advanced Structures Materials. Vol. 164). Cham, Switzerland: Springer International Publishing, 2022. Pp. 209−225.

14. **Sun Y., Cheng Y. F.** Hydrogen-induced degradation of high-strength steel pipeline welds: A critical review // Engineering Failure Analysis. 2022. Vol. 133. March. P. 105985.

15. **Sedova Y. S., Polyanskiy V. A., Belyaev A. K., Yakovlev Y. A.** Modeling the skin effect, associated with hydrogen charging of samples, within the framework of the HEDE mechanism of cracking // Materials Physics and Mechanics. 2023. Vol. 51. No. 6. Pp. 152−159.

16. **Mori T., Tanaka K.** Average stress in matrix and average elastic energy of materials with misfitting inclusions // Acta Metallurgica. 1973. Vol. 21. No. 5. Pp. 571−574.

THE AUTHORS

FROLOVA Ksenia P.
Institute for Problems in Mechanical Engineering of RAS
61 Bolshoi Ave. V. O., St. Petersburg, 199178, Russia
fkp@ipme.ru
ORCID: 0000-0003-0376-4463

BESSONOV Nikolay M.
Institute for Problems in Mechanical Engineering of RAS
61 Bolshoi Ave. V. O., St. Petersburg, 199178, Russia
nickbessonov1@gmail.com
ORCID: 0000-0001-6462-5980

VILCHEVSKAYA Elena N.
Technical University of Berlin, Germany
Straße des 17. Juni 135 10623, Berlin
vilchevska@gmail.com
ORCID: 0000-0002-5173-3218

СВЕДЕНИЯ ОБ АВТОРАХ

ФРОЛОВА Ксения Петровна — *кандидат физико-математических наук, старший научный сотрудник лаборатории прикладных исследований*
Института проблем машиноведения РАН.
199178, Россия, г. Санкт-Петербург, Большой проспект В. О., 61.
fkp@ipme.ru
ORCID: 0000-0003-0376-4463

БЕССОНОВ Николай Михайлович — *доктор физико-математических наук, главный научный сотрудник лаборатории микромеханики материалов Института проблем машиноведения РАН.*
199178, Россия, г. Санкт-Петербург, Большой проспект В. О., 61.
nickbessonov1@gmail.com
ORCID: 0000-0001-6462-5980

ВИЛЬЧЕВСКАЯ Елена Никитична — *доктор физико-математических наук, приглашенный специалист Берлинского технического университета.*
Straße des 17. Juni 135 10623, Berlin
vilchevska@gmail.com
ORCID: 0000-0002-5173-3218

SELF-SYNCHRONIZATION STABILITY OF VIBRATION EXCITERS OF A TWO-MASS APPARATUS FOR PROCESSING GRANULAR MATERIALS

V. S. Sizikov✉

Institute for Problems of Mechanical Engineering of RAS, St. Petersburg, Russia

✉ sizikovvs@yandex.ru

Abstract. The article studies stability conditions for self-synchronization of vibration exciters in antiphase oscillation regime of working tools of an apparatus for granular materials processing. The apparatus operating regime provides grinding, attrition and mixing processing of material grains combined with a transportation process. The condition of stable antiphase rotation regime of vibration exciters' rotors has been found with implementation of integral criterion of stability of synchronous motions. The condition of stable self-synchronization rotation regime of vibrational exciters' rotors was found with the usage of integral criterion of stability of synchronous movements. The obtained relationships allow one to choose parameters of apparatus construction and to specify vibrational working tool's operating regimes that perform effective implementation of process of granular material treatment.

Keywords: two-mass apparatus, working tools walls, self-synchronization of vibrators, integral criterion of synchronization stability, granular materials

УСТОЙЧИВОСТЬ САМОСИНХРОНИЗАЦИИ ВИБРОВОЗБУДИТЕЛЕЙ ДВУХМАССОВОГО АППАРАТА ДЛЯ ПЕРЕРАБОТКИ ЗЕРНИСТЫХ МАТЕРИАЛОВ

В. С. Сизиков✉

Институт проблем машиноведения РАН, Санкт-Петербург, Россия

✉ sizikovvs@yandex.ru

Аннотация. Работа направлена на поиск условий устойчивой самосинхронизации вибраторов для противофазного режима колебаний рабочих органов аппарата для переработки зернистых сред. Режим работы аппарата обеспечивает процессы измельчения, истирания и перемешивания зерен материала, совмещенные с процессом транспортирования. С использованием интегрального критерия устойчивости синхронных движений получено условие устойчивой самосинхронизации роторов вибровозбудителей в противофазном режиме их вращения. Найденные соотношения позволяют выбирать оптимальные значения параметров конструкции аппарата и задавать режимы колебаний вибрационных рабочих органов, обеспечивающие эффективное осуществление процессов технологической переработки зернистых материалов.

Ключевые слова: двухмассовый аппарат, стенки рабочих органов, самосинхронизация вибраторов, критерий устойчивости синхронизации

Introduction

The phenomenon of self-synchronization of unbalanced rotors of vibration exciters consists of vibration-induced interaction between them, so that they rotate synchronously at equal or commensurate speeds and with specified mutual phases [1]. This interaction is particularly important for processing of granular materials, including such stages as crushing, transportation, attrition, mixing, and others.

A key requirement for mechanical processing of a material is controlled excitation of vibration patterns. This involves generating specific directions of vibrational loads and trajectories of the machine's components. Such synthesis allows to optimize many processes.

Vibration is widely used in technologies for processing rocks, powders and other granular materials in the mining, construction, chemical and foundry industries. The main directions for improving these technological processes are reducing the energy and material consumption throughout design and production of vibration machinery.

The discovery of the self-synchronization effect led to a qualitative leap in vibration technology. Introducing this effect into engineering practices has contributed to great advances in a wide range of vibration technology in our country and abroad. Large contributions to this field were made by such outstanding scientists as Blekhman, Vaisberg, Lavrov, Ragulskis and others [1−6].

Self-synchronization of vibration exciters remains a promising direction; a class of multi-mass vibration systems has appeared, allowing to optimize various processes during operation at resonance, reduce loads on the base and implement specialized operating modes for treating granular materials using several components [1]. In view of this, multi-mass machines with self-synchronizing vibration exciters mounted on several components present an attractive option. Examples of such machines are two-mass vibration crushers, vibrating screens, equipment for beneficiation of granular materials [2, 4].

Modern systems and methods for forced synchronization control of rotors in vibration equipment allow to preset phase relationships and rotational speeds, allowing to further optimize the material processing techniques based on vibration methods [10, 12].

A promising method for vibrational processing of granular materials is impact on the material layer by the working tools of a two-mass system, forming a longitudinal channel with flat walls, with an unbalanced vibration exciter installed on each wall (Fig. 1) [9]. The rotation of the vibration exciter rotors induces plane-parallel oscillations of each wall along elliptical trajectories.

The processing of the material layer includes two main periods of impact from the walls on the layer:

compression of the layer by compressive forces when the walls approach each other (Fig. 1,*a*), accompanied by generation of stresses in the layer and intense abrasion of the surface of material grains during their relative movement within the layer;

decompression of the layer when the walls move away from each other (Fig. 1,*b*), accompanied by loosening of the layer and its relative movement along the working channel by microthrow motion.

Simultaneously with processing, the material is transported along the working channel.

An extensive monograph [1] considers the phenomenon of self-synchronization of dynamic systems, obtaining various conditions for stability of self-synchronization of vibration exciters in single-mass and multi-mass systems. Furthermore, a recent paper reports on synchronous antiphase and in-phase rotation of rotors in vibration exciters of a two-mass system in a single assembly [11]. However, self-synchronization of rotors in such systems with vibration exciters located on both walls is insufficiently studied.
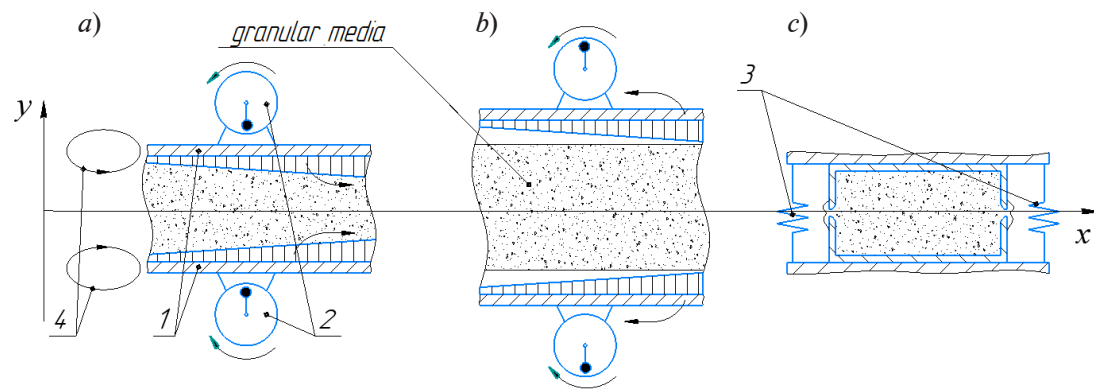
Fig. 1. Schematic for volumetric vibrational impact on layer of processed granular medium by walls of two-mass system generating synchronous anti-phase oscillations along elliptical trajectories (*4*): *a*, *b* correspond to periods of compression and decompression of the layer, respectively; *c* is the cross-section of the working channel

The figure shows walls (*1*), unbalanced vibration exciters (*2*), springs (*3*) connecting the walls; arrows indicate the movements of walls *1* and rotations of vibration exciter rotors *2*

Analysis of the operating modes in a two-mass system based on the described mathematical model allows to determine the parameters for attrition of granular material in with the highest compressive forces simultaneously with transportation. The best combination of these parameters is achieved under synchronous anti-phase oscillations of the walls along elliptical trajectories in opposite directions, maintained by self-synchronization of anti-phase counter-rotation of rotors in vibration exciters (see Fig. 1).

The goal of our study is therefore to find the optimal values of the design and operating parameters of the two-mass system, ensuring stable self-synchronization of anti-phase rotation of vibration exciter rotors in opposite directions.

The design parameters include the masses and dimensions of the walls, their moments of inertia, the stiffness of the springs and their positions along the walls. The operating parameters include the frequencies and amplitudes of the wall oscillations.

The solution to this problem should help determine the range of parameter values for the impact of the walls on the processed material, which serves as a basis for formulating recommendations for design and operation of systems for beneficiation of mineral granular materials [7].

Depending on the direction and phase difference of rotation of unbalanced rotors, the system can generate various modes of relative motion of the walls, each the most favorable for a specific type of processing procedure [8]. For example, one of the oscillation modes for attrition of material grains involving the walls moving with relative oscillation phase shifts in the transverse and longitudinal directions equal to π (Fig. 2). In this case, the walls move in one direction with co-rotation of the vibration exciter rotors (for example, clockwise). This allows to induce two types of deformations in the material layer: compression and shear deformations.

The requirements for the magnitude of compressive and shear stresses generated in the layer for attrition of the material depend on the oscillation frequency of the walls and the magnitude of the exciting force induced by vibration exciters.

Self-synchronization in vibration exciters under the described synchronous anti-phase counter-rotation of their rotors is analyzed in two stages:

research of self-synchronization stability in vibration exciters of a two-mass system under load taking into account the interaction with the processed material;

research of self-synchronization stability in vibration exciters in idle motion regime.

This study focuses only on the second stage, analyzing the stability of rotation in the system's vibration exciter rotors in idle motion regime.

Calculations

To analyze the self-synchronization stability in rotors of the system's vibration exciters, we used the integral criterion for stability of synchronous motion [1], consisting of finding the condition
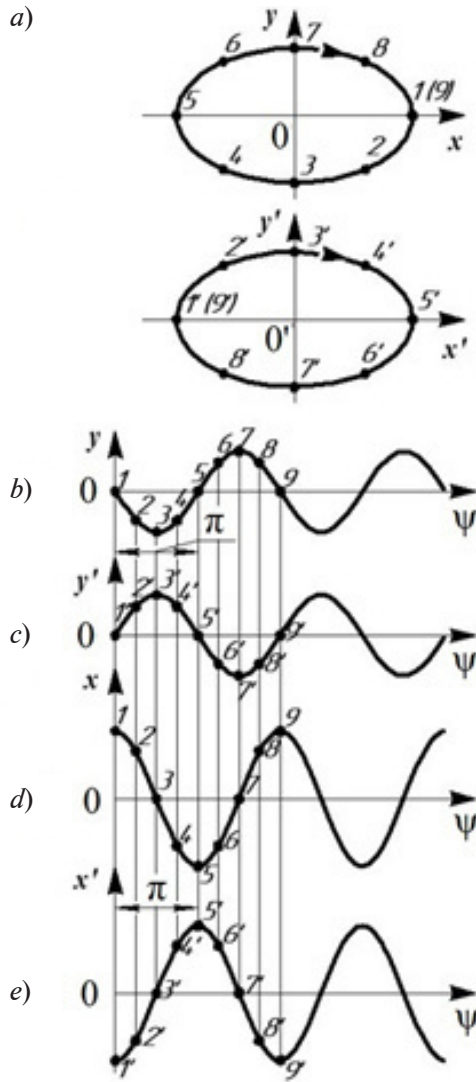
a)

for positive quadratic form of the function D, which is the average value of the Lagrange function of the system over the period:

$$D = \frac{\omega}{2\pi} \int_0^{2\pi/\omega} (T^{(I)} - \Pi^{(I)})dt, \qquad (1)$$

where $T^{(I)}$ and $\Pi^{(I)}$ are the kinetic and potential energies of the oscillatory subsystem.

We compose the equations for kinetic and potential energy of the two-mass mechanical system. The mathematical model for analyzing the self-synchronization stability of the rotors is shown in Fig. 3.

Two unbalanced vibration exciters in the mathematical model are placed on identical flat walls with mass M, each with a moment of inertia I relative to the CoM. The walls are placed parallel to each other and are connected by a pair of elastic springs with the total stiffness c_x and c_y in the longitudinal and transverse directions, placed at the same distances l relative to the wall CoM. The walls can move in a plane perpendicular to the rotation axes of the rotors. The position of the walls is determined by the absolute coordinates x_1, y_1 and x_2, y_2 of their CoM and the rotation angles ψ_1 and ψ_2 of each wall relative to the CoM. The rotors of each of the two vibration exciters, assumed to be identical, are characterized by angles φ_1 (φ_2) around the rotation axis, mass m of unbalanced part of the rotor, eccentricity ε and distance r from the rotation axis to the CoM of each wall. The subscript 1 refers to the lower wall, and 2 to the upper one.

The equations of translational motion of the walls have the form:

$$-M\ddot{x}_1 + F\cos\varphi_1 - c_x(x_1 - x_2) = 0; \qquad (2)$$

$$-M\ddot{x}_2 + F\cos\varphi_2 - c_x(x_2 - x_1) = 0; \qquad (3)$$

$$-M\ddot{y}_1 - F\sin\varphi_1 - c_y(y_1 - y_2) = 0; \qquad (4)$$

$$-M\ddot{y}_2 - F\sin\varphi_2 - c_y(y_2 - y_1) = 0, \qquad (5)$$

where $F = m\varepsilon\omega^2$ is the amplitude value of the exciting force of one vibration exciter.

Fig. 2. Trajectories and phase diagrams for wall oscillations with phase ψ at phase shift $\varepsilon = \pi$ in longitudinal (ε_x) and transverse (ε_y) directions:

trajectories of upper and lower walls (*a*), arrows indicate their directions; vertical coordinates of lower (*y'*) and upper (*y*) walls (*b*, *c*); horizontal coordinates of lower (*x'*) and upper (*x*) walls (*d*, *e*); numbers of points *1−9* and *1'−9'* correspond to positions of the walls at the same points in time

The laws of rotation for the rotors can be written as follows:

$$\varphi_1 = \sigma_1(\omega t + \alpha_1), \quad \varphi_2 = \sigma_2(\omega t + \alpha_2), \qquad (6)$$

where σ_1, σ_2 are the counterclockwise (+1) and clockwise (−1) directions of rotation of the rotors; α_1, α_2 are the initial phases of their rotation.

The strains of the left and right springs connecting the walls under rotation at angles ψ_1 and ψ_2 relative to the CoM (Fig. 4) are expressed as follows:

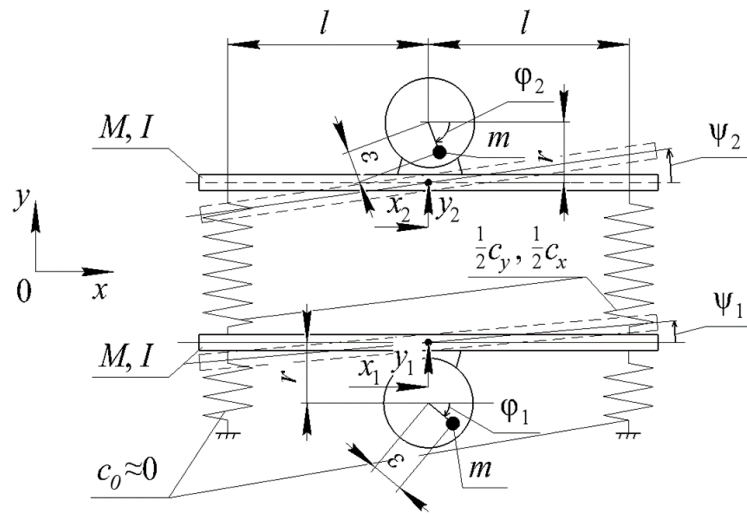$$\Delta_{left} = -l\sin\psi_2 + l\sin\psi_1, \quad \Delta_{right} = l\sin\psi_2 - l\sin\psi_1. \qquad (7)$$

Fig. 3. Mathematical model for synchronous anti-phase oscillations of walls in two-mass system: mass of each wall M; moment of inertia I of each wall; stiffnesses c_x, c_y of the springs in the longitudinal and transverse directions; distances l from centers of mass (CoM) of the walls to the springs; coordinates x_i, y_i of wall CoM; rotation angles ψ_i of each wall relative to CG; rotation angles φ_i of the rotors around the rotation axis; eccentricity ε and distance r from the rotation axis of the rotors to wall CGs (subscripts 1 and 2 correspond to the lower and upper walls, respectively)
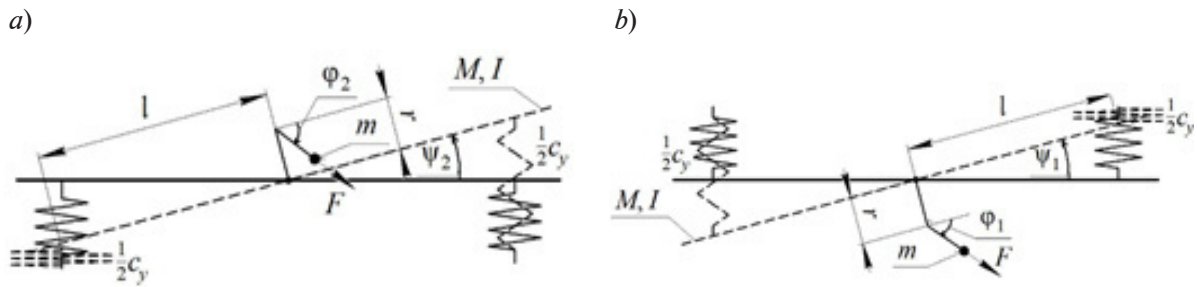
a) *b)*

Fig. 4. Models used to determine the deformations of springs and moments arising upon rotation of upper (*a*) and lower (*b*) walls relative to the CoM

Eqs. (7) do not take into account the deformations of elastic elements in the transverse direction because they are small compared with longitudinal deformations.

Taking into account expressions (7), each wall of the system is subjected to moments from rotational inertia, exciting force of the vibration exciter, and deformations of the right and left springs (see Fig. 4). The equations of rotational motion of the walls relative to the CoM have the form:

$$-I\ddot{\psi}_1 + Fr\cos\varphi_1 - \frac{c_y}{2}l\Delta_{left} + \frac{c_y}{2}l\Delta_{right} = 0; \tag{8}$$

$$-I\ddot{\psi}_2 - Fr\cos\varphi_2 - \frac{c_y}{2}l\Delta_{right} + \frac{c_y}{2}l\Delta_{left} = 0. \tag{9}$$

Because the rotation angles of the walls ψ_1 and ψ_2 are small ($\sin\psi_1 \approx \psi_1$, $\sin\psi_2 \approx \psi_2$), they can be rewritten as follows:

$$-I\ddot{\psi}_1 + Fr\cos\varphi_1 + c_yl^2(\psi_2 - \psi_1) = 0; \tag{10}$$

$$-I\ddot{\psi}_2 - Fr\cos\varphi_2 + c_yl^2(\psi_1 - \psi_2) = 0. \tag{11}$$

We search for a solution for steady-state forced oscillations of the walls in the form

$$x_1 = A_1 \cos \varphi_1 + A_2 \cos \varphi_2; \tag{12}$$

$$x_2 = B_1 \cos \varphi_2 + B_2 \cos \varphi_1; \tag{13}$$

$$y_1 = C_1 \sin \varphi_1 + C_2 \sin \varphi_2; \tag{14}$$

$$y_2 = D_1 \sin \varphi_2 + D_2 \sin \varphi_1. \tag{15}$$

After substituting solutions (12) and (13) into the equations of motion of system (2) and (3), we determine the unknown constants A_1, A_2, B_1 and B_2:

$$A_1 = \frac{F(c_x - M\omega^2)}{(M\omega^2)^2(1-\lambda_x^2)}, \quad A_2 = \frac{Fc_x}{(M\omega^2)^2(1-\lambda_x^2)}; \tag{16}$$

$$B_1 = \frac{F(c_x - M\omega^2)}{(M\omega^2)^2(1-\lambda_x^2)}, \quad B_2 = \frac{Fc_x}{(M\omega^2)^2(1-\lambda_x^2)}, \tag{17}$$

where $\lambda_x = \dfrac{p_x}{\omega}$, $p_x = \sqrt{\dfrac{2c_x}{M}}$.

Evidently, the parameter p_x in the expressions obtained determines the natural frequency of the walls in the longitudinal direction for an equivalent mechanical model for the two-mass system with identical masses M, connected by a spring with the stiffness c_x (Fig. 5,a).

Substituting expressions (14) and (15) for transverse displacements of the walls into equations of motion (4) and (5), we similarly determine the unknown constants C_1, C_2, D_1 and D_2:

$$\tilde{N}_1 = \frac{F(M\omega^2 - c_y)}{(M\omega^2)^2(1-\lambda_y^2)}, \quad \tilde{N}_2 = \frac{-Fc_y}{(M\omega^2)^2(1-\lambda_y^2)}; \tag{18}$$

$$D_1 = \frac{F(M\omega^2 - c_y)}{(M\omega^2)^2(1-\lambda_y^2)}, \quad D_2 = \frac{-Fc_y}{(M\omega^2)^2(1-\lambda_y^2)}, \tag{19}$$

where $\lambda_y = \dfrac{p_y}{\omega}$, $p_y = \sqrt{\dfrac{2c_y}{M}}$.

Similar to the oscillations of the walls in the longitudinal direction, the parameter p_y in the expressions obtained characterizes the natural frequency of the wall oscillations in the transverse direction for the equivalent mechanical model of the system consisting of two masses M connected by a spring with the stiffness c_y (see Fig. 5,b).
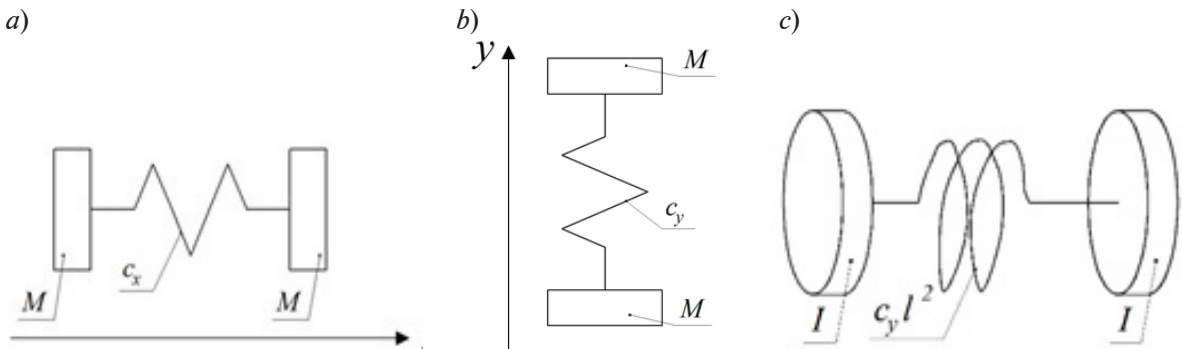

Fig. 5. Equivalent mechanical models for free oscillations of walls in longitudinal (*a*) and transverse (*b*) directions; equivalent mechanical model for their rotational oscillations (*c*)

We also search for solutions to the equations of rotational oscillations of the walls relative to the CoM as harmonic functions of the form

$$E_1 = \frac{Fr(c_y l^2 - I\omega^2)}{(I\omega^2)^2(1-\lambda_c^2)}, \quad E_2 = \frac{-Frc_y l^2}{(I\omega^2)^2(1-\lambda_c^2)};$$
(22)

$$F_1 = \frac{Frc_y l^2}{(I\omega^2)^2(1-\lambda_c^2)}, \quad F_2 = \frac{-Fr(c_y l^2 - I\omega^2)}{(I\omega^2)^2(1-\lambda_c^2)},$$
(23)

where $\lambda_{\tilde{a}} = \dfrac{p_c}{\omega}, \; p = \sqrt{\dfrac{2c_y l^2}{I}}.$

The obtained frequency p_c of free rotational oscillations of the walls corresponds to the equivalent mechanical model of the two-mass system with the same moments of inertia I connected to each other by a spring with the torsional stiffness $c_y l^2$ (see Fig. 5,c).

In accordance with the accepted mathematical model (see Fig. 3), kinetic and potential energies of oscillatory motion of the walls have the form:

$$T^{(I)} = M\frac{(\dot{x}_1^2 + \dot{y}_1^2)}{2} + M\frac{(\dot{x}_2^2 + \dot{y}_2^2)}{2} + I\frac{(\dot{\psi}_1^2 + \dot{\psi}_2^2)}{2},$$
(24)

$$\Pi^{(I)} = \frac{1}{2}c_y\Delta_{left}^2 + \frac{1}{2}c_y\Delta_{right}^2 \approx c_y l^2(\psi_1^2 + \psi_2^2 - 2\psi_1\psi_2).$$
(25)

The condition for stable self-synchronization of the rotors is that the averaged Lagrange function of the system taking the form [1] be positive definite:

$$D = \langle T^{(I)} - \Pi^{(I)} \rangle = \frac{\omega}{2\pi}\int_0^{\frac{2\pi}{\omega}} (T^{(I)} - \Pi^{(I)})dt.$$
(26)

Substituting solutions (12)−(15), (20), (21) for wall displacements into expressions for kinetic and potential energies (24) and (25) and calculating integral (26) for one period of the system's oscillations, we obtain the following form for the averaged Lagrange function:

$$D = \frac{M}{2}\omega^2(\sigma_1\sigma_2(C_1C_2 + D_1D_2)) + \frac{I}{2}\omega^2(F_1F_2 + E_1E_2) -$$
$$-c_y l^2(E_1E_2 + F_1F_2 - 2(E_1F_2 + E_2F_1))\cos(\alpha_1 - \alpha_2) = N\cos(\alpha_1 - \alpha_2),$$
(27)

where $N = \dfrac{M}{2}\omega^2(\sigma_1\sigma_2(C_1C_2 + D_1D_2)) + \dfrac{I}{2}\omega^2(F_1F_2 + E_1E_2) - c_y l^2(E_1E_2 + F_1F_2 - 2(E_1F_2 + E_2F_1)).$

For self-synchronization of vibration exciter rotors to be stable under oppositely directed synchronous rotation of the rotors, i.e., at zero initial phase difference $\alpha_1 - \alpha_2$ and at $\sigma_1 = +1$, $\sigma_2 = -1$, the quadratic form of the averaged Lagrange function D must be positive definite. This is ensured when it has a rough minimum and the multiplier N in expression (27) is negative, i.e.,

$$-\frac{M}{2}\omega^2(C_1C_2 + D_1D_2) + \frac{I}{2}\omega^2(F_1F_2 + E_1E_2) - c_y l^2(E_1E_2 + F_1F_2 - 2(E_1F_2 + E_2F_1)) < 0.$$
(28)

After substituting the constants C_1, C_2, D_1, D_2, E_1 and E_2 from the expressions (18), (19), (22) and (23) into this inequality, we obtain a condition for stable self-synchronization of vibration exciters in the given mode, allowing to optimize the design and operating parameters of the two-mass system:

$$\frac{l^2 r^2(c_y l^2 - 3M\omega^2)}{(I\omega^2)^2(I\omega^2 - 2c_y l^2)} > \frac{M\omega^2 - c_y}{M\omega^2(M\omega^2 - 2c_y)^2}.$$
(29)

Let us analyze the expression obtained for oscillations of the walls below resonance, defined by the relations $c_y > 3M\omega^2$ and $2c_y l^2 > I\omega^2$.

In this case, the following inequality must hold true for self-synchronization of vibration exciters:

$$\frac{c_y - M\omega^2}{M\omega^2(M\omega^2 - 2c_y)^2} > \frac{l^2 r^2(c_y l^2 - 3M\omega^2)}{(I\omega^2)^2(2c_y l^2 - I\omega^2)}. \tag{30}$$

It can be seen from here that the stability of the given oscillation mode can be increased by increasing the frequency ω of the exciting force and the moment of inertia J of the wall, decreasing the mass M of the wall, the distance l from the wall CoM to the points where the springs are attached and the distance r from the wall's center of mass to the axis of rotor.

The stability condition for synchronous anti-phase oscillations of the walls is satisfied automatically for oscillations below resonance for which the relations $c_y > M\omega^2/2$ и $c_y l^2 > I\omega^2$ hold true, since the left-hand side of inequality (29) is always negative and the right side is positive.

Numerical values of the design parameters based on the solution of inequality (29) can be selected by any suitable numerical method, for example, the iteration method.

Conclusion

We found a condition for stable self-synchronization of vibration exciters in a system with two flat walls generating synchronous anti-phase oscillations along elliptical trajectories in opposite directions. The obtained expression allows to optimize the design and operating parameters of the system (frequency of the exciting force, mass of the walls and their moments of inertia, distances from the CoM of the walls to the points where the springs are attached and the distance from the CoM of each wall to the axis of the vibration exciter rotor) at the design stage to ensure the required oscillation mode of the walls, combining crushing of the material grains with transportation.

Further research will be aimed at finding the conditions for stable self-synchronization of rotors in vibration exciters of two-mass systems in operating modes with relative phase shifts and rotation directions providing optimal parameters for attrition and compression procedures in granular materials.

REFERENCES

1. **Blekhman I. I.,** Sinkhronizatsiya dinamicheskikh system [Synchronization of dynamical systems], Nauka Publishing, Moscow, 1971 (in Russian).

2. **Vaisberg L. A., Zarogatsky L. P., Turkin V. Y.,** Vibratory crushers: principles of calculation, design and technological application, Published by VSEGEI [All-Union Geological Institute], Saint-Petersburg, 2004 (in Russian).

3. **Vaisberg L. A.,** Proektirovanie i raschyot vibratsionnykh grohotov [Design and calculation of vibrating screens], Nedra Publishing, Moscow, 1986 (in Russian).

4. **Chelomey V. N.** (Head of Ed.), Vibrations in technology. Reference Book in 6 Vols. Vol. 4. Vibration processes and machines /G. G. Azbel, I. I. Blekhman, I. I. Bykhovsky, et al., Edited by E. E. Lavendel, Mashinostroenie [Machine Building Publ.], Moscow, 1979 (in Russian).

5. **Lavrov B. P.,** Vibratsionnye mashiny s samosinkhroniziruyushchimisya vibratorami (konstruktivnye skhemy i spetsificheskiye osobennosti rascheta) [Vibrational machines with self-synchronizing vibrators (structural design and special aspects of calculation)], Proceedings on theory and application of synchronization phenomenon in machines and devices, Mintis Publ., Vilnius (1966) 55−63 (in Russian).

6. **Ragulskis K. M.,** Self-synchronization of mechanical systems, in 2 Vols., Vol. 1. Ragulskis K. M., Vitkus I. I., Ragulskene V. L., Self-synchronous and vibroimpact systems; Edited by K. M. Ragulskis, Mintis Publ., Vilnius, 1965 (in Russian).

7. **Sizikov V. S., Sizikov S. A.,** K vyboru konstruktsii apparata dlya mekhanoaktivatsii i ottirki mineral'nykh zernistykh sred [On the selection of apparatus construction for mechanical activation and attritioning of mineral granular media], Obogashchenie Rud [Benefication of Ores]. (3) (2023) 49−56 (in Russian).

8. **Sizikov V. S., Sizikov S. A.,** Rational regimes of fine concrete aggregate enrichment using the method of volumetric vibrational impact, Bulletin of Civil Engineers. (6 (71)) (2018) 156−162 (in Russian).

9. **Sizikov V. S., Sizikov S. A.,** Method for processing granular materials and a device for its implementation, Pat. No. 2675554, Russian Federation, MPK B01F 3/18, B01F 11/00, B02C 19/18; Sizikov Valentin S. is a declarant and patentee. No. 2016140584/05; declar. 14.10.2016, publ. 19.12.2018. Bull. No. 35.

10. **Tomchina O. P., Reznichenko V. V., Gorlatov D. V.,** Algorithms of controlling the oscillation field of a vibration unit for transportation of bulk construction materials, Bulletin of Civil Engineers. (1 (48)) (2015) 115−121 (in Russian).

11. **Shokhin A. E., Nikiforov A. N., Salamandra K. B.,** Experimental analysis of oscillations of a two-mass system with self-synchronizing inertial exciters, Bulletin of Science and Technical Development. (12 (124)) (2017) 58−65 (in Russian).

12. **Shagniev O. B., Tomchina O. P., Fradkov A. L.,** Learning speed-gradient synchronization control of the two-rotor vibration setup, IFAC-PapersOnLine. 55 (12) (2022) 144−148.

СПИСОК ЛИТЕРАТУРЫ

1. **Блехман И. И.** Синхронизация динамических систем: М.: Наука, 1971. 894 с.

2. **Вайсберг Л. А., Зарогатский Л. П., Туркин В. Я.** Вибрационные дробилки: основы расчета, проектирования и технологического применения. СПб.: Изд-во ВСЕГЕИ, 2004. 306 с.

3. **Вайсберг Л. А.** Проектирование и расчет вибрационных грохотов. М.: Недра, 1986. 144 с.

4. Вибрации в технике: Справочник в 6 тт. Ред. совет: В. Н. Челомей (пред., гл. ред.) и др. Т. 4. Вибрационные процессы и машины. / Г. Г. Азбель, И. И. Блехман, И. И. Быховский и др. Под ред. Э. Э. Лавендела. М.: Машиностроение, 1981. 509 с.

5. **Лавров Б. П.** Вибрационные машины с самосинхронизирующимися вибраторами (конструктивные схемы и специфические особенности расчета) // К. М. Рагульскис (ред.). Труды по теории и приложению явления синхронизации в машинах и устройствах. Вильнюс: Минтис, 1966. С. 55−63.

6. **Рагульскис К. М.** Самосинхронизация механических систем. В 2 тт. Т. 1. Рагульскис К. М., Виткус И. И., Рагульскене В. Л. Самосинхронные и виброударные системы. Под ред. д-ра техн. наук К. М. Рагульскиса. Вильнюс: Минтис, 1965. 186 с.

7. **Сизиков В. С., Сизиков С. А.** К выбору конструкции аппарата для механоактивации и оттирки минеральных зернистых сред // Обогащение руд. 2023. № 3. С. 49−56.

8. **Сизиков В. С., Евтюков С. А.** Рациональные режимы обогащения мелких заполнителей бетонов методом виброобъемного воздействия // Вестник гражданских инженеров. 2018. № 6 (71). С. 156−162.

9. **Сизиков В. С., Сизиков С. А.** Способ переработки зернистых материалов и устройство для его осуществления. Пат. 2675554 Российская Федерация, МПК B01F 3/18, B01F 11/00, B02C 19/18; заявитель и патентообладатель Сизиков В. С. № 2016140584/05; заявл. 14.10.2016; опубл. 19.12.2018. Бюл. № 35. 2 с.

10. **Томчина О. П., Резниченко В. В., Горлатов Д. В.** Алгоритмы управления вибрационным полем виброустановки для транспортирования сыпучих строительных материалов // Вестник гражданских инженеров. 2015. № 1 (48). С. 115−121.

11. **Шохин А. Е., Никифоров А. Н., Саламандра К. Б.** Экспериментальный анализ колебаний двухмассовой системы с самосинхронизирующимися инерционными вибровозбудителями // Вестник научно-технического развития. 2017. № 12 (124). С. 58−65.

12. **Shagniev O. B., Tomchina O. P., Fradkov A. L.** Learning speed-gradient synchronization control of the two-rotor vibration setup // IFAC-PapersOnLine. 2022. Vol. 55. No. 12. Pp. 144−148.

THE AUTHOR

SIZIKOV Valentin S.
Institute for Problems of Mechanical Engineering of RAS
61 Bolshoi Ave. of Vasilievsky Island, St. Petersburg, 199178, Russia
sizikovvs@yandex.ru
ORCID: 0000-0001-9438-5711

СВЕДЕНИЯ ОБ АВТОРЕ

СИЗИКОВ Валентин Станиславович – *кандидат технических наук, научный сотрудник Института проблем машиноведения РАН.*

199178, Россия, г. Санкт-Петербург, Большой проспект В. О., 61.
sizikovvs@yandex.ru
ORCID: 0000-0001-9438-5711

УСЛОВИЯ ПУБЛИКАЦИИ СТАТЕЙ
в журнале «Научно-технические ведомости
Санкт-Петербургского государственного политехнического университета.
Физико-математические науки»

1.ОБЩИЕ ПОЛОЖЕНИЯ

Журнал «Научно-технические ведомости Санкт-Петербургского государственного политехнического университета. Физико-математические науки» является периодическим печатным научным рецензируемым изданием. Зарегистрирован в Федеральной службе по надзору в сфере информационных технологий и массовых коммуникаций (Свидетельство ПИ №ФС77-52144 от 11 декабря 2012 г.) и распространяется по подписке агентства «Роспечать» (индекс издания 71823).

С 2008 года журнал издавался в составе сериального издания "Научно-технические ведомости СПбГПУ". **Сохраняя преемственность и продолжая научные и публикационные традиции сериального издания «Научно-технические ведомости СПбГПУ», журнал издавали под сдвоенными международными стандартными сериальными номерами ISSN 1994-2354 (сериальный) 2304-9782.** В 2012 году он зарегистрирован как самостоятельное периодическое издание **ISSN 2304-9782** (Свидетельство о регистрации ПИ № ФС77-52144 от 11 декабря 2012 г.). С 2012 г. начат выпуск журнала в двуязычном оформлении.

Издание входит в Перечень ведущих научных рецензируемых журналов и изданий (перечень ВАК) и принимает для печати материалы научных исследований, а также статьи для опубликования основных результатов диссертаций на соискание ученой степени доктора наук и кандидата наук по следующим основным научным направлениям: **Физика, Математика, Механика**, включая следующие шифры научных специальностей: 1.1.8., 1.1.9., 1.3.2., 1.3.3., 1.3.4., 1.3.5., 1.3.6., 1.3.7., 1.3.8., 1.3.11., 1.3.19.

Журнал представлен в Реферативном журнале ВИНИТИ РАН и включен в фонд научно-технической литературы (НТЛ) ВИНИТИ РАН, а также в международной системе по периодическим изданиям «Ulrich's Periodicals Directory». Индексирован в базах данных «Российский индекс научного цитирования» (РИНЦ), Web of Science (Emerging Sources Citation Index).

Периодичность выхода журнала – 4 номера в год.

Редакция журнала соблюдает права интеллектуальной собственности и со всеми авторами научных статей заключает издательский лицензионный договор.

2. ТРЕБОВАНИЯ К ПРЕДСТАВЛЯЕМЫМ МАТЕРИАЛАМ
2.1. Оформление материалов

1. Рекомендуемый объем статей – 12-20 страниц формата А-4 с учетом графических вложений. Количество графических вложений (диаграмм, графиков, рисунков, фотографий и т.п.) не должно превышать шести.

2. Число авторов статьи, как правило, не должно превышать пяти человек.

3. Авторы должны придерживаться следующей обобщенной структуры статьи: вводная часть (актуальность, существующие проблемы – объем 0,5 – 1 стр.); основная часть (постановка и описание задачи, методика исследования, изложение и обсуждение основных результатов); заключительная часть (предложения, выводы – объем 0,5 – 1 стр.); список литературы (оформление по ГОСТ 7.0.5-2008).

В списки литературы **рекомендуется** включать ссылки на научные статьи, монографии, сборники статей, сборники конференций, электронные ресурсы с указанием даты обращения, патенты.

Как правило, **нежелательны** ссылки на диссертации и авторефераты диссертаций (такие ссылки допускаются, если результаты исследований еще не опубликованы, или не представлены достаточно подробно).

В списки литературы **не рекомендуется** включать ссылки на учебники, учебно-методические пособия, конспекты лекций, ГОСТы и др. нормативные документы, на законы и постановления, а также на архивные документы (если все же необходимо указать такие источники, то они оформляются в виде сносок).

Рекомендуемый объем списка литературы для обзорных статей – не менее 50 источников, для остальных статей – не менее 10.

Доля источников давностью менее 5 лет должна составлять не менее половины. Допустимый процент самоцитирования – не выше 10 – 20. Объем ссылок на зарубежные источники должен быть не менее 20%.

4. УДК (UDC) оформляется и формируется в соответствии с ГОСТ 7.90-2007.

5. Набор **текста** осуществляется в редакторе **MS Word.**

6. **Формулы** набираются в редакторе MathType (не во встроенном редакторе Word) (мелкие формулы, символы и обозначения набираются без использования редактора формул). **Таблицы** набираются в том же формате, что и основной текст. В тексте буква «ё» заменяется на букву «е» и оставляется только в фамилиях.

7. **Рисунки** (в формате .tiff, .bmp, .jpeg) и **таблицы** оформляются в виде отдельных файлов. Шрифт – **Times New Roman**, размер шрифта основного текста – 14, интервал – 1,5. Таблицы большого размера могут быть набраны кеглем 12. Параметры страницы: поля слева – 3 см, сверху и снизу – 2 см, справа – 1,5 см. Текст размещается без знаков переноса. Абзацный отступ – 1 см.

2.2. Представление материалов

1. Представление всех материалов осуществляется в электронном виде через электронную редакцию (http://journals.spbstu.ru). После регистрации в системе электронной редакции автоматически формируется персональный профиль автора, позволяющий взаимодействовать как с редакцией, так и с рецензентом.

2. Вместе с материалами статьи должно быть представлено экспертное заключение о возможности опубликования материалов в открытой печати.

3. Файл статьи, подаваемый через электронную редакцию, должен содержать только сам текст без названия, списка литературы, аннотации и ключевых слов, фамилий и сведений об авторах. Все эти поля заполняются отдельно через электронную редакцию.

2.3. Рассмотрение материалов

Предоставленные материалы (п. 2.2) первоначально рассматриваются редакционной коллегией и передаются для рецензирования. После одобрения материалов, согласования различных вопросов с автором (при необходимости) редакционная коллегия сообщает автору решение об опубликовании статьи. В случае отказа в публикации статьи редакция направляет автору мотивированный отказ.

При отклонении материалов из-за нарушения сроков подачи, требований по оформлению или как не отвечающих тематике журнала материалы не публикуются и не возвращаются.

Редакционная коллегия не вступает в дискуссию с авторами отклоненных материалов.

При поступлении в редакцию значительного количества статей их прием в очередной номер может закончится **ДОСРОЧНО**.

E-mail: physics@spbstu.ru,
Тел. редакции 8 (812) 552-62-16.
Сайт журнала: https://physmath.spbstu.ru/